Numerical Simulation of Flow and Chemical Transport in Integrated Surface-Subsurface Hydrologic Systems

By

Joel E. VanderKwaak

A thesis

presented to the University of Waterloo

in fulfillment of the

thesis requirement for the degree of

Doctor of Philosophy

in

Earth Sciences

Waterloo, Ontario, Canada, 1999

The University of Waterloo requires the signatures of all persons using or photocopying this thesis. Please sign below, and give address and date.

Abstract

Stream water quality is affected by processes occurring in and below the stream channel, by baseflow contributions from groundwater, and by the short-duration, high-volume contributions from precipitation events. Defining the source and pathway of stream water inputs is a prerequisite to understanding the impact of contaminants originating in rainfall, from industry and agriculture, and from urban runoff. Numerical models provide a useful tool in evaluating possible flowpaths and the timing and magnitude of stream inputs from various sources.

An integrated numerical model is developed and evaluated in this work. This numerical model considers the flow of water and transport of multiple solutes on the two-dimensional land surface and three-dimensional, dual continua subsurface. Linkage is through first-order, physically based flux relationships or through continuity assumptions. Coupling of flow and transport is achieved by assembling and solving one system of discrete algebraic equations so that water and solute fluxes between continua are determined as part of the solution. Specified boundary conditions can be spatially- and temporally variable, or in the case of state-dependent flux boundaries, can be specified as nonlinear functions of the local flow or transport solution.

The numerical model is modular in form, is tailored towards irregular geological, surficial and areal geometries, and utilizes robust and efficient discretization and solution techniques. A new prism-based discretization is introduced and shown to be consistent with two and three-dimensional finite elements, while utilizing less memory and computational effort and generating significantly fewer negative influence coefficients. An adaptive temporal-weighting scheme is presented which partitions the flow and transport equations into active and inactive zones. Solutions for inactive equations are calculated using explicit temporal weighting and are excluded from the flow or transport Jacobians, reducing assembly and solution time.

The numerical model is evaluated by simulating two-dimensional laboratory and three-dimensional field experiments of coupled surface-subsurface flow and transport. Observed surface discharge volumes and timings are simulated with reasonable accuracy using published or measured

parameter values and minimal calibration. The observed dynamic response is a nonlinear function of multiple parameters, affected by subsurface permeability, surface roughness, topography, and initial conditions. Excess rainfall and groundwater seepage flow overland, generating surface ponding and streamflow along topographic lows. The ponded surface water forms an internal, transient constraint on the porous medium pressure head at the land surface. Solutions based on traditional seepage face algorithms do not reflect the effects of this ponded surface water on the distribution of subsurface head gradients. Groundwater seepage is therefore overestimated during rainfall events while infiltration of ponded surface water is neglected at all times.

Simulations of the transport of a conservative tracer introduced with rainfall indicate that processes affecting solute concentrations in the surface water are restricted to a relatively thin region adjacent to the land surface. Concentrations in surface water are very sensitive to which equations the rainfall boundary condition (i.e. specified flux) is applied. For rainfall applied to the surface equations, mixing between the surface and subsurface continua is more heavily influenced by the magnitude of diffusive/dispersive exchange coefficient. The magnitude of advective exchange is controlled by hydrodynamics within the porous medium and not by the movement of excess rainfall from the porous medium to the surface continuum. While having little affect on the flow solution, subtleties in rainfall boundary condition assignment in the discrete equations impact predictions of tracer concentrations in discharge water and, therefore, also affect interpretations of water origin.

Application of the coupled surface-subsurface model to the transport of conservative tracer in the field-scale experiment re-enforces the conclusion that mixing processes occurring at the land surface interface dominate tracer concentrations in stream discharge. Simulated hydrograph separations (i.e. relative concentration multiplied by stream discharge) replicate separations based on measured values with reasonable accuracy only if rainfall is applied to the surface equations and both advective (i.e. infiltration/seepage) and diffusive exchange processes are considered. Simulated flux-weighted concentrations, however, exceed measured concentrations during hydrograph rise. Simulation of field-scale transport processes is considerably more complicated than at the laboratory-scale, where topography is better defined and extremely fine spatial discretization can be

utilized. Successful simulation of coupled surface-subsurface transport depends on the accurate representation of the spatial and temporal variability of water exchange processes (i.e. advection) and diffusive-type processes associated with concentration differences between continua.

The field-scale simulations clarify the role of the capillary fringe on streamflow generation in the relatively homogeneous sand underlying CFB Borden. The coupled surface-subsurface flow model is able to reproduce the observed rapid water table response and resulting overland and stream flow. Observed surface discharge volumes and timing are simulated with reasonable accuracy using published or measured parameter values and minimal calibration. The simulated response of the capillary fringe to rainfall is consistent with both theory and observations but suggest that increased subsurface head gradients do not cause significant groundwater seepage. Rather, infiltration rates along the stream axis are reduced, with runoff formed largely by excess rainfall over a dynamic contributing area. The corresponding transport simulations suggest that, despite the rapid, large-scale response of the capillary fringe, rainfall tracer dilution occurs largely by diffusive processes as water flows over the land surface to the stream, over relatively short flow paths, and subsequently down the stream channel. Tracer originating above the initial water table enters the surface water by similar processes, augmenting the small volumes of seepage (advective transport) caused by increased subsurface hydraulic gradients. The simulations suggest that hydrograph separation theory is fundamentally flawed if diffusive modification of tracer concentrations in surface water is prevalent in nature.

Table of Contents

List of Tables

List of Figures

Acknowledgments

Special thanks to:

Ed Sudicky and Keith Loague, for encouragement, patience and the occasional kick in the butt.

Bill and Sheri Annable, for continued friendship, diversion, digitizing, and office space.

Additional thanks to:

Jos and Lavinia Beckers; Ken Bencala; Bill 'Spook' Blackport; Jim Clark; Bill 'Harley' Davidson; Mike and Mary Diepstra; Ray and Erma Eshenour; Mark Etringer; Paul 'Ty' Ferré; Peter Forsyth; Shaun and Nori Frape; Emil Frind; Horst Gerke; Bob Gillham; Steve Gorelick; Dan Green; Peter Huyakorn; Bob, Marge and Jesse Ingleton (and the Pandemonium Blues Band); C. Rhett Jackson; Nick Kouwen; Dave Lawson; Sanford Leetsma; Kerry and Carol MacQuarrie; Klaus Ulrich 'Uli' Mayer; Margaret Mayne; Rob McLaren; Clarence Menninga; Chris Miron; Gavin Mudd; Larry Nyhoff; Vico and Theresa Paloschi; Sorab Panday; Rob Pockar; Will and Beth Robertson; Dave Rudolph; Frank Schwartz; Ken and Karen Skene; Kelly Slough; Leslie Smith; Jeff Sutherland; René Therrien; Lloyd Townley; André Unger; Rien van Genuchten; Craig VandenBerg; Jeanette, Joe, Joyce, and Rodger VanderKwaak; Bert and Sheri Webb; Steve Wheatcraft; Dave Young; John-Paul, Shima and adopted-family Zonneveld; and George Zyvoloski.

Funding provided by:

My wife, Jeanette; Department of Earth Sciences, University of Waterloo; OGS (Ontario Graduate Scholarship Program); NSERC (National Sciences and Engineering Research Council of Canada); EPRI (Electric Power Research Institute, Palo Alto, California); CESIR (Stanford University-U.S. Geological Survey Center for Earth Science Information Research)

Dedication

For my wife,

Jeanette VanderKwaak,

for support exceeding that stipulated in the fine print;

For my parents,

Joe and Joyce Vander Kwaak,

again, for planting the seeds;

And for my grandparents,

Nicolaas and Bastiaantje van der Kwaak

and

Simon and Hilda Viss,

for courage.

Chapter 1 Introduction

Streams, rivers and lakes are visible expressions of the terrestrial hydrologic cycle. These features represent the intersection and interaction of precipitation with water originating from both above and below the land surface. Surface water is in intimate contact with the biosphere and chemically reflects the biology, the local geology and climate. Recent reporting in the United States [*USEPA*, 1998] indicates that the leading cause of surface water quality impairments is polluted runoff (see Table 1-1). Degradation of surface water quality is widespread (see Table 1-2), arising from human activities in urban areas and from forestry, farming, ranching, and mining operations. Surface water quality impairments affect wetlands, stream corridors, and coastal areas critical to the health of aquatic systems. Impairments include siltation and habitat alteration and the addition of excess nutrients (e.g. nitrogen and phosphorus), bacteria, oxygen-depleting substances, metals, pesticides, and organic toxic chemicals.

Understanding and predicting stream water quality requires the concomitant knowledge of water origin and flow paths [e.g. *Burns*, 1980; *Wheater et al.*, 1986; *Blowes and Gillham*, 1988; *Christopherson and Neal*, 1990; *Beck et al.*, 1990; *Mulholland et al.*, 1990; *Bishop et al.*, 1990; *Wilson et al.*, 1990; *Lundin*, 1995; *Mulder et al.*, 1995; *Elsenbeer et al.*, 1995; *Lundin*, 1995; *Al and Blowes*, 1996; and others] as stream water chemistry is intimately linked with catchment hydrology [e.g. *Baily et al.*, 1974; *Braden and Uchtmann*, 1985; *Ahuja*, 1986; *Pionke et al.*, 1988; *McKnight and Bencala*, 1990; *Leonard*, 1990; *Cirmo and McDonnell*, 1997; *Anderson et al.*, 1997 a,b]. While groundwater baseflow can provide long-term, low-concentration contributions of contaminants to surface water bodies, short-duration, high concentration contributions to surface water bodies may arise during precipitation or snow-melt events. Flow over the land surface or through preferential subsurface pathways may minimize soil contact and the associated buffering process. Concentrations of contaminants arriving at surface

water bodies may differ little from concentration values at the source [e.g. *Sklash*, 1990; *Eshleman et al.*, 1993]. The dominance of sluggish flowpaths through the porous medium or fast flowpaths on the land surface, or through preferential subsurface pathways, is difficult to determine, yet is crucial to developing the ability to predict and protect surface water quality.

As stated in *USEPA* [1998]: "More accurate estimates of the sources, transport, and impacts of polluted runoff are needed to guide the implementation of management actions. Effective monitoring of polluted runoff is challenging because of many variables, including intensity of storms, the time of year, and a mosaic of different environmental settings and land uses. Because of its wide distribution, monitoring alone cannot adequately characterize polluted runoff. Better survey methods and computerized models are needed, with special attention given to determine the location and relative contribution of sources of nitrogen and phosphorus. Modeled estimates need to be validated using available water quality data from stations at the mouth of the watersheds." In the opinion of this author, however, numerical models also require validation against information internal to the catchment, ensuring that the conceptual models of hydrologic response and solute transport are self-consistent. This thesis presents the development and evaluation of an integrated, physically-based numerical model of surface and subsurface hydrologic response to precipitation and the transport of multiple chemical species within such coupled hydrologic systems.

Rank	Rivers	Lakes	Estuaries
1	Agriculture	Agriculture	Industrial Discharges
2	Municipal Point Sources	Unspecified Point Sources	Urban Runoff/Storm Sewers
3	Hydrologic Modification	Atmospheric Deposition	Municipal Point Sources
4	Habitat Modification	Urban Runoff/Storm Sewers	Upstream Sources
5	Urban Runoff/Storm Sewers	Municipal Point Sources	Agriculture

Table 1-1. Five leading sources of surface water quality impairment related to human activities [after *USEPA*, 1998].

Surveyed	Partially or fully impaired	Threatened water quality
72% of coastal estuaries	38 %	4 %
94 % of Great Lakes shore miles	97 %	1 %
40 % of all lake acres	39 %	10 %
19 % of all stream miles	36 %	8 %

Table 1-2. Summary of state reports on surface water conditions in 1996 [after *USEPA*, 1998].

1.1 Previous Work: Field Observations

Results from numerous laboratory and field observations provide a rather extensive list of surface and subsurface processes affecting the transport of solutes in coupled surface-subsurface flow regimes. These processes form a continuum, but have been broadly categorized into those occurring in the hillslope and riparian zones, and into in- and near-stream (hyporeic) regions. Processes affecting water and solute exchange between streams and the underlying and adjacent porous medium can be summarized as: "pumping effects" due to the iteration of small-scale water depth (pressure) variations and stream bed geometry (i.e. ripples and dunes) [e.g. *Thibodeaux and Boyle*, 1987; *Savant*, 1987; *Elliot and Brooks*, 1997a,b]; shallow water exchange due to variations in water surface slopes, in turn caused by stream bed topographic variation [e.g. *Harvey and Bencala*, 1993; *McMahon and Bohlke*, 1996]; shallow substream flow via preferential pathways in the stream bed, enhanced by stream curvature [e.g. *Vaux*, 1968; *Kennedy et al.*, 1984; *Jackman et al.*, 1984; *Castro and Hornberger*, 1991; *Harvey and Bencala*, 1993; *McMahon and Bohlke*, 1996]; and interaction between stream stage and the local groundwater flow system (bank storage) [e.g. *Cooper and Rorabaugh*, 1963; *Pinder and Sauer*, 1971; *Nolan and Hill*, 1990].

The local groundwater flow system provides base flow to streams [*Toth*, 1963; *Freeze and Witherspoon*, 1968] and lakes [e.g. *Winter*, 1983], and is largely driven by topography and the slow drainage of water from the unsaturated zone between precipitation events. *Harvey and Bencala* [1993] suggest that small-scale topographic controls on surface-subsurface water exchange can affect solute transport processes at larger scales, that stream exchanges may intersect regional flow, and that the volume of water exchange may be greater than total baseflow. Water fluxes from riparian zones and hillslopes increase sharply in response to precipitation events, overwhelming both baseflow and near- and in-stream exchange processes. Surface and subsurface flow processes interact to transport water and solutes to the stream during these high-flux events.

Hillslope and vadose zone hydrology have received considerable attention in the past 40 years, and a complete review of relevant field observations and associated theory is clearly beyond

the scope of this brief introduction. The following paragraphs attempt to summarize extensive discussions provided in the texts edited by *Kirkby* [1978] and *Anderson and Burt* [1985, 1990], and the reviews by *Freeze* [1974], *Beven and Germann* [1981], *Dunne* [1983], *White* [1985], *Nielsen et al.* [1986], *van Genuchten and Jury* [1987], *Kirkby* [1988], *Feddes et al.* [1988], *Gee et al.* [1991], *Aqua Terre Consultants* [1991], *Bren* [1993], and *Bonell* [1993].

Hillslope hydrology can be described by combinations of subsurface and surface processes, which interact at the land surface. Processes by which subsurface flow can rapidly contribute to streamflow are as follows: increasing hillslope transmissivity as infiltration generates higher saturations and/or perched water tables above relatively low hydraulic conductivity layers [e.g. *Whipkey*, 1965; *Kirkby and Chorley*, 1967; *Whipkey and Kirkby*, 1978; *Dunne*, 1978; *Rodhe*, 1989; *Bishop et al.*, 1990]; unsaturated water flow (interflow or throughflow) may arise from rapid saturation of near-surface porous medium causing a transient anisotropy in the hydraulic conductivity [*Whipkey and Kirkby*, 1978; *Zalevsky and Sinai*, 1981; *McCord et al*, 1991; *Jackson*, 1992]; near-stream groundwater ridging resulting from a rapid change to positive water pressure in a tension-saturated porous medium following the addition of a small volume of water at the land surface [e.g. *Ragan*, 1968; *Sklash and Farvolden*, 1979; *Gillham*, 1984; *Stauffer and Dracos*, 1986; *Abdul and Gillham*, 1985, 1989]; and preferential (bypass) flow through lower storage capacity, higher permeability features such as root holes, cracks or pipes in soils, or through fractures or dissolution features in bedrock [e.g. *Whipkey*, 1965; *Whipkey and Kirkby*, 1978; *Moseley*, 1979, 1982; *Beven and Germann*, 1982; *Germann*, 1990; *Luxmoore et al.*, 1990; *McDonnell*, 1990; *Montgomery et al.*, 1997; *Anderson et al.*, 1997]. Such higher permeability features may extend outside local topographic boundaries, linking rapid streamflow response to the regional groundwater system [e.g. *Generaux et al.*, 1993].

Surface saturation and possible subsurface discharge (seepage or return flow) can occur [e.g. *Chorley*, 1978]: when subsurface flow converges in slope concavities and water arrives faster than can be transmitted downslope as subsurface flow [e.g. *Kirkby and Chorley*, 1967; *Dunne and Black*, 1970; *Hewlett and Nutter*, 1969, 1970; *Beven*, 1977]; where soil layers conducting subsurface flow are locally thin [e.g. *Kirkby and Chorley*, 1967]; where perched water tables or capillary fringes intersect the land

surface [e.g. *O'Loughlin*,1981; *Gillham*, 1984]; and by water displacement or translation of pressure waves (piston flow) from the hillslope to near-stream saturated or wetland areas [e.g. *Hewlett and Hibbert*, 1967; *Hewlett and Nutter*, 1970; *Waddington et al.*, 1993].

Rainfall may be converted directly to overland flow via: precipitation rates in excess of the maximum saturated hydraulic conductivity and durations longer than the time required for surface saturation [*Horton*, 1933]; and precipitation onto saturated soil generated in dynamic (variable) source areas [*Hewlett and Hibbert*, 1967; *Kirkby and Chorley*, 1967; *Ragan*, 1968; *Betson and Marious*, 1969; *Dunne and Black*, 1970]. Overland flow velocities may be considerably greater than those in the subsurface. The flow regime may be classified as mixed sheet or rill (channels and gullies) and is neither fully turbulent or fully laminar [e.g. *Moore and Foster*, 1990]. Water may be stored in surface depressions or infiltrate downslope. Many of the surface-subsurface exchange mechanisms defined previously for streams may also apply to overland flow [e.g. *Snyder and Woolhiser*, 1985]. Rainfall directly onto streams bypasses the hillslope entirely, providing an early peak in stream discharge. Superimposed upon the previous processes are evaporation and transpiration.

Some or all of the streamflow generating mechanisms may operate simultaneously on a given watershed [e.g. *Pilgrim et al.*, 1978]. The relative importance of each may fluctuate seasonally or even during a single precipitation event as a function of precipitation intensity and antecedent conditions [*Whipkey*, 1965; *Beven*, 1978]. As stated by *Whipkey and Kirkby* [1978] "there are thus a bewildering number of possibilities for the dominant processes and response times in forming a slope hydrograph. At very low rainfall intensities (relative to soil permeability), unsaturated subsurface flow or groundwater flow may be dominant, leading to response times of many weeks. At moderate storm intensities, saturated subsurface flow often becomes more important in well-horizonated soils, with or without some saturation overland flow. At extreme storm intensities, infiltration-excess overland flow may dominate. It becomes easy to see how the wide range of observed responses can arise, and how difficult it is to make detailed generalizations or models for more than a narrow range of soil conditions at a time."

1.2 *Previous Work: Numerical Modelling*

The basic components of an integrated surface-subsurface flow model have been known for some time [*Freeze and Harlan*, 1969]. A general overview of physically based watershed hydrologic modeling can also be found in papers by *Freeze* [1974, 1978], *Dunne* [1983], *Germann* [1988], *Kirkby* [1988], *Bonell* [1993], and *O'Connell and Todini* [1996]. The texts by *Anderson and Burt* [1985] and *Singh* [1996 a,b] summarize a large number of existing surface and watershed hydrologic models. Numerical models have been developed for surface water flow [e.g. *Wooding*, 1965 a,b; *Crawford and Linsley*, 1966; *Chow and Ben-Zvi*, 1973; *Xanthopoulos and Koutitas*, 1976; *Ponce*, 1978; *Vieira*, 1983; *Hromadka et al.*, 1985, 1987; *Zhang and Cundy*, 1989; *Woolhiser et al.*, 1990, 1996; *Meselhe and Holly*, 1993; *Gottardi and Venutelli*, 1993; *Playan et al.*, 1994; *di Giammarco et al.*, 1996; *Feng and Moltz*, 1997]; for variably-saturated flow in porous media [e.g. *Freeze and Witherspoon*, 1968; *Freeze*, 1971; *Neuman*, 1973; *Narasimhan and Witherspoon*, 1976; *Narasimhan et al.*, 1978; *Beven*, 1977, 1978; *Huyakorn et al.*, 1984, 1986 a,b; *Simunek et al.*, 1985; *Beven et al.*, 1987; *Binley et al.*, 1987, 1989 a,b; *Paniconi and Wood*, 1993; *Calver and Wood*, 1996]; and for flow in dual-continua subsurface materials [e.g. *Edwards et al.*, 1979; *Hoogmoed and Bouma*, 1980; *Neretnieks and Rasmuson*, 1984; *Davidson*, 1985 a,b; *Germann*, 1985; *Beven and Clarke*, 1986; *Pruess*, 1991; *Jarvis et al.*, 1991; *Gerke and van Genuchten*, 1993a,b, 1996; *Updegraff et al.*, 1991; *Smettem et al.*, 1991; *Gwo et al.*, 1994]. Numerical models of surface water flow generally consider subsurface processes using an infiltration mass sink [e.g. *Green and Ampt*, 1911], while models of subsurface water flow consider surface processes via a seepage face sink [e.g. *Neuman*, 1973]. Coupling of dual continua subsurface flow processes is accomplished using a one-way Green-Ampt type sink [e.g. *Beven and Clarke*, 1986]; first-order, quasi-steady, exchange relationships driven by pressure gradients [e.g. *Barenblatt et al.*, 1960; *Warren and Root*, 1963]; or pressure continuity assumptions [e.g. *Therrien and Sudicky*, 1996].

Coupled surface-subsurface flow models have also been developed [e.g. *Smith and Woolhiser*, 1971; *Freeze*, 1972 a,b, 1974; *Beven and Kirkby*, 1979; *Cunningham and Sinclair*, 1979; *Akan and Yen*, 1981; *Smith and Hebbert*, 1983; *Abbott et al.*, 1986a,b; *Govindaraju and Kavvas*, 1991; *Brown*, 1995; *Pohll et*

al., 1996; *Perkins and Koussis*, 1996; *Querner*, 1997; *Bronstert and Plate*, 1997]. With the exception of *Brown* [1995], coupling in surface-subsurface flow models is accomplished by matching boundary conditions at the land surface interface. The boundary at the land surface is assumed to be a specified flux until surface ponding occurs, at which point the pressure head at the land surface is constrained to a value equivalent to the surface water depth. Such an approach presents both algorithmic and computational difficulties, as subsurface response is both transient and spatially variable in complex topography overlaying a heterogeneous subsurface hydraulic conductivity. Coordinating the interaction between coupled models at internal boundaries represents a severe numerical challenge for transient system responses [e.g. *Beven*, 1985; *Perkins and Koussis*, 1996]. Further complexity arises in the boundary conditions describing the partitioning of rainfall between the porous medium and macropores or between the porous medium and surface continua [e.g. *Brown*, 1995].

Several of the referenced studies deserve further discussion. Using the finite difference method, *Freeze* [1971, 1972 a,b] coupled three-dimensional variably-saturated subsurface flow with one-dimensional channel flow, with groundwater seepage routed to the stream with a simple time-delay algorithm. His simulations of hypothetical hillslopes illustrate the role of subsurface flow on streamflow generation, and the rarity of Hortonian overland flow. *Beven* [1977, 1978] utilized the finite element method to simulate subsurface flow in two-dimensional hillslopes, thereby demonstrating the role of topography, slope convergence, and antecedent moisture conditions on hydrologic response. More recently, *Brown* [1995] investigated coupled surface-subsurface flow on hillslopes by redefining the capacitance and conductivity of the uppermost layer in the TRUST flow simulator [*Narasimhan et al.*, 1978]. Surface flow was represented by a one-dimensional form of the Darcy-Weisbach equation with the two-dimensional Richards' equation governing subsurface flow. Modified porous medium characteristic curves were utilized to include effects of relatively high macropore permeabilities near saturation. His simulations indicate macropores enhance stream discharge contributions from soil horizons, and that channel geometry and structural heterogeneity affects the relative contribution of surface and subsurface flow. Brown's work is significant, as the

discrete surface and subsurface flow equations are solved simultaneously, eliminating iterative matching of boundary conditions. None of these efforts considered solute transport.

The Système Hydrologique Européen (SHE) [*Beven*, 1985; *Abbott et al.*, 1986 a,b; *Bathurst*, 1986a,b; *Bathurst et al.*, 1996; *Refsgaard and Storm*, 1996] represents the most elaborate suite of physically-based catchment models in existence. In its original form [*Beven*, 1985; *Abbott et al.*, 1986 a,b; *Bathurst*, 1986a,b], SHE consisted of code modules describing one-dimensional channel flow, two-dimensional (rectangular plan) overland flow, one-dimensional vertical unsaturated flow in porous media, and two-dimensional (rectangular plan) saturated groundwater flow. Additional code modules provided source/sink terms for evapotranspiration, snowmelt, and canopy interception. Flow processes were simulated separately, with independent time steps and a mixture of explicit and implicit techniques. An interface module synchronized time steps and provided matching boundary conditions. Subsurface discretization in SHE precludes consideration of a significant number of the runoff generation mechanisms discussed above, while boundary condition convergence is reported to be difficult [e.g. *Beven*, 1985]. *Bathurst et al.* [1996] and *Refsgaard and Storm* [1996] indicate ongoing improvements in numerical methods, and the inclusion of modules describing solute and sediment transport, geochemical processes, erosion, dual subsurface porosity, and an extension to three dimensional groundwater (saturated) flow. Further elaboration is omitted here due to a paucity of published documentation.

Bailey et al. [1974] described the basic components of a coupled surface-subsurface solute transport model which, when "piggybacked" onto a coupled flow model [e.g. *Freeze and Harlan*, 1969], would provide a tool useful for predicting pesticide and nutrient runoff. A large number of models have been developed along these lines [e.g. *Metcalf and Eddy et al.*, 1971; *Donigian et al.*, 1977; *Huber and Dickenson*, 1988; *Bicknell et al.*, 1993; *Donigian et al.*, 1996; *Huber*, 1996], but, while integrating a substantial number of surface flow and transport processes, these models generally lack rigorous consideration of subsurface processes.

A step towards integration of surface and subsurface processes was presented by *Govindaraju* [1996], who, by matching boundary conditions, could couple two-dimensional variably-saturated

subsurface flow and transport with one-dimensional flow and transport on the land surface. Empirical mass-transfer coefficients were utilized to describe solute movement between a thin mixing zone and the surface and subsurface continua. This mixing zone concept is utilized in many surface water quality models [e.g. *Ahuja*, 1986]. In contrast, *Wallach et al.* [1988, 1989 a,b] and *Wallach and van Genuchten* [1990] describe surface-subsurface solute transfer by a mixture of diffusion and advection. The diffusive coupling parameter can be viewed as equivalent in function to the first-order exchange coefficients utilized by *Bencala* [1984 a,b] and *Bencala et al.* [1984] to couple transport in streams with the underlying porous medium. First-order exchange coefficients are well established to couple transport in dual subsurface continua [e.g. *van Genuchten and Wierenga*, 1976; *van Genuchten and Dalton*, 1986; *Rasmuson et al.*, 1990; *Jarvis et al.*, 1991; *Gerke and van Genuchten*, 1993a,b, 1996], and are utilized in many of the dual-continua numerical models currently available.

1.3 Objectives and Scope

The objective of this thesis is to develop and evaluate a general, physically-based numerical model that incorporates all of the streamflow generation mechanisms discussed above, including the transport of multiple dissolved-phase chemicals. Snowmelt, and canopy interception, and sediment transport are not considered at present. The two-dimensional diffusion-wave equation is implemented to describe flow in shallow surface water, while flow in variably-saturated dual subsurface continua (porous medium and macropores/fractures) is described by the three-dimensional Richards equation. Transport in both the surface and subsurface continua is described by advection-dispersion equations. Linkage is through first-order, physically based flux relationships or through continuity assumptions. One system of discrete algebraic equations is assembled and solved such that fluxes between continua are determined as part of the solution. The term *integrated* is used, therefore, to differentiate the numerical model developed here from previous efforts [e.g. *Freeze*, 1978]. Utilization of the first-order coupling approach eliminates many convergence and boundary condition assignment algorithms. The numerical model is modular in form, is tailored towards irregular geological, surficial and areal geometries, and utilizes robust and efficient

discretization and solution techniques. Surface topography and the associated effect on storage and potential gradients is imbedded in the structure of the numerical model.

The flow of water and transport of solutes on the land surface is integrated with processes occurring within a variably-saturated porous medium containing macropores or fractures. To the author's knowledge, this work presents the first rigorous attempt to link flow and transport processes on the land surface with those in variably-saturated, dual-continua subsurface. The intended application is the evaluation of conceptual models of hydrologic response, solute transport, and stream water origin developed on hillslopes and subcatchments. Many other applications are possible, although data requirements may be prohibitive [e.g. *Beven*, 1989]. While the objective of this work is the development of an integrated numerical model of surface and dual-continua subsurface flow and transport, model application is restricted to allow a detailed analysis of hydrologic response and tracer transport in coupled surface-porous medium systems. Transport simulations are restricted to address conservative solutes.

1.4 Thesis Organization

The governing equations and related assumptions are discussed in Chapter 2. Chapter 3 presents spatial and temporal discretization methods and methods utilized to solve the resulting nonlinear, coupled system of discrete equations. All component modules of the numerical model are tested in Chapter 4 by comparing solutions with published experiments, analytical solutions, or the results of existing numerical models. Coupled surface-subsurface flow and transport is investigated in detail by comparing solutions with a laboratory experiment [*Abdul*, 1985]. Chapter 5 presents simulations of a field-scale experiment of coupled surface-subsurface flow and transport [*Abdul*, 1985] and investigates the sensitivity of predicted discharge volumes and tracer concentrations to topography and channel incision, initial water table elevations, hydraulic conductivity, and stream roughness. Comparisons are made with solutions based on traditional seepage face boundary conditions, and the relationships between rainfall-runoff response, tracer transport processes and hydrograph separation of stream discharge are investigated. Summary and conclusions are presented

in Chapter 6. Appendix A discusses spatial discretization issues, evaluates solution sensitivity to grid refinement, and introduces and compares an alternative, prism-based discretization scheme with isoparametric prism and tetrahedral finite elements. References follow the appendix.

Chapter 2 Theoretical Development

This chapter presents the development of equations governing the flow of water and transport of solutes on the land surface and in an underlying porous medium which contains macropores. First-order flux relationships are presented for use in coupling flow and transport between continua.

2.1 Governing Flow Equations

The movement of water on the land surface and in the porous medium, including its macropores, is assumed to be proportional to hydraulic potential gradients. The air phase is assumed infinitely mobile in the subsurface and hysteresis is not considered, although the latter could be included. Water density and temperature are assumed constant: water is assumed incompressible. Variably-saturated subsurface flow is assumed laminar and Richards' equation is applied under unsaturated conditions. Macropores (fractures), if present, form a second variably-saturated subsurface continuum in which Richards' equation is taken to be valid. Surface flow is described by the diffusion wave and Manning equations. Coupling between continua is implemented with first-order exchange flux relationships driven by pressure head gradients [e.g. *Barenblatt et al.*, 1960; *Warren and Root*, 1963] or by continuity of the pressure head [e.g. *Therrien and Sudicky*, 1996].

Preferential flow paths in the porous medium may be caused by root or worm holes, by desiccation cracks, or by fractures. These features, referred to here as macropores, may be represented as discrete entities if widely spaced [e.g. *Therrien and Sudicky*, 1996]. The macropores may be grouped into a second overlapping continuum if spacings are small such that the porous medium representative elementary volume (REV) contains sufficient numbers of macropores. Two pressure heads then can be defined for every point in the flow domain, representing the average head in the REV for the porous medium (ψ_p) and macropores (ψ_m), respectively. This dual continuum

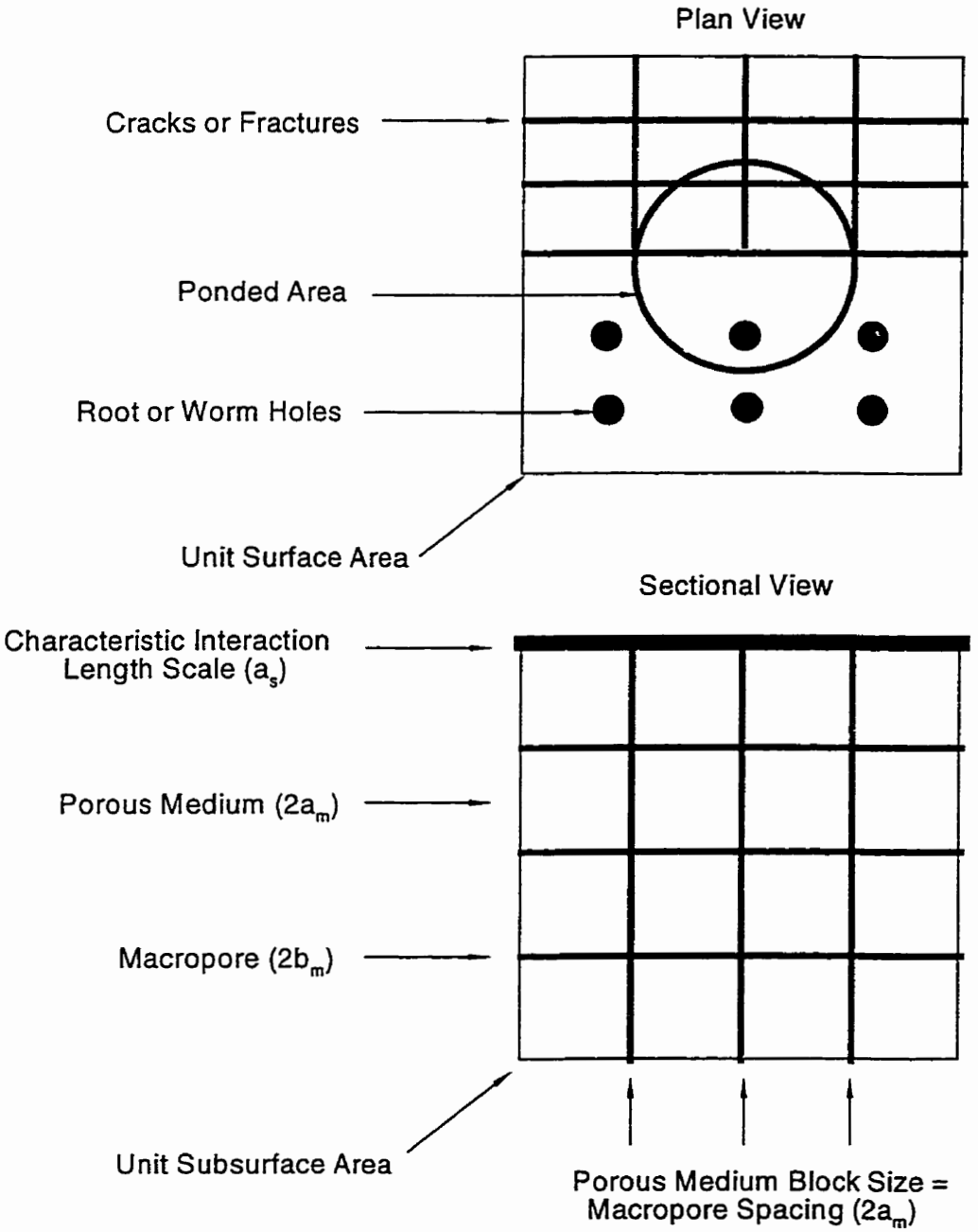

Figure 2-1. Schematic diagram of water flow and solute transport in surface water overlaying a porous medium containing macropores.

conceptualization is referred to as a dual porosity model if one continuum dominates storage potential while flow processes dominate in the second [e.g. *Warren and Root*, 1963]. If significant flow occurs in both continua, the conceptualization is known as a dual-permeability model. Many

variations of these conceptualizations are possible if multiple continua can be identified. The volume fraction of porous medium (2.11) may be subdivided further to more accurately calculate transient water exchange, following the multiple interacting continua (MINC) approach of *Preuss and Narashimhan* [1985]. The following paragraphs present the development of equations governing the movement of water on the land surface and in the dual-continua subsurface. The subscripts *p*, *m*, and *s*, denote porous medium, macropore, and surface variables, respectively.

The flow of water in a variably-saturated porous medium and inside the macropores is assumed to be described by [*Richards*, 1931]:

$$f^v \frac{\partial \phi S_w}{\partial t} = \nabla \cdot f^a \bar{q} \pm q^b \pm q^e \tag{2.1}$$

where t = time [T]; S_w = water saturation [-]; ϕ = porosity [-]; q^b = specified rate source/sink [T^{-1}]; q^e = rate of water exchange with macropores or the surface continuum [T^{-1}]; f^v = volume fraction associated with each continuum [-]; and f^a = area fraction associated with each continuum [-]. The Darcy flux is given by:

$$\bar{q} = -k_{rw} \frac{\rho_w g}{\mu_w} \bar{k} \nabla (\psi + z) \tag{2.2}$$

where ψ = pressure head [L]; z = elevation head [L]; k_{rw} = relative permeability [-]; $\bar{k}$ = intrinsic permeability vector [L^2]; ρ_w = density of water [ML^{-3}]; μ_w = viscosity of water [$ML^{-1}T^{-1}$]; and g = gravitational acceleration [LT^{-2}]. The porosity of the porous medium is assumed a function of pressure head and is approximated as [*Kropinski*, 1990]:

$$\phi_p = \phi_{p_o} \left[1 + \beta_p \rho_w g \psi_p \right] \tag{2.3}$$

where β_p = compressibility of porous medium [LT^2M^{-1}] and ϕ_{p_o} = a reference porosity at atmospheric pressure. Macropore deformation is not considered in this work $(\beta_m = 0)$.

Saturation, $S_w(\psi)$, and relative permeability, $k_{rw}(S_w)$, are assumed to be nonhysteretic and can be described by tabulated laboratory data or by functional relationships [e.g. *Brooks and Corey*, 1964; *Mualem*, 1976; *Gillham et al.*, 1976; *van Genuchten*, 1980]. For example, the *van Genuchten* [1980] functional relationships are given by:

$$S_w(\psi) = S_{w_r} + (1 - S_{w_r})\left[1 + |\alpha\psi|^n\right]^{-m}; m = 1 - 1/n \tag{2.4}$$

$$k_{rw}(S_w) = S_e^{1/2}\left[1 - (1 - S_e^{1/m})^m\right]^2$$

where α [L^{-1}] and n are empirical curve-fitting parameters. The effective saturation, S_e, is defined as:

$$S_e = \max\left(0, \frac{S_w - S_{w_r}}{1 - S_{w_r}}\right) \tag{2.5}$$

where S_{w_r} = residual saturation. The van Genuchten-type relative permeability curves for macropores are scaled at low saturations using:

$$k_{rw} = \chi k_{rw} \tag{2.6}$$

$$\chi = \begin{cases} 0 & S_e \le S_e^{active} \\ \left[(S_e - S_e^{active})/2S_e^{active}\right]^2 & S_e^{active} < S_e \le 2S_e^{active} \\ 1 & 2S_e^{active} < S_e \end{cases}$$

where S_e^{active} is the effective saturation at which flow begins. This scaling introduces an additional degree of independence between the saturation and relative permeability functions and provides explicit control over the initiation of macropore flow at low saturation.

The effect of hysteresis and saturation-dependent anisotropy on the combined relative permeability-hydraulic conductivity tensor [*Bear et al.*, 1987; *McCord et al.*, 1991] is not considered in this study. The combined effect of these processes on flow and transport at the watershed scale will be difficult to predict as wetting and drainage states are spatially- and temporally-variable, affecting both the initial state of the system and its transient response during multiple precipitation and evaporation sequences. An investigation of these effects in the context of a fully coupled numerical model with multiple interacting continua is left for future studies.

Macropore geometry, effective permeability, and effective porosity values may represent laboratory or field measurements or can be calculated directly given measurements of macropore distributions and sizes and a geometric model [e.g. *Luxmoore et al.*, 1990]. Volume and area fractions can also be derived from geometric models. Assuming the macropore aperture or radius to be much

less than the spacing between macropores ($b_m << a_m$), one can define the effective interfacial area, A_m^e [L^2], between the macropore and porous medium continua [e.g. *Preuss and Narasimhan*, 1985; *Barker*, 1985; *Gerke and van Genuchten*, 1996] as:

$$A_m^e = \zeta_m V_T \tag{2.7}$$

where $V_T = V_p + V_m$ is the total averaging volume [L^3]; and V_p and V_m are the volumes associated with the porous medium and macropores, respectively. For rectangular porous medium blocks, the surface area to volume ratio, ζ_m^e [L^2L^{-3}], of the macropore-porous medium interface is approximated as:

$$\zeta_m^e \approx \frac{6(2a_m)^2}{(2a_m)^3} = \frac{3}{a_m}; \beta^e = 3 \tag{2.8}$$

for equal macropore spacings of $2a_m$ and:

$$\zeta_m^e = \frac{1}{a_{m_x}} + \frac{1}{a_{m_y}} + \frac{1}{a_{m_z}} \tag{2.9}$$

for unequal spacings, where $2a_{m_x}$, $2a_{m_y}$, and $2a_{m_z}$ are the macropore spacings in the x-, y-, and z-directions, respectively (Figure 2-1). Other geometric models will yield different parameters or functions. The volume fraction associated with the macropores is given by:

$$f_m^v = \frac{b_m A_m^e}{V_T} = b_m \zeta_m^e \tag{2.10}$$

with the remaining volume fraction:

$$f_p^v = 1 - f_m^v = 1 - b_m \zeta_m^e \tag{2.11}$$

being associated with the porous medium, which may be subdivided further [e.g. *Preuss and Narashimhan* [1985]. The effective porosity of the macropore system given by (2.11) is unity but may be reduced due to mineralization or sedimentation [e.g. *Neretnieks and Rasmuson*, 1984].

Macropore permeability can be derived from geometric models as well. Macropores could be conceptualized, for example, as consisting of a set of parallel tubes to represent root or worm holes, with intrinsic and effective permeability calculated using the Hagen-Poiseuille equation [e.g. *Dunne*

and Phillips, 1991; *Brown*, 1995]. Macropores can also be conceptualized to consist of non-deforming parallel plates representing, for example, desiccation cracks in structured soils [*Davidson*, 1985 a,b]. Intrinsic and effective permeabilities are then given as [*Snow*, 1969; *Bear*, 1972]:

$$k_m = \frac{(2b_m)^2}{12} \tag{2.12}$$

$$k_{m_{eff}}^{xx} = k_{m_{eff}}^{yy} = k_{m_{eff}}^{zz} = k_m f_m^a$$

where $2b_m$ is an effective macropore aperture [L], and:

$$f_m^a = \frac{2b_m}{(a_m + b_m)} \approx \frac{2b_m}{a_m}; b_m << a_m \tag{2.13}$$

defines the approximate fractional area available for macropore flow per total unit area in each principle direction. The area available for flow within the porous medium is reduced by an equivalent fraction:

$$f_p^a = 1 - f_m^a \tag{2.14}$$

Effective permeabilities for unequal macropore apertures or spacings can be calculated as:

$$k_{m_{eff}}^{xx} = \frac{(2b_{m_y})^2}{12}\frac{b_{m_y}}{a_{m_y}} + \frac{(2b_{m_z})^2}{12}\frac{b_{m_z}}{a_{m_z}}; f_{m_x}^a \approx \frac{b_{m_y}}{a_{m_y}} + \frac{b_{m_z}}{a_{m_z}} \tag{2.15}$$

$$k_{m_{eff}}^{yy} = \frac{(2b_{m_x})^2}{12}\frac{b_{m_x}}{a_{m_x}} + \frac{(2b_{m_z})^2}{12}\frac{b_{m_z}}{a_{m_z}}; f_{m_y}^a \approx \frac{b_{m_x}}{a_{m_x}} + \frac{b_{m_z}}{a_{m_z}}$$

$$k_{p_{eff}}^{zz} = \frac{(2b_{m_x})^2}{12}\frac{b_{m_x}}{a_{m_y}} + \frac{(2b_{m_y})^2}{12}\frac{b_{m_y}}{a_{m_z}}; f_{m_z}^a \approx \frac{b_{m_x}}{a_{m_x}} + \frac{b_{m_y}}{a_{m_y}}$$

Gerke and van Genuchten [1996] approximate area fractions with volume fractions:

$$f_m^a \approx f_m^v = \frac{V_m}{V_T} \qquad f_p^a \approx f_p^v = \frac{V_p}{V_T} = 1 - f_m^v \tag{2.16}$$

This approximation is reasonable, as the fractional area associated with each continuum is often an assumed or fitted parameter.

The conceptualization introduced above effectively groups systems of connected macropores together to form a second subsurface continuum. The average properties of this continuum may be spatially variable. Tacit additional assumptions are that a representative elementary volume exists, that macroscopic potential gradients drive the flow of water within the system of connected macropores, and that the flow of water ***is laminar.*** However, not all macropores may be fully active in the flow process at a given macroscopic water saturation: this process is described functionally in this work by the characteristic relationships. These assumptions could be relaxed in future studies to include flow channeling through subsets of connected macropores, although parameterization would be exceedingly difficult at the field scale.

Two-dimensional surface flow is conceptualized as a third continuum that interacts with the porous medium and macropores through a thin soil layer at the land surface interface. The thickness of this layer, a_s [L], is assumed to be proportional to the permeability of the underlying porous medium [e.g. *Richardson and Parr*, 1991]:

$$a_s \propto \sqrt{k_p} \tag{2.17}$$

and represents a characteristic length scale related, for example, to momentum exchange between the surface water and underlying porous medium. Assuming a unit interface area $\left(\zeta_s^e = 1\right)$, a_s is equivalent to the volume fraction f_s^v [-] and pressure head, through continuity, is assumed equivalent to the water depth [e.g. *Freeze*, 1978].

The transient flow of surface water can be described by the diffusion wave approximation of the depth-integrated shallow water equations. This simplified surface flow equation adequately resolves backwater effects and is applicable to flow on flat surfaces except in situations involving very steep waves [*Di Giammarco et al.*, 1996]. Assuming a negligible influence of inertial forces and a shallow depth of water, ψ_s [L], one can describe the conservation of water on the land surface by [*Xanthopoulos and Koutitas*, 1976; *Ponce et al.*, 1978; *Vieira*, 1983]:

$$\frac{\partial\left(S_{w_s} h_s + \psi_{s_s}\right)}{\partial t} = \nabla \cdot \psi_s \bar{q}_s \pm a_s q^b \pm a_s q^e \tag{2.18}$$

where $\bar{q}_s$ = surface water velocity [LT^{-1}]; q^b = source/sink [T^{-1}], and q^e = surface-subsurface exchange [T^{-1}]. The surface saturation S_{w_s} and storage depth, ψ_{s_s}, are defined as:

$$S_{w_s} = \min\left[1, \max\left[0, \psi_s / h_s\right]\right] \qquad \psi_{s_s} = \max\left[0, \psi_s - h_s\right] \qquad h_s \geq a_s \tag{2.19}$$

where h_s [L] represents the average height of non-discretized surface microtopography [*Woolhiser et al.*, 1990; 1996]. The mobile water depth, $\psi_{s'}$, is defined as:

$$\psi_{s'} = \max\left[0, \psi_s - \psi_s^{pond}\right] \qquad \psi_s^{pond} \geq S_{w_r} h_s \tag{2.20}$$

where ψ_s^{pond} is the depth of ponded water that does not participate in overland flow (e.g. depression storage) and S_{w_r} is the residual surface saturation. Variables utilized in the surface flow equations are defined in Figure 2-2.

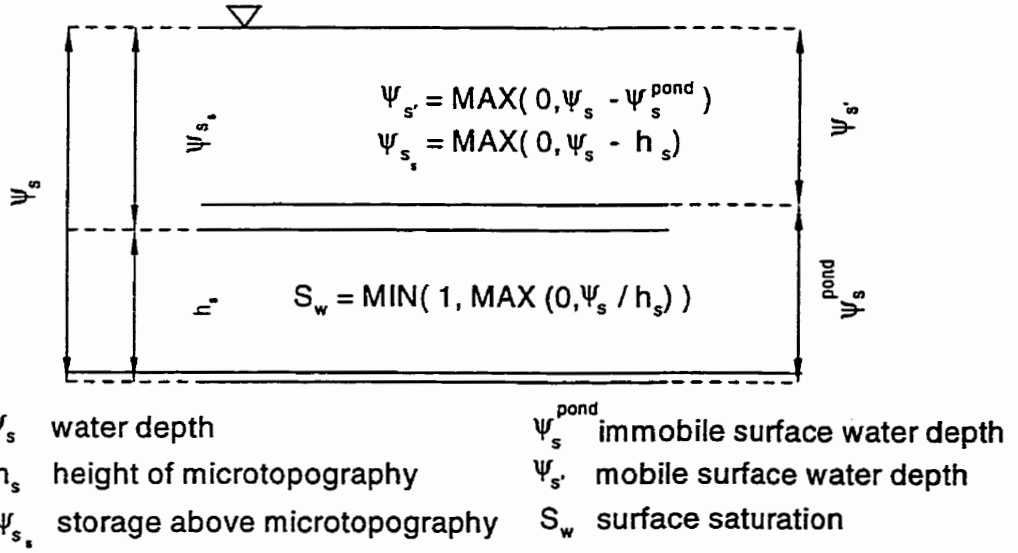

Figure 2-2. Definition of surface water flow variables.

The surface velocities are calculated utilizing a two-dimensional form of the empirical, though well-established, Manning water depth/friction-discharge equation [*Manning*, 1891]:

$$\bar{q}_s = -\frac{\psi_{s'}^{2/3}}{\bar{n}\Phi^{1/2}} \nabla\left(\psi + z\right)_s \tag{2.21}$$

where $\bar{n}$ = Manning's surface roughness tensor [$TL^{-1/3}$]. The friction or energy slope, Φ [-], is approximated as:

$$\Phi = \left[\left(\frac{\partial(\psi_s + z_s)}{\partial x} \right)^2 + \left(\frac{\partial(\psi_s + z_s)}{\partial y} \right)^2 \right]^{1/2} \tag{2.22}$$

The Manning roughness coefficient in (2.21) is assumed to incorporate all surface boundary friction and turbulence effects. The numerical value of the local Manning roughness should, furthermore, be viewed in a spatially-averaged sense, as it can represent both mixed sheet and concentrated (i.e. rill or gully) flow in the overland portions of a watershed [*Moore and Foster*, 1990].

Surface water flow is assumed to be gradually varying with respect to space such that pressure and velocity are distributed uniformly over a flow cross section; land surface slopes are also assumed to be gradually varying. Following *Chow and Ben-Zvi* [1973], equation (2.18) is assumed to describe both overland and channelized stream flows. Special consideration for one-dimensional channel flow can be included in future studies, although the morphology of natural channels is often an assumed parameter in most routing models and can be emulated through variation of the surface roughness coefficient [*Grayson et al.*, 1992] and discretization of the channel topography.

2.2 Governing Transport Equations

The equation describing advective-dispersive transport of each species in each variably-saturated subsurface continuum is:

$$f^v \left[\frac{\partial CR}{\partial t} + \lambda CR \right] = -\nabla \cdot f^a \bar{q} C + \nabla \cdot f^a \left[\left(\phi S_w \bar{D}_w + \phi S_a \bar{D}_a \right) \nabla C \right] + \left[\lambda CR \right]_{par} \pm q^b (C - C^*) \pm f^v \left(q^e C^e + q^{e_D} \right) \tag{2.23}$$

where C = concentration in water [ML^{-3}]; R = composite storage/retardation term [-]; $\bar{D}$ = dispersion coefficient tensor [L^2T^{-1}]; λ = first-order decay constant [T^{-1}]; par = indicates chain decay parents; C^* = concentration in injected water [ML^{-3}]; C^e = concentration in upstream continua [ML^{-3}]; and q^{e_D} = diffusive exchange between continua [MT^{-1}]. Equilibrium partitioning is assumed between the mass of each species in the water phase and the masses in the sorbed and air

phases, respectively. Water-solid partitioning is assumed to be described by linear isotherms. Water-air partitioning is assumed to follow Henry's Law. Under these assumptions, the porous medium composite storage/retardation term is defined as:

$$R_p = \phi_p S_{w_p} + K_h \phi_p S_{a_p} + K_{d_p} \rho_p \tag{2.24}$$

where $S_{a_p} = 1 - S_{w_p}$ = air phase saturation [-]; K_h = water-air partitioning coefficient [-]; K_{d_p} = macropore surface partitioning coefficient [L^3M^{-3}]; and ρ_p = porous medium bulk density [ML^{-3}]. The macropore composite storage/retardation term is defined as:

$$R_m = \phi_m S_{w_m} + K_h \phi_m S_{a_m} + \phi_m S_{w_m} K_{d_m} / b_m \tag{2.25}$$

where K_{d_m} = water-interface wall partitioning coefficient [L]. The mass in all phases is allowed to decay at the same rate. This latter restriction can be removed by defining separate first-order decay constants for each phase.

Dispersion tensors, $\bar{D}$ [L^2T^{-1}], are, for the mechanical mixing and diffusion in the mobile water phase [*Bear*, 1972]:

$$\phi S_w \bar{D}_w = (\alpha_l - \alpha_t)\frac{q_i q_j}{|q|} + \alpha_t |q| \delta_{ij} + \phi S_w \tau_w D^* \delta_{ij} \qquad i, j = x, y, z \tag{2.26}$$

and, for diffusion in the passive air phase:

$$\phi S_a \bar{D}_a = K_h \phi S_a \tau_a D^* \delta_{ij} \qquad i, j = x, y, z \tag{2.27}$$

where D_w^* = diffusion coefficient in water [L^2T^{-1}]; D_a^* = diffusion coefficient in air [L^2T^{-1}]; α_l = longitudinal dispersivity [L]; α_t = transverse dispersivity [L]; $|q|$ = magnitude of Darcy flux [LT^{-1}]; and δ_{ij} = Kronecker delta [-]. A modified form of (2.26) is used to allow different transverse vertical, α_{t_v}, and transverse horizontal, α_{t_h}, dispersivities [*Burnett and Frind*, 1987]. Tortuosity, τ [-], for each phase can be specified or defined as a function of saturation and porosity [*Millington*, 1959; *Millington and Quirk*, 1961]:

$$\tau = \frac{(S\phi)^{7/3}}{\phi^2} \tag{2.28}$$

Transport in the surface water is described by [*Peyton and Sanders*, 1990; *Rivlin and Wallach*, 1995; *Govindaraju*, 1996]:

$$\left[\frac{\partial C_s R_s}{\partial t} + \lambda C_s R_s\right] = -\nabla \cdot \psi_s \bar{q}_s C_s + \nabla \cdot \left[\psi_s \bar{D}_{w_s} \nabla C_s\right] + \left[\lambda C_s R_s\right]_{par} \pm a_s q^b \left(C - C^*\right) \pm a_s \left[q^e C^e + q^{D_e}\right] \tag{2.29}$$

Surface storage/retardation, R_s [L], is described by:

$$R_s = \left[S_{w_s} K_{d_s} + \psi_{s_s}\right] \tag{2.30}$$

where K_{d_s} = linear water-surface soil/vegetation partitioning coefficient [L]. Note that surface concentrations represent depth-averaged quantities because rapid vertical mixing in shallow water is assumed. The two-dimensional dispersion tensor, $\bar{D}_w$, representing diffusion and spreading due to turbulent mixing, is assumed to be described by:

$$\bar{D}_{w_s} = \left(\alpha_{l_s} - \alpha_{t_s}\right)\frac{q_{s_i} q_{s_j}}{|q_s|} + \alpha_{t_s}|q_s|\delta_{ij} + D_w^* \delta_{ij} \qquad i,j = x,y \tag{2.31}$$

2.3 First-Order Coupling Relationships

Exchange of water and solutes between continua is approximated with first-order relationships:

$$q^e = \alpha^e \Delta\psi \qquad\qquad q^{e_D} = \alpha^{e_D} \Delta C \tag{2.32}$$

which describe the rate at which continua interact. The interaction or exchange coefficients, α^e [$L^{-1}T^{-1}$], and α^{e_D} [T^{-1}], can be interpreted as: (1) lumped fitting parameters utilized to match observed responses [e.g. *Bencala*, 1984; *Brusseau and Rao*, 1990; *Govindaraju*, 1996; *Ray et al.*, 1997] or (2) functions of interface geometry (2.8) and characteristic length scales:

$$\alpha^e = k_{rw}^e \varphi^e \frac{\zeta^e}{a} \qquad\qquad \alpha^{e_D} = \varphi^{e_D} \frac{\zeta^e}{a} \tag{2.33}$$

where the parameters φ^e [LT^{-1}] and φ^{e_D} [L^2T^{-1}] are defined as functions of fluid or solute properties and system parameters such as saturation or permeability [e.g. *van Genuchten and Dalton*, 1986; *Wallach*

et al., 1988, 1989; *Sudicky*, 1990; *Gerke and van Genuchten*, 1993a,b, 1996]. This later approach is utilized in this work, with water and solute exchange assumed to be described by one-dimensional Darcy and advection-dispersion equations, respectively. Use of large exchange coefficient values promote concentration and pressure head continuity between two interacting continua, and small values promote disequilbrium. The following sections provide functional definitions of the coupling coefficients α^{e} and α^{e_D}.

2.3.1 Water Exchange

First-order coupling relationships, while approximate, have a long history in coupled subsurface flow [e.g. *Barenblatt et al.*, 1960; *Warren and Root*, 1963]. The use of such relationships to couple surface and subsurface flow, however, is unique. The coupled system of equations utilized in this work is:

$$
\begin{aligned}
f_p^{v}\frac{\partial \phi_p S_{w_p}}{\partial t} &= \nabla\cdot f_p^{a}\bar{q}_p \quad \pm q_p^{b} \quad \pm q_{p_m}^{e} \quad\quad \pm q_{p_s}^{e} \\
f_m^{v}\phi_m\frac{\partial S_{w_m}}{\partial t} &= \nabla\cdot f_p^{a}\bar{q} \quad \pm q_m^{b} \quad \pm q_{m_p}^{e} \quad \pm q_{m_s}^{e} \\
\frac{\partial\left(S_{w_s}h_s+\psi_{s_s}\right)}{\partial t} &= \nabla\cdot\psi_{s'}\bar{q}_s \quad \pm a_s q_s^{b} \quad\quad \pm a_s q_{s_m}^{e} \quad \pm a_s q_{s_p}^{e}
\end{aligned}
\tag{2.34}
$$

which provides for distinct porous medium and macropore storage capacities and velocities, and allows an analysis of the effects of by-pass flow on infiltration and solute transport. The first-order flux relationship (2.32) eliminates iteration between the surface and subsurface flow solutions to determine matching boundary conditions. In this way, specified fluxes are apportioned between continua in an implicit, natural manner [*VanderKwaak and Sudicky*, 1995, 1996]. Water added to one continuum is stored, transported within the continuum, or transferred between continua. The time scale of response associated with each continuum is maintained but is intimately linked to the dynamics of the coupled system. In contrast, *Brown's* [1995] coupled system of equations can be written as:

$$\begin{aligned} \frac{\partial \phi_{p,m} S_{w_{p,m}}}{\partial t} &= \nabla \cdot \bar{q}_{p,m} \quad \pm q^b_{p,m} \quad \pm q^e_{p,m_z} \\ \frac{\partial S_w(\psi_s)}{\partial t} &= \nabla \cdot \bar{q}_s \quad \pm q^b_s \quad \pm q^e_{s_{p,m}} \end{aligned} \tag{2.35}$$

where the interface area and characteristic length scale are determined by the spacings of the discretized volumes.

The exchange of water between continua is assumed analogous to a one-dimensional variably-saturated form of Darcy's equation. The exchange coefficients are thus nonlinear and the magnitude of pressure head disequilbrium between any two coupled continua is affected by the degree of saturation. Subsurface water exchange is assumed to be described by [e.g. *Barenblatt et al.*, 1960; *Warren and Root*, 1963]:

$$q^e_{p_m} = \alpha^e_{mp}\left(\psi_m - \psi_p\right) = -q^e_{m_p} \tag{2.36}$$

For equal macropore spacings and an isotropic porous medium, the water exchange coefficient is:

$$\alpha^e_{mp} = k^e_{rw}\varphi^e_{mp}\frac{\zeta^e_m}{a_m} \tag{2.37}$$

$$\varphi^e_{mp} = \chi^e \frac{\rho_w g}{\mu_w} k^e$$

The interface permeability, k^e [L^2], is approximated by a harmonic average of the respective continua, weighted by volume or area fractions:

$$k^e = \frac{k_p k_m\left(f_p^v + f_m^v\right)}{k_p f_m^v + k_m f_p^v} = \frac{k_p k_m}{k_m f_m^v + k_p\left(1 - f_m^v\right)} \tag{2.38}$$

This average is dominated by the porous medium permeability if macropore volumes are small. The exchange coefficient utilized for rectangular porous medium blocks with unequal spacings is given by:

$$\alpha^e = k^e_{rw}\chi^e \frac{\rho_w g}{\mu_w}\left[\frac{k^{e_x}}{a^2_{m_x}} + \frac{k^{e_y}}{a^2_{m_y}} + \frac{k^{e_z}}{a^2_{m_z}}\right] \tag{2.39}$$

The dimensionless parameter, χ^e, is utilized to scale the magnitude of (2.36). This scaling may represent an altered effective permeability due to interface mineralization or microfracturing [e.g. *Preuss and Wang*, 1987], or an altered interfacial area caused by channeling of flows along macropore walls [e.g. *Hoogmoed and Bouma*, 1980]. *Gerke and van Genuchten* [1993a,b] utilize a scaling parameter to compensate, in part, for the first-order coupling relationship (2.37), which tends to underestimate water exchange under large potential gradients. This inaccuracy can be minimized by further subdivision of the porous medium into multiple interacting continua (MINC), as demonstrated by *Pruess and Narashimhan* [1985]. In the study by *Gerke and van Genuchten* [1993a,b], the macropore continuum was both fully saturated and the source of water, the macropore continua, was taken to be upstream of the porous medium continuum at all times. The validity of a constant scaling parameter for bi-directional exchange under variably-saturated conditions is unclear. One possible functional form of χ^e is:

$$\chi^e \equiv S_{w_m} \tag{2.40}$$

which scales the degree of interaction (or area) by the macropore saturation [e.g. *Wang and Narasimhan*, 1985]. If evaluated implicitly, (2.40) will represent an additional nonlinearity in the first-order coupling.

The relative permeability, k_{rw}^e [-], is defined in the upstream continuum:

$$k_{rw}^e = \begin{cases} k_{rw_p} : \psi_p \geq \psi_m \\ k_{rw_m} : \psi_m > \psi_p \end{cases} \tag{2.41}$$

which ensures that the discretized solution is monotone [e.g. *Kropinski*, 1990]. *Gerke and van Genuchten* [1993a,b] and *Zimmerman et. al* [1996] suggest that the relative permeability be evaluated using the porous medium characteristic curves and the interface potential which, through continuity, is equal to that in the macropore system:

$$k_{rw}^e = k_{rwp}\left(S_{w_p}\left(\psi_m\right)\right) \tag{2.42}$$

The relative permeabilities predicted by (2.41) and (2.42) will be within an order of magnitude in value, which is reasonable given the uncertainty associated with the geometry (2.7) and interface

permeability (2.38). Use of a scaling factor such as (2.40), furthermore, reduces water exchange by a similar order of magnitude.

Large subsurface water exchange coefficients, α^e_{mp}, cause rapid equilibration of pressure head between interconnected continua [e.g. *Gerke and van Genuchten*, 1993 a,b, 1996]. The subsurface continua then respond concurrently to pressure changes, with the influence of the macropore permeability becoming more dominant as the pressure head approaches the macropore entry value. This represents one possible form of an equivalent porous medium representation of the coupled subsurface flow process. A small influence (i.e. a small α^e) decreases the macropore-porous medium interaction and provides for increased by-pass flow to depth.

Surface-subsurface water exchange is given by:

$$q^e_{s_p} = \alpha^e_{s_p}\left(\psi_s - \psi_p\right) = -q^e_{p_s} \qquad q^e_{s_m} = \alpha^e_{s_m}\left(\psi_s - \psi_m\right) = -q^e_{m_s} \tag{2.43}$$

where the water exchange coefficients are:

$$\alpha^e_{s_p} = k^e_{rw}\varphi^e_{sp}\frac{\zeta^e_s}{a_s} \qquad \alpha^e_{s_m} = k^e_{rw}\varphi^e_{sm}\frac{\zeta^e_s}{a_s} \tag{2.44}$$

$$\varphi^e_{sp} = \chi^e\frac{\rho_w g}{\mu_w} f_p^{a_z} k_p^z \qquad \varphi^e_{sm} = \chi^e\frac{\rho_w g}{\mu_w} f_m^{a_z} k_m^z$$

The upstream-weighted relative permeability (2.41) will be unity if groundwater discharge (seepage) is occurring at the land surface. For infiltration conditions, interface relative permeabilities can be specified using the empirical surface saturation function (2.19) in combination with the relative permeability function of the underlying porous medium. Psuedo-relative permeability is defined in this work as a simple power function of an effective saturation (2.5):

$$k_{rw_s} = S_e^{2(1-S_e)} \tag{2.45}$$

which ensures continuous derivatives as water depths approach zero. Continuous derivatives are also generated as water depths approach the height of the microtopography (see Figure 2-3), with the relative permeability attaining a constant value of unity when water depths are greater than the height of surface microtopography. Specification of a non-zero residual saturation, S_{w_r}, in combination

with a nonzero mobile water depth (2.20) ensures that the surface transport equation is defined at all values of water depth (including negative). This depth-based function can be interpreted as reducing the area utilized in coupling the surface and subsurface flow continua, resulting in restricted infiltration from concentrated ponding in rills [*Dunne et al.*, 1991]. This reduced area limits infiltration from ponded water, which will also affect surface hydrodynamics, as more water is available for overland or stream flow. Such effects may be significant once rainfall ceases or when subsurface heterogeneity causes spatially variable infiltration and surface water run-on [*Woolhiser et al.*, 1996]. Semi-permeable surfaces (i.e. crusted soils, roads or leaky concrete channels) can also be considered through the scaling coefficient $(0 < \chi^{\epsilon} < 1)$. Setting this coefficient to zero accommodates impermeable surfaces by decoupling the surface and subsurface flow systems entirely.

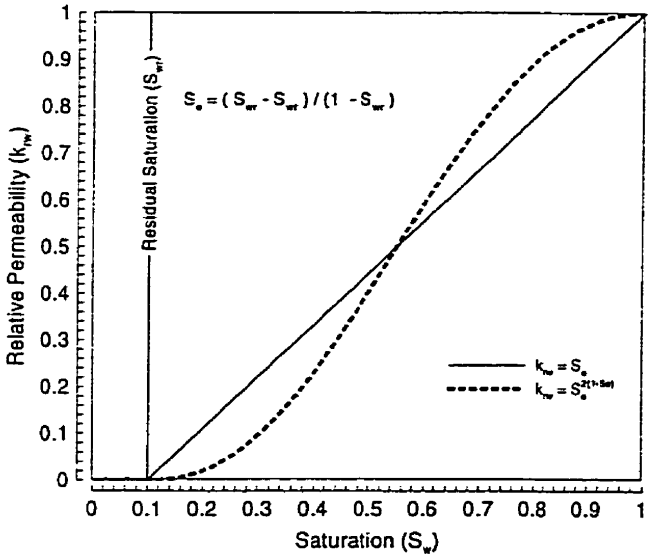

Figure 2-3. Illustration of the empirical surface relative permeability function.

Infiltration and discharge seepage rates are determined by pressure head gradients and the properties of the underlying porous medium and macropores. Subsurface heterogeneity and its influence on infiltration, subsurface flow, and seepage, is implicitly considered through possible spatial variability of the vertical permeability [*Freeze*, 1980; *Sharma et al.*, 1987; *Binley et al.*, 1989 a,b; *Smith et al.*, 1996]. While the area associated with the macropores $\left(f_m^{a_m}\right)$ may be small, the effective

permeability contrast between the two subsurface continua may allow significant water movement directly into and through the macropores once surface ponding occurs [*Edwards et al.*, 1979; *Hoogmoed and Bouma*, 1980; *Davidson*, 1985 a,b; *Beven and Clarke*, 1986]. This enhanced surface flux is likely to occur when the rainfall at the land surface exceeds the infiltration capacity of the porous medium, but not the combined infiltration capacity of the porous medium-macropore system [e.g. *Beven and Germann*, 1982; *McDonnell*, 1990]. This effect may be irregular in space and time, varying with macropore vertical permeability (aperture and spacing) and topography [*Dunne et al.*, 1991]. Penetration depth will depend on the magnitude of subsurface water exchange, and, in effect, increases the area available for infiltration by the area of the subsurface interface.

2.3.2 Solute Exchange

The subsurface diffusive/dispersive exchange coefficient, including diffusion in the air phase is given by [*van Genuchten and Wierenga*, 1976; *Rasmuson et al.*, 1990; *Jarvis et al.*, 1991; *Gerke and van Genuchten*, 1993a,b, 1996]:

$$q_{p_m}^{\epsilon_D} = \alpha_{pm}^{\epsilon_D}\left(C_m - C_p\right) = -q_{m_p}^{\epsilon_D} \tag{2.46}$$

For equal macropore spacings and an isotropic porous medium, the solute exchange coefficient is defined as:

$$\alpha_{pm}^{\epsilon_D} = \varphi_{pm}^{\epsilon_D}\frac{\zeta_m^{\epsilon}}{a_m} \tag{2.47}$$

$$\varphi_{pm}^{\epsilon_D} = \chi^{\epsilon_D}\left[\left|q_{p_m}^{\epsilon}\right|\alpha^{*} + \left(\phi S_w \tau_w\right)_{p_m}^{\epsilon} D_w^{*} + \left(\phi S_a \tau_a\right)_{p_m}^{\epsilon} K_h D_a^{*}\right]$$

where α^{*} = exchange dispersivity [L]. The scaling parameter χ^{ϵ_D} can be constant or a function similar to (2.40). Volume fraction weighting (2.38) is again assumed valid and is utilized to determine interface porosity, saturation, and tortuosity. Unless macropore saturation is small, solute exchange in both phases will be dominated by the porous medium values [e.g. *van Genuchten and Dalton*, 1986]. The magnitude of the diffusive exchange (2.46) will affect solute bypass of the porous medium. Concentration gradients will be large if the porous medium storage capacity is significantly greater

than that of the macropores. In the absence of mechanical mixing $(\alpha^* = 0)$, the magnitude of (2.47) is likely to be less than the magnitude of the water exchange coefficient (2.37) for moderate-to-high permeability porous media, providing a greater degree of concentration disequilbrium than may exist for pressure.

Considerable uncertainty exists in both the mechanism and the parameterization of surface-subsurface solute mass transfer. *Wallach et al.* [1988, 1989] approached the problem of diffusive solute transfer by assuming the existence of a thin immobile water film at the land surface interface. The thickness of this water film was assumed to be proportional to the Manning surface roughness, the water depth, and the surface hydraulic gradient. *Richardson and Parr* [1988, 1991] derived an expression with similar physical meaning but from the perspective of the depth of penetration of the surface water shear stress into the porous medium, with the water film thickness being proportional to the square root of the soil permeability. The ability to predict the depth of shear stress interaction or the thickness of a thin immobile water layer is debatable, however, in the context of irregular surface topography and vegetation cover, porous medium heterogeneity, and macropore flow. *Havis et al.* [1992] utilized a more empirical approach to describe the interaction of agricultural runoff with a thin mixing zone, treating the conceptual mixing zone as a fitting parameter to match observed discharge concentrations. *Govindaraju* [1996] treated both the exchange coefficient and mixing zone thickness as constants whereas *Bencala* [1983, 1984] characterized the diffusive transfer of solutes between stream and sediments as a simple first-order kinetic process.

The coupling approach utilized in this work is similar to *Bencala* [1983, 1984], with the exchange coefficient derived from porous medium and solute properties [e.g. *Wallach et al.*, 1988, 1989] and an assumed characteristic length scale of interaction [e.g. *Gerke and van Genuchten*, 1993 a,b]. Dispersive-diffusive surface-subsurface solute exchange, therefore, is assumed described by:

$$q_{s_p}^{e_D} = \alpha_{s_p}^{e_D}\left(C_s - C_p\right) = -q_{p_s}^{e_D} \qquad q_{s_m}^{e_D} = \alpha_{s_m}^{e_D}\left(C_s - C_m\right) = -q_{m_s}^{e_D} \tag{2.48}$$

where the diffusive exchange coefficients are:

$$\alpha_{s_p}^{e_D} = \varphi_{sp}^{e_D} \frac{\zeta_s^e}{a_s} \qquad \alpha_{s_m}^{e_D} = \varphi_{sm}^{e_D} \frac{\zeta_s^e}{a_s} \tag{2.49}$$

$$\varphi_{sp}^{e_D} = \chi^{e_D} f_p^{a_z} \left[\left| q_{s_p}^e \right| \alpha^* + (\phi S_w \tau_w)_{s_p}^e D_w^* \right] \qquad \varphi_{sm}^{e_D} = \chi^{e_D} f_m^{a_z} \left[\left| q_{s_m}^e \right| \alpha^* + (\phi S_w \tau_w)_{s_m}^e D_w^* \right]$$

Porosity of the interface is assumed equivalent to the underlying continua and tortuosity is evaluated using (2.28) [e.g. *Wallach et al.*, 1988, 1989]. The exchange dispersivity, α^*, represents mixing due to raindrop impacts or to pumping effects. Saturation is evaluated as a harmonic average, weighted by volume fraction:

$$S_w^e = \frac{S_{wp} S_{ws} \left(f_p^v + f_s^v \right)}{S_{wp} f_s^v + S_{ws} f_p^v} \qquad S_w^e = \frac{S_{wm} S_{ws} \left(f_m^v + f_s^v \right)}{S_{wm} f_s^v + S_{ws} f_m^v} \tag{2.50}$$

which is equivalent to the surface saturation if the subsurface continua are fully saturated, thus scaling the diffusive exchange by the degree of surface ponding. Dispersive/diffusive exchange as described by (2.49) will increase as the characteristic length scale decreases. Small length scale values are equivalent to assuming concentration continuity between surface water and the underlying porous medium [*Donigian et al.*, 1977; *Steenhuis and Walter*, 1980] whereas larger length scales promote disequilbrium.

Chapter 3 Discretization and Solution Methods

This chapter presents discretization and solution methods for a fully coupled numerical model describing water flow and solute transport on the land surface and within subsurface porous medium that may contain fractures or macropores [*VanderKwaak and Sudicky*, 1995, 1996]. Considerable emphasis is placed upon the use of robust and efficient methods appropriate for the discretization and solution of large-scale problems. The governing equations are discretized in space using the control volume finite element (CVFE) method [e.g. *Forsyth*, 1991; *Forsyth and Simpson*, 1991; *Gottardi and Venutelli*, 1994; *Costa et al.* 1995; *Di Giammarco et al.*, 1996], which permits a consistent interpretation of flow and transport processes both within and between continua. The CVFE method combines the geometric flexibility of finite elements with the local conservation characteristics of control volumes. Coupling of continua is accomplished by assuming continuity of pressure or concentration [e.g. *Therrien and Sudicky*, 1996], or by specifying a first-order flux relationship between continua [e.g. *Warren and Root*, 1963; *van Genuchten and Dalton*, 1986]. Transport of multiple species is solved sequentially after each transient flow timestep, beginning with the first parent if chain decay is occurring. Nonlinear flux limiters are utilized in solving advective transport to minimize numerical dispersion. Each system of coupled nonlinear equations is solved simultaneously using Newton iteration, and numerical derivatives are employed in the Jacobian assembly. Efficient and robust iterative sparse matrix methods are used to solve the large Jacobian systems. Solution accuracy and mass balances are stipulated by the convergence tolerances of the Newton iteration loops and iterative solver, respectively.

3.1 Spatial Discretization and Equation Coupling

Simple element types are utilized to allow the efficient use of influence coefficients in the evaluation of spatial integrals [*Frind*, 1982; *Huyakorn et al.*, 1984]. Subsurface element types include triangles, prisms, rectangles, tetrahedra and blocks. Surface equations are discretized using a second finite element mesh corresponding to the top of the subsurface elements (Figure 3-1). Surface elements overlaying subsurface prisms or tetrahedra consist of triangles, those overlaying blocks are rectangles, and those overlaying two-dimensional subsurface elements are lines. Element types can be spatially variable, a useful option in simulations combining complex geologic and topographic geometries. Following *Panday et al.* [1993], modified influence coefficient matrices are utilized for rectangles and blocks to emulate finite difference connections. This approach is extended in this work to include prisms (See Appendix A).

Each node in the finite element mesh may have multiple unknowns, with each unknown associated with different continua. A mixture of coupling schemes may be utilized, allowing different continua to be coupled via continuity or by first-order flux relationships. The spatial distribution of continua can also be variable, allowing, for example, a layer of macroporous soil adjacent to the land surface or surface processes only in topographic lows. Such spatial variability of continua is illustrated in Figure 3-2, which presents a portion of a prism-based mesh with surface equations at the uppermost nodes, a layer of macropore equations at the nodes adjacent to the land surface, and porous medium equations at all nodes.

The structure of the corresponding coefficient matrix (Jacobian) is presented in Figure 3-3 for first-order coupling and both standard and modified finite element connections. In both cases, the diagonal consists of blocks related to the number of equations per node while the off-diagonal connections are associated with the element types selected for the spatial discretization. Use of modified elements eliminates cross-element connections (See Appendix A), reducing the size of the coefficient matrix by approximately twenty-eight percent in this example. Such reduced connectivity will lower storage requirements and both the Jacobian assembly and the solution effort [e.g. *Panday et*

al., 1993]. Storage and computational effort may be minimized further if coupling is accomplished by assuming pressure and concentration continuity between continua [e.g. *Therrien and Sudicky*, 1996]. Figure 3-4 presents the coefficient matrices that result by assuming continuity between the porous medium and macropores, while utilizing a first-order relationship to couple the surface continua. Subsurface connections are coincident, reducing the size of the coefficient matrix by forty-one and fifty-nine percent for the standard and modified finite element connections, respectively. The sparsity pattern is constant for a given spatial discretization and equation numbering: only the nonzero terms in the Jacobian are stored and operated on. Judicious selection of coupling approaches and element types can significantly lower computational effort, as the Jacobian assembly and solution time is directly proportional to the nodal spatial connectivity and the number of primary variables per node.

The multiple equation and general coupling methodology can be utilized to include additional continua or discrete features such as fractures [*Therrien and Sudicky*, 1996], wells [*Sudicky et al.*, 1995; *Wu et al.*, 1996], or tile drains [*MacQuarrie and Sudicky*, 1996]. Coupling of these features with other continua may be accomplished via either continuity assumptions or first-order exchange relationships. Exchange relationships are similar to those utilized to couple the surface continuum. The multiple-interacting continuum (MINC) method of *Pruess and Narasimhan* [1985] and *Pruess* [1991] can be easily implemented by further subdivision of the porous medium volume. Additional equations describing flow and transport in each continuum are assigned to each node, thereby increasing both the size of the diagonal blocks and the number of off-diagonal entries in the Jacobian. The first-order relationships utilized to couple the multiple porous medium continua are similar in form to those developed to couple porous medium and macropores. A dual-porosity approach can be implemented by eliminating off-diagonal entries, corresponding to flow and transport within a continuum, while retaining entries in the diagonal block, which correspond to exchange between continua.

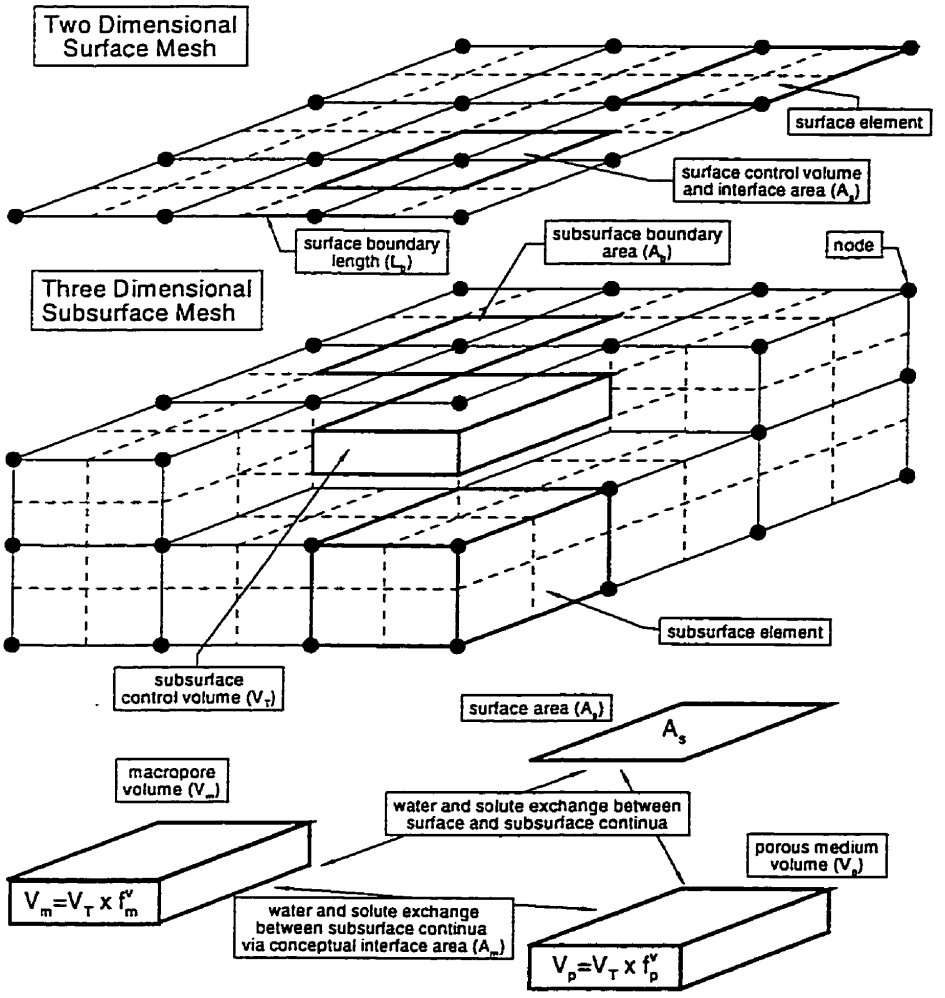

Figure 3-1. Illustration of the relationship between simple surface and subsurface finite element meshes, the relationship between finite elements and nodal control volumes, and the coupling of flow and transport on the land surface with that in a dual-continua subsurface. Nodes along the top of the three-dimensional mesh are assigned both surface and subsurface equations. The surface mesh is coincident with the top of the subsurface mesh.

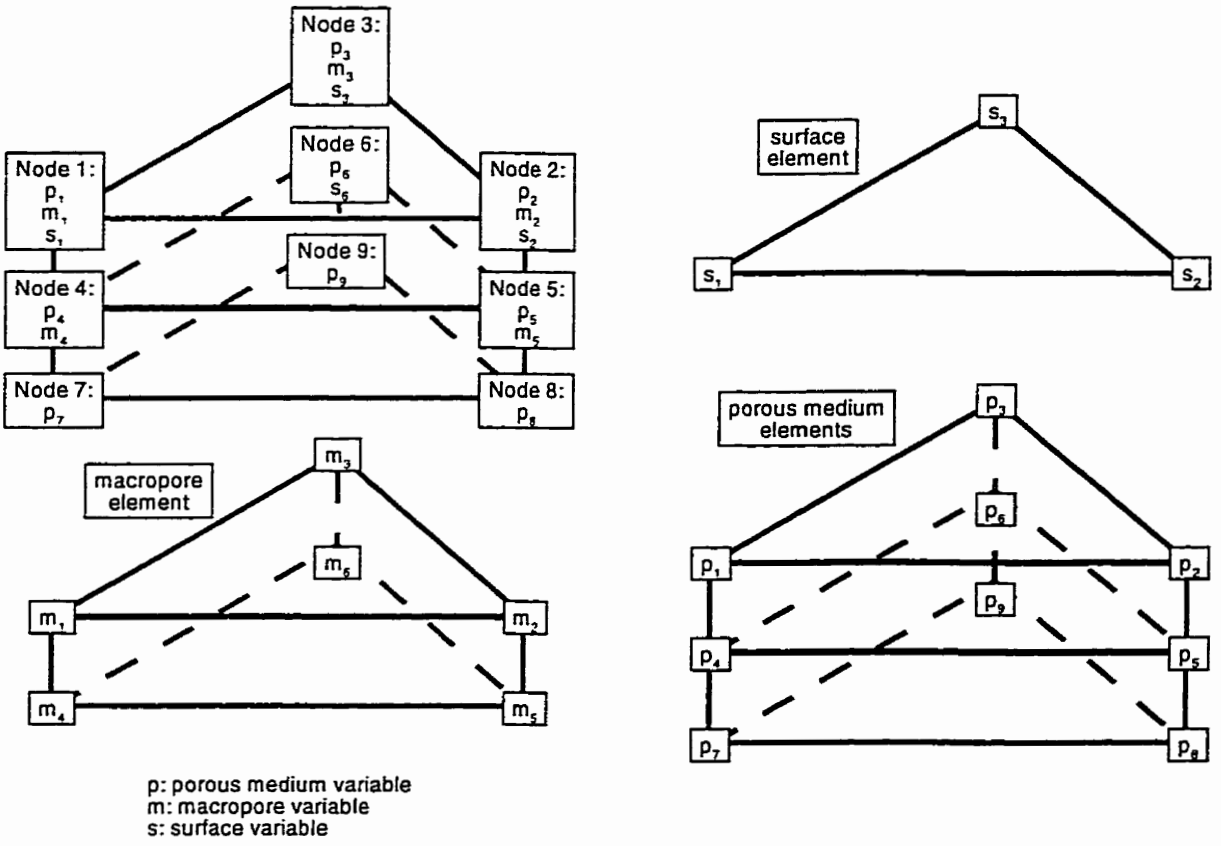

Figure 3-2. A portion of a prism-based finite element mesh illustrating multiple unknowns per node and spatially-variable subsurface continua.

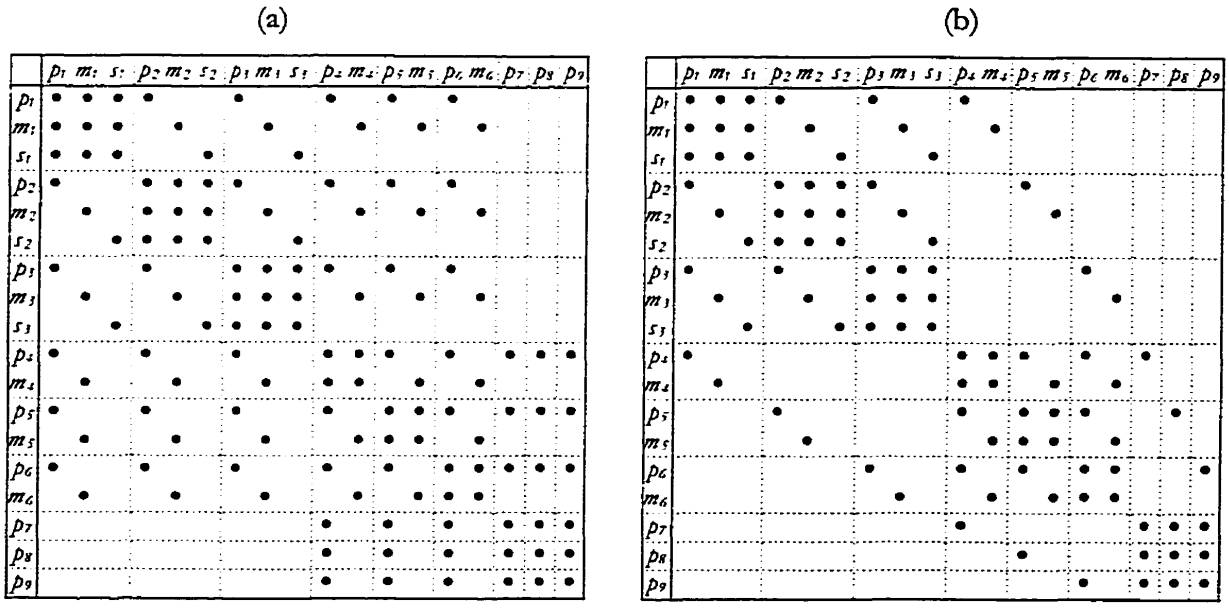

Figure 3-3. Jacobian structure for illustrative finite element mesh (Figure 3-2): (a) connectivity arising from prism finite elements (132 entries) and (b) connectivity resulting from modified prisms (95 entries).

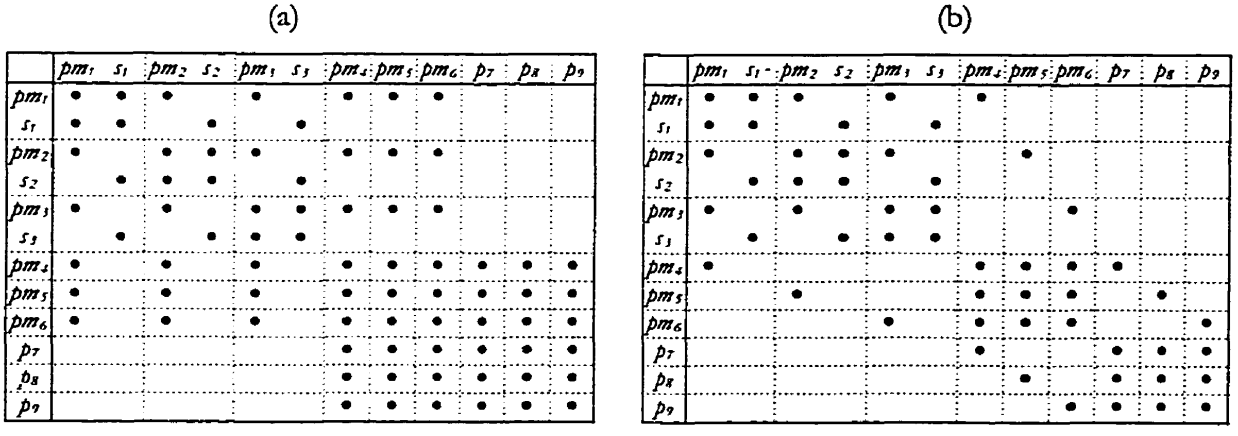

Figure 3-4. Jacobian structure for illustrative finite element mesh (Figure 3-2) assuming continuity of porous medium and macropore solutions: (a) connectivity arising from prism finite elements (78 entries) and (b) connectivity resulting from modified prisms (54 entries).

3.2 *Discrete Flow Equations*

The discrete form of the coupled surface and subsurface flow equations is:

$$\begin{aligned}
&\frac{V_i f_{i_p}^{v}}{\Delta t_{global}}\left[(\phi S_w)^{L+1}-(\phi S_w)^{L}\right]_{i_p}+ \\
&\frac{V_i f_{i_m}^{v}}{\Delta t_{global}}\left[\phi\left(S_w^{L+1}-S_w^{L}\right)\right]_{i_m}+ \\
&\frac{A_{i_s}}{\Delta t_{global}}\left[\left(S_w h_s+\psi_{s_s}\right)^{L+1}-\left(S_w h_s+\psi_{s_s}\right)^{L}\right]_{i_s} \\
&=\sum_{j\in\eta_{i_p}}\omega_f Q_{i_p j}^{L+1}+\sum_{j\in\eta_{i_p}}\left(1-\omega_f\right)Q_{i_p j}^{L}+\sum_{i_p}Q_b^{L+1} \\
&\sum_{j\in\eta_{i_m}}\omega_f\, Q_{i_m j}^{L+1}+\sum_{j\in\eta_{i_m}}\left(1-\omega_f\right)Q_{i_m j}^{L}+\sum_{i_m}Q_b^{L+1} \\
&\sum_{j\in\eta_{i_s}}\omega_f\, Q_{i_s j}^{L+1}+\sum_{j\in\eta_{i_s}}\left(1-\omega_f\right)Q_{i_s j}^{L}+\sum_{i_s}Q_b^{L+1}
\end{aligned} \tag{3.1}$$

$$i_p\in\eta_p; i_m\in\eta_m; i_s\in\eta_s; j\in\eta_n$$

where i, j = nodes in the finite element mesh; η_p = the node set containing porous medium primary variables; η_m = the node set containing macropore primary variables; η_s = the node set containing surface primary variables; $\eta_n=\eta_p\cup\eta_m\cup\eta_s$ = the set of all primary variables; η_i = the set of nodes in the equation of unknown i; $\sum Q$ = sum of volumetric fluxes within and between continua; $\sum Q_b$ = sum of volumetric sources/sinks; L = time level; ω_f = flow solution time weighting $\left(\omega_f=0,1\right)$; and Δt_{global} = global time step. This discrete matrix equation is nonlinear and is independent of element type and dimensionality.

Discrete water fluxes for subsurface flow and for all coupling terms are defined as:

$$Q_{ij}^{L+1}=\left(k_{rw}\gamma\right)_{ij}^{L+1}\Gamma_{ij} \tag{3.2}$$

where Γ_{ij} = flow influence or water transfer term. The hydraulic head difference, γ_{ij}, is given by:

$$\gamma_{ij}=\left(\psi+z\right)_j-\left(\psi+z\right)_i \tag{3.3}$$

which is the difference in pressure head for primary variables located at the same node. Discrete surface fluxes are defined as:

$$Q_{s_{ij}}^{L+1} = \left(\kappa\Gamma^{I}\right)_{ij}^{L+1} \tag{3.4}$$

where I = Newton iteration level. Note that surface influence terms, $\left(\Gamma^{I}\right)_{ij}^{L+1}$, are a function of water depth and are evaluated semi-implicitly (see equation (3.14)). The nonlinear relative permeability utilized in (3.2) is upstream weighted:

$$k_{rw_{ij}} = \begin{cases} k_{rw_j} & if \quad \gamma_{ij}\Gamma_{ij} > 0 \\ k_{rw_i} & if \quad \gamma_{ij}\Gamma_{ij} \le 0 \end{cases} \tag{3.5}$$

as is the nonlinear surface conveyance term, κ:

$$\kappa_{ij} = \begin{cases} \left(\psi_{s'}^{5/3}\right)_j & if \quad \gamma_{ij}\Gamma_{ij} > 0 \\ \left(\psi_{s'}^{5/3}\right)_i & if \quad \gamma_{ij}\Gamma_{ij} \le 0 \end{cases} \tag{3.6}$$

Upstream weighting, while diffusive, ensures solution monotonicity [*Kropinski,* 1990; *Meselhe and Holley,* 1993] and is consistent with the hyperbolic tendencies of the governing equations.

The coupling influence coefficient for an isotropic porous medium containing equally-spaced macropores can be expressed as:

$$\begin{aligned} \Gamma_{i_p i_m} &= \varphi_{i_p i_m}^{e} \frac{A_{m_i}}{a_{m_i}} \\ &= \varphi_{i_p i_m}^{e} \frac{\zeta_{m_i} V_i}{a_{m_i}} \\ &= \Gamma_{i_m i_p} \end{aligned} \tag{3.7}$$

Porous medium-surface influence coefficients are defined as:

$$\begin{aligned} \Gamma_{i_s i_p} &= \varphi_{i_s i_p}^{e} \frac{f_{p_i}^{az} A_{s_i}}{a_s} \\ &= \Gamma_{i_p i_s} \end{aligned} \tag{3.8}$$

and the macropore-surface influence coefficients are given as:

$$\begin{aligned} \Gamma_{i_s i_m} &= \varphi_{i_s i_m}^{e} \frac{f_{m_i}^{az} A_{s_i}}{a_s} \\ &= \Gamma_{i_m i_s} \end{aligned} \tag{3.9}$$

The subsurface flow influence coefficients, Γ [L^2T^{-1}], in (3.1) are linear and are defined as [*Forsyth and Simpson*, 1991; *Forsyth*, 1993]:

$$\begin{aligned}\Gamma_{ij} &= -\frac{\rho_w g}{\mu_w}\int_v \nabla N_i f^a k \nabla N_j dv \\ &= -\frac{\rho_w g}{\mu_w}\sum_{ij\in\eta_e}\left[\left(f^a k\right)^{xx}_{ij+1/2} I^{xx}_{ij} + \left(f^a k\right)^{yy}_{ij+1/2} I^{yy}_{ij} + \left(f^a k\right)^{zz}_{ij+1/2} I^{zz}_{ij}\right]^e \\ &= \Gamma_{ji}\end{aligned} \tag{3.10}$$

where $\left(f^a k\right)_{ij+1/2}$ = harmonic-weighted effective permeabilities, η_e = the set of elements containing the node pair ij, and N = linear basis functions. The coefficients I^{xx}_{ij}, I^{yy}_{ij}, and I^{zz}_{ij} [L] contain all elemental geometry and integration information and are defined as [e.g. *Huyakorn et al.*, 1984, 1986a,b]:

$$I^{xx}_{ij} = \frac{\partial N_i}{\partial x}\frac{\partial N_j}{\partial x} \qquad I^{yy}_{ij} = \frac{\partial N_i}{\partial y}\frac{\partial N_j}{\partial y} \qquad I^{zz}_{ij} = \frac{\partial N_i}{\partial z}\frac{\partial N_j}{\partial z} \tag{3.11}$$

Interfaces are assumed to lie at the midpoint between two nodes. Element-based coefficients are equivalent in function to those based upon a control volume discretization [e.g. *Patankar*, 1980]:

$$I_{ij} = -\frac{A_{ij}}{\Delta_{ij}} \tag{3.12}$$

where A_{ij} = interface area and Δ_{ij} = separation distance between adjacent volumes i and j.

Influence coefficients (3.10) must be non-negative for physically meaningful water and advective solute flux calculations. Discrete fluxes with incorrect orientations can be generated for negative values, causing time step reduction and requiring large numbers of Newton iterations to achieve convergence [*Letniowski and Forsyth*, 1991]. An ideal discretization method would be based on (3.12), as influence coefficients are derived from positive-valued permeabilities, areas and distances. The finite element-based requirement of non-negative transmissibility:

$$\sum_{ij\in\eta_e}\left[k^{xx}_{ij+1/2} I^{xx}_{ij} + k^{yy}_{ij+1/2} I^{yy}_{ij} + k^{zz}_{ij+1/2} I^{zz}_{ij}\right]^e \geq 0 \tag{3.13}$$

is a function of the nodal permeability tensors, the elemental geometry, and the choice of basis functions. For linear basis functions, *Letniowski and Forsyth* [1991] indicate that horizontal values of

(3.13) are negative for block elements with large aspect ratios, assuming a constant, isotropic permeability tensor. A similar analysis of large aspect linear prisms, presented in Appendix A , leads to the same conclusion. Tetrahedra tend to produce negative values along diagonal connections. The simulation of dynamic coupling using large, irregular, three-dimensional grids with spatially variable properties effectively guarantees the existence of some negative influence coefficients. Aspect ratios are likely to be largest adjacent to the land surface where vertical refinement is desired to resolve large pressure head gradients. The magnitude and number of these negative influence coefficients should be minimized to ensure Newton iteration convergence [*Letniowski and Forsyth*, 1991]. Utilization of finite-difference approximations for finite-element coefficient matrices aids in such minimizations.

The surface influence coefficients, Γ_s [$L^{4/3}T^{-1}$], are linear functions of the surface roughness and elemental geometry and a nonlinear function of the magnitude of the water potential (friction slope):

$$\Gamma_{ij}^{I,L+1} = -\sum_{ij\in\eta_e}\left(\frac{1}{\Phi^{1/2}}\right)_e^{I,L+1}\left[\left(\frac{1}{n^{xx}}\right)_{ij+1/2} I_{ij}^{xx} + \left(\frac{1}{n^{yy}}\right)_{ij+1/2} I_{ij}^{yy}\right]^e \qquad (3.14)$$
$$= \Gamma_{ji}^{I,L+1}$$

and, therefore, is a nonlinear function of water depth. The friction slope, Φ [-], is evaluated as an elemental parameter at the previous Newton iteration level as:

$$\Phi^{I,L+1} = \left[\max\left(\varepsilon, \nabla\left(\psi_{s'} + z_s\right)\right)\right]^{I-1,L+1} \qquad (3.15)$$

where ε is a small number (e.g. 10^{-3} to 10^{-6}) that, in the event of a zero fluid potential gradient, avoids a divide by zero in (3.14) by enforcing a minimum value of Φ. This is equivalent to specifying a large finite influence. Lagging the evaluation of (3.14) by one Newton iteration assumes that the influence is second-order relative to the water depths in the conveyance term. Note that a nonlinear surface roughness function could easily be included, subject to the same assumption. This formulation differs from that used by *Hromadka et al.* [1985, 1987] and *Brown* [1995] who set the water flux to zero if the friction slope, Φ, or water depth, ψ_s, is less than some threshold value. The

approach is similar to that utilized by *Feng and Molz* [1997], who avoided the divide-by-zero singularity by adding a small number to the calculated gradient.

The discretization and weighting schemes utilized in this work eliminates the need for special treatment of alternating wet and dry conditions on the land surface due to topographic variability. Similar to *Meselhe and Holly* [1993] and *Feng and Molz* [1997], internal boundaries at the land surface are implicitly considered as the surface conveyance (3.6) and the discrete surface water flux (3.4) are zero when upstream water depths fall below the height of the storage depressions. *Meselhe and Holly* [1993] provide a review of previous numerical approaches to this nonlinear internal boundary condition, including the use of an inverse Preissman's slot [e.g. *Schuurmans*, 1991] and moving or deforming finite element grids [e.g. *Akanbi and Katapodes*, 1988].

Use of the surface saturation and relative permeability functions given by equations (2.19) and (2.45) ensures mass conservation, as infiltration is an implicit function of the surface water depth. This contrasts to *Playán et al.* [1994] who minimized mass balance errors by arbitrarily reducing the infiltrated water volume to maintain mass conservation and solution monotonicity. *Playán et al.* [1994] and *Meselhe and Holly* [1993], furthermore, ignore water depths below some user-specified value by resetting water depth to a small positive value if non-positive values were generated by their solution method. The spatial and temporal discretization scheme utilized for the surface equations provides a mass conservative solution strategy consistent with that utilized for the subsurface flow equations. The Jacobian assembly strategy follows the efficient node-based algorithm described by *Forsyth and Simpson* [1991] and is discussed in Section 3.2.2.

3.2.1 Boundary Conditions

Specified or functional boundary conditions can vary in time and space and are implemented through the manipulation of the source/sink terms in (3.1) [*Forsyth*, 1988; *Costa et al.*, 1995; *Wu et al.*, 1996]. The large influence approach is used to enforce specified conditions:

$$Q_b^S = \Gamma_{\text{large}}\left(\psi_b^* - \psi_b\right) \tag{3.16}$$

where ψ_b = current pressure head or water depth; ψ_b^* = desired pressure head or water depth; and Γ_{large} = an influence significantly greater in magnitude than the sum of all other nodal influences (e.g. 10^4). *Wu et al.* [1996] demonstrate that the use of (3.16) emulates the effect of a fine spatial discretization adjacent to the boundary $\left(\Gamma_{large} \propto 1/a\right)$.

Rainfall is assigned per unit area of the land surface [*Huyakorn et al.*, 1986b]:

$$Q_b^R = q_R A_b \tag{3.17}$$

where q_R = the rainfall intensity per unit area [LT^{-1}] and A_b = the area associated with a surface water equation (A_s), equivalent to the boundary area of a subsurface volume (Figure 3-1). Flux boundary conditions may be spatially and temporally variable, allowing non-uniform rainfall distribution.

In considering coupled surface-subsurface flow and transport, a decision must be made regarding where to apply specified sources such as rainfall or irrigation water. Rainfall interacts with the porous medium until such time that the surface water depth becomes sufficient to absorb any vertical inertial forces generated by raindrop impact [*Izzard*, 1946]. While this may have little effect on the surface flow solution beyond an increased resistance at small depths [*Akan and Yen*, 1981], the impact on the transport solution may be significant. Furthermore, rainfall mixes with water contained in the specified boundary volume and, therefore, may alter solute concentrations within that volume. One possible approach is to use back-calculated maximum infiltration rates at each node at the land surface to apportion rainfall between the surface and subsurface equations. To maintain an implicit solution and avoid the additional computational cost of the back-calculations, the numerical model developed here can apportion the applied flux as an implicit function of surface saturation. This can be written as:

$$Q_b^R = q_R A_b S_{e_i}; i \in \eta_s \tag{3.18}$$

$$Q_b^R = q_R A_b \left(1 - S_{e_i}\right); i \in \eta_p, j \in \eta_s \cap \eta_{i_p}$$

which states that the rainfall is applied to the porous medium surface when water depths are below residual values $\left(S_{e_i} = 0\right)$. Rainfall is applied to both the porous medium and surface continua prior

to surface water ponding above the surface microtopography $\left(0 < S_{e_s} < 1\right)$, but rainfall is applied exclusively to the surface continua if water depths are at or above the height of the microtopography $\left(S_{e_s} = 1\right)$. Solute mixing occurs, therefore, in the correct water volume. Note that channel precipitation (i.e. rainfall directly onto streams) is included naturally with this dual boundary condition. Furthermore, available subsurface storage must be utilized before rainfall is applied to the surface continuum. Small subsurface discretization volumes will ensure both accurate resolution of subsurface potential gradients and appropriate storage response timing.

Several additional nonlinear water sink boundary conditions are implemented. These conditions are also evaluated within the Newton iteration loop and form part of the solution. Free drainage at the base of the subsurface finite element grid can be specified per boundary area, A_b, as:

$$Q_b^D = -k_{rw} k^{zz} f_z^a A_b \tag{3.19}$$

which assumes a unit fluid potential gradient (gravity drainage) at the boundary [e.g. *Simunek et al.*, 1985]. Surface outflow flux (e.g. stream discharge leaving computational domain) may be specified by:

$$Q_b^C = -\left[g(\psi_s - h_w)^3 \right]^{1/2} L_b ; h_w \geq S_{w_r} h_s \tag{3.20}$$

which relates boundary flux per unit boundary length L_b to critical water depth to represent, for example, free-fall over a weir of height h_w [*Chow*, 1959; *Freeze*, 1978]. Surface outflow boundaries can also be specified by normal flow conditions [e.g. *Chow*, 1959; *Freeze*, 1978]:

$$Q_b^N = -\psi_s^{5/3} \frac{S^{1/2}}{n} L_b \tag{3.21}$$

where S is a specified stream gradient. Equation (3.21) is equivalent to multiplying the Manning-derived velocity by the stream cross-sectional area.

Evaporation and plant transpiration are considered using sink functions of the general form:

$$Q_b^{ET} = \alpha(\psi) S_{\max}^{ET} V \tag{3.22}$$

$$Q_b^E = \alpha(\psi_s) S_{\max}^E A_b$$

where Q_b^T and Q_b^E represent the actual transpiration and evaporation sinks [L^3T^{-1}], S_{max}^{ET} [T^{-1}] is the potential evapotranspiration rate per unit volume of soil, and S_{max}^{E} [LT^{-1}] is the potential evaporation rate per unit area of surface water. The forms of the dimensionless response functions $\alpha(\psi)$ and $\alpha(\psi_s)$ depend, for example, upon the distribution of roots with depth, type of plant, the availability of liquid water, and the minimum permissible pressure head. Reviews of the many possible functional forms of the stress functions are provided by *Feddes et al.* [1978, 1988], *Molz* [1981] and *van Genuchten* [1987]. Additional functional relationships may consider atmospheric humidity (vapor pressure), wind speed, and solar radiation inputs. Note that multiple sources and sinks can be applied at the same position in space. For example, evaporation, rainfall and critical depth boundary conditions can be applied simultaneously to the same surface equation.

The surface-subsurface flow coupling described in Section 2.3 eliminates the need for special iterative algorithms to handle seepage faces on non-vertical porous medium boundaries. Seepage is implicitly accommodated through discharge into the surface continuum. Further, this water is not lost to the system, but ponds or flows overland, possibly to reinfiltrate elsewhere as conditions allow. A variant of traditional seepage face boundary conditions are included, however, for vertical outflow boundaries where the surface flow equations are invalid.

Seepage faces in most existing numerical models are initially assigned zero-flux boundary conditions with the seepage face algorithm performing an iterative search for the locations on the boundary at which the back-calculated fluid flux:

$$Q_{b_i}^{back} = -\sum_{j \in \eta_i} (\gamma k_{rw})_{ij} \Gamma_{ij} \tag{3.23}$$

is directed out of the domain (i.e. negative) and the calculated pressure head is at or above the atmospheric reference value (i.e. zero). Once located, the solution is recalculated with the pressure head at these locations constrained at zero. Pressure heads are not allowed to rise above atmospheric conditions at seepage faces. This restriction is equivalent to assuming a negligible ponding depth and that discharged water is immediately removed via a fast mechanism such as overland flow [*Neuman*, 1973; *Cooley*, 1983; *Huyakorn et al.*, 1986].

The seepage face algorithm utilized in this work compares the back-calculated flux to the specified boundary flux (i.e. rainfall), and constrains the pressure head at zero using (3.16) if the applied flux is larger. This algorithm can be viewed as an adaptation of that presented by *Huyakorn et al.* [1986a,b] and can be written in pseudo code as:

$$\begin{aligned}
&\text{IF } (constrained) \text{ THEN} \\
&\quad \text{IF } \left(Q_b^{back} > Q_b^R \text{ AND } \psi < -\varepsilon\right) constrained := \text{ FALSE} \\
&\text{ELSE} \\
&\quad \text{IF } \left(Q_b^{back} < Q_b^R \text{ AND } \psi > +\varepsilon\right) constrained := \text{TRUE} \\
&\text{ENDIF}
\end{aligned} \tag{3.24}$$

where ε is a small number that minimizes node state oscillation within the Newton iteration loop [*Cooley*, 1983]. A consequence of this algorithm is that water may continue to be injected into the subsurface at a 'seepage' face [e.g. *Forster and Smith*, 1988]. In the coupled surface-subsurface approach developed in this work, the applied water ponds on the land surface until it is removed via infiltration, surface flow, or evaporation. Such conditions are equivalent to applying a transient pressure head constraint to the subsurface nodes. Ponded water, if available, continues to infiltrate at the rate dictated by the subsurface hydrodynamics, ceasing when the rainfall ceases and surface storage is exhausted. The modified seepage face algorithm constrains the pressure head at zero until the rainfall ceases and the subsurface water infiltrates. The seepage face algorithm (3.24) is imbedded in the Newton iteration loop.

An additional complexity is introduced at vertical subsurface outflow boundaries located below nonlinear surface water boundaries (i.e. at the outlet of a truncated hillslope or catchment). The boundary condition for surface flow at these locations is described by (3.20) so that the surface water depth is transient in time and dependent upon the rainfall rate and water flowing from up-gradient. The pressure head in the immediate subsurface, therefore, is also transient but neither the pressure heads nor boundary fluxes are known *a priori*. The back calculated water flux, (3.23), is utilized as a subsurface nodal sink term in these situations:

$$Q_b^O = Q^{back} = -\sum_{j\in\eta_i} (\gamma k_{rw})_{ij} \Gamma_{ij} \tag{3.25}$$

to allow subsurface water to exit the computational domain without discharging through the surface boundary. Neither the pressure heads nor water fluxes are specified, but instead are both determined as part of the solution.

3.2.2 Linearization

The system of equations describing flow in all continua are solved in a fully coupled fashion so that fluid exchanges and nonlinear boundary conditions are determined as part of the iterative solution. The discrete flow equations are linearized using Newton's method and numerical derivatives [*Forsyth and Simpson*, 1991; *Forsyth et al.* [1995]. For example, if the surface terms in equation (3.1) are rewritten in the form of residuals:

$$\begin{aligned} r_{i_s}^{I,L+1} = & \frac{A_{i_s}}{\Delta t_{global}} \left[\left(S_w h_s + \psi_{s_s} \right)^{L+1} - \left(S_w h_s + \psi_{s_s} \right)^{L} \right]_{i_s} \\ & - \sum_{j\in\eta_{i_s}} \omega_f Q_{ji_s}^{L+1} - \sum_{j\in\eta_{i_s}} \left(1-\omega_f\right) Q_{ji_s}^{L} - \sum_{i_s} Q_b^{L+1} \end{aligned} \tag{3.26}$$

then off-diagonal Jacobian entries are approximated as:

$$\frac{\partial Q_{ji_s}^{I,L+1}}{\partial \psi_{i_s}^{I,L+1}} \approx \frac{Q(\psi+\varepsilon)_{ji_s}^{I,L+1} - Q(\psi)_{ji_s}^{I,L+1}}{\varepsilon} \tag{3.27}$$

where ε represents a small numerical shift (i.e. 10^{-6}) in the water depth values. The Jacobian diagonal entries can be expressed as:

$$\frac{\partial r_{i_s}^{I,L+1}}{\partial \psi_{i_s}^{I,L+1}} = \frac{r(\psi)_{i_s}^{I,L+1} - r(\psi+\varepsilon)_{i_s}^{I,L+1}}{\varepsilon} \tag{3.28}$$

The flux terms on the right-hand side of (3.27) are calculated during the formation of the numerical derivatives (3.27) and the flux derivatives in the Jacobian columns are calculated within the diagonal-entry flux summations. Subsurface Jacobian terms are determined in a similar manner. The complete system of linearized equations:

$$[J]^{I,L+1}\{\Delta\psi\}^{I+1,L+1} = -\{r\}^{I,L+1} \tag{3.29}$$

can be efficiently constructed by calculating only the diagonal derivative entries [*Forsyth and Simpson*, 1991]. Further details of the Jacobian assembly method can be found in *Forsyth and Simpson* [1991] and *Forsyth et al.* [1995].

The simulations performed in subsequent chapters, being highly dynamic, are solved fully-implicitly. However, one can anticipate scenarios in which the time step required for convergence of the Newton iteration loop is dictated by the dynamics of surface flow or flow in the unsaturated zone [*S. Panday, per. comm.*, 1998]. These timesteps may be considerably smaller than required for a stable and monotone solution (1) to the linear equations arising from flow in saturated porous medium or macropores, (2) to the nonlinear equations in stagnant regions of the unsaturated zone, or (3) to nonlinear equations in dry regions of the land surface. If variable temporal weighting is utilized in (3.1), the linearized system of equations (3.29) can be partitioned into implicit $(\omega_f = 1)$ and explicit $(\omega_f = 0)$ submatrices:

$$\left[\begin{array}{c:c} J_i & \\ \hdashline & J_e \end{array}\right]^{I,L+1} \left\{\begin{array}{c} \Delta\psi_i \\ \hdashline \Delta\psi_e \end{array}\right\}^{I+1,L+1} = -\left\{\begin{array}{c} r_i + r_e \\ \hdashline r_e \end{array}\right\}^{I,L} \tag{3.30}$$

where:

$$[J_i]^{I,L+1}\{\Delta\psi_i\}^{I+1,L+1} = -\{r_i + r_e\}^{I,L+1} \tag{3.31}$$

represents equations with explicitly and implicitly evaluated fluxes, including boundary conditions, and where:

$$[J_e]^{I,L+1}\{\Delta\psi_e\}^{I+1,L+1} = -\{r_e\}^{I,L+1} \tag{3.32}$$

represents equations with all fluxes evaluated explicitly. The explicit Jacobian submatrix, $[J_e]^{I,L+1}$, contains storage derivatives only:

$$\frac{\partial Q_{ji_s}^{I,L+1}}{\partial \psi_{i_s}^{I,L+1}} = 0 \tag{3.33}$$

and has no off-diagonal entries and can be evaluated inexpensively prior to the Newton iteration loop:

$$\begin{aligned}\{\psi_e\}^{L+1} &= \{\psi_e\}^{L} + \{\Delta\psi_e\}^{L+1} \\ &= \{\psi_e\}^{L} - \{r_e/J_e\}^{L}\end{aligned} \tag{3.34}$$

The explicitly derived solutions $\{\psi_e\}^{L+1}$ are thus known at the new time level. By eliminating the explicit equations, the linearized system of equations, (3.30), is solved only for those equations containing implicit terms (3.31). The two systems of equations are linked, and mass is conserved, via explicitly evaluated fluxes in the residual or forcing vectors $\{r_i + r_e\}^{I,L+1}$ and $\{r_e\}^{I,L+1}$. Such coupling is effectively external and is updated at the beginning of each time step for each equation.

Equations with active boundary conditions are always solved implicitly. Adaptive time weighting on the remaining equations is implemented by pre-calculating the explicit solution to all equations. Those explicit solutions that are unstable (i.e. violate the Courant criteria), or result in primary variable changes larger than the Newton convergence tolerances are also flagged as implicit. Consistent temporal weighting is utilized on all coupled equations such that all equations at a given node are solved implicitly if the previous criteria select one equation for implicit solution. This conservative strategy partitions the discrete equations into temporally variable subsets corresponding to nonlinear or highly dynamic regions and linear or slowly changing regions of the finite element grid, respectively (see Section 4.4).

The primary variable switching algorithm of *Forsyth et al.* [1995] is implemented to aid convergence of the subsurface flow equations. *Forsyth et al.* [1995] demonstrate that use of pressure head as the primary variable in dry regions of the subsurface can cause convergence problems for the Newton iteration due to the extreme non-linearity of the $\psi - S_w$ relationship. The time steps required for convergence are often much smaller than those needed for reasonable time-truncation errors. Selecting saturation as the primary variable in dry regions can significantly reduce these convergence difficulties. Variable substitution is accomplished by inverting the $\psi - S_w$ relationship to make pressure head a function of saturation $\psi = \psi(S_w)$, and by calculating the numerical

derivatives using a small shift in saturation instead of pressure head. The same sets of subsurface flow equations are solved and are independent of the chosen primary variable. Primary variables at adjacent nodes may differ, as characteristic curves and hydraulic conductivities are defined as nodal parameters in the control volume finite element method (i.e. properties are assigned by equation, not element). Similarly, primary variable switching may be performed if first order coupling is utilized, but cannot be performed where continua are coupled by pressure continuity assumptions.

Newton linearization proceeds until a specified maximum number of iterations are exceeded or until the magnitude of the solution updates at each node are smaller than specified tolerances for each primary variable. A check of nodal solution residual errors is performed once the primary variables have converged. This check is implemented to ensure a monotone transport solution. Trial simulations of flow and transport in coupled porous media-fracture systems demonstrate that subtle changes in pressure head can shift the location of the upstream point used in calculating the coupling flux. This shifted upstream point can result in a large change in the discrete flux if the two continua have drastically different saturations and relative permeabilities at approximately the same pressure head. For a very dry fracture, this additional flux can result in a large fluid mass balance error (residual), resulting in a non-monotone transport solution (e.g. artificial minima and maxima develop). Similar behavior may occur when the upstream point on the land surface shifts, indicating a change from infiltration to exfiltration, or *visa versa*. Forcing additional flow Newton iterations usually corrects this error.

The residual error tolerance is defined for each equation as [*P. Forsyth, personal communication*, 1997]:

$$\max\left(\left|1-|\alpha|\right|\right) < tol^{error} \tag{3.35}$$

$$\alpha = \frac{V_w^L/\Delta t + \sum_i \max(0,Q) + \max(0,Q_b)}{V_w^{L+1}/\Delta t + \sum_i \min(0,Q) + \min(0,Q_b)}$$

where V_w = water volume. Equation (3.35) is a measure of the magnitude of the local residual error in relation to the volume of water present at the beginning of the timestep. Note that it may

be quite difficult to satisfy (3.35) if the surface depths or subsurface saturations are small as small errors in saturation or water depth may represent a large relative residual error. Calculation of this error measure is nearly as expensive as to build a Jacobian, and is only performed once the primary variables have converged due to the update tolerances. The relative error tolerance, tol^{error}, is generally taken to be 10^{-2}. The time step is reduced and the Newton iteration loop is restarted if convergence is not attained *via* both the solution update tolerances and the residual error criteria. Convergence update tolerances are generally specified to be an order of magnitude larger than the numerical derivative increment to minimize both residual error and the additional computational cost associated with the evaluation of (3.35).

The convergence behavior of the Newton iterations is aided by applying the under-relaxation scheme of *Cooley* [1983], modified to operate independently on each primary variable. Furthermore, negative influences $\left(\Gamma_p, \Gamma_m, \Gamma_s\right)$ can be set to zero, ensuring that discrete water and species fluxes occur in the correct physical direction (see Appendix A). Global timesteps are selected based upon target changes for each primary variable [*Forsyth and Simpson*, 1991; *Therrien and Sudicky*, 1996], target residual errors (3.35), and the number of flow Newton iterations required for convergence [*S. Panday, per. comm.*, 1997], a measure of solution difficulty. Basing time step selection on macropore or surface saturation changes can be quite restrictive.

3.2.3 Solution

Approximate solutions to the linearized equations are generated using an iterative sparse-matrix solver [*VanderKwaak et al.*, 1997] employing Bi-CGSTAB [*van der Vorst*, 1992] or GMRES [*Saad and Schultz*, 1986] acceleration and reverse Cuthill-McKee ordering [*Cuthill and McKee*, 1969; *George*, 1971] of a red-black reduced system of equations. Preconditioning is provided by incomplete lower-upper factorization (ILU) or drop-tolerance incomplete lower-upper (ILUT) factorization [*Behie and Forsyth*, 1984; *Saad*, 1996]. ILUT factorizations are performed only on the Jacobian generated in the first Newton iteration. Solutions to subsequent Newton iterations are preconditioned using the ILU algorithm and the data structure provided by the drop tolerance

factorization. Accurate factorizations are generated, therefore, while the higher computational cost of the drop tolerance algorithm is amortized over the total number of nonlinear iterations. Convergence of the iterative solver is determined to occur when solution updates are small or a specified relative residual reduction is attained. Solution update tolerances are generally specified as one or two orders of magnitude less than the Newton convergence tolerances: residual reduction tolerances are generally set to 10^{-6}. These relatively tight tolerances aid in minimizing local residual errors (3.35).

3.3 Discrete Solute Transport Equations

Following convergence of the flow Newton iterations, the concentration distribution of multiple solutes is determined via the sequential solution of the transport equations, beginning with the first parent if chain decay is occurring. The spatial distribution of pressure head, saturation, water depth and boundary water flux is known from the solution of the non-linear flow equations. Given the finite element grids utilized in solving flow, the final form of the discretized transport equations for each species in water is:

$$
\begin{aligned}
&V_i f_{i_p}^{v}\Big[(RC)^{M+1}(1/\Delta t_{sub}+\lambda\omega)-(RC)^{M}(1/\Delta t_{sub}+\lambda(\omega-1))\Big]_{i_p}+ \\
&V_i f_{i_m}^{v}\Big[(RC)^{M+1}(1/\Delta t_{sub}+\lambda\omega)-(RC)^{M}(1/\Delta t_{sub}+\lambda(\omega-1))\Big]_{i_m}+ \\
&A_{i_s}\Big[(RC)^{M+1}(1/\Delta t_{sub}+\lambda\omega)-(RC)^{M}(1/\Delta t_{sub}+\lambda(\omega-1))\Big]_{i_s} \\
&=\sum_{j\in\eta_{i_p}}\Big[\omega C_{\text{adv}}^{M+1}+(1-\omega)C_{\text{adv}}^{M}\Big]Q_{i_p j}^{L+1}+\sum_{j\in\eta_{i_p}}\Big[\omega\xi^{M+1}+(1-\omega)\xi^{M}\Big]\Lambda_{i_p j}^{M+1} \\
&+\sum_{j\in\eta_{i_m}}\Big[\omega C_{\text{adv}}^{M+1}+(1-\omega)C_{\text{adv}}^{M}\Big]Q_{i_m j}^{L+1}+\sum_{j\in\eta_{i_m}}\Big[\omega\xi^{M+1}+(1-\omega)\xi^{M}\Big]\Lambda_{i_m j}^{M+1} \\
&+\sum_{j\in\eta_{i_s}}\Big[\omega C_{\text{adv}}^{M+1}+(1-\omega)C_{\text{adv}}^{M}\Big]Q_{i_s j}^{L+1}+\sum_{j\in\eta_{i_s}}\Big[\omega\xi^{M+1}+(1-\omega)\xi^{M}\Big]\Lambda_{i_s j}^{M+1} \\
&-V_i f_{i_p}^{v}\sum_{k\in par_{sp}}\lambda_k\Big[\omega(RC)_k^{M+1}+(1-\omega)(RC)_k^{M}\Big]_{i_p}+\sum_{i_p}Q_b^{L+1}C_b^{M+1} \\
&-V_i f_{i_m}^{v}\sum_{k\in par_{sp}}\lambda_k\Big[\omega(RC)_k^{M+1}+(1-\omega)(RC)_k^{M}\Big]_{i_m}+\sum_{i_m}Q_b^{L+1}C_b^{M+1} \\
&-A_{i_s}\sum_{k\in par_{sp}}\lambda_k\Big[\omega(RC)_k^{M+1}+(1-\omega)(RC)_k^{M}\Big]_{i_s}+\sum_{i_s}Q_b^{L+1}C_b^{M+1}
\end{aligned}
\tag{3.36}
$$

$$i_p\in\eta_p;\ i_m\in\eta_m;\ i_s\in\eta_s;\ j\in\eta_n;\ par\in\eta_{species}$$

where $\xi_{ij}=C_j^{\cdot}-C_i$; L and $L+1$ are global previous and current time levels, respectively; M and $M+1$ are the current and target time levels for the transport sub-timestep; and ω = time weighting $(0\le\omega\le 1)$. Subtimesteps are determined as specified functions of the global timestep, by target concentration changes, or by monotonicity considerations based upon the time weighting utilized. Subtimesteps are used during periods of slowly changing flow solutions to minimize computational effort while maintaining transport solution accuracy. Saturations are interpolated linearly from the known values at the old and current global times:

$$
\begin{aligned}
&\frac{\partial S}{\partial t}\approx\left(\frac{\Delta S}{\Delta t}\right)_{global}=\frac{(S^{L+1}-S^{L})}{(t^{L+1}-t^{L})} \\
&S^{M}=S^{L}+(t^{M}-t^{L})\left(\frac{\Delta S}{\Delta t}\right)_{global} \\
&S^{M+1}=S^{L}+(t^{M+1}-t^{L})\left(\frac{\Delta S}{\Delta t}\right)_{global}\equiv S^{M}+\Delta t_{sub}\left(\frac{\Delta S}{\Delta t}\right)_{global}
\end{aligned}
\tag{3.37}
$$

Pressure heads and water depths are interpolated in the same manner. Water fluxes are assumed constant over the entire global timestep and are evaluated with temporal weighting consistent with that utilized in the flow equation solution. Note that $M = L$ if subtimesteps are not used.

The dispersive coupling influence coefficients for an isotropic porous medium containing equally-spaced macropores can be expressed as:

$$\begin{aligned}\Lambda_{i_p i_m}^{M+1} &= \left[\varphi_{pm}^{e_D}\right]_{i_p i_m}^{M+1} \frac{A_{m_i}}{a_m} \\ &= \left[\varphi_{pm}^{e_D}\right]_{i_p i_m}^{M+1} \frac{\zeta_{m_i} V_i}{a_{m_i}} \\ &= \Lambda_{i_m i_s}^{M+1}\end{aligned} \tag{3.38}$$

Where the Darcy velocity, $|q|$, is given by

$$\left|q_{i_p i_m}\right| = \frac{\left|Q_{i_p i_m}\right|}{A_{m_i}} = \frac{\left|Q_{i_p i_m}\right|}{\zeta_{m_i} V_i} \tag{3.39}$$

Unequal macropore spacing is included in a manner identical to (2.19). Porous medium-surface influence coefficients are defined as:

$$\begin{aligned}\Lambda_{i_s i_p}^{M+1} &= \left[\varphi_{sp}^{D_e}\right]_{i_s i_p}^{M+1} \frac{f_{p_i}^{a_{\perp}} A_{s_i}}{a_s} \\ &= \Lambda_{i_p i_s}^{M+1}\end{aligned} \tag{3.40}$$

and the macropore-surface influence coefficients are given as:

$$\begin{aligned}\Lambda_{i_s i_m}^{M+1} &= \left[\varphi_{sm}^{e_D}\right]_{i_s i_m}^{M+1} \frac{f_{m_i}^{a_{\perp}} A_{s_i}}{a_s} \\ &= \Lambda_{i_m i_s}^{M+1}\end{aligned} \tag{3.41}$$

where the Darcy velocities, $|q|$, are given by:

$$\left|q_{i_p i_s}\right| = \frac{\left|Q_{i_p i_s}\right|}{f_{p_i}^{a_{\perp}} A_{s_i}} \qquad \left|q_{i_s i_m}\right| = \frac{\left|Q_{i_s i_m}\right|}{f_{m_i}^{a_{\perp}} A_{s_i}} \tag{3.42}$$

Dispersive influence coefficients for the three continua are, for transport in the porous medium:

$$\Lambda_{i_p j_p}^{M+1} = -\int_v \nabla N_i \cdot f^a \left(\phi S_w \bar{D}_w + \phi S_a \bar{D}_a\right)_{i_p j_p}^{M+1} \cdot \nabla N_j \, dv \qquad (3.43)$$
$$= \Lambda_{j_p i_p}^{M+1}$$

for transport in macropores:

$$\Lambda_{i_m j_m}^{M+1} = -\int_v \nabla N_i \cdot f^a \left(\phi S_w \bar{D}_w + \phi S_a \bar{D}_a\right)_{i_m j_m}^{M+1} \cdot \nabla N_j \, dv \qquad (3.44)$$
$$= \Lambda_{j_m i_m}^{M+1}$$

and, for transport in the surface water:

$$\Lambda_{i_s j_s}^{M+1} = -\int_a \nabla N_{i_s} \cdot \left(\psi_{s'} \bar{D}_w\right)_{i_s j_s}^{M+1} \cdot \nabla N_{j_s} \, da \qquad (3.45)$$
$$= \Lambda_{j_s i_s}^{M+1}$$

Harmonic weighting of interface areas, saturations and water depths are utilized in (3.43), (3.44) and (3.45). The dispersion tensors, while updated at each timestep for each species, are constant during Newton linearization.

Boundary conditions can vary in time and space and are implemented through manipulation of nodal source and sink terms. The solute source/sink terms are defined as:

$$(QC)_{b_i} = Q_{b_i}^{+} C_b^{*} + Q_{b_i}^{-} C_i \qquad (3.46)$$

where Q_b^+ = the sum of volumetric water sources; C_b^* = the solute concentration in the injected water; Q_b^- = the sum of volumetric water sinks; and C_i = the current solute concentration.

The advective concentration terms, C_{adv}, can be defined as a linear function using central weighting:

$$C_{\text{adv}_{ij}} = C_{\text{cent}_{ij}} = \frac{C_j + C_i}{2} \qquad (3.47)$$

or upstream weighting:

$$C_{\text{adv}_{ij}} = C_{\text{ups}_{ij}} = \begin{cases} C_j & \text{if} \quad \gamma_{ij}\Gamma_{ij} > 0 \Rightarrow j = \text{ups}_{ij};\ i = \text{dwn}_{ij} \\ C_i & \text{if} \quad \gamma_{ij}\Gamma_{ij} \le 0 \Rightarrow i = \text{ups}_{ij};\ j = \text{dwn}_{ij} \end{cases} \qquad (3.48)$$

where ups_{ij} and dwn_{ij} indicate the upstream and downstream nodes, respectively. Upstream weighting is first-order accurate and maintains monotonicity at a cost of increased numerical

dispersion. Central weighting, while second-order accurate, can produce non-monotone solutions in advection-dominated systems. High velocities can occur in both the macropore and surface continua.

The advective concentration can also be defined by nonlinear functions that reduce numerical dispersion while maintaining solution monotonicity. The van Leer flux limited concentration is defined as [*van Leer*, 1974]:

$$C_{\mathrm{adv}_{ij}} = C_{\mathrm{ups}_{ij}} + \sigma(r_{ij})\frac{\xi_{ij}^{-}}{2} \tag{3.49}$$

where:

$$\sigma(r_{ij}) = \begin{cases} 0 & r_{ij} \le 0 \\ 2r_{ij}/(1+r_{ij}) & r_{ij} > 0 \end{cases} \qquad r_{ij} = \left(\frac{\xi_{ij}^{+}}{\Delta^{+}}\right)\Big/\left(\frac{\xi_{ij}^{-}}{\Delta^{-}}\right) \qquad \begin{aligned} \xi_{ij}^{+} &= C_{\mathrm{ups}_{ij}} - C_{\mathrm{2ups}(\mathrm{ups}_{ij})} \\ \xi_{ij}^{-} &= C_{\mathrm{dwn}_{ij}} - C_{\mathrm{ups}_{ij}} \end{aligned} \tag{3.50}$$

and Δ^{+} = the distance between the upstream and second upstream nodes and Δ^{-} = the distance between the upstream and downstream nodes [*Forsyth et al.*, 1998]. The second upstream point, $\mathrm{2ups}(\mathrm{ups}_{ij})$, is defined as the node connected to the upstream node, ups_{ij}, which contributes the largest water flux. This definition is equivalent to the maximum potential method of *Forsyth* [1994] and *Unger et al.* [1996]. Numerical dispersion reduction is accomplished in (3.49) by shifting the spatial weighting from upstream (most dispersive) to downstream (least dispersive) as a function of the local concentration gradients. Note that the flux limiter is not applied in coupling transport between continua: the advective concentration is discretized using upstream weighting in such cases [e.g. *Gerke and van Genuchten*, 1993a]. Monotonicity criteria for the possible combinations of spatial and temporal weighting are discussed in detail by *Unger et al.* [1996].

3.3.1 Linearization and Solution

Use of the flux limiting function (3.49) causes the discrete transport equations (3.36) to become nonlinear. The nonlinear system is solved using Newton's method using assembly algorithms similar to those introduced in Section 3.2.2 for flow. Approximate transport Jacobians are implemented to avoid the increased computational cost associated with the inclusion of the second

upstream points in the advective flux derivatives. In the first approximation, referred to here as a partial Jacobian, the nonlinear flux limiter is utilized in both the Jacobian and residual, while the second upstream points are excluded in the Jacobian data structure. In the second approximation, the Jacobian is constructed using the default first-order advective weighting scheme (upstream or central). The nonlinear flux limiters are applied in the residual calculation only, allowing the Jacobian to be generated once per subtimestep for each species with the residual updated during successive Newton iterations [*Forsyth et al.*, 1998].

For example, the residual utilized in generating a surface equation entry in the constant Jacobian, $[J]_{ups}^{M+1}$, is:

$$r_{i_s} = A_{i_s}\left[(RC)^{M+1}(1/\Delta t_{sub} + \lambda\omega) - (RC)^{M}(1/\Delta t_{sub} + \lambda(\omega - 1))\right] - \sum_{i_s} Q_b^{L+1} C_b^{M+1} - \omega \sum_{j \in \eta_{i_s}} \left[C_{ups}^{M+1} Q^{L+1} + \xi^{M+1}\Lambda^{M+1}\right]_{i_s} \tag{3.51}$$

while the residual utilized to calculate the forcing vector, $\{r\}_{FL}^{I,M+1}$, is:

$$r_{i_s} = A_{i_s}\left[(RC)^{M+1}(1/\Delta t_{sub} + \lambda\omega) - (RC)^{M}(1/\Delta t_{sub} + \lambda(\omega - 1))\right] + A_{i_s} \sum_{k \in par_{sp}} \lambda_k \left[\omega (RC)_k^{M+1} + (1-\omega)(RC)_k^{M}\right]_{i_s} - \sum_{i_s} Q_b^{L+1} C_b^{M+1} - \omega \sum_{j \in \eta_{i_s}} \left[C_{FL}^{M+1} Q^{L+1} + \xi^{M+1}\Lambda^{M+1}\right]_{i_s} - (1-\omega) \sum_{j \in \eta_{i_s}} \left[C_{FL}^{M} Q^{L+1} + \xi^{M}\Lambda^{M+1}\right]_{i_s} \tag{3.52}$$

Subsurface residuals are calculated in an identical manner. The matrix equation for the constant, first order Jacobian can be written as:

$$[J]_{ups}^{M+1}\{\Delta C\}^{I+1,M+1} = -\{r\}_{FL}^{I,M+1} \tag{3.53}$$

while the matrix equation resulting from the partial Jacobian is:

$$[J]_{FL}^{I,M+1}\{\Delta C\}^{I+1,M+1} = -\{r\}_{FL}^{I,M+1} \tag{3.54}$$

and is generated using (3.52). *Forsyth et al.* [1998] provide a detailed discussion of the first-order solution approach and conclude that convergence requires "about the same number of nonlinear iterations as full Newton iterations, yet resulted in considerably less computational cost." Simulations performed in this work, however, indicate that the partial Jacobian consistently outperforms the

first-order Jacobian in solving for transport in advective-dominated, variably-saturated, coupled continua. The solution of equations (3.53) or (3.54) is repeated until the sizes of the concentration updates are less than a specified value (e.g. 10^{-4}).

Additional computation savings may be attained if variable temporal and spatial weighting is utilized in (3.36). The development follows that presented for the flow equations (Section 3.2.2) and is repeated here for completeness. Using the constant, first order Jacobian for example, the linearized matrix equation, (3.53), is partitioned as:

$$\left[\begin{array}{c:c} J_i & \\ \hdashline & J_e \end{array}\right]_{ups}^{M+1} \left\{\begin{array}{c} \Delta C_i \\ \hdashline \Delta C_e \end{array}\right\}^{I+1,M+1} = -\left\{\begin{array}{c} r_{i_{FL}} + r_{e_{ups}} \\ \hdashline r_{e_{ups}} \end{array}\right\}^{I,M+1} \tag{3.55}$$

where:

$$\left[J_i\right]_{ups}^{M+1}\left\{\Delta C_i\right\}^{I+1,M+1} = -\left\{r_{iFL} + r_{eups}\right\}_{FL}^{I,M+1} \tag{3.56}$$

represents nonlinear equations with explicitly and implicitly evaluated fluxes, including boundary conditions, and where:

$$\left[J_e\right]_{ups}^{M+1}\left\{\Delta C_e\right\}^{I+1,M+1} = -\left\{r_e\right\}_{ups}^{I,M+1} \tag{3.57}$$

represents linear equations in which all fluxes evaluated explicitly with upstream weighting in the advective terms. The two submatrices are coupled via explicitly evaluated fluxes in the residual or forcing vectors $\left\{r_{i_{FL}} + r_{e_{ups}}\right\}_{FL}^{I,M+1}$ and $\left\{r_e\right\}_{ups}^{I,M+1}$. The explicit Jacobian submatrix, $\left[J_e\right]_{ups}^{M+1}$, represents storage derivatives only (i.e. has no off-diagonal entries) and the explicit solution can be calculated inexpensively prior to the Newton iteration loop:

$$\begin{aligned} \left\{C_e\right\}^{M+1} &= \left\{C_e\right\}^{M} + \left\{\Delta C_e\right\}^{M+1} \\ &= \left\{C_e\right\}^{M} - \left\{r/J\right\}_e^{M} \end{aligned} \tag{3.58}$$

By eliminating the explicit equations, (3.53) is solved only for those equations containing nonlinear implicit terms (3.56), resulting in decreased Jacobian assembly and solution expense if the number of explicit equations is significant. Equations with active boundary conditions are always included in the nonlinear system. Adaptive time weighting on the remaining equations is implemented by pre-

calculating the explicit, upstream-weighted solution to all equations. Those explicit solutions which are non-monotone, or result in concentration changes larger than the Newton convergence tolerance, are also included in the nonlinear system. Consistent temporal weighting is utilized on all coupled equations.

The adaptive temporal weighting scheme was developed to reduce the computational cost associated with the transport of multiple tracer species located in spatially-restricted regions of the finite element mesh. For example, tracers originating below the groundwater table are unlikely to be distributed in the unsaturated zone at later time, while tracers originating within rainfall are likely to be distributed adjacent to the land surface at early time. Conservative by design, this adaptive Jacobian reduction strategy is effective in partitioning the discrete transport equations into dynamic subsets corresponding to spatial zones of active and inactive transport processes. Such partitioning typically decreased solution times by about fifty-percent for the simulations of multiple tracer species performed in this work (see Section 4.4).

The data structure (i.e. spatial connectivity or graph) of the reduced Jacobian is dynamic, changing with time as solutes migrate through the finite element mesh. Therefore, an ILUT factorization is performed on the first Newton iteration during each timestep to simultaneously update both the data structure and the numerical values of the approximately inverted Jacobian (i.e. preconditioning matrix). As first-order Jacobians are constant during a given Newton iteration loop, solutions during subsequent Newton iterations can be generated inexpensively by repeated applications of the same preconditioner. Jacobians constructed using the partial approach, however, are updated during the Newton iteration loop, and preconditioners are calculated using the ILU algorithm and the ILUT data structure generated during the first Newton iteration.

An additional adaptive temporal and spatial weighting scheme can be utilized in the calculation of (3.52) to maintain solution monotonicity in implicit or Crank-Nicholson time-weighted equations. If Crank-Nicholson time weighting is utilized and the resulting solution is not monotone, time weighting for the flux terms in equations in violation is switched to implicit. If solutions to implicit equations are not monotone, the spatial weighting of advective fluxes is

switched to upstream. This adaptive weighting scheme was implemented in response to non-monotone solutions generated at and adjacent to the water table in simulations of dual continua subsurface flow and transport. The complex interaction of flow in the porous medium capillary fringe with high water velocities in the saturated macropore system can place severe restrictions on the size of stable time steps in small regions of the finite element mesh. The adaptive temporal and spatial weighting technique ensures solution motonicity at a small number of troublesome equations while maintaining solution accuracy at the remaining stable equations [e.g. *Unger et al.*, 1996].

Chapter 4 Verification and Validation Problems

The numerical model developed in Chapter 3 couples water flow and solute transport on the land surface with that in the subsurface. The subsurface can be further subdivided into two interacting continua representing a porous medium and either macropores or fractures. Solutions for variably-saturated flow produced by the current numerical model have been compared with results presented in *Clement et al.* [1994], *Forsyth et al.* [1995], and *Therrien and Sudicky* [1996]. Surface flow solutions have been compared with those generated by the numerical model of *Gottardi and Venutelli* [1993] and with analytical solutions presented by *Stephenson and Meadows* [1986]. The following sections present a representative subset of the large number of verification and validation problems performed in this study. Theses problems demonstrate that the modules controlling boundary conditions, unsaturated flow and transport, nonlinear flux limiter, chain decay, sorption, adaptive time weighting, subsurface couplings, surface-subsurface couplings, seepage faces, and surface flow and transport are functioning correctly.

4.1 Chain Decay with Sorption

The flux limiter, sorption, and chain decay modules were tested by comparing results from the numerical model with those from an existing analytical solution CMM [*HydroGeoLogic*, 1991] for one-dimensional transport of a three component, sorbing decay chain (Uranium^{234}, Thorium^{230}, and Radium^{226}) [*Therrien et al.*, 1995]. The input data are presented in Table 4-1. Flow boundary conditions and parameters are set to generate a constant velocity along a one-dimensional 500-m long grid. The concentration of Uranium^{234} is fixed at unity at the inlet node: initial conditions are zero for all species. Summary graphs of the resulting concentration profiles for each species are presented in Figure 4-1 at a time of 1000 years. The most accurate numerical solutions are generated

using Crank-Nicholson temporal weighting in combination with the van Leer flux limited spatial weighting [e.g. *Unger et al.*, 1996]. This combination of weighting schemes maintains accuracy over a concentration range of eight orders of magnitude.

4.2 Tritium Transport Through Parallel Fractures

Porous medium-macropore transport coupling was tested under steady flow conditions by comparing results from the numerical model with those from the analytical solution of *Sudicky and Frind* [1982] for the case of tritium transport through a system of parallel fractures 300 meters in length. Parameters utilized in this simulation are presented in Table 4-2. The concentration of tritium is fixed at unity at the inlet fracture volume. The initial concentration is zero throughout the remaining fracture and porous medium volume. Time weighting is fully implicit and the van Leer flux limiter (3.49) is utilized to minimize numerical dispersion. Figure 4-2 compares the model results with those obtained with the analytic solution at times equal to 1,000, 10,000 days and at steady-state. The numerical solution compares well with the analytical, even though the 10-meter nodal spacing and 1000-day timestep yielded a relatively high Peclet number of 100.

Transport		Uranium^{234}	Thorium^{230}	Radium^{226}
storage	R	1.43×10^{4}	5×10^{4}	5×10^{2}
decay (year^{-1})	λ	2.83×10^{-6}	9×10^{-6}	4.33×10^{-6}
diffusion	D_w	0	0	0
Velocity	$\vec{V}$	100 m/year		
Dispersivity	α	10 m		
Nodal Spacing	Δx	5 m		
Time Step	Δt	100 years		

Table 4-1. Parameterization of sorbing chain decay solute transport verification problem [*Therrien et al.*, 1995].

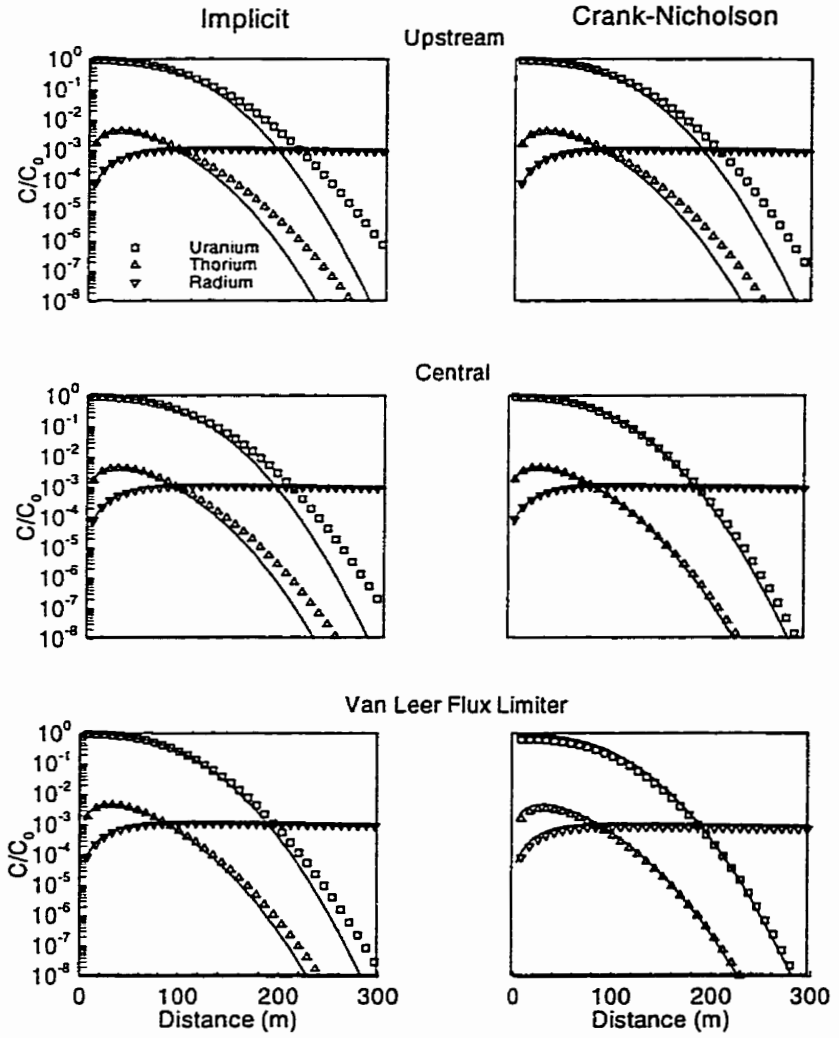

Figure 4-1. Concentration versus distance for chain-decay verification problem. Solid lines and symbols represent concentrations predicted by the analyical and numerical models, respectively.

Tritium		
decay	λ	1.54×10^{-4} days^{-1}
diffusion coefficient	D_w	1.38×10^{-4} m^2/day
Fractures		
velocity	$\vec{V}$	0.1 m/day
dispersivity	α_l	0.1 m
aperture	$2b_m$	10^{-4} m
spacing	$2a_m$	0.1 m
geometry coefficient	β^c	3
porosity	ϕ_m	1
volume fraction	f_m^v	10^{-3}
Porous Medium		
velocity	$\vec{V}$	0
porosity	ϕ_{p_o}	0.01
volume fraction	f_p^v	0.999
tortuosity	τ	0.1
Nodal Spacing	Δx	10 m
Time Step	Δt	10^3 days

Table 4-2. Parameterization of parallel-fracture, tritium transport verification problem [*Sudicky and Frind*, 1982].

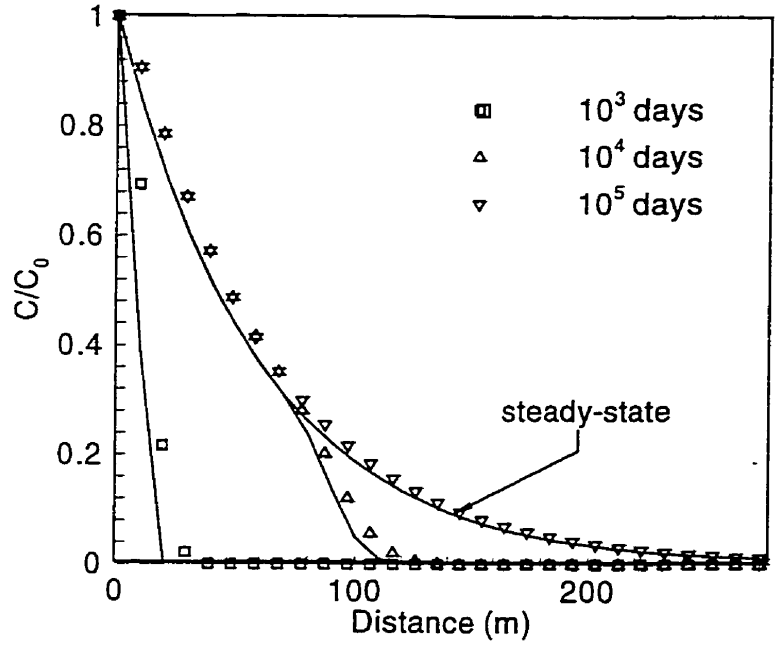

Figure 4-2. Concentration versus distance for parallel fracture transport verification problem [*Sudicky and Frind*, 1982]. Solid lines and symbols represent concentrations predicted by the analyical and numerical models, respectively.

4.3 Variably-Saturated Flow

The modules describing water flow through a variably-saturated porous medium were tested by comparing results from the numerical model with the laboratory measurements of *Vauclin et al.* [1979] as presented in *Clement et al.* [1994]. The two-dimensional problem considers infiltration into a 2 m deep by 3 m long rectangular-shaped sandy porous medium in which the initial water table is located at an elevation of 0.65 m. Recharge is applied at a rate of 3.55 m day^{-1} for eight hours over a 0.5 m-long portion of the left side of the surface, with the water table location being maintained at the initial position at the right boundary for the same period. Table 4-3 presents the parameters utilized in the simulation. Figure 4-3 presents the simulated and measured [*Vauclin et al.*, 1979] water table locations at two, three, four and eight hours. Good agreement is illustrated, verifying that the

variably-saturated flow and primary variable switching modules are functioning correctly. These same modules are utilized for variably-saturated flow through macropores.

4.4 Adaptive Time Weighting

The adaptive time-weighting modules were tested by including the transport of three conservative tracers in the simulation of the *Vauclin et al.* [1979] experiment (Section 4.3). The first tracer is injected with the rainfall, while the second and third tracers are present initially above and below the water table, respectively. Injected and initial concentrations are unity and have identical diffusion coefficients of 1.2×10^{-9} m^2/s. Tortuosities are evaluated with (2.28) and longitudinal and transverse dispersivities are 0.01 m and 0.001 m, respectively.

Table 4-4 compares flow solution statistics for simulations performed with fully-implicit time weighting and with adaptive implicit-explicit time-weighting. It can be seen from Table 4-4 that the computational effort is decreased by solving the flow problem with adaptive time weighting, as given by (3.30). Figure 4-4 presents contours of total head at two, four and eight hours for implicit and adaptive implicit-explicit time weighting, and indicates that the two solutions are identical at the chosen contour intervals. Also presented in Figure 4-4 is the spatial distribution of time weighting utilized in the discrete flow equations (3.1), indicating that explicit weighting is largely restricted to the upper-right quadrant of the finite element mesh. This region is stagnant, relative to the timesteps utilized, and responds very slowly to water injection and water table rise. Partitioning these equations from the linearized flow equations (3.29) results in less computation effort in the Jacobian assembly and solution, thereby decreasing total solution time by about 33 percent. This adaptive implicit-explicit time weighting strategy may be beneficial for watershed- or regional-scale coupled flow simulations with large regions of slowly-changing pressure heads or water depths [*S. Panday, per. comm*, 1998].

Table 4-5 compares transport solution statistics for simulations performed with fully-implicit and Crank-Nicholson time weighting, with partial and first-order Jacobians, and with and without utilizing the adaptive upstream-explicit system reduction. Solution of the partial Jacobian systems is

shown to be less expensive than that of the first order Jacobian, and application of adaptive weighting to the transport equations is shown to reduce computational effort by about fifty percent. Concentration contours for the three tracers at two (Figure 4-5a), six (Figure 4-6a), and eight (Figure 4-7a) hours indicates that there is no notable difference in solutions generated with the full and reduced systems. The distribution of spatial and temporal weighting is presented in part b of the figures. Use of adaptive weighting in the transport equations (3.36) results in explicit evaluation in large regions of the finite element mesh. Equations included in the nonlinear Jacobian arise adjacent to boundary conditions and where concentration gradients are large, and increase in proportion as tracers spread through the finite element mesh. As subtimesteps are not utilized in this example, the transport timestep is equivalent to the global timestep, the variation of which is dominated by saturation and pressure changes in the unsaturated zone. Timesteps increase with time as pressure and saturation changes decrease, causing greater proportions of explicit equations to violate stability and motonicity criteria [e.g. *Unger et al.*, 1996]. The decreased computational cost of the adaptive implicit-explicit weighting of transport equations is advantageous for simulations in which global timesteps are controlled by nonlinear surface or subsurface flow, or in which sub-timesteps are controlled by stability and motonicity criteria for advection-dominated transport in macropores or on the land surface.

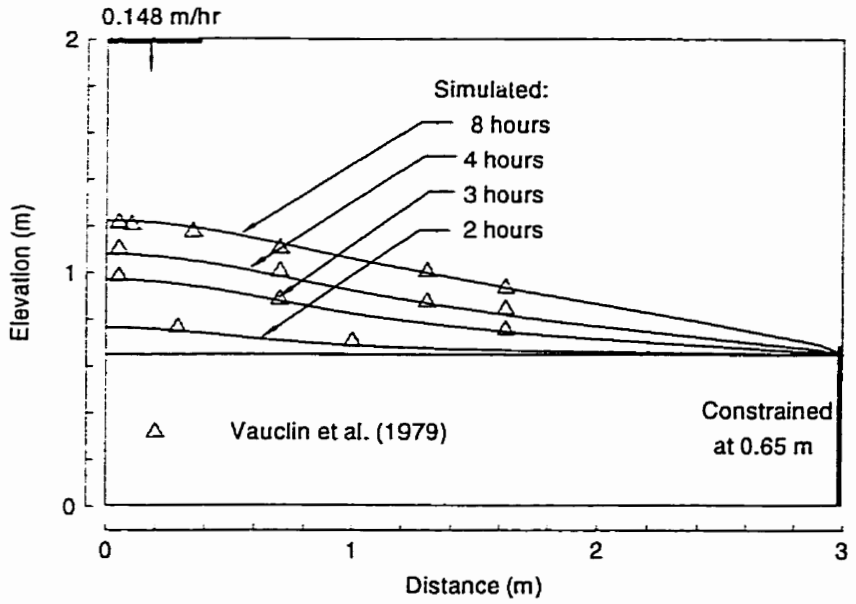

Figure 4-3. Water table location for variably-saturated flow verification problem [*Vauclin et al.*, 1979; *Clement et al.*, 1994]

Porous Medium		
hydraulic conductivity	$\bar{K} = \frac{\rho_w g}{\mu_w}\bar{k}$	8.4 m/d
porosity	ϕ_{p_o}	0.3
compressibility	β_p	0.0
characteristic relationships	$S_w(\psi); k_{rw}(S_w)$	$\alpha = 3.3; n = 4.1; S_{w_r} = 0.01$
initial total head	$\psi_p + z$	0.65 m
Mesh		
nodal spacing	Δx	0.1 m
	Δz	0.05 m
rectangular elements	η_e	1200
porous medium unknowns	η_p	1271
Solution		
maximum timestep	Δt_{global}	1 hour

Table 4-3. Parameterization of the two-dimensional, variable-saturated water table recharge verification problem [*Vauclin et al.*, 1979; *Clement et al.*, 1994].

		Full System	Reduced Adaptive System
Flow Solution	Total Time[1]	0.15	0.10
	Newton Iterations	284	286
	Solver Iterations	848	841

[1] minutes (300 MHz Pentium II)

Table 4-4. Comparison of solution statistics for full and reduced system solution of variably-saturated flow.

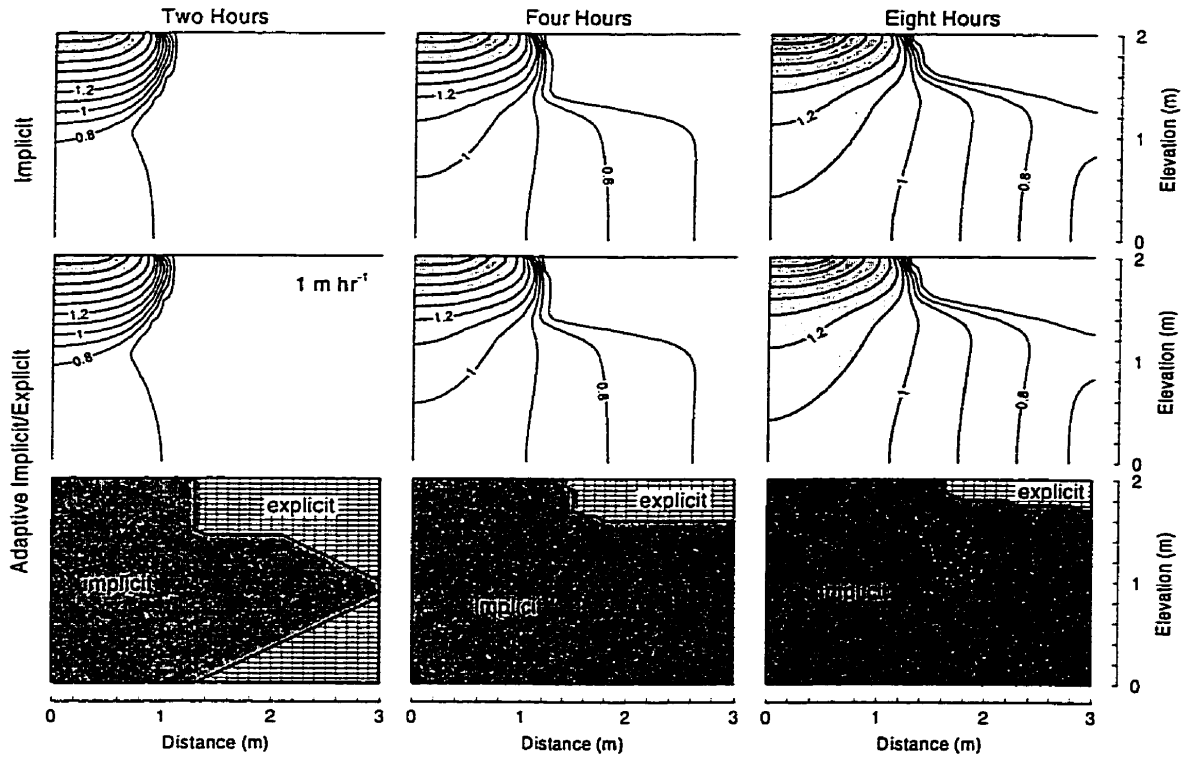

Figure 4-4. Comparison of flow solutions with implicit and adaptive implicit-explicit time weighting; contours of total head (m) and time weighting distribution at two, four and eight hours. Note that solutions are nearly identical for both time-weighting schemes.

Time Weighting	Jacobian	Constant-First Order		Partial-Flux Limiter	
		Non-Adaptive	Adaptive	Non-Adaptive	Adaptive
Implicit	Total Time[1]	0.65	0.34	0.53	0.27
	Newton Iterations	1363	1348	899	897
	Solver Iterations	2019	1997	1287	1295
Crank-Nicholson	Total Time[1]	0.68	0.31	0.53	0.25
	Newton Iterations	1210	1211	819	815
	Solver Iterations	1495	1494	995	998

[1] minutes (300 MHz Pentium II), transport of three solutes

Table 4-5. Comparison of statistics for full and reduced system transport solution.

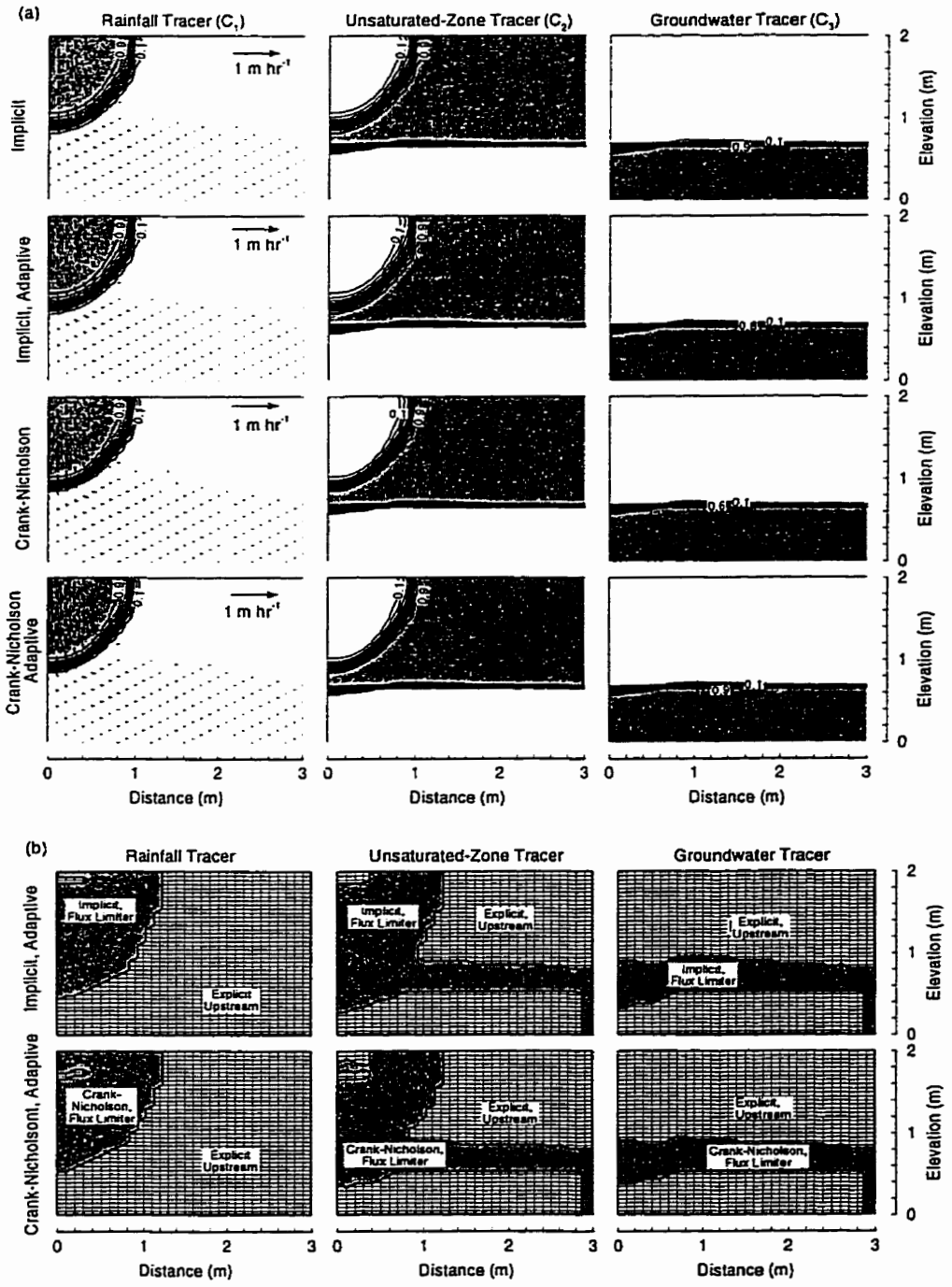

Figure 4-5. Comparison at two hours of transport solutions for three tracer species and four combinations of temporal and spatial weighting methods: (a) concentration contours for the three tracer species and (b) temporal and spatial weighting distribution for the reduced adaptive systems. The van Leer flux limiter is utilized in all four simulations.

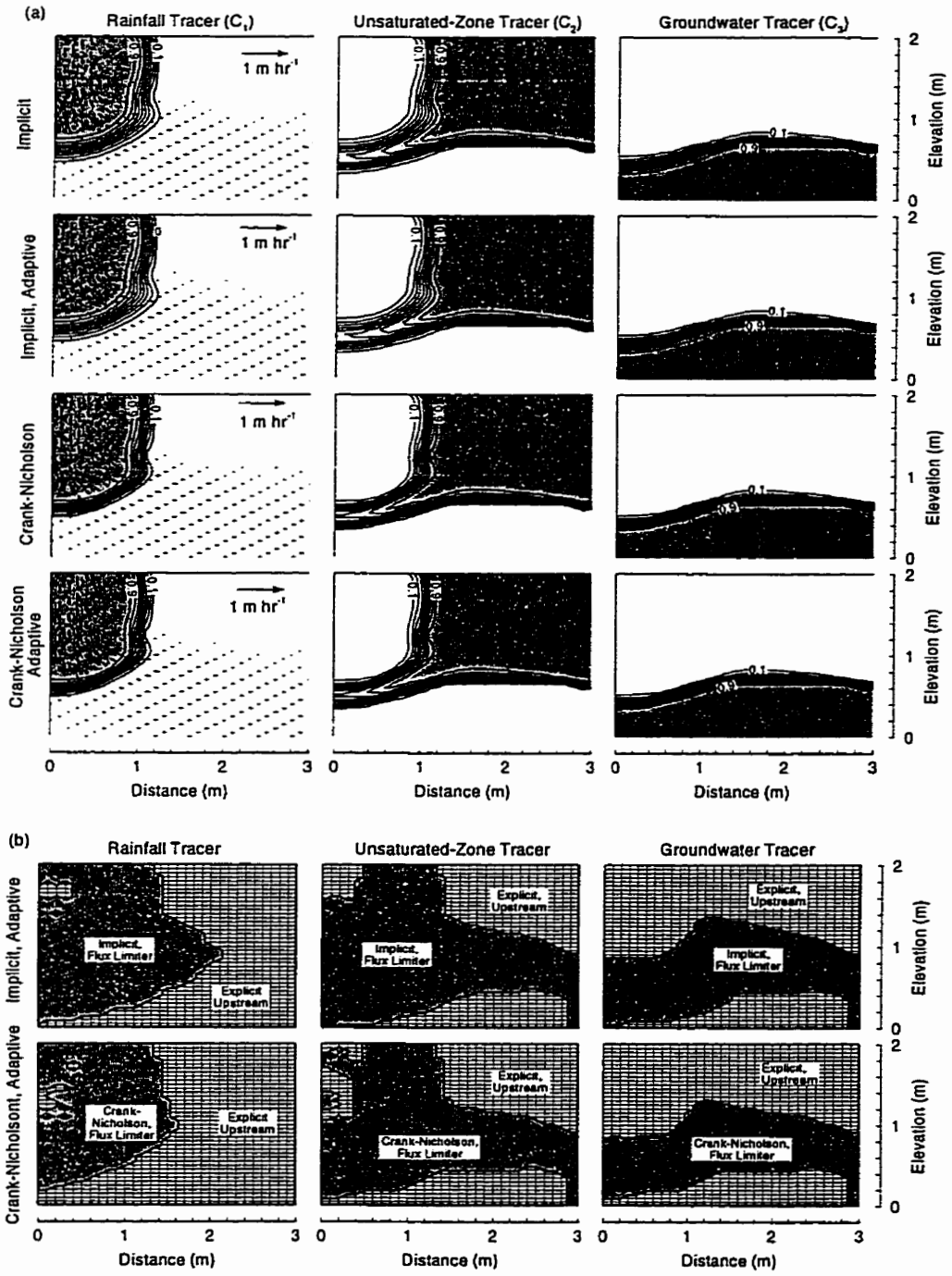

Figure 4-6. Comparison at four hours of transport solutions for three tracer species and four combinations of temporal and spatial weighting: (a) concentration contours for the three tracer species and (b) temporal and spatial weighting distribution for the reduced adaptive systems. The van Leer flux limiter is utilized in all four simulations.

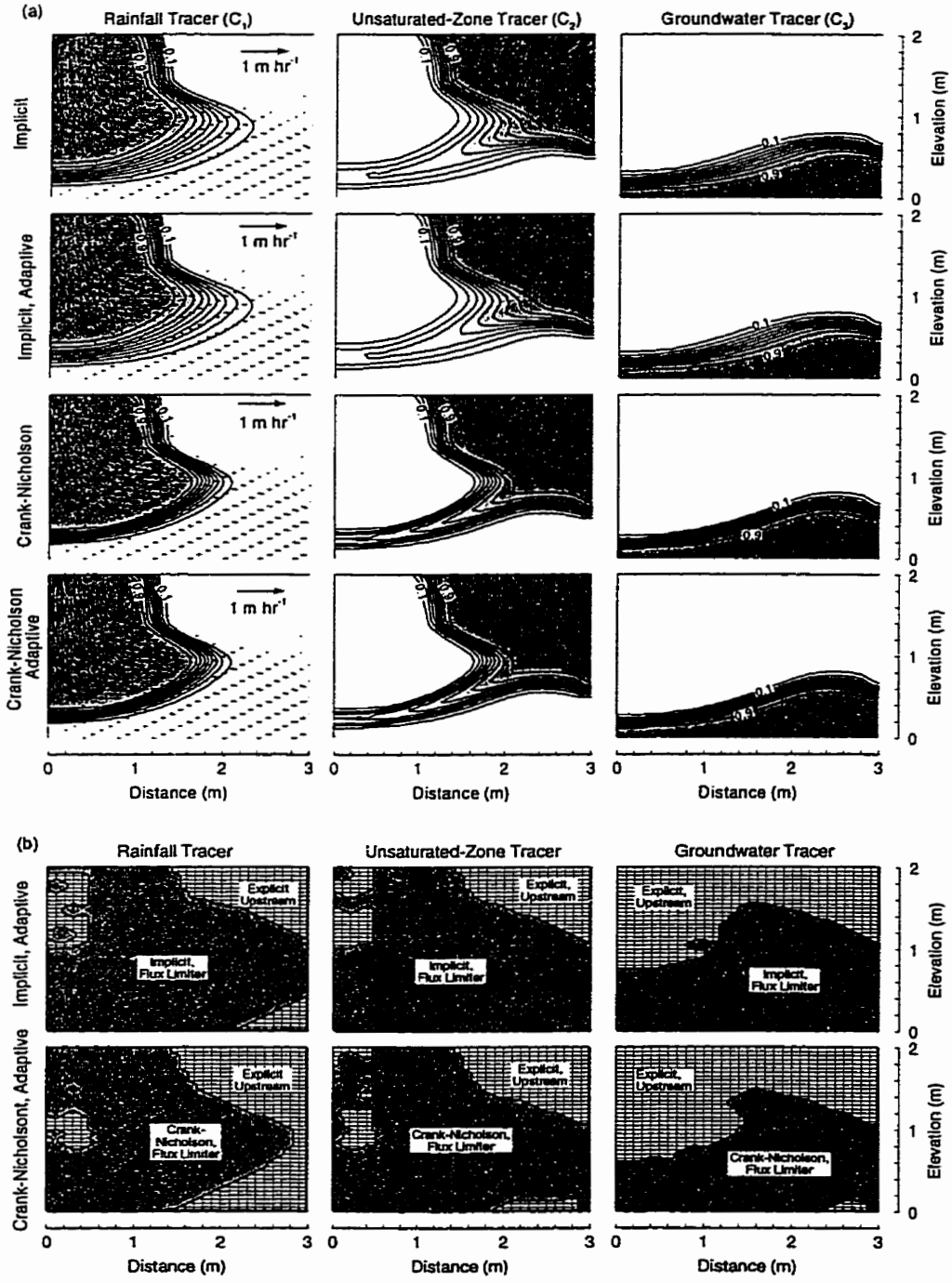

Figure 4-7. Comparison at eight hours of transport solutions for three tracer species and four combinations of temporal and spatial weighting: (a) concentration contours for the three tracer species and (b) temporal and spatial weighting distribution for the reduced adaptive systems. The van Leer flux limiter is utilized in all four simulations.

4.5 Surface Water Flow

This section evaluates the surface flow modules by comparing predicted discharges from a simple rainfall-runoff example with results presented by *di Giammarco et al.* [1996]. *di Giammarco et al.* [1996] develop a control-volume finite element model of the diffusion wave/Manning surface flow equations, comparing discharge predictions with results from an integrated finite difference model and the surface flow module of SHE [*Abbott et al.*, 1986a,b]. All three models presented by *di Giammarco et al.* [1996] externally couple two-dimensional overland flow with one dimensional channel flow via critical depth conditions at the interface (Figure 4-8a). Backwater effects (i.e. flow from the channel onto the slope) cannot be considered. The numerical model developed in this work utilizes the same equations on the slopes and channel, solving the entire system simultaneously, without inhibiting water movement from the channel to the slopes (Figure 4-8b).

The verification problem considers rainfall-runoff from a tilted V-catchment (Figure 4-8) with slopes of size 1000 m by 800 m connected to a channel 20 m in width. Symmetry allows the consideration of only one half of the verification problem (Figure 4-9a) if discharges are multiplied by two. Surface slopes are 0.05 and 0.02 along the x- and y-coordinates, respectively (Figure 4-9b). Rainfall is applied at a rate of 10.8 mm hr^{-1} for 90 minutes to both the slopes and channel, whereas critical depth conditions are enforced at the end of the channel until 180 minutes, the end of the simulation. Manning roughness coefficients are assigned values of 0.015 and 0.15 for the slopes and channel, respectively. *di Giammarco et al.* [1996] neglected rainfall onto the channel and assumed that the channel lies one meter below the slopes.

Figure 4-10a compares discharges predicted by the model developed in this work with discharges presented by *di Giammarco et al.* [1996]. Excellent agreement is illustrated, indicating that the surface flow modules are functioning correctly. Further, the simulation indicates that channel flow is adequately described by the same two-dimensional equations utilized on the slopes, thereby eliminating the external coupling and channel offset assumptions utilized in the other three models. Figure 4-10b presents water depth contours at 90 minutes, illustrating the continuity of water depth

at the channel-slope interface and the build-up of water depths and diversion of flow towards the channel along the left boundary. Water depth distributions are not presented by *di Giammarco et al.* [1996].

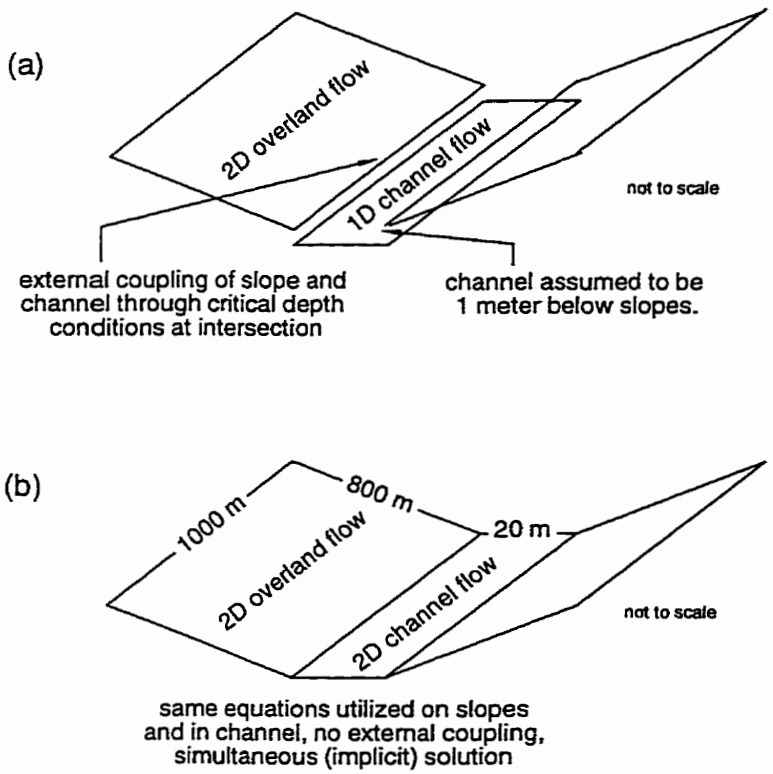

Figure 4-8. Geometry of the tilted V-catchment problem and (a) illustration of flow equation coupling utilized in the integrated finite difference model, the control volume finite element model, and in SHE [after *di Giammarco et al.*, 1996]; and (b) equation coupling method used in this work.

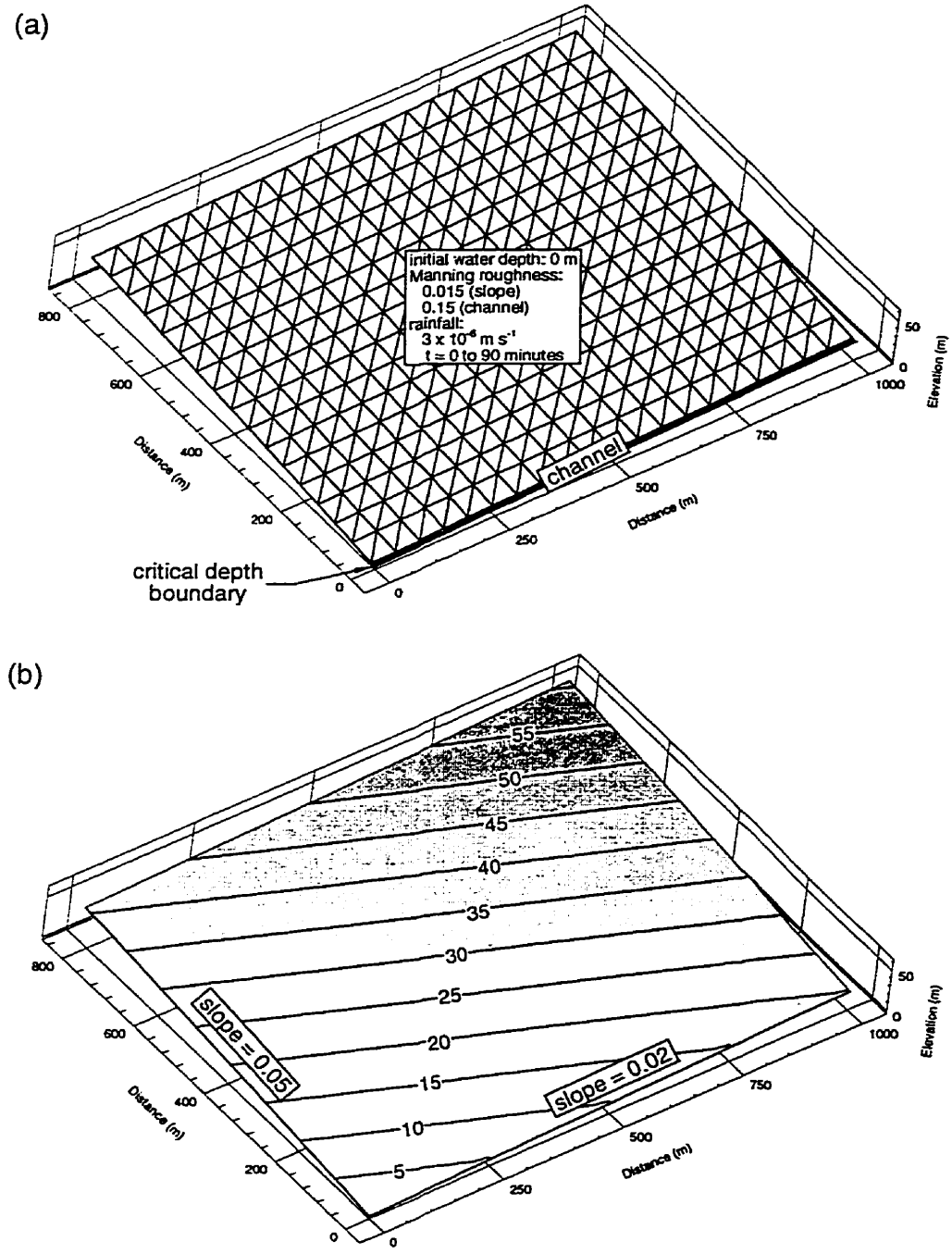

Figure 4-9. Definition of parameters and geometry for the tilted V-catchment simulation: (a) finite element grid and initial and boundary conditions, and (b) land surface elevations (m).

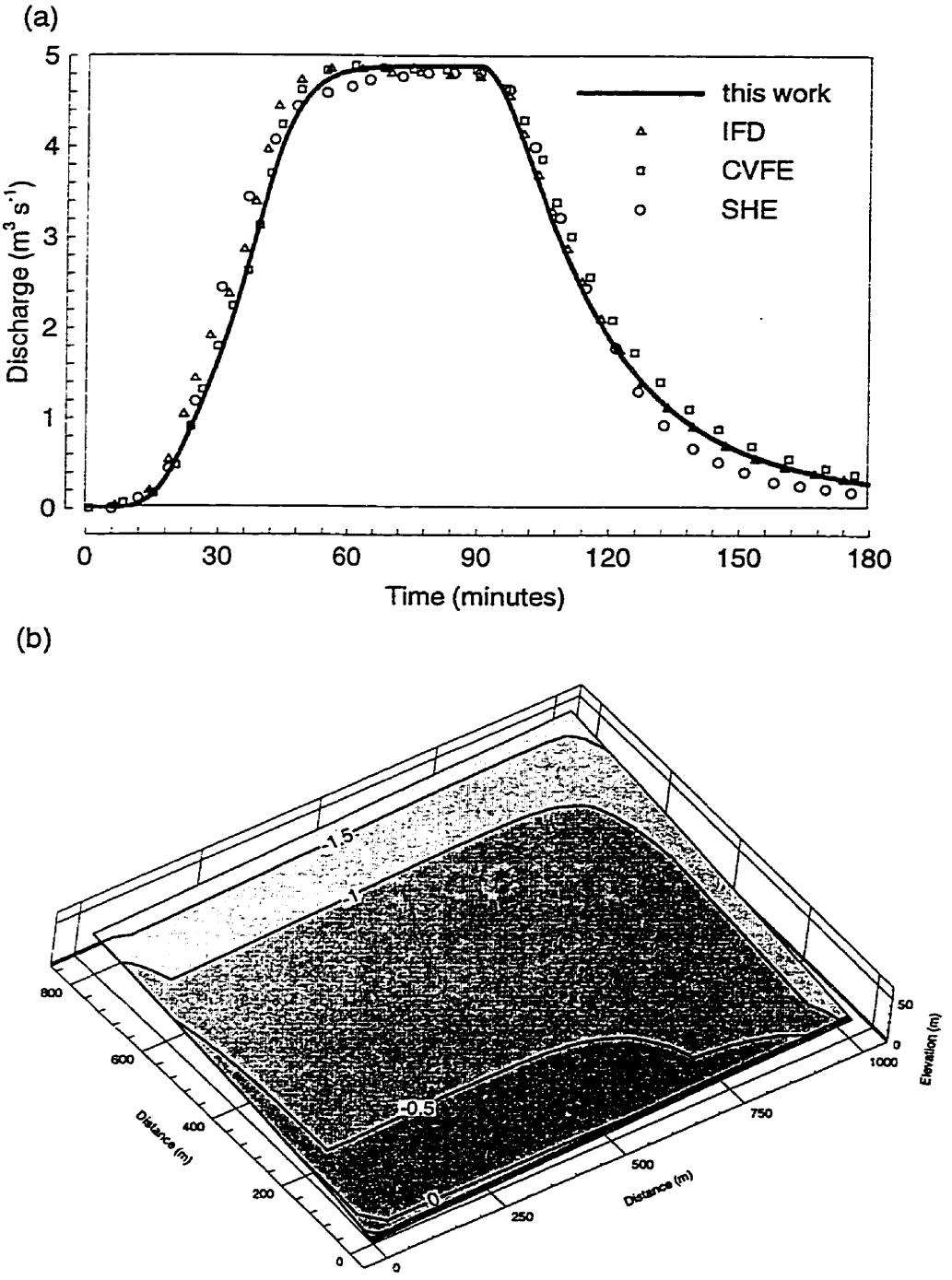

Figure 4-10. Evaluation of surface flow solution for tilted V-catchment verification problem: (a) comparison of simulated discharge with discharges presented by *di Giammarco et al.* [1996] for an integrated finite difference (IFD) model, a control volume finite element model (CVFE) and the SHE surface flow module, and (b) simulated water depths ($\log_{10}$(cm)) at ninety minutes (peak discharge) using the surface flow module developed in this work.

4.6 Coupled Variably-Saturated Subsurface Flow and Transport

Coupled porous medium-macropore flow and transport was tested under transient conditions by comparing results from the numerical model with those from a simulation presented in *Gerke and van Genuchten* [1993a]. The problem considered involves infiltration into a 40-cm deep unsaturated porous medium-macropore system containing a conservative solute. Macropores are assumed to be planes, with the porous medium consisting of blocks. Rainfall is applied to the macropores at a rate of 50-cm/day, with free-drainage conditions, given by (3.19), applied at the base of the macropores and the porous medium. Parameters for this simulation are presented in Table 4-6. Figure 4-11 presents pressure head distributions in the macropores and the porous medium at 0.01, 0.04, and 0.08 days for simulations conducted using a specified interface relative permeability, see equation (2.42), as utilized by *Gerke and van Genuchten* [1993a], and upstream-weighted relative permeabilities, as given by equation (2.41). Results for the specified interface relative permeability curve compare well with the published results, although the vertical discretization is an order of magnitude larger than that utilized by *Gerke and van Genuchten* [1993a]. Upstream weighting of relative permeability is shown to allow a greater depth of water penetration into the macropores, as the magnitude of the macropore relative permeability is less than that of the interface function under negative pressure heads. Figure 4-12 presents corresponding tracer concentrations versus depth at 0.01, 0.04, and 0.08 days. Again, results for the specified interface relative permeability compare well with the published values, with the sharp concentration front in the macropores maintained by the flux limiter. By limiting advective exchange, upstream weighting of relative permeability is shown to enhance concentration discontinuity between the porous medium and macropores.

Porous Medium		
hydraulic conductivity	$\bar{K} = \frac{\rho_w g}{\mu_w} \bar{k}$	1.0526 cm/d
porosity	ϕ_{p_o}	0.5
volume fraction	f_p^v	0.95
characteristic relationships[1]	$S_w(\psi)$	$\alpha = 0.005; n = 1.5; S_{w_r} = 0.2$
	$k_{rw}(S_w)$	
dispersivity	α_l	2 cm
initial pressure head	ψ_p	-10,000 cm
initial concentration	C_0	1
Macropore		
hydraulic conductivity	$\bar{K} = \frac{\rho_w g}{\mu_w} \bar{k}$	1.0526 cm/d
porosity	ϕ_m	0.5
volume fraction	f_m^v	0.05
spacing	$2a_m$	2 cm
characteristic relationships[1]	$S_w(\psi)$	$\alpha = 0.1; n = 2; S_{w_r} = 0$
	$k_{rw}(S_w)$	$S_e^{active} = 0$
dispersivity	α_l	2 cm
initial pressure head	ψ_m	-10,000 cm
initial concentration	C_0	1
Interface		
hydraulic conductivity	$\bar{K} = \frac{\rho_w g}{\mu_w} \bar{k}$	0.01 cm/d
geometry	β	3
characteristic relationships[1]	$S_w(\psi); k_{rw}(S_w)$	$\alpha = 0.005; n = 1.5; S_{w_r} = 0.2$
water transfer scaling	χ^e	0.4
solute transfer scaling	χ^{e_D}	0.01
Solute		
effective diffusion coefficient	τD_w	0.5 cm^2/d
Mesh		
nodal spacing	Δz	1 cm
line elements	η_e	40
porous medium unknowns	η_p	41
macropore unknowns	η_m	41
Solution		
maximum timestep	Δt_{global}	60 s

[1] *van Genuchten* [1980]

Table 4-6. Parameterization of fracture-porous medium unsaturated flow and transport verification example [*Gerke and van Genuchten*, 1993a].

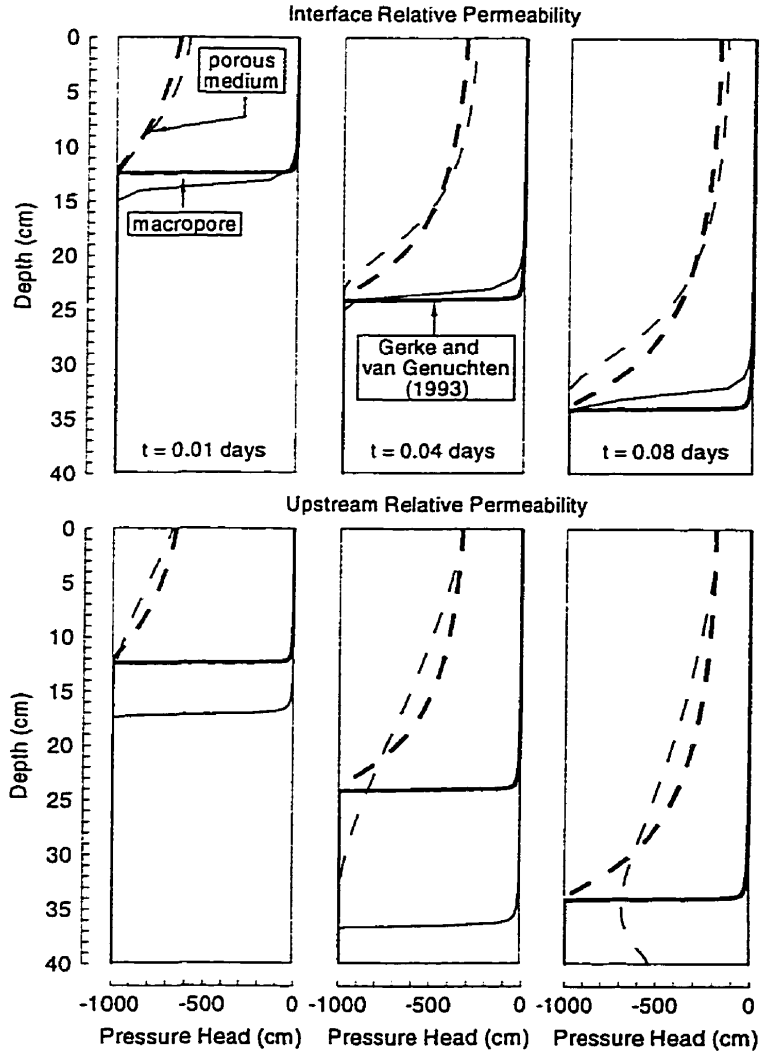

Figure 4-11. Pressure head versus depth at 0.01, 0.04, and 0.08 days for coupled porous medium-macropore verification problem. Comparison of solutions based on interface and upstream relative permeability (thin lines) with published results (thick lines) of *Gerke and van Genuchten* [1993a]. Vertical discretization is an order of magnitude larger than that utilized by *Gerke and van Genuchten* [1993a].

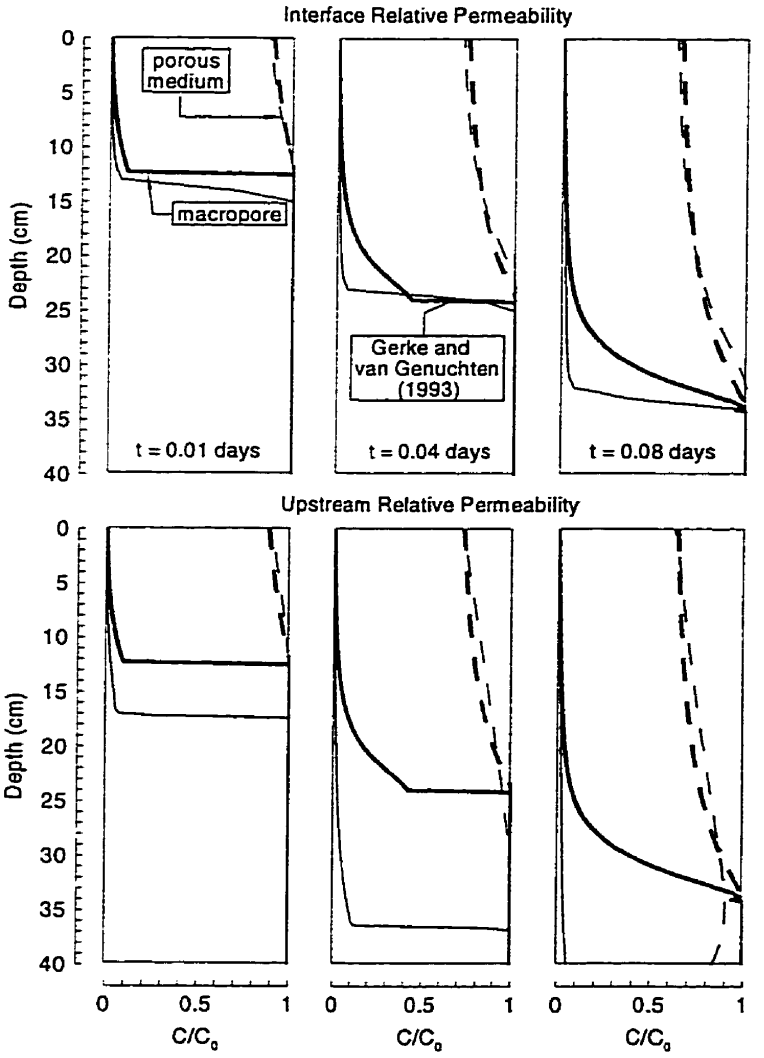

Figure 4-12. Graphs of concentration versus depth at 0.01, 0.04, and 0.08 days for coupled porous medium-macropore verification problem. Comparison of solutions based on interface and upstream relative permeability (thin lines) with published results (thick lines) of *Gerke and van Genuchten* [1993a]. Vertical discretization is an order of magnitude larger than that utilized by *Gerke and van Genuchten* [1993a].

4.7 Coupled Surface-Porous Medium Flow and Transport

This section applies the integrated numerical model to a laboratory-scale experiment of coupled surface-subsurface flow and transport. The simulations are based on laboratory experiments conducted by *Abdul* [1985] to demonstrate the rapid capillary zone response of *Sklash and Farvolden* [1979] and *Gillham* [1984]. The laboratory experiments of *Abdul* [1985] were conducted in a Plexiglas box 140 cm long, 120 cm high, and 8 cm wide (Figure 4-13). The box was packed with medium-to-fine sand with a uniform 12-degree slope on the upper surface. A screened tube at the toe of the slope drained runoff water, considered to represent streamflow. Initial conditions for the experiment under consideration here placed the water table at a level of 74 cm, corresponding to the location of the stream outlet tube. The wetting and draining characteristic curves for the sand were measured by *Abdul* [1985] and indicated the existence of a capillary fringe approximately 30 cm thick. Recharge water containing bromide was applied at a rate of 4.3 cm/hour for twenty minutes; discharge volumes and concentrations were measured for thirty-five minutes.

Abdul [1985] simulated the laboratory experiment using a finite element model of water flow in variably-saturated porous medium with a seepage face condition imposed at the land surface. He considered both air phase compression and hysteresis and was able to match observed subsurface responses and peak seepage discharge with reasonable accuracy. Simulated early time discharge was affected by the degree of air phase saturation, with air phase compression causing increased water storage capacity at early time, thereby delaying seepage face development. Separation of discharge into event and pre-event components was accomplished by tracking the location and amount of seepage.

The following paragraphs present the results of simulations conducted using the integrated numerical model of coupled surface-subsurface flow and transport developed in Chapter 3. First-order coupling is compared with coupling via concentration and pressure head continuity and with a single-subsurface continuum with seepage faces at the land surface. Discharge volumes and concentrations are compared with measured values and the effect of three rainfall boundary

conditions is illustrated for the transport solution. Simulation parameters (Table 4-7) are from literature sources and *Abdul's* [1985] laboratory measurements. Simulated rainfall is assumed to contain a relative bromide concentration of unity. Two additional tracers are utilized to differentiate simulated discharge water originating above and below the initial water table. Characteristic curves, initial and boundary conditions, and the finite element grid are provided in Figure 4-13. Nodal spacing in the finite element mesh is on the order of two centimeters horizontally and vertically.

4.7.1 Water Flow

Simulated surface water discharges versus time are compared with *Abdul's* [1985] measured values in Figure 4-14 for a variety of surface water-groundwater coupling schemes. Peak discharges are shown to be equivalent to the rate of rainfall input for coupling of surface and subsurface flow via continuity of pressure head and by first-order exchange relationships. The location of the applied rainfall rate and the type of coupling used is seen from Figure 4-14 to have has little effect on the simulated surface water discharge. The rise and fall of the simulated hydrographic precedes the measured discharge, consistent with the neglect of air phase compression.

Figure 4-15 presents a comparison of total heads in the porous medium at 100 and 200 seconds. These times represent snapshots of the subsurface flow solution during the transient and steady-state periods, respectively. A simulation of a single subsurface continua performed using seepage faces at the land surface is compared with simulations of dual surface-subsurface continua coupled using both pressure head continuity and first-order exchange approaches. Solutions are virtually identical at the chosen contour intervals and indicate infiltration and discharge in the upper and lower regions, respectively, with subsurface flow parallel to the land surface in the central region.

Figure 4-16 presents results for pressure head and water depth (not measured in the experiment) versus time on the surface/subsurface interface at three locations for the first-order-coupled solution. The three locations presented are on the land surface, corresponding with points where infiltration (x = 20 cm), parallel subsurface flow (x = 70 cm), and discharge (x = 120 cm) are occurring. As indicated previously by the discharge hydrograph (Figure 4-14), response to the

applied rainfall is rapid due to the low storage capacity of the capillary fringe. Pressure head values in the porous medium and water depths on the land surface attain steady-state values after about 100 seconds. Pressure heads rise until the water table intersects the land surface, at which point values are equivalent to the surface water depth. Although increasing downslope, surface water depths are maintained by rapid flow towards the critical depth (outflow) boundary.

Figure 4-17 illustrates the spatial distribution of infiltration and discharge at the land surface during the steady-state period of the laboratory experiment. Water exchange rates (min^{-1}) are presented for three surface-subsurface (dual continua) simulations with different rainfall boundary condition assignments. Also presented are seepage rates (min^{-1}) for a single continuum simulation with seepage faces at the land surface which is consistent with the design of the experiment. Seepage rates for the single subsurface continuum example are defined as the back-calculated volumetric boundary rate ($cm^3\ min^{-1}$), normalized by the volume of the boundary node (cm^3) to be consistant with the governing equations:

$$q_{i_p}^{seep} = \frac{Q_{b_{i_p}}^{back}}{V_{i_p}} = \frac{-\sum_{j \in \eta_{i_p}} (\gamma k_{rw})_{i_p j_p}^{L+1} \Gamma_{i_p j_p}}{V_{i_p}} \tag{4.1}$$

These rates are negative for discharge (porous medium sink) and positive for infiltration (porous medium source). Exchange rates for the dual surface-subsurface continua examples are defined as the back-calculated volumetric flux ($cm^3\ min^{-1}$) between the surface and porous medium equations divided by the volume associated with the porous medium equation (cm^3):

$$q_{i_p i_s}^{e} = \frac{Q_{i_p i_s}}{V_{i_p}} = \frac{(k_{rw}\gamma)_{i_p i_s}^{L+1} \Gamma_{i_p i_s}}{V_{i_p}} \tag{4.2}$$

Again, these rates are negative for discharge (porous medium sink) and positive for infiltration (porous medium source). For consistency, specified rainfall rates (3.17) are presented as:

$$q_{i_p}^{R} = \frac{Q_{b_i}^{R}}{V_{i_p}} \tag{4.3}$$

where volumetric rates are again normalized by the subsurface nodal volumes.

The seepage face algorithm (3.24) is shown to allow both infiltration and discharge, depending on the dynamics of subsurface flow (Figure 4-17a). Rainfall is applied at the specified rate in the upper left portion (0 to about 5 cm), which remained under negative pressure during the course of the laboratory experiment. The remaining nodes are constrained at zero pressure head, as the back-calculated (maximum) infiltration rate is less than the specified rainfall rate. The back-calculated rates are positive along the upper portion of the land surface, indicating infiltration, and decrease to zero at a distance of about 70-cm from the left boundary. This point represents a hinge line, as seepage rates from a distance of about 70-cm towards the right boundary are negative, indicating discharge from the porous medium. The coupling of surface and subsurface flow provides a temporal and spatial constraint on pressure head at the land surface (Figure 4-16). These constraints are not significantly different than those introduced by assigning seepage faces $(\psi_p = 0)$ at the land surface, as water depths in these examples are on the order of millimeters.

Figure 4-17b presents the spatial distribution of water exchange for the case where rainfall boundary conditions are applied to the surface equations. Considering discrete surface and porous medium flow equations at the same node:

$$\frac{A_{i_s}}{\Delta t_{global}}\left[\left(S_w h_s + \psi_{s_s}\right)^{L+1} - \left(S_w h_s + \psi_{s_s}\right)^{L}\right]_{i_s} = Q_{i_s j_p}^{L+1} + \sum_{j \in \eta_{i_s}} Q_{i_s j_s}^{L+1} + \sum_{i_s} Q_b^{L+1} \tag{4.4}$$

$$\frac{V_i f_{i_p}^{\nu}}{\Delta t_{global}}\left[\left(\phi S_w\right)^{L+1} - \left(\phi S_w\right)^{L}\right]_{i_p} = Q_{i_p j_s}^{L+1} + \sum_{j \in \eta_{i_p}} Q_{i_p j_p}^{L+1}$$

we can note that water is conserved:

$$Q_{i_p j_s}^{L+1} = \left(k_{rw}\gamma\right)_{i_p i_s}^{L+1} \Gamma_{i_p i_s} = -Q_{i_s j_p}^{L+1} \tag{4.5}$$

and that water exchange between continua at the land surface interface is implicitly linked to hydrodynamics both within the porous medium and on the land surface:

$$\left[\frac{V_i f_{i_p}^{\nu}}{\Delta t_{global}}\left[(\phi S_w)^{L+1}-(\phi S_w)^{L}\right]_{i_p}-\sum_{j\in\eta_{i_p}} Q_{i_p j_r}^{L+1}\right] \tag{4.6}$$

$$= Q_{i_p j_s}^{L+1}$$

$$=\left[\sum_{j\in\eta_{i_s}} Q_{i_s j_s}^{L+1}+\sum_{i_s} Q_b^{L+1}-\frac{A_{i_s}}{\Delta t_{global}}\left[\left(S_w h_s+\psi_{s_s}\right)^{L+1}-\left(S_w h_s+\psi_{s_s}\right)^{L}\right]_{i_s}\right]$$

Infiltration occurs where $Q_{i_p j_s}^{L+1} > 0$ and seepage or groundwater discharge occurs where $Q_{i_p j_s}^{L+1} < 0$. Above the hinge line (70 cm), rainfall in excess of the local infiltration rate (infiltration excess) contributes directly to surface storage, as does discharge (seepage) below the hinge line. Surface water flows overland to exit the system at the critical depth boundary (Figure 4-13), producing the hydrograph presented in Figure 4-14. Note that, although the rate and location of water exchange is virtually identical to that determined using seepage faces (Figure 4-17a), both infiltration excess and seepage are lost to the system if seepage faces are utilized at the land surface.

Figure 4-17c presents the spatial distribution of water exchange for the case where rainfall boundary conditions are applied to the porous medium equations at the land surface. In this example, exchange rates are zero from the left boundary, extending to about 12 centimeters, indicating the infiltration is occurring at the specified rainfall rate. Exchange rates are negative beyond this distance to the right boundary, indicating the movement of water from the porous medium continuum to the surface continuum. The rate of water exchange represents infiltration excess in the region above the hinge line and is equivalent to the rainfall rate at the hinge line. Below the hinge line, exchange rates represent the sum of the rainfall and seepage rates.

Figure 4-17d presents the spatial distribution of water exchange for the case where rainfall boundary conditions are applied to both the surface and porous medium equations as a function of surface saturation (3.18). The surface and porous medium rainfall rates sum to the total specified at all points on the land surface. The rate of rainfall application to the surface equations is zero adjacent to the left boundary, where the pressure head in the porous medium is negative and surface saturations are at residual values. Rainfall rates input to the surface regime increase in value and the

portion that enters porous medium directly decreases in value as water depths increase along the slope. Water exchange rates are negative, indicating movement of water from the porous medium to the surface continuum. Rates are decreased in magnitude relative to those presented in Figure 4-17c for the case of rainfall applied to the porous medium equations.

The laboratory-scale simulations demonstrate that first-order coupling of surface and subsurface flow can replace iterative boundary conditions at the land surface. Infiltration and discharge occur at the correct location and time, interacting in a natural manner with flow processes on the land surface. Similarly, partitioning of rainfall between the surface and subsurface continua occurs as a function of the local hydrodynamics. Surface-subsurface interactions are governed by the form of the coupling relationship. Small values of the characteristic length scale generate large influence coefficients (see, e.g. (3.8)), enforcing near-continuity between surface water depths and subsurface pressure heads at the land surface when the porous medium is fully saturated. Solutions in the current study were found to be insensitive the actual numerical value of the influence coefficient, providing the coefficient was sufficiently large. Newton iteration convergence increased in difficulty with increasing coefficient values, and convergence of the continuity-coupled simulation required much smaller time steps than the simulation employing first-order coupling.

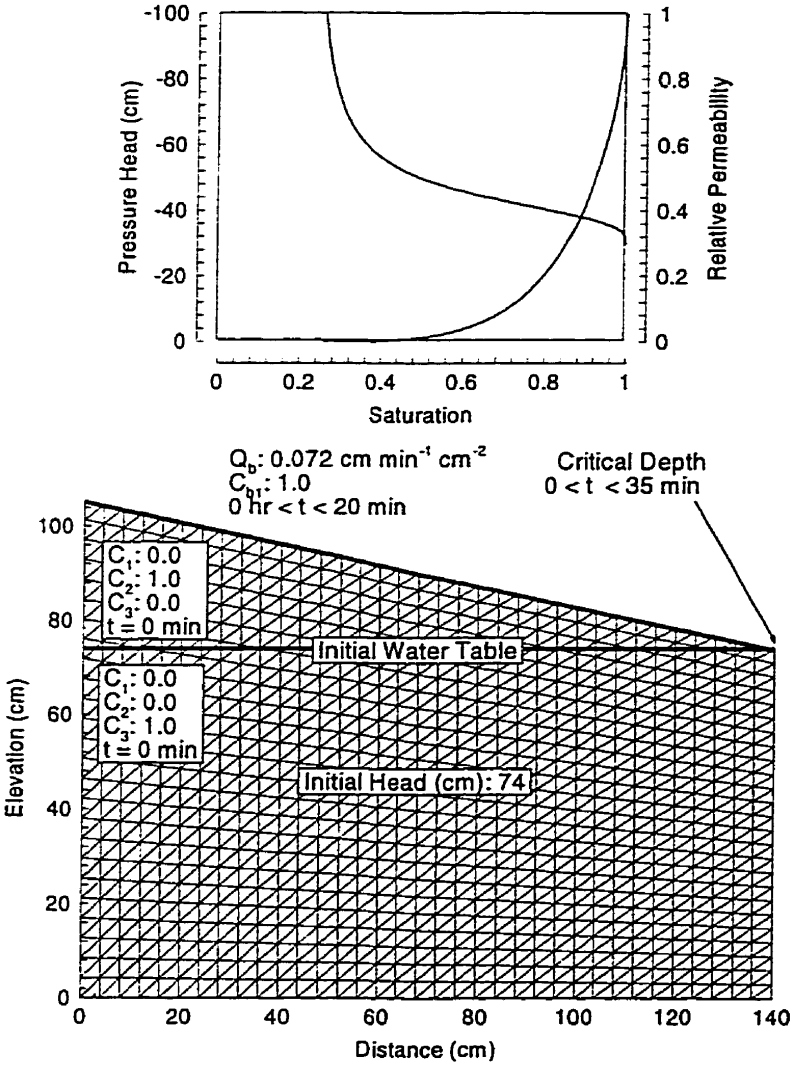

Figure 4-13. Characteristic curves, finite element mesh, and initial and boundary conditions for laboratory-scale coupled surface-subsurface example [*Abdul*, 1985].

Porous Medium		
hydraulic conductivity[1]	$\bar{K}$	3.5×10^{-3} cm/s
porosity[1]	ϕ_{p_o}	0.34
capillary pressure relationship[1]	$S_w(\psi), \psi(S_w)$	tabulated (drainage)
saturation-relative permeability relationship[1]	$k_{rw} = a(S_w \phi_{p_o})^b$ $\approx (S_w)^b$	$a = 140$ $b = 4.5$
compressibility[2]	β_p	1×10^{-5} cm s^2/kg
longitudinal dispersvity[3]	α_l	0.01 cm
transverse dispersivity[3]	α_{th}, α_{tv}	0.001 cm
initial total head	$\psi_p + z$	74 cm
Surface		
surface roughness[4]	$\bar{n}$	0.04 s/cm$^{1/3}$
dispersivity	α_l, α_t	0.1 cm
microtopography	h_s	1×10^{-1} cm
mobile water depth	ψ_s^{pond}	1×10^{-4} cm
residual saturation	S_{w_r}	1×10^{-6}
initial water depth	ψ_s	1×10^{-4} cm
Solute		
diffusion coefficient[5]	D_w	1.2×10^{-5} cm^2/s
Coupling		
characteristic length	a_s	1×10^{-2} cm
exchange dispersivity	α^e	0.0 m
Mesh		
porous medium triangle elements	η_{e_p}	1,750
porous medium unknowns	η_p	936
surface line elements	η_{e_s}	35
surface unknowns	η_s	36
maximum timestep	Δt_{global}	60 s

[1]*Abdul* [1985]; [2]*Akindunni and Gillham* [1992]; [3]*Sudicky* [per. comm., 1997]; [4]*Chow* [1959]; [5]*Wallach et al.* [1988]

Table 4-7. Parameterization of laboratory-scale coupled surface-subsurface simulations [*Abdul*, 1985].

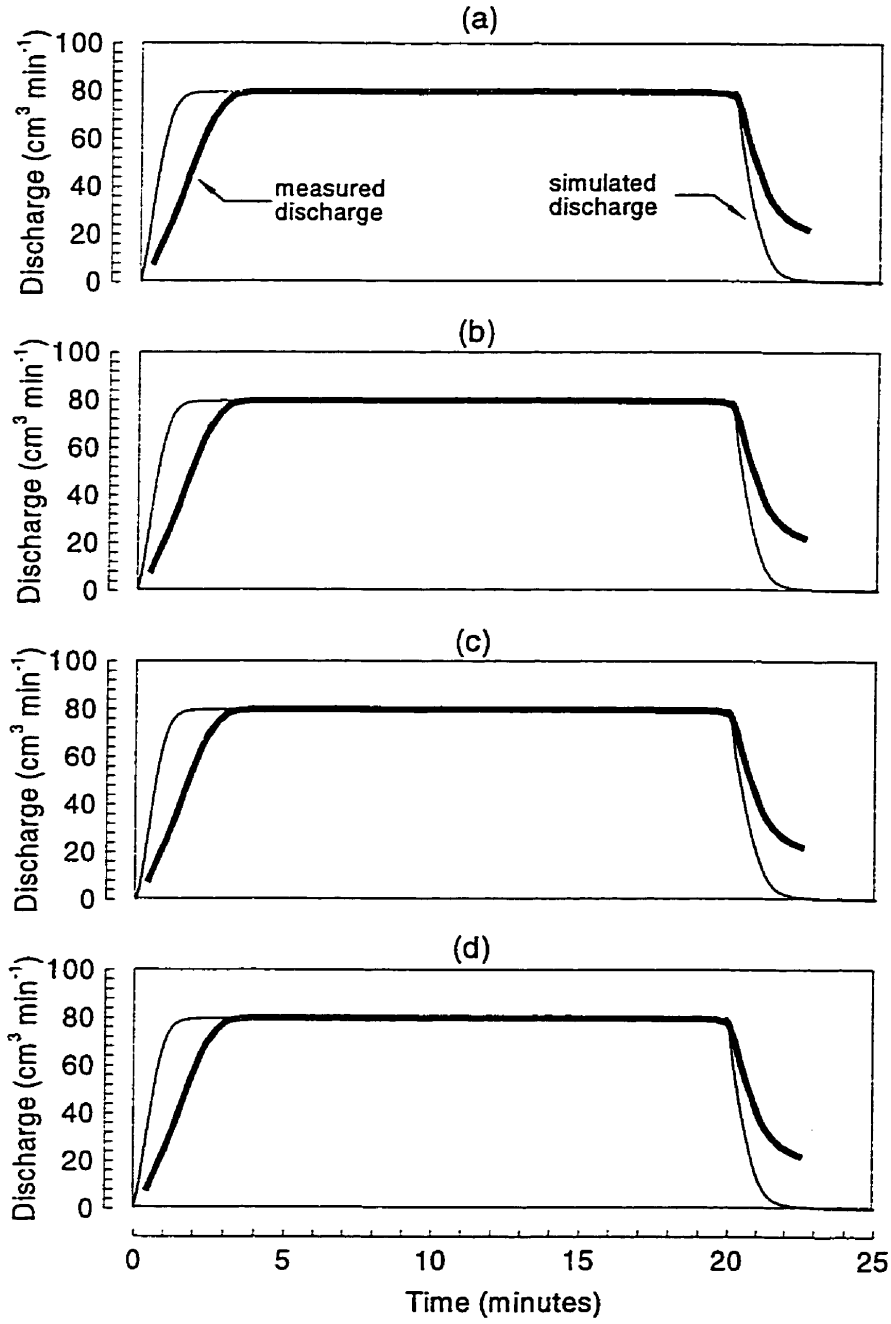

Figure 4-14. Graphs of surface water discharge versus time for the coupled surface-subsurface laboratory experiment of *Abdul* [1985]. Comparison of measured discharge with those predicted by (a) assuming pressure head continuity, and by first-order surface-subsurface coupling with (b) rainfall applied to surface equations, (c) rainfall applied using dual boundary condition, and (d) rainfall applied to porous medium equations.

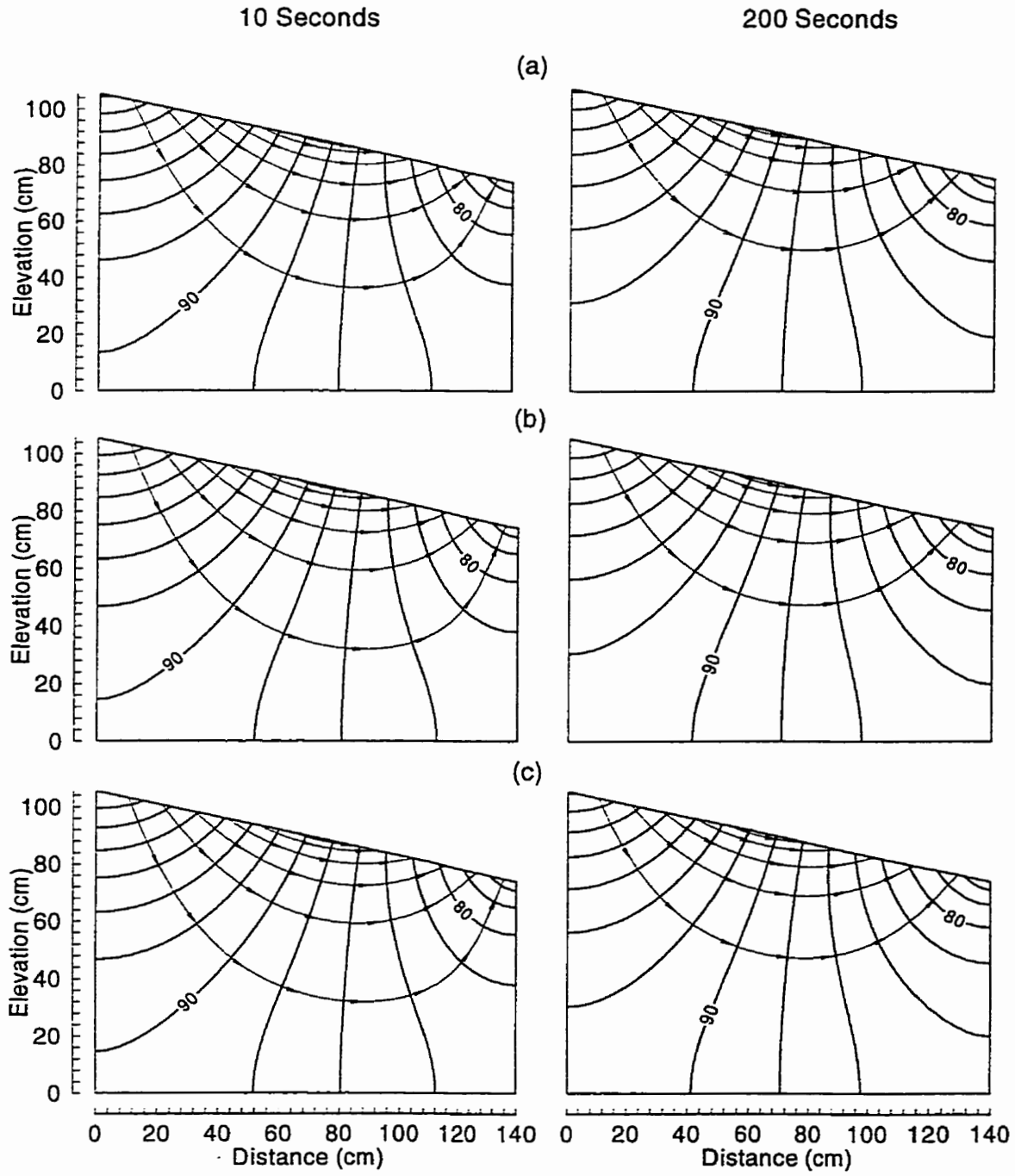

Figure 4-15. Total head (cm) and stream lines (flow paths) at 100 and 200 seconds for laboratory scale coupled surface-subsurface example. Comparison of (a) single subsurface continuum with seepage faces at the land surface, with (b) coupled surface-subsurface solutions generated using pressure head/water depth continuity and (c) first-order water exchange relationship.

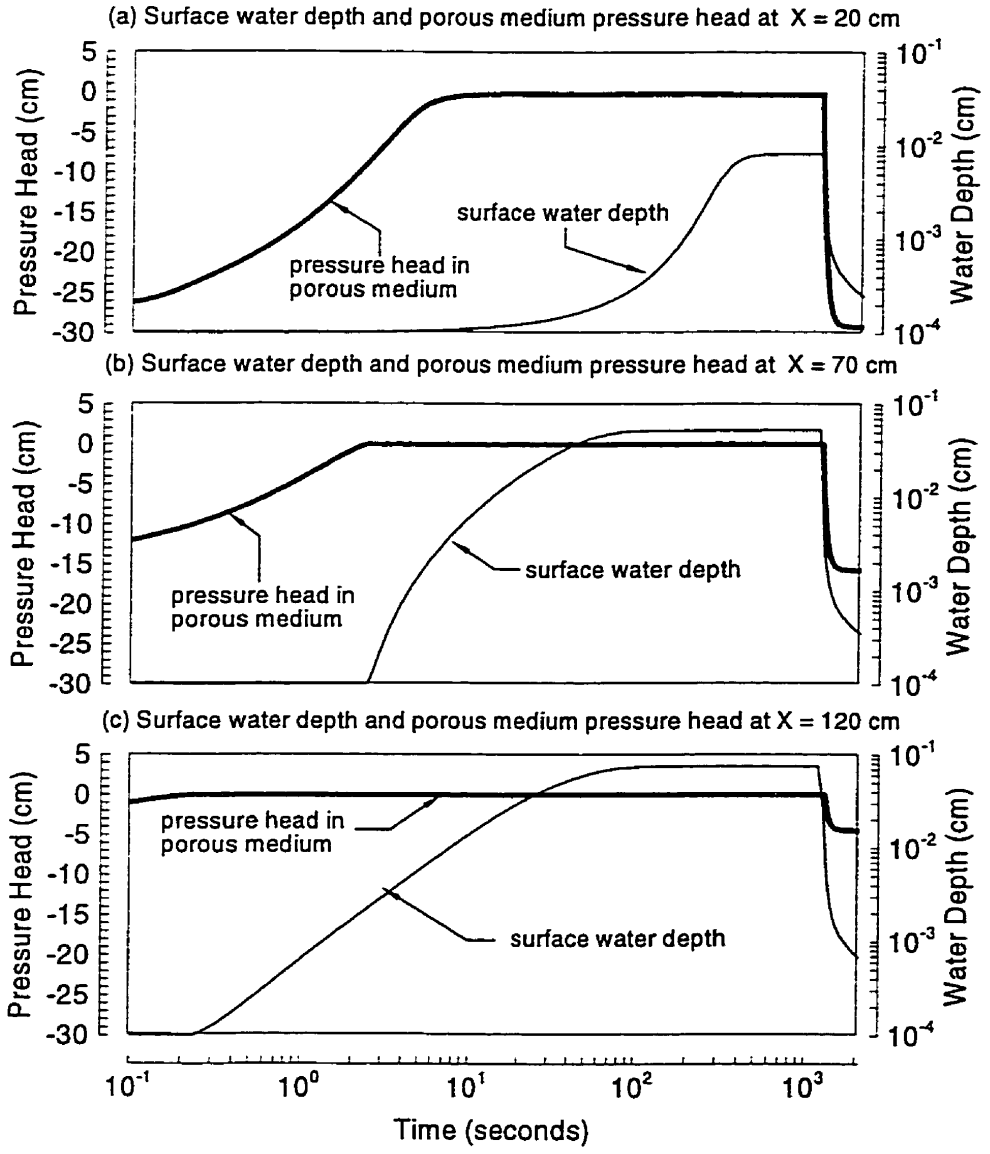

Figure 4-16. Pressure head and water depth versus time for three locations on the land surface.

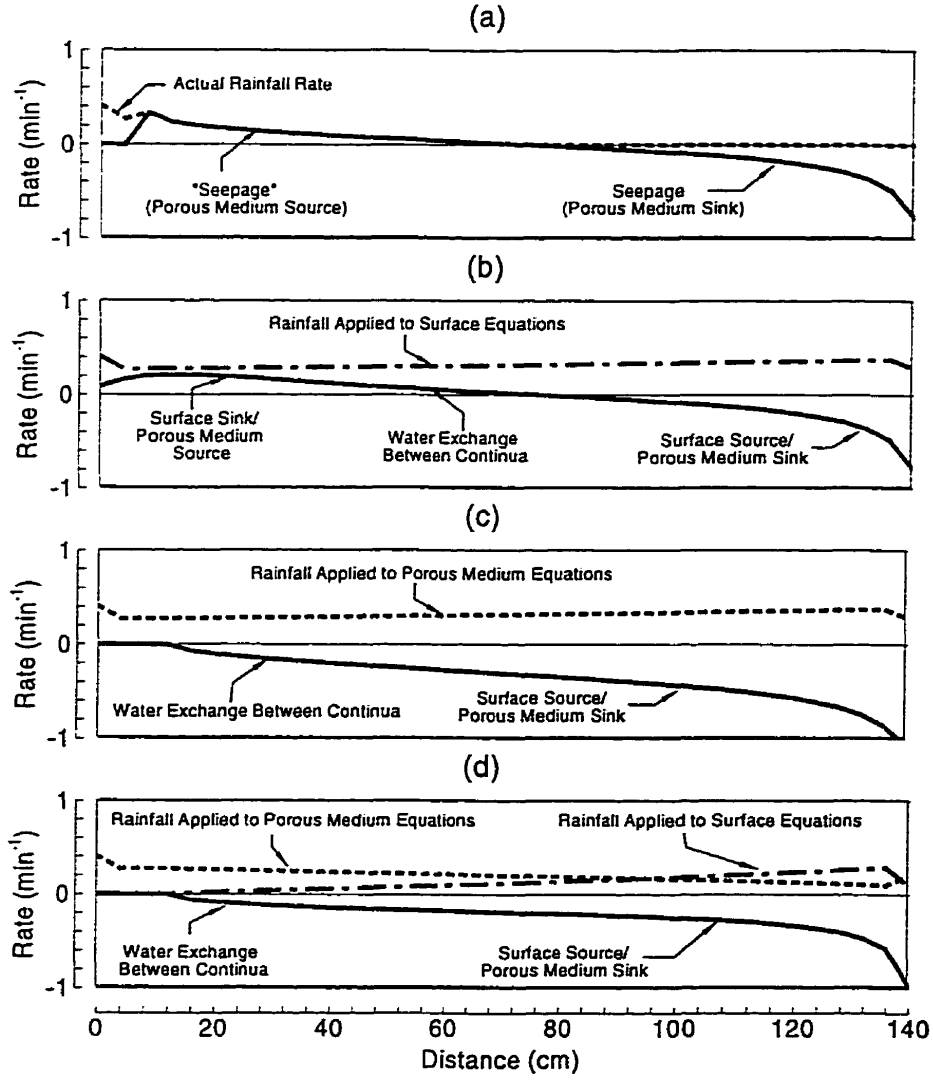

Figure 4-17. Seepage, exchange and rainfall rates at the land surface interface at three minutes. Comparison of (a) seepage face solution and coupled surface-surface solutions with (b) rainfall applied to surface equations, (c) rainfall applied to porous medium equations and (d) rainfall applied using dual algorithm to both surface and porous medium equations.

4.7.2 Solute Transport

Measured and simulated rainfall tracer (C_1) in the discharge water are compared in Figure 4-18 for the first-order-coupled approaches with the three rainfall boundary conditions (i.e. surface-application, porous medium-application, and dual-application). Also presented is the concentration predicted by assuming continuity between the surface and porous medium at the land surface, equivalent to assuming complete mixing between surface water and water in the porous medium at the land surface $\left(\Lambda_{i_p j_s}^{M+1} = \text{large}\right)$. Figure 4-18 also presents concentrations of the two additional tracers initially specified to be resident above (C_2) and below (C_3) the water table (Figure 4-13). The reader should keep in mind that the experiment of *Abdul* [1985] involved only the application of tracer to the rainfall (i.e. C_1) so that experimental results for C_1 can be directly compared. The additional tracers (C_2 and C_3) are added to the model to assist in determining the origin of discharge water (hydrograph separation).

As the tracer concentrations sum to unity at each point in space and time, simple hydrograph separations suggest that the concentration of each individual tracer represents the fraction of discharge water originating in the corresponding source location [i.e. *Sklash and Farvolden*, 1979]. These hydrograph separations can be written as:

$$Q_{c_1} = Q_b^T C_1 \Rightarrow C_1 = \frac{Q_{c_1}}{Q_b^T} \qquad Q_{c_2} = Q_b^T C_2 \Rightarrow C_2 = \frac{Q_{c_2}}{Q_b^T} \qquad Q_{c_3} = Q_b^T C_3 \Rightarrow C_3 = \frac{Q_{c_3}}{Q_b^T} \tag{4.7}$$

where Q_b^T = total surface discharge, and Q_{c_1}, Q_{c_2}, and Q_{c_3} represent the rainfall, groundwater and tension-saturated zone contributions, respectively. Such separations assume that the dominant mixing and transport process is advection (i.e. plug flow or $|QC| \gg |\Lambda\xi|$).

Direct comparison of simulated and measured concentrations during hydrograph rise and fall is hampered due to inaccuracies in the simulated surface discharge volumes (Figure 4-14). In general terms, however, one can note that application of rainfall to the surface equations (Figure 4-18a) indicates early-time discharge (i.e. up to about eight minutes) is dominated by water originating as rainfall (C_1). Such water origins contrast those indicated by the dual (Figure 4-18b) and

porous medium (Figure 4-18c) rainfall applications and with the continuity-coupled simulation (Figure 4-18d). These latter simulations suggest early-time discharge is dominated by pre-event water (i.e. water originating within the porous medium). Note that for rainfall applied to the surface equations, discharge at very early time is entirely rainfall (i.e. $C_t = 1$). Advective and diffusive mixing rapidly reduces rainfall tracer concentrations in surface discharge.

Large early-time contributions of pre-event water follow the measured trend and were attributed by *Abdul and Gillham* [1984] to mixing within a thin layer of the porous medium at the land surface upslope from the hinge line. Such mixing was hypothesized to increase pre-event tracer contributions to surface water with a corresponding decrease in rainfall tracer. Contributions of pre-event tracer were thought to decrease with time as pre-event tracer in the porous medium is replaced with rainfall tracer.

Simulated and observed rainfall tracer concentrations correspond well after about eight minutes if rainfall is applied to the surface equations. Rainfall contributions to surface discharge are underestimated by the remaining simulations during this period. Rainfall tracer concentrations predicted by all boundary condition and coupling approaches correspond well with measured values at the end of the rainfall period (20 minutes). With the exception of the continuity-coupled simulation, tracer concentrations during hydrograph recession are poorly represented.

Figure 4-19 presents the distribution of rainfall and tension-saturated zone tracers in surface water and of tension-saturated zone tracer within the porous medium at three times, representing the beginning (e.g. three minutes), middle (e.g. ten minutes) and end (e.g. 20 minutes) of the steady flow period. Results are presented for simulations with rainfall applied to the surface and porous medium equations, respectively. These figures indicate that, while rainfall affects the hydrologic response of the entire system (Figure 4-15), processes affecting solute concentrations in the surface water are restricted to a relatively thin region adjacent to the land surface. Groundwater tracer (C_3) enters the surface water in a narrow zone adjacent to the outflow boundary. As this zone is of constant extent during the steady portion of the hydrograph, groundwater tracer rapidly displaces

tension-saturated zone tracer (C_2) and attains near-constant concentrations in the surface water for all boundary condition assignments (Figure 4-18).

The total volumetric rate ($cm^3\ min^{-1}$) of all negative water exchanges between continua is illustrated in Figure 4-20 each of the dual continua simulations. These values represent the sum of subsurface sinks, $\sum \min\left(0, Q_{i_p i_s}\right)$, and are equivalent to the contribution of subsurface water sources to the surface water continuum (4.6). Also presented is the sum of the back-calculated groundwater seepages, $\sum \min\left(0, Q_{b_{i_p}}^{back}\right)$, (i.e. sinks or negative values) for the single subsurface continuum simulation with seepage faces at the land surface. For rainfall applied to the porous medium equations, the volumetric rates indicate all of the surface water originates in the porous medium. The dual rainfall boundary condition indicates approximately 64 percent of surface water discharge originates in the porous medium. The volumetric exchange rates indicated by the surface-applied rainfall condition agree well the seepage face values, indicating approximately 22 percent of surface water discharge originates below the land surface, with the remaining 78 percent originating as rainfall.

As represented in this work, mixing or solute exchange results from the movement of water between continua (i.e. advective transport) or a diffusive/dispersive process driven by concentration differences. Considering a single node at the land surface interface with rainfall boundary conditions only, the coupled system of discrete surface and porous medium transport equations can be written in implicit form as:

$$\left[\frac{V_i f_{i_p}^v}{\Delta t_{sub}}\left[(RC)^{M+1}-(RC)^{M}\right]_{i_p}-\sum_{j\in\eta_{i_p}} C_{adv}^{M+1} Q_{i_p j_p}^{L+1}-\sum_{j\in\eta_{i_p}} \xi^{M+1}\Lambda_{i_p j_p}^{M+1}-\sum_{i_p} Q_b^{L+1} C_b^{M+1}\right]= \tag{4.8}$$

$$= C_{ups}^{M+1} Q_{i_p j_s}^{L+1}+\xi^{M+1}\Lambda_{i_p j_s}^{M+1}$$

$$=\left[\sum_{j\in\eta_{i_s}} C_{adv}^{M+1} Q_{i_s j_s}^{L+1}+\sum_{j\in\eta_{i_s}} \xi^{M+1}\Lambda_{i_s j_s}^{M+1}+\sum_{i_s} Q_b^{L+1} C_b^{M+1}-\frac{A_i}{\Delta t_{sub}}\left[(RC)^{M+1}-(RC)^{M}\right]_{j_s}\right]$$

where $C_{ups}^{M+1} Q_{i_p j_s}^{L+1}$ and $\xi^{M+1}\Lambda_{i_p j_s}^{M+1}$ represent advective and diffusive/dispersive solute exchange rates, respectively, between the porous medium and surface continua. For rainfall applied to the porous medium, (4.8) becomes:

$$\left[\frac{V_i f_{i_p}^{v}}{\Delta t_{sub}}\left[(RC)^{M+1}-(RC)^{M}\right]_{i_p}-\sum_{j\in\eta_{i_p}} C_{adv}^{M+1} Q_{i_p j_p}^{L+1}-\sum_{j\in\eta_{i_p}} \xi^{M+1}\Lambda_{i_p j_p}^{M+1}-\sum_{i_p} Q_b^{L+1} C_b^{M+1}\right]= \tag{4.9}$$

$$= C_{i_p}^{M+1} Q_{i_p j_s}^{L+1}+\xi^{M+1}\Lambda_{i_p j_s}^{M+1}$$

$$=\left[\sum_{j\in\eta_{i_s}} C_{adv}^{M+1} Q_{i_s j_s}^{L+1}+\sum_{j\in\eta_{i_s}} \xi^{M+1}\Lambda_{i_s j_s}^{M+1}-\frac{A_i}{\Delta t_{sub}}\left[(RC)^{M+1}-(RC)^{M}\right]_{i_s}\right]$$

such that the porous medium is always upstream $\left(C_{ups}^{M+1}\equiv C_{i_p}^{M+1}\right)$ during the rainfall event. As rainfall mixes within the porous medium prior to discharge to the surface, solute concentrations in the surface water are strongly influenced by mixing within the porous medium volume, $V_i f_{i_p}^{v}$, adjacent to the land surface. Advective solute exchange is dominant if both the diffusive/dispersive exchange coefficient $\left(\Lambda_{i_p j_s}^{M+1}\right)$ and the concentration difference $\left(\xi^{M+1}\right)$ are small. Indeed, applying rainfall to the porous medium equations results in rainfall tracer concentrations nearly identical to assuming concentration continuity at the land surface (Figure 4-18).

For rainfall applied to the porous medium equations, the spatial and temporal distribution of solute exchange (Figure 4-21) is affected by the movement of excess rainfall from the porous medium to the surface continuum. The dual rainfall condition (Figure 4-22) limits mixing due to infiltration excess. For rainfall applied to the surface equations (Figure 4-23), mixing between the surface and subsurface continua is more heavily influenced by the magnitude of diffusive/dispersive exchange coefficient. The magnitude of advective exchange (i.e. transport of tracer induced by water movement between continua) is controlled by hydrodynamics within the porous medium (see Figure 4-20 and Section 4.7.1), not by the movement of excess rainfall from the porous medium to the surface continuum. The spatial and temporal distribution of solute exchange therefore reflects both concentration discontinuity and hydrodynamics. While having little affect on the flow solution (Figure 4-14), these subtleties in rainfall boundary condition assignment impact predictions of tracer concentrations in discharge water and, therefore, interpretations of water origin.

The sensitivity of simulated concentration to rainfall boundary condition assignment emphasizes the importance of mixing at the land surface interface. As illustrated in Figure 4-19, water flowing on the land surfaces interacts with a very thin region of the porous medium, providing

some support for the mixing and interaction zone coupling concepts utilized by previous workers [e.g. *Havis et al.*, 1992; *Govindaraju*, 1996]. In the context of the discrete equations (4.8), the mixing or interaction zone is represented by the discretized and constant volume of porous medium at the land surface.

The sensitivity of predicted discharge concentration to rainfall boundary condition assignment should be reduced as the volume associated with the porous medium equation decreases, as concentrations equilibrate rapidly with rainfall sources and with porous medium and surface sources and sinks. Indeed, equilibrium between continua could be a reasonable assumption with sufficiently fine spatial discretization at the land surface. To investigate this hypothesis, the simulations were repeated with the vertical discretization refined by a factor of two at the land surface (Figure 4-24). Porous medium volumes are reduced by one-half, while the area associated with the surface equations and rainfall boundary conditions remains constant (see Figure 3-1). The resulting tracer concentrations in the discharge water are presented in Figure 4-25 for simulations conducted with the three rainfall boundary conditions and with the concentration continuity assumption.

Applying rainfall to the surface water equations (Figure 4-25a) generates concentrations in discharge water nearly identical to those produced with the coarser discretization (Figure 4-18a). Results for the remaining simulations are improved during early time, however, indicating that the smaller porous medium volumes at the land surface do decrease the sensitivity of predicted concentrations to boundary condition assignment. However, concentrations during hydrograph recession are replicated well only by assuming concentration continuity, suggesting that mixing is related to more than the interaction of rainfall with the porous medium. Application of rainfall to the surface equations replicates measured rainfall tracer concentrations from about eight to twenty minutes (Figure 4-18a), indicating that solute exchange between continua is adequately represented by the specified combination of advective and diffusive processes (Figure 4-23b,c) during that time period. Concentrations at early time and late times are over- and under-estimated, respectively, suggesting an additional mixing process is active.

In the context of the coupling approach developed in Section 2.3.2, the diffusive coupling relationship may be augmented with an empirical exchange dispersivity, α^e, which enhances diffusive exchange in regions where water exchange is also occurring. The effect of this exchange dispersivity is illustrated in Figure 4-26, which presents tracer concentrations in discharge water for four simulations conducted by applying rainfall to the surface equations. For the smallest dispersivity value (0.005 cm), rainfall tracer concentrations at early time are only slightly reduced while concentrations predicted using the second value (0.01 cm) resemble those indicated by the dual rainfall boundary condition. Both values underestimate mixing during hydrograph recession. The two larger values of dispersivity (0.05 cm and 0.1 cm) mimic the correct magnitude of solute exchange during both hydrograph rise and fall. These simulations suggest that the empirical exchange dispersivity could be utilized as a calibration parameter to match simulated and observed concentrations: the value of such empirical coefficients is undoubtedly related to spatial discretization. Successful simulation of coupled surface-subsurface transport will also depend on the correct representation of the spatial and temporal variability of water exchange processes. Field-scale simulations of coupled surface-subsurface flow and transport are presented in Chapter 5.

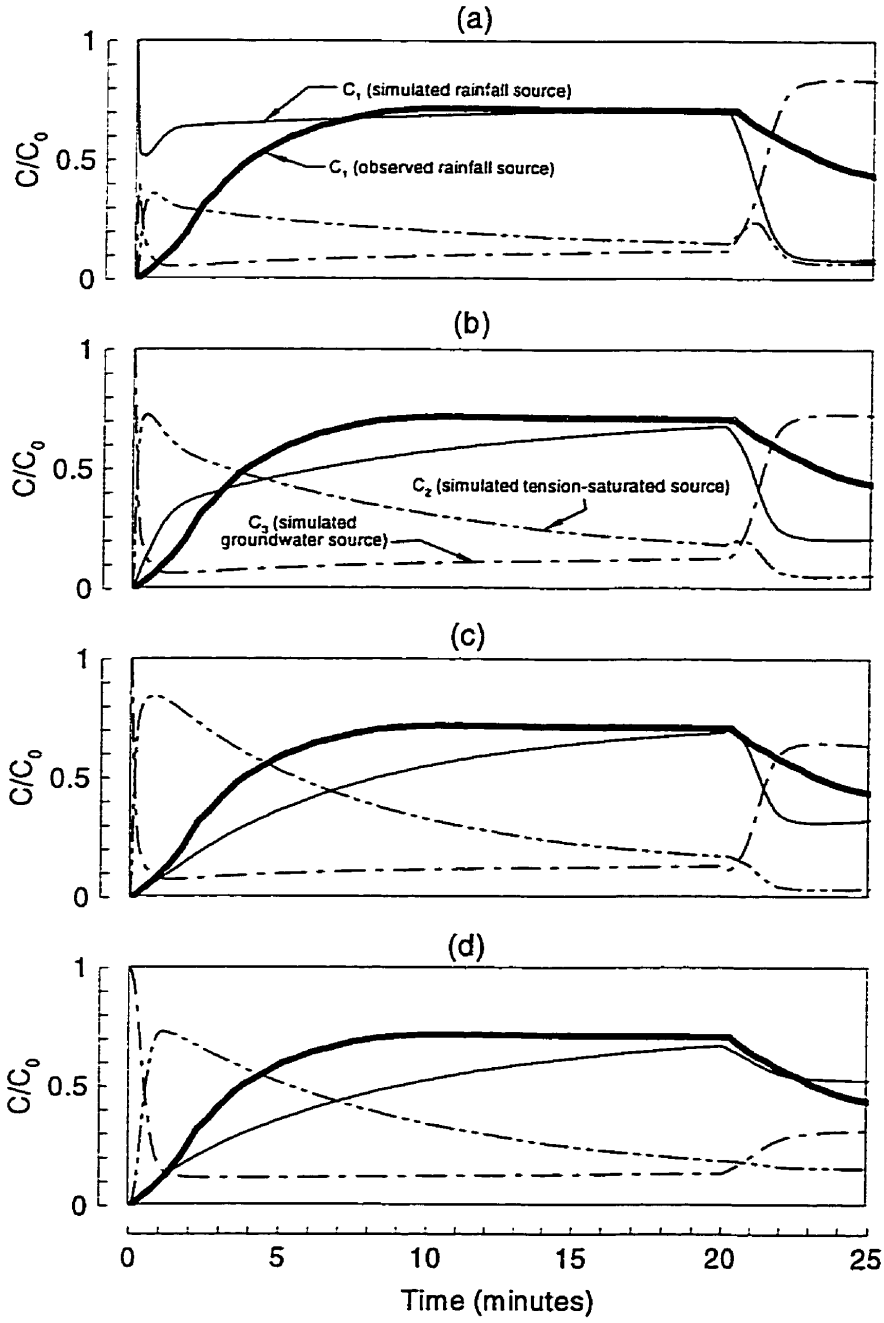

Figure 4-18. Discharge tracer concentration versus time for laboratory-scale coupled surface-subsurface example with base-case discretization nx = 35, nz = 25). Comparison of measured concentrations with those predicted by first-order surface-subsurface coupling with (a) rainfall applied to surface equations, (b) rainfall applied using dual boundary condition, (c) rainfall applied to porous medium equation, and (d) transport coupling utilizing concentration continuity at the land surface interface.

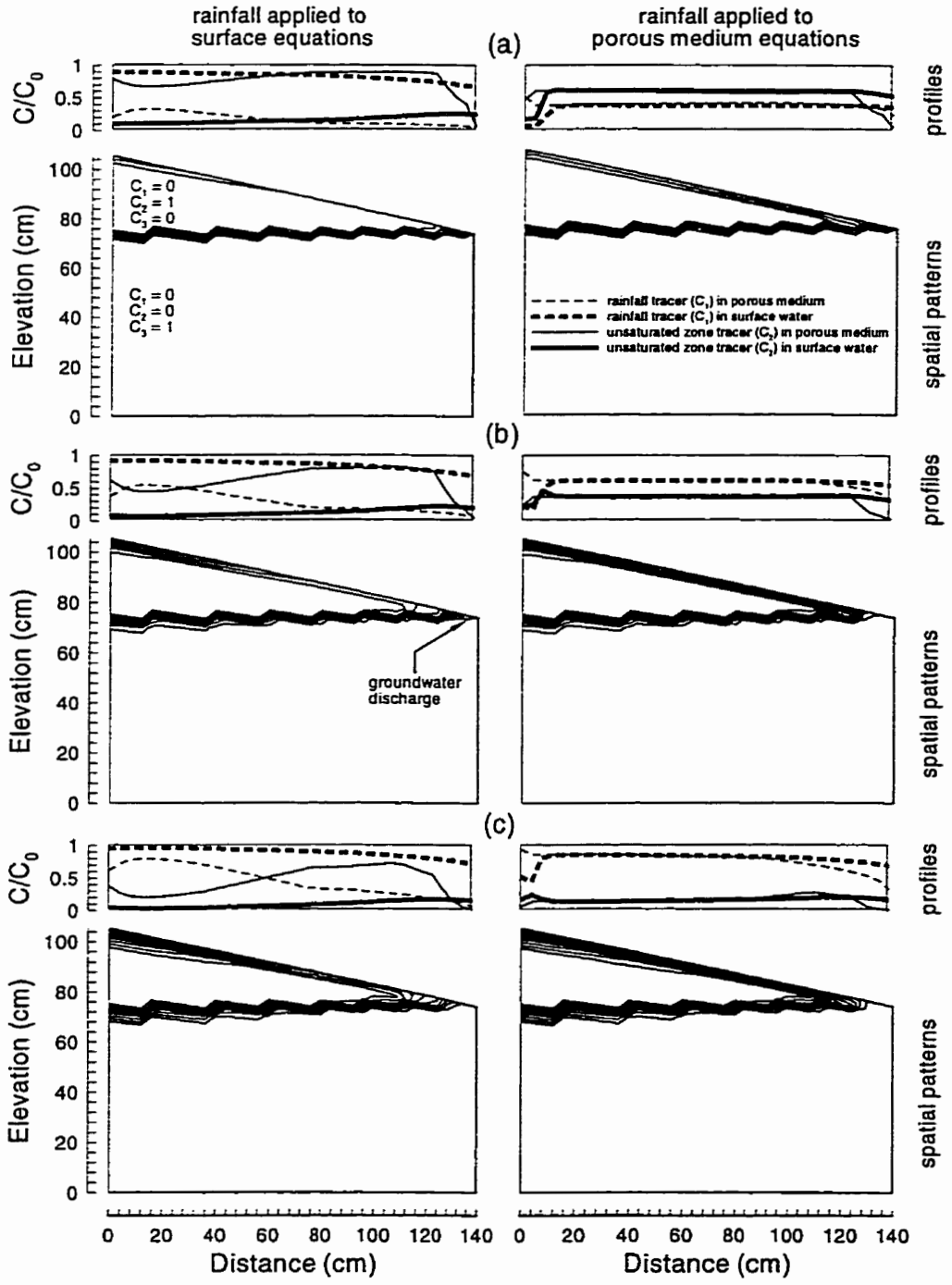

Figure 4-19. Profiles of rainfall and unsaturated zone tracer concentrations in surface water and in the porous medium at the land surface, and the spatial patterns of unsaturated zone tracer in the porous medium. Solutions for base-case discretization (nz = 25) with rainfall applied to surface equations and porous medium equations at (a) three minutes, (b) ten minutes, and (c) twenty minutes.

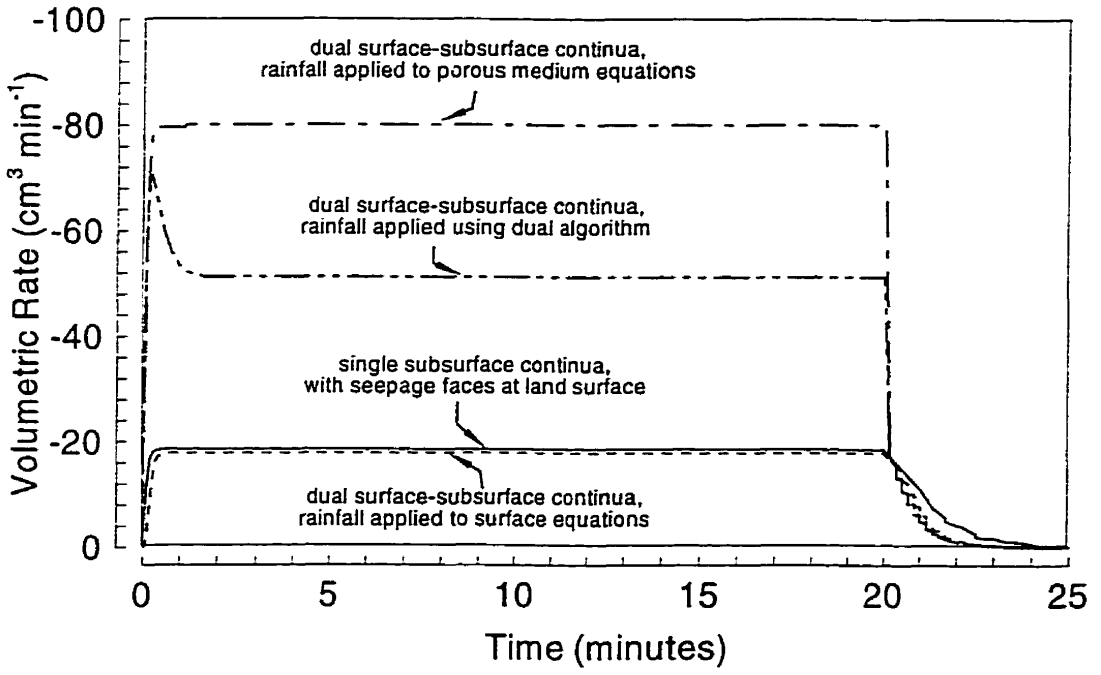

Figure 4-20. Volumetric seepage rate versus time for simulation with seepage faces at land surface and volumetric exchange rates versus time for coupled surface-subsurface simulations with three rainfall boundary conditions. Seepage rates are the sum of all negative seepage and exchange rates are the sum of all negative exchanges: both represent subsurface discharge.

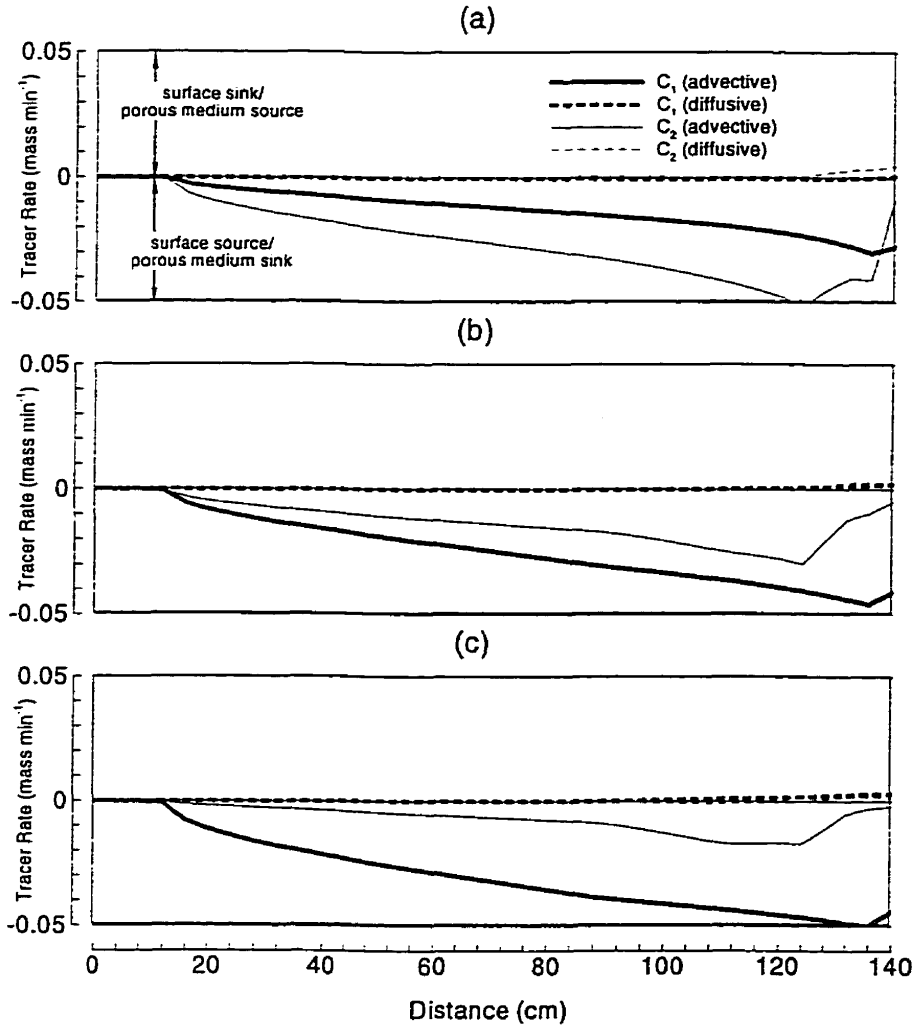

Figure 4-21. Graphs of tracer exchange rates versus distance for the rainfall and tension-saturated zone tracers. Solutions for base-case discretization with rainfall applied to porous medium equations at (a) three minutes, (b) ten minutes, and (c) twenty minutes.

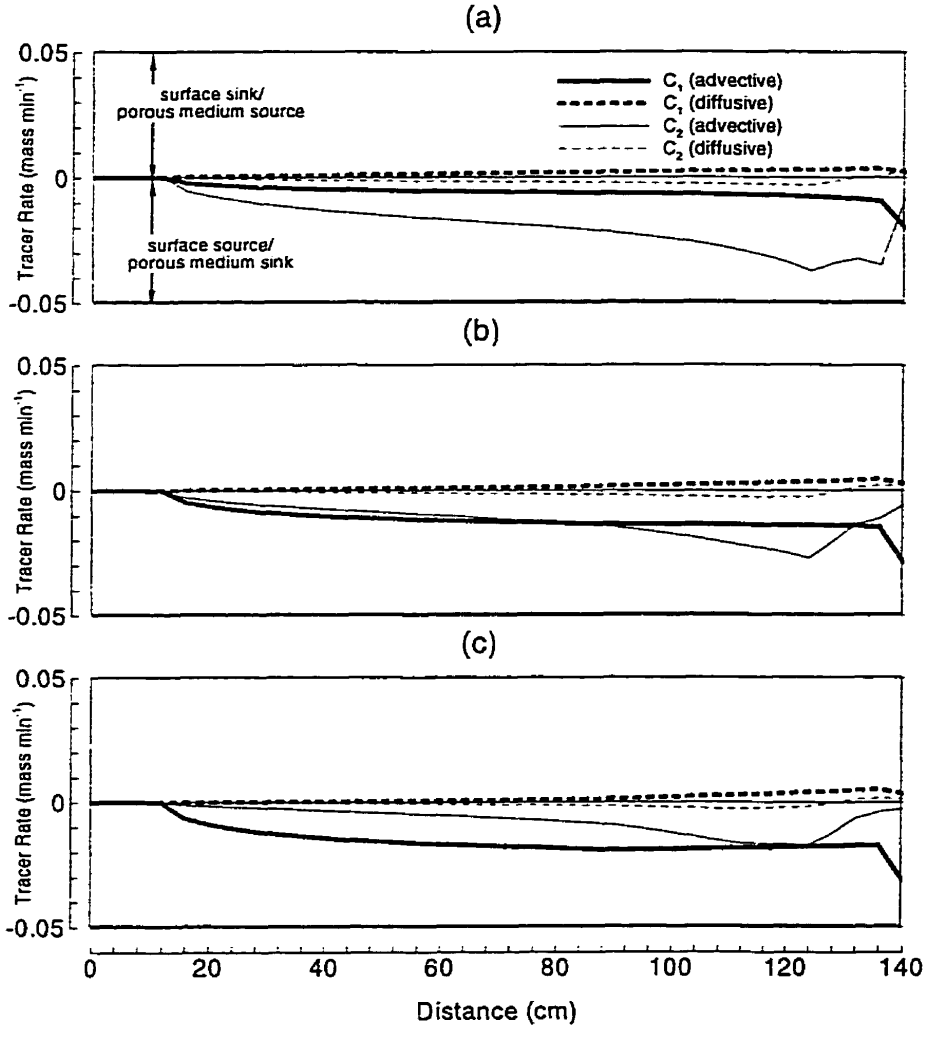

Figure 4-22. Graphs of tracer exchange rates versus distance for the rainfall and tension-saturated zone tracers. Solutions for base-case discretization with rainfall applied using the dual algorithm to both surface and porous medium equations at (a) three minutes, (b) ten minutes, and (c) twenty minutes.

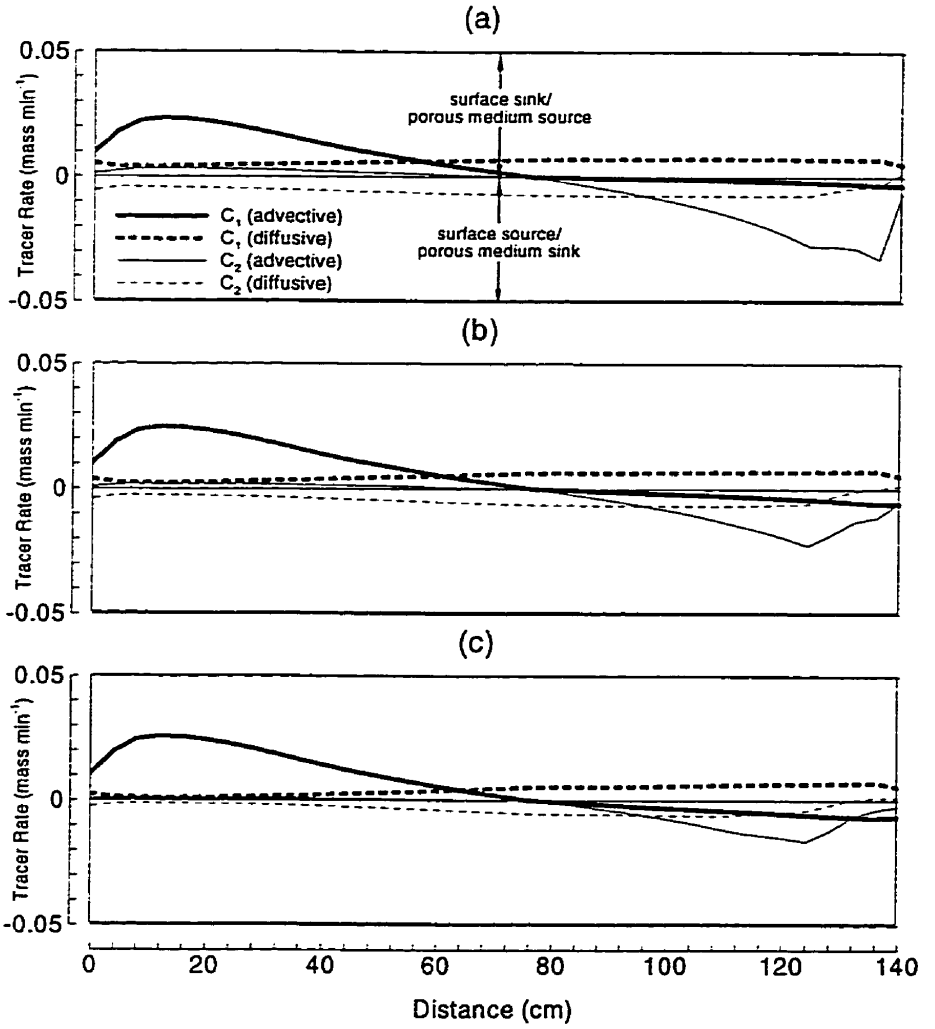

Figure 4-23. Graphs of tracer exchange rates versus distance for the rainfall and tension-saturated zone tracers. Solutions for base-case discretization with rainfall applied to surface equations at (a) three minutes, (b) ten minutes, and (c) twenty minutes.

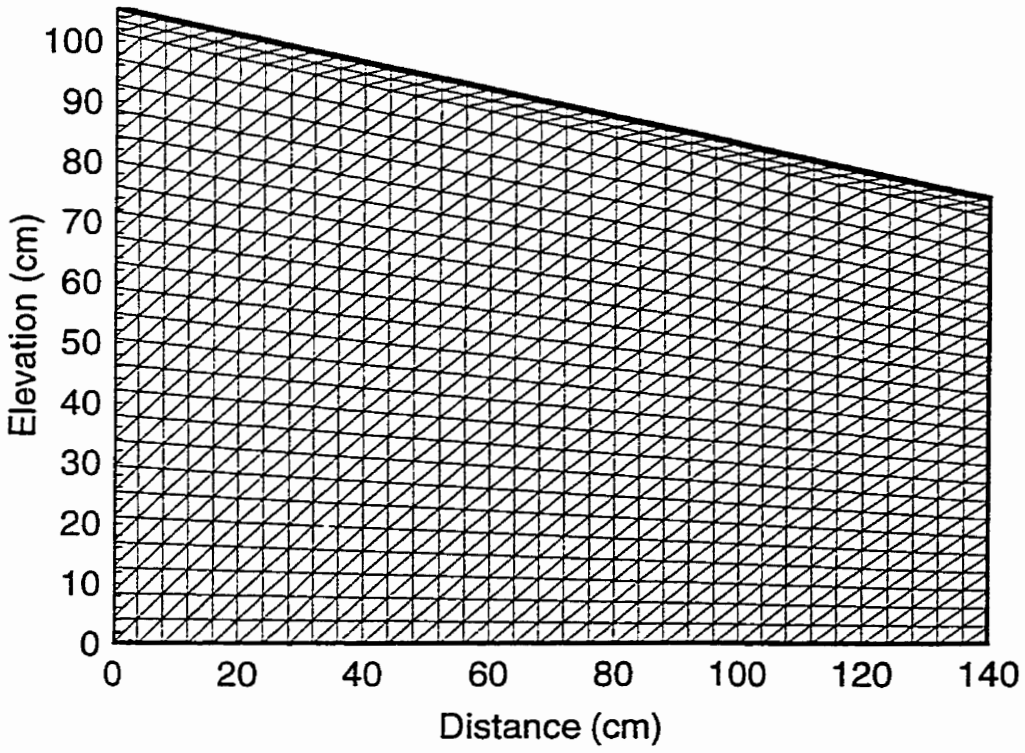

Figure 4-24. Finite element mesh with vertical discretization at land surface refined by a factor of two.

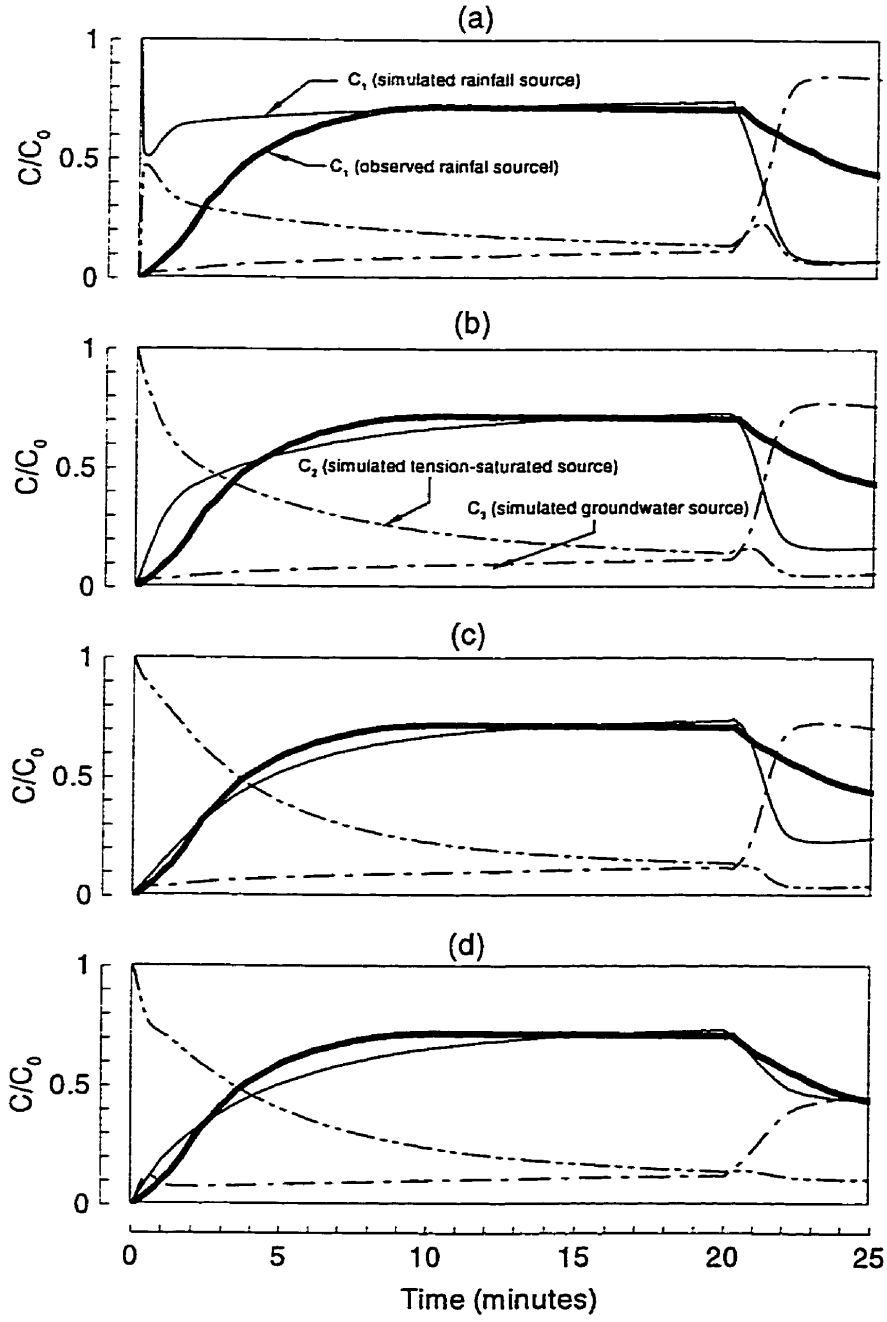

Figure 4-25. Discharge tracer concentration versus time for laboratory-scale coupled surface-subsurface example with refined vertical discretization. Comparison of measured concentrations with those predicted by first-order surface-subsurface coupling with (a) rainfall applied to surface equations, (b) rainfall applied using dual boundary condition, (c) rainfall applied to porous medium equation, and (d) transport coupling utilizing concentration continuity at the land surface interface.

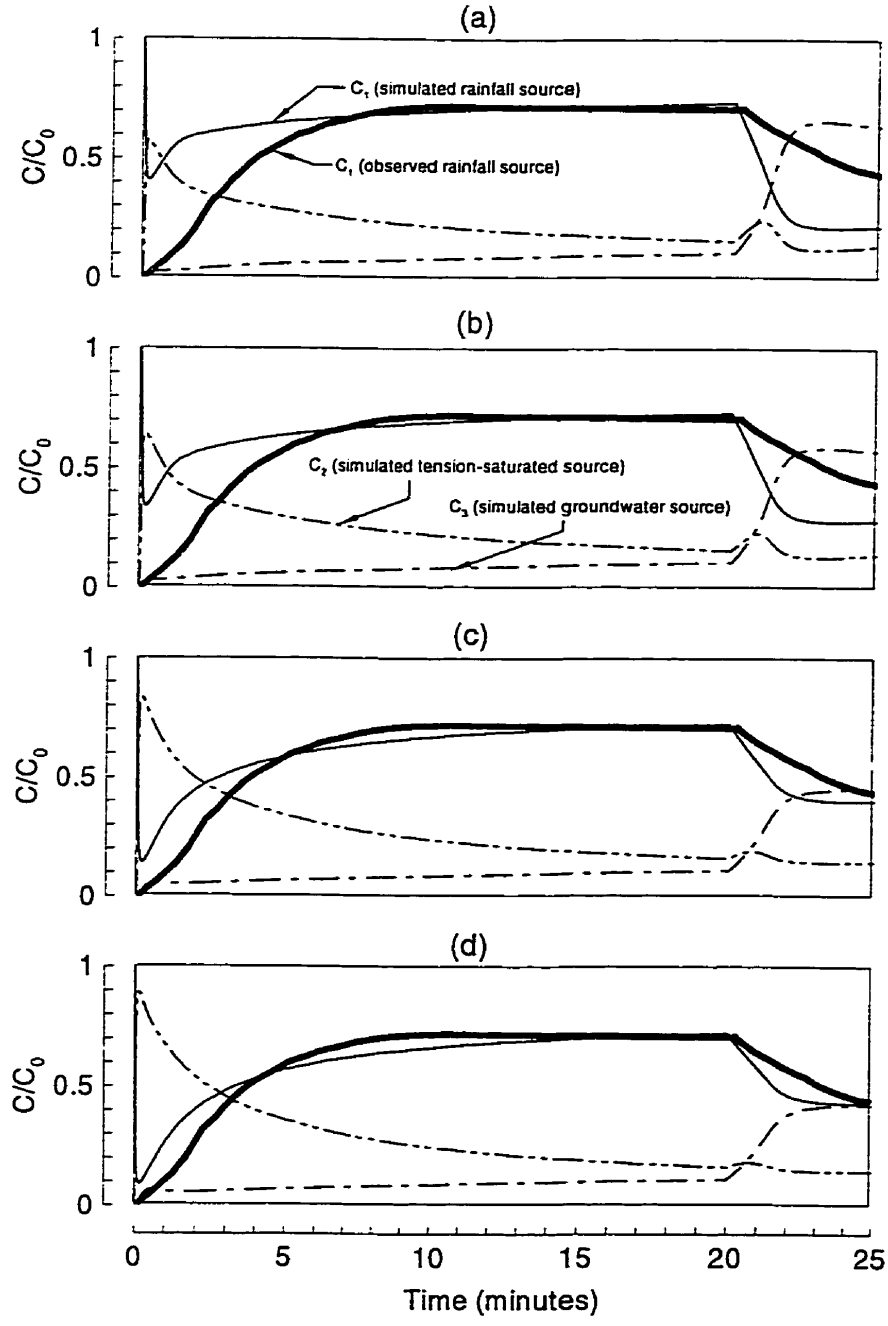

Figure 4-26. Discharge tracer concentration versus time for laboratory-scale coupled surface-subsurface example with refined vertical discretization. Comparison of measured concentrations with those predicted by first-order surface-subsurface coupling with rainfall applied to surface equations and exchange dispersivities of (a) $\alpha^* = 0.005$ cm, (b) $\alpha^* = 0.01$ cm, (c) $\alpha^* = 0.05$ cm, and (d) $\alpha^* = 0.1$ cm.

Chapter 5 Field-Scale Coupled Surface-Porous Medium Flow and Transport

The coupled surface-subsurface example presented in Section 4.5 demonstrates the ability of the numerical model to reproduce, with reasonable accuracy, observed discharge volumes and concentrations at the laboratory scale. The integrated numerical model is applied in this chapter to *Abdul's* [1985] field experiment [see also *Abdul and Gillham*, 1989]. Specific objectives in this chapter are to (1) evaluate the ability of the numerical model to capture relevant processes at an intermediate scale in a relatively homogeneous environment, (2) compare the flow solution given by the coupled surface-subsurface approach with that generated using seepage faces at the land surface, and to investigate (3) the relationship between hydrologic response, streamflow generation, and tracer concentrations in discharge water, and (4) the sensitivity of stream discharge volume and tracer-based separations of discharge to system parameters.

5.1 Problem Description

The field-scale experiments of *Abdul* [1985] were conducted at Canadian Forces Base Borden, located north of Toronto, Ontario, Canada. The area selected for the experiment is described as being grass covered and approximately 18 m by 90 m in plan view (Figure 5-1). A man-made stream channel, grass-free and approximately 60 cm wide, is located approximately 1.2 meters below the surrounding topographic highs. The underlying porous medium consists of an organic-rich sandy layer, approximately ten to twenty cm thick, overlying sand containing small-scale interbeds with occasional silty layers and lenses [*MacFarlane et al.*, 1983; *Abdul*, 1985; *Sudicky*, 1986]. A thick deposit of clayey silt underlies the aquifer at a depth of about four meters [*Akindunni and*

Gillham, 1992]. The measured characteristic saturation-pressure relationship [*Abdul*, 1985] indicates that the sand is saturated for a distance of about 30 cm above the water table (Figure 5-2).

For the experiment under consideration, the initial water table lies about 22 cm below the streambed, indicating that the capillary fringe extends to the land surface along and adjacent to the stream. *Abdul* [1985] applied artificial recharge for 50 minutes at a rate of 2.0 cm/hour, observing a rapid rise of the water table and both overland and stream flow. The recharge water contained bromide, providing a conservative tracer to differentiate 'event' and 'pre-event' water (Figure 5-3). *Abdul* [1985] utilized a two-dimensional porous medium flow model to evaluate the development of seepage faces along two transects, with the predicted seepage discharge and excess recharge routed along the stream channel using a one-dimensional kinematic wave model. The simulated hydrographs were in reasonable agreement with measured values. The essential conclusion of Abdul's field experiments and simulations was that the rapid response of the capillary fringe to rainfall was responsible for observed streamflow. The interpreted streamflow generation mechanisms were: (1) increased overland flow due to rainfall excess onto regions of saturated sand and (2) groundwater discharge due to increased subsurface hydraulic head gradients. Groundwater or pre-event contributions were interpreted to form up to 37% of streamflow, based both on chemically based hydrograph separations (Figure 5-3) and on groundwater discharge volumes (seepage) calculated using flow nets.

5.2 Field-Scale Simulations

The finite element meshes utilized in the three-dimensional field-scale simulations are presented in Figure 5-4. Vertical discretization is on the order of one centimeter adjacent to the land surface, increasing to about one meter at depth. Horizontal discretization is on the order of 20 centimeters in and adjacent to the stream channel, increasing to about one meter on the topographic highs. Both isoparametric prisms and subdivision of prisms into tetrahedra generated large numbers (greater than 25%) of negative influence coefficients for the subsurface finite element mesh. The modified prism elements are therefore utilized exclusively, generating significantly fewer negative

values (0.21%) and required considerably less memory and computational effort. Appendix A presents both the development and verification of the modified prism elements and a brief investigation of solution sensitivity to grid refinement.

Boundary and initial conditions are presented in Figure 5-5 for simulations of first-order coupled surface-subsurface flow and transport. Rainfall is applied to the top nodes for fifty minutes at a rate of two cm/hour, followed by fifty minutes of drainage. Critical depth conditions are utilized at the stream outflow, representing the weir utilized in the field experiment. No additional boundary conditions are specified. Parameters for all simulations (Table 5-1) are derived from measured or published values and a sensitivity analysis presented in Section 5.3. Although a single tracer was applied in the field experiment, three tracers are utilized in the simulations to allow differentiation of rainfall from water originating above and below the initial water table.

The following discussion focuses on the ability of the integrated numerical model to predict surface discharge volumes and bromide concentrations, as little information is available regarding surface water depths or tracer distributions. No attempt is made to exactly match pressure head measurements collected by *Abdul* [1985], since the elevations of his measurement locations are not well defined. One simulation of subsurface flow using seepage faces is also presented to compare and contrast the first-order-coupled simulations. While rainfall boundary conditions are consistent with the first-order-coupled simulations, each node on the land surface is also considered as a possible seepage face for the duration of the simulation. Transport is not considered in the seepage face simulation. The following section presents a detailed analysis of the hydrologic response of the coupled system and makes comparisons with the simulation performed with seepage face conditions enforced at the land surface.

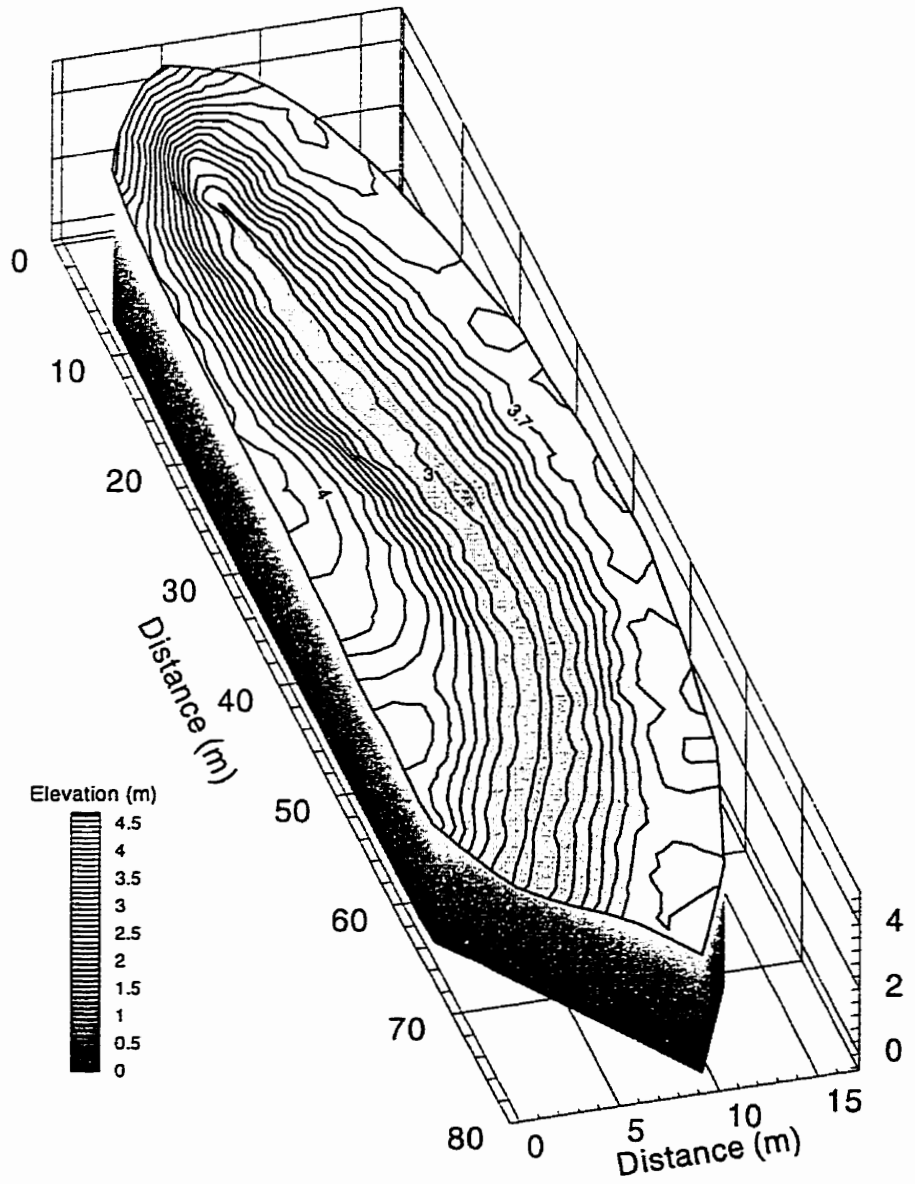

Figure 5-1. Surface topography of the site of the Borden rainfall-runoff field experiment [after *Abdul*, 1985].

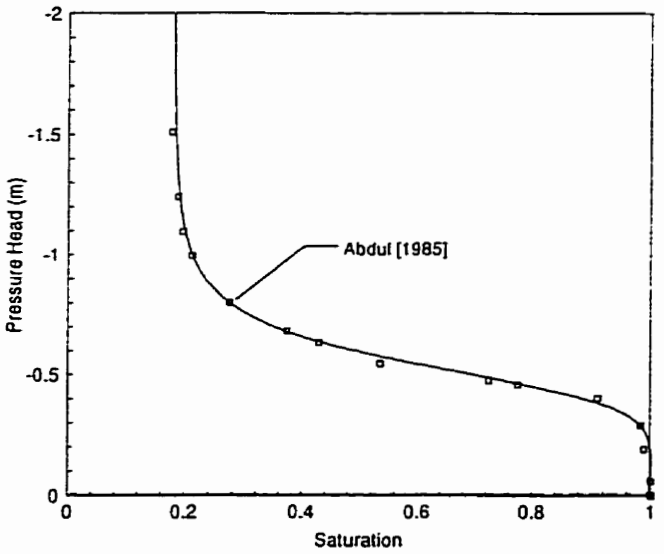

Figure 5-2. Measured [*Abdul*, 1985] and functional drainage pressure-saturation relationship for the Borden field experiment.

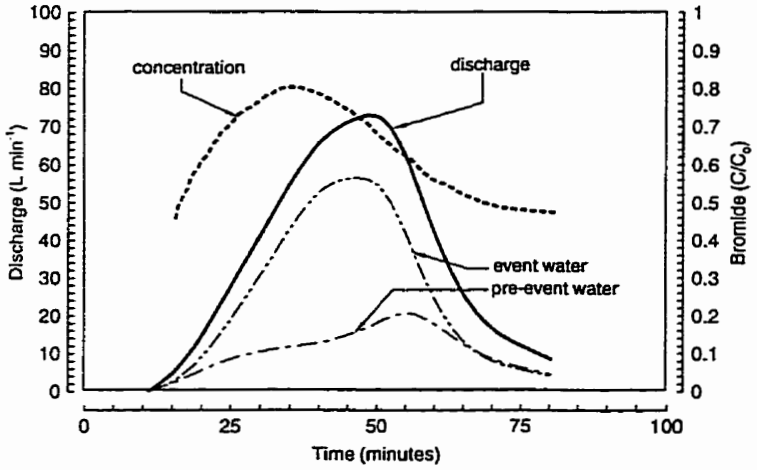

Figure 5-3. Measured discharge volumes, normalized tracer concentrations and hydrograph separation for the Borden field experiment [after *Abdul*, 1985].

Porous Medium		
porosity[1]	ϕ_{p_o}	0.37
saturation-pressure head relationship[1]	$S_w(\psi), \psi(S_w)$	$\alpha = 1.9; n = 6;$ $S_{wr} = 0.18$
saturation-relative permeability relationship[1]	$k_{rw} = a\left(S_w \phi_{p_o}\right)^b$ $\approx (S_w)^b$	$a = 110$ $b = 4.5$
compressibility[2]	β_p	3.3×10^{-8} m s^2/kg
longitudinal dispersivity[3]	α_l	0.5 m
transverse dispersivity[3]	α_{th}, α_{tv}	5×10^{-3} m
initial total head	$\psi_p + z$	2.78 m
Surface		
surface roughness (channel)[1,4]	$\bar{n}$	0.03 s/m$^{1/3}$
surface roughness (slopes)[5]	$\bar{n}$	0.3 s/m$^{1/3}$
initial water depth	ψ_s	1×10^{-4} m
microtopography	h_s	1×10^{-2} m
residual saturation	S_{w_r}	1×10^{-2}
mobile water depth	ψ_s^{pond}	1×10^{-4} m
dispersivity	α_l, α_t	0.1 m
Solute		
diffusion coefficient[6]	D_w	1.2×10^{-9} m^2/s
Coupling		
characteristic length	a_s	1×10^{-4} m
dispersivity	α^*	0.0 m
Solution		
minimum timestep	Δt_{global}	5 s
maximum timestep	Δt_{global}	100 s
local residual tolerance	tol^{error}	1×10^{-2}

[1] *Abdul* [1985], [2] *Akindunni and Gillham* [1992], [3] *Sudicky* [1986], [4] *Chow* [1959], [5] *Kouwen* [1992], [6] *Wallach et al.* [1988]

Table 5-1. Parameterization of the field-scale coupled surface-subsurface simulations.

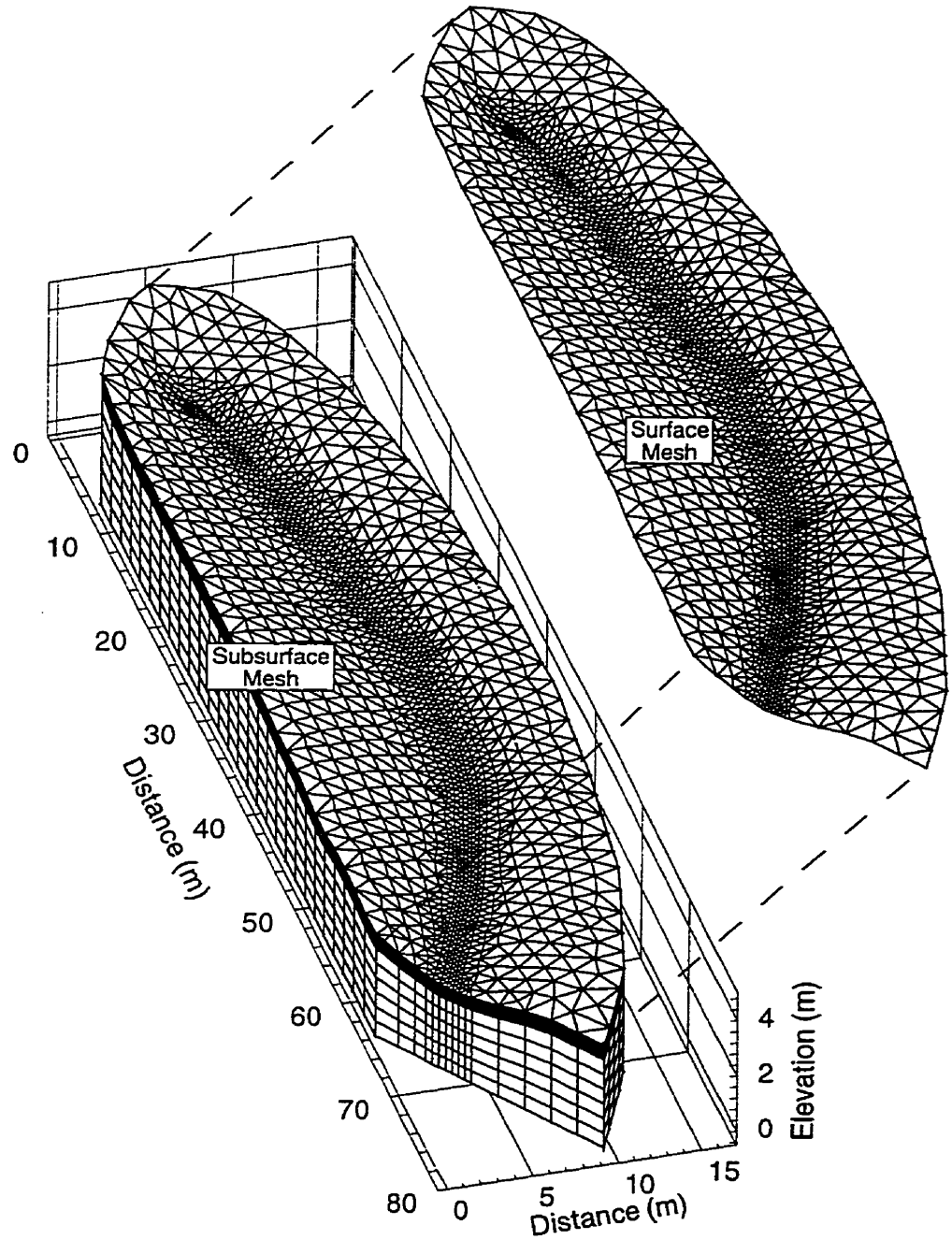

Figure 5-4. Finite element meshes utilized in field-scale coupled surface-subsurface simulations (16464 nodes, 29161 porous medium elements, and 2651 surface elements).

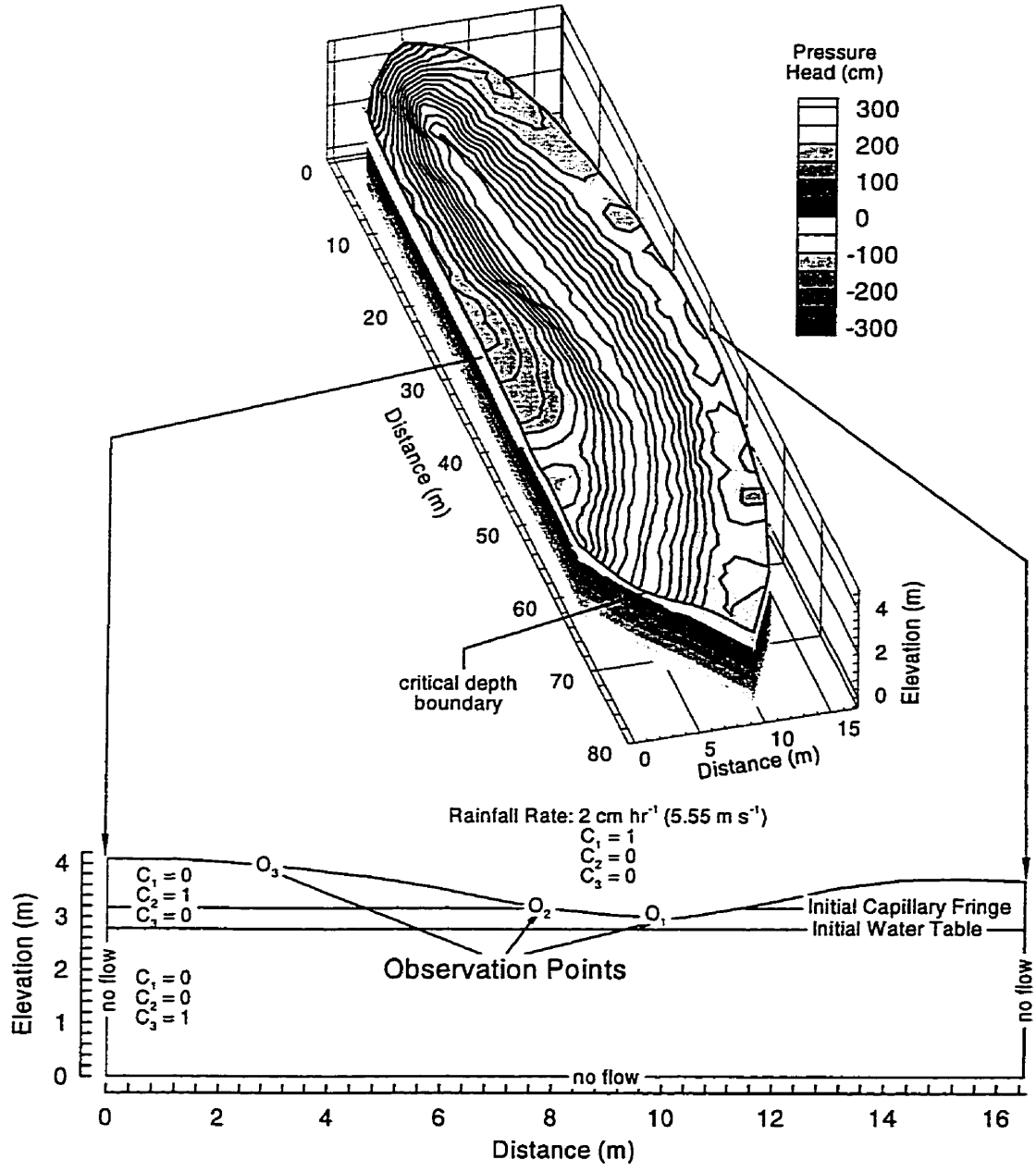

Figure 5-5. Illustration of initial and boundary conditions for field-scale first-order-coupled surface-subsurface simulations, and the locations of three observation points and a representative cross section.

5.2.1 Rainfall-Runoff Response and Comparison with Seepage Faces

A comparison of the measured stream discharge with that predicted with the coupled surface-subsurface numerical model is presented in Figure 5-6. The simulated hydrograph slightly overpredicts both early-time response and peak discharge, while reproducing both the time to peak and the recession portions of the measured hydrograph with reasonable accuracy. Also presented in Figure 5-6 is the approximate area of the land surface contributing to stream flow via overland flow. This area is calculated by dividing the ponded area of the land surface (i.e. the total area of the land surface where water depths are greater than the minimum mobile depth of 10^{-4} m) by the total surface area. The figure indicates that, while increased surface discharge correlates with increased surface ponding, the relationship between surface discharge and contributing area is nonlinear. Simulated contributing areas increase more rapidly than stream discharge at early time (i.e. less than about fifteen minutes) while decreasing more rapidly than stream discharge when rainfall ceases. This nonlinearity is caused by the relationship between water depth and velocity imbedded in the Manning equation, and by the spatially- and temporally-variable storage and infiltration capacities of the porous medium, which acts as a source/sink term in the surface water flow equation.

Figure 5-7 presents graphs of pressure head and water depth versus time for three observation points located on the land surface along a cross section at x = 40 meters. These observation points correspond to the streambed, the valley bottom, and the upland region, respectively (Figure 5-5). High initial saturation and reduced storage capacity beneath (Figure 5-7a) and adjacent (Figure 5-7b) to the stream channel causes a rapid change of negative pressure heads to positive values. Water depths in the stream rise to about five centimeters at peak discharge, decreasing slowly during recession. Water depths are smaller on the slopes adjacent to the stream, and decrease rapidly following the end of the rainfall event. Pressure head values remain negative at the upland observation point (Figure 5-7c) as initial saturations are near residual values and significant storage capacity exists in the porous medium.

Total head gradients beneath the stream (Figure 5-8a) indicate infiltration into the streambed for about five minutes, corresponding to the delay in surface discharge initiation and the time required to occupy the small storage capacity of the capillary fringe. Hydraulic head gradients adjacent to the stream (Figure 5-8b) indicate infiltration for the duration of the simulation, with vertical gradients decreasing after about the first 20 minutes. Not all rainfall enters the porous medium at this location, but instead contributes to overland and stream flow as a function of spatially and temporally variable infiltration rates. Surface discharge timing and volume, therefore, are intimately related to the storage capacity and hydraulic conductivity of the porous medium. Head gradients beneath the uppermost observation point (Figure 5-8c) indicate infiltrating conditions for the duration of the simulation, with the wetting front penetrating to a depth of about 40 centimeters at the end of the rainfall event.

The responses to rainfall presented at the observation locations are indicative of those occurring throughout the domain. The following paragraphs discuss the spatial and temporal variability of hydrologic response and compare the first-order-coupled simulation with a single-continuum simulation performed with seepage faces at the land surface. A sense of the temporal variability of hydrologic response is indicated by presenting results at times of twenty-five, fifty and seventy-five minutes. These times represent hydrograph rise, the end of the rainfall event (and peak surface water discharge), and hydrograph recession.

Pressure heads at the land surface and rates of water exchange between continua for the first-order-coupled simulation are presented in Figure 5-9 and Figure 5-13 at times of twenty-five and seventy-five minutes, respectively. Graphed results correspond to the nodes lying along the top of the representative cross section located at $x = 40$ m. Also presented in these figures are the boundary source/sink rates for the corresponding seepage face simulation and hydraulic head distributions and water table elevations in the porous medium for both simulations. Figure 5-10 presents profiles of water depths and exchange/seepage rates along the stream channel, at times of twenty-five, fifty and seventy-five minutes.

Boundary source/sink rates are equivalent to the rainfall rate if seepage faces are inactive, and, for active seepage faces, are equivalent to the back-calculated boundary flux. Exchange rates in the coupled simulation and boundary source/sink rates in the seepage face simulation are both positive for infiltration. Rates have been normalized by the volume associated with the subsurface flow equations to be consistent with the governing equations. Note that the volume-normalization performed on the seepage and exchange fluxes introduces some variability in the seepage and exchange rates, as the volume associated with each porous medium node varies with nodal spacings in the finite element mesh. Nodal spacings and volumes are relatively constant along the stream axis, but increase with distance from the stream.

The graphs of total head profiles below the three observation points indicate that hydrologic response of the porous medium to rainfall is more rapid at observation point one (Figure 5-8a), located at the stream, than at the second observation point, located near the top of the initial capillary fringe (Figure 5-8a). Water table elevations along the cross section at twenty-five minutes intersect the land surface along topographic lows for both the coupled (Figure 5-9a) and seepage face (Figure 5-9b) simulations. Contours of total head indicate that head gradients are greatest at the toe of the slopes, where the rising water table interacts with higher land surface elevations to direct flow both into the slope and towards the stream. Head contours vary in space and are asymmetric across the stream due to varying land-surface slope configurations.

Spatial variability in subsurface head gradients is reflected in the rate of water exchange in the coupled simulations (Figure 5-9a) and the back-calculated boundary source/sink rates for the seepage face simulation (Figure 5-9b). While both rates are equivalent to the specified rainfall rate in upland regions, positive rates (indicating infiltration) decrease with elevation, becoming zero or negative (indicating discharge or seepage) adjacent to the stream. Exchange rates in the coupled simulation differ from the back-calculated seepage rates at the stream itself, however (Figure 5-10). In the coupled simulation, both rainfall in excess of local infiltration rates and groundwater discharge pond on the land surface, flowing overland to the stream, and along the stream channel towards the discharge boundary. Ponded surface water fills the stream channel after twenty-five minutes of

rainfall in the coupled simulation (Figure 5-10a), forming a positive constraint of about three centimeters on pressure heads in the adjoining porous medium. The effects of small-scale topographic variability associated with the stream channel are therefore diminished, reducing subsurface head gradients and groundwater seepage. These effects are not considered in the traditional seepage face approach, as the maximum head constraint is equivalent to the land surface elevation. Water depths adjacent to the stream are not significantly different from zero and act in a manner similar to the zero pressure head constraint imposed in the seepage face simulation (Figure 5-9b).

Figure 5-11 presents a summary of the coupled flow solution at 50 minutes, corresponding to both the end of the rainfall event and peak surface water discharge. Pressure head contours on seven cross sections are depicted, as are contours of surface water depth on the land surface and the rate of water exchange between continua. The corresponding summaries of the seepage face simulation are shown in Figure 5-12, which presents pressure head contours, seepage face status (i.e. active or inactive), and source/sink rates at the land surface boundary. Water table elevations in both simulations are similar adjacent to and beneath the slopes. Surface ponding in the stream channel, where depths have risen to about five centimeters (Figure 5-10b), is reflected in decreased seepage along the channel axis in the coupled simulation. Surface water depths adjacent to the stream have also risen (Figure 5-11d), subtly altering the spatial distribution of infiltration and groundwater discharge by filling small depressions in the land surface topography. Little differences are evident between the coupled and seepage face simulation at the toe of the slopes or beneath the topographic highs, however. Indeed, in the slopes and upland areas, boundary source/sink rates for the seepage face simulation are virtually identical to the rate of water exchange between the surface and porous medium continua in the coupled simulation.

Figure 5-13a presents a summary of the coupled flow solution at 75 minutes along the representative cross section. As surface water depths in the stream channel are about three centimeters (Figure 5-10c) the stream continues to act as a constraint on subsurface head values in the adjoining porous medium during hydrograph recession. Infiltration rates are low, as head

gradients in the porous medium are small. Most water flows laterally away from the stream, raising water table elevations beneath the topographic highs. Examining the seepage face simulation at seventy-five minutes one can note that the water table has fallen below the land surface elevation (Figure 5-13b), and, therefore, that all seepage faces are inactive, and boundary source/sink rates are zero. Hydraulic head contours indicate lateral subsurface flow beneath the topographic highs as water introduced during the rainfall moves away from the area of the stream. Continued flow towards the stream channel is also evident, adjacent to the land surface, as slow drainage through the unsaturated zone follows the topography, raising water table elevations slightly at the toe of the slopes. Subsurface flow directions predicted by the seepage face and coupled simulations are reversed along the valley axis after rainfall ceases.

Excess rainfall and groundwater seepage to the surface water regime is not lost from the system in the coupled simulation, but is either stored or flows on the land surface. Transient and spatially-variable surface water depths provide a constraint on pressure head in the porous medium at the land surface, with seepage and infiltration rates determined by subsurface hydraulic gradients and the permeability of the porous medium. These processes are reversed after rainfall cessation, as total head in the adjacent porous medium falls below the elevation of the land surface and the stream becomes a source of water (Figure 5-10c). Such dynamics are precluded if conventional seepage faces are utilized in the numerical model, as both rainfall excess and groundwater discharge during the rainfall event are assumed to be instantaneously removed from the subsurface flow regime. By not considering surface ponding, the seepage face simulation over-predicts groundwater discharge into the stream during the rainfall event, and ignores the possible infiltration of ponded surface water both during and after the rainfall event.

Figure 5-14a presents graphs of the total volumetric rates of groundwater discharge versus time for both the coupled and seepage face simulations. For the coupled simulation, rates represent the sum over the entire upper boundary of the finite element mesh of the volume of water leaving the porous medium and entering the surface continuum (i.e. seepage). For the simulation performed with seepage faces, rates represent the sum of all back-calculated seepage rates at the land surface

(i.e. water leaving the porous medium). As indicated in the previous analyses, the seepage face solution predicts greater groundwater discharge into the stream channel during the rainfall event. This increased discharge results in total seepage volumes nearly double those predicted by the coupled solution. Further, assuming discharge is immediately available at the stream outflow boundary and that there is no subsequent reinfiltration, both simulations indicate that groundwater discharge accounts for less than five percent of total surface water discharge (Figure 5-14b).

The coupled surface-subsurface numerical model was able to simulate observed stream discharge for the Borden field experiment with reasonable accuracy using measured or literature-derived parameters and minimal calibration. The response of the porous medium to rainfall is spatially variable, depending upon initial saturation and water table depth. The simulated response of the capillary fringe to rainfall is consistent with both theory [*Gillham*, 1985] and observations [*Abdul*, 1985; *Abdul and Gillham*, 1989]. However, the predominant streamflow generation indicated by the simulation is infiltration excess overland flow, with groundwater discharge (i.e. seepage) forming a relatively minor component of stream discharge volumes. This contrasts *Abdul* [1985] and *Abdul and Gillham* [1989] whom, by separating surface discharge using the rainfall tracer (hydrograph separation), concluded that groundwater forms up to 37% of stream flow. *Abdul* [195] provided further support for large groundwater contributions by routing seepage from two-dimensional hillslopes into a one-dimensional kinematic streamflow model. The three-dimensional seepage face simulation performed here also indicates that groundwater seepage is small in volume, relative to measured streamflow, and shows that groundwater discharge is overestimated if surface water ponding is not considered. The following section presents the results of the tracer transport simulations and discusses the relationship between the hydrologic response simulated with the coupled surface-subsurface model and simulated tracer concentrations in stream discharge water.

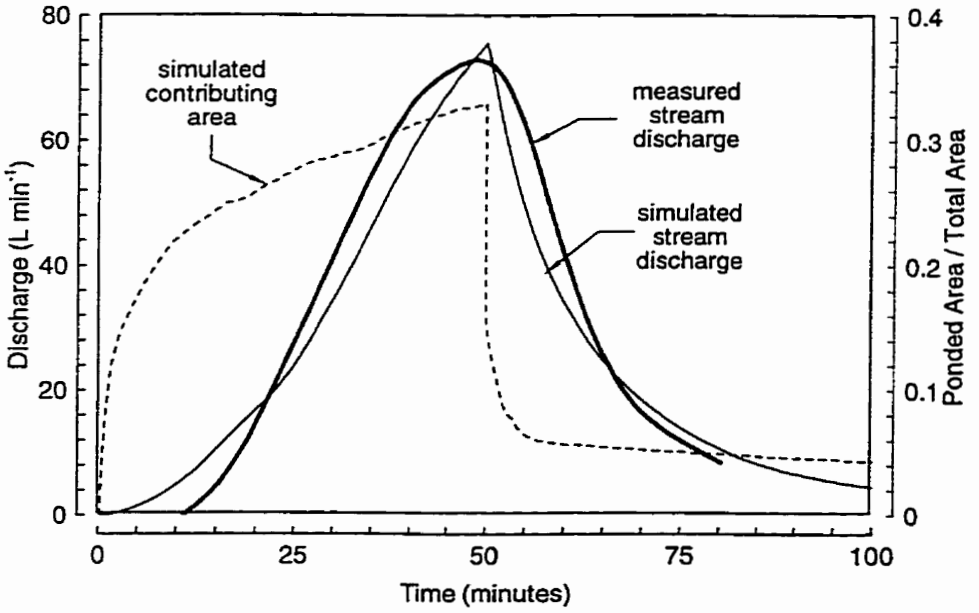

Figure 5-6. Comparison of measured and simulated stream discharges versus time (hydrographs) and the illustration of the simulated area contributing water to the stream via overland flow. Solution for initial hydraulic head of 278 cm and porous medium hydraulic conductivity of 1×10^{-5} m s^{-1}.

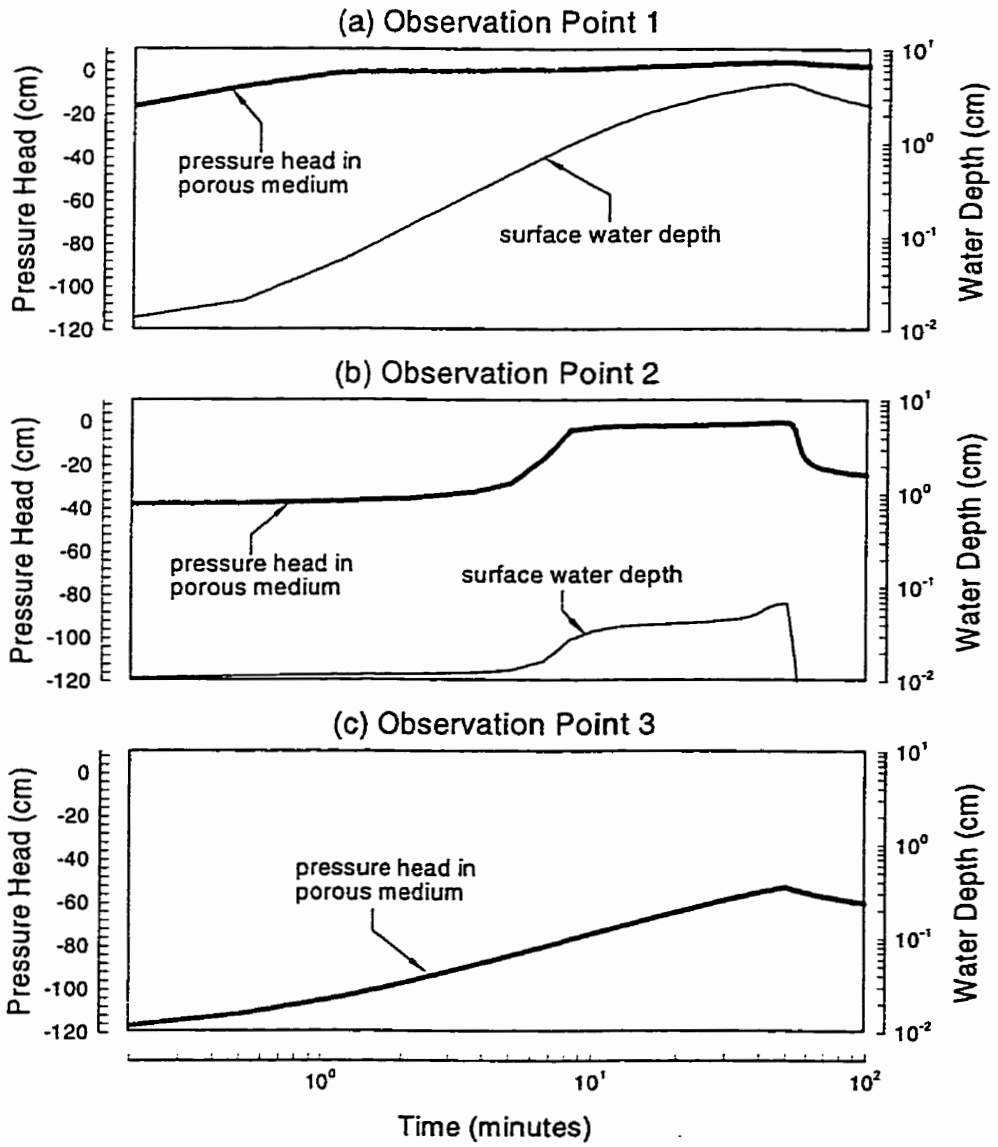

Figure 5-7. Graphs of pressure head and water depth versus time at three locations on the land surface: (a) observation point one located at the stream, (b) observation point two located adjacent to the stream, and (c) observation point three located in the upland region. Observation point locations are indicated in Figure 5-5. Solution for initial hydraulic head of 278 cm and porous medium hydraulic conductivity of 1×10^{-5} m s^{-1}.

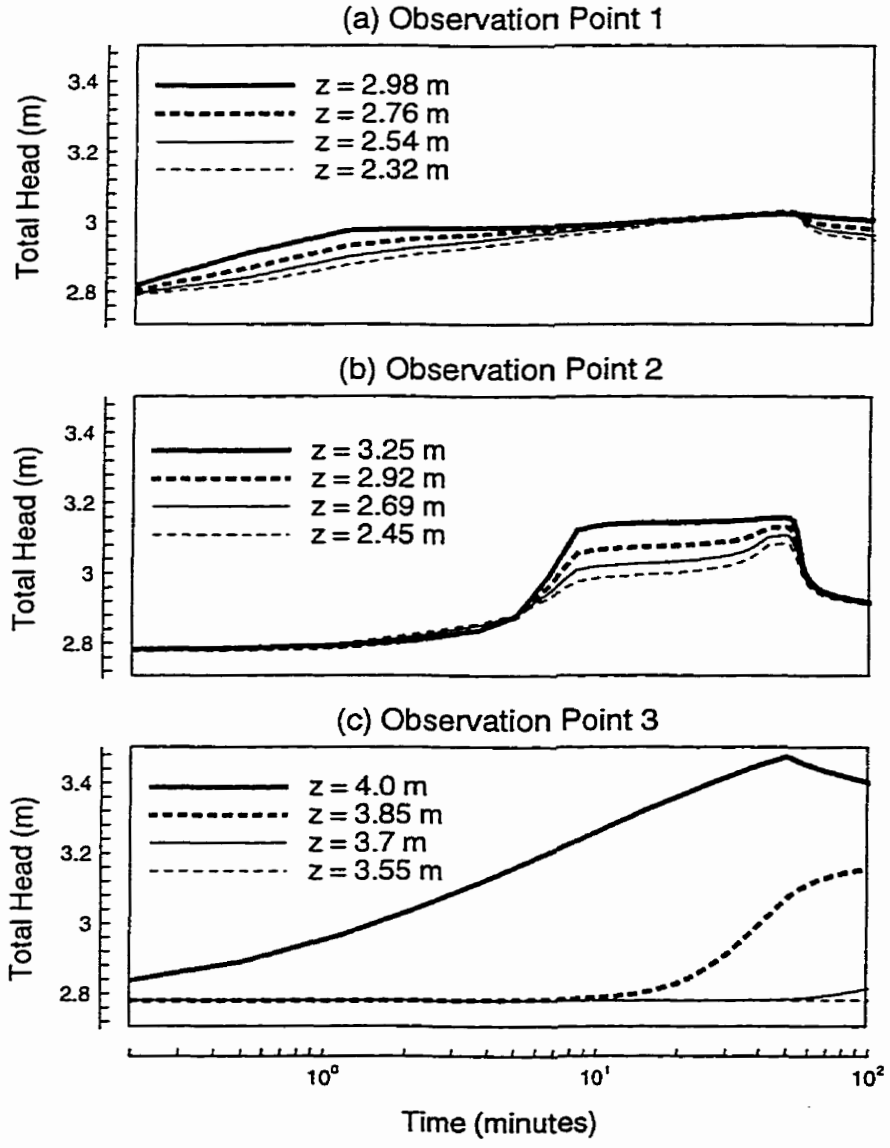

Figure 5-8. Graphs of total head versus time and elevation (a) observation point one located at the stream, (b) observation point two located adjacent to the stream, and (c) observation point three located in the upland region. Observation point locations are indicated in Figure 5-5. Solution for initial hydraulic head of 278 cm and porous medium hydraulic conductivity of 1×10^{-5} m s^{-1}.

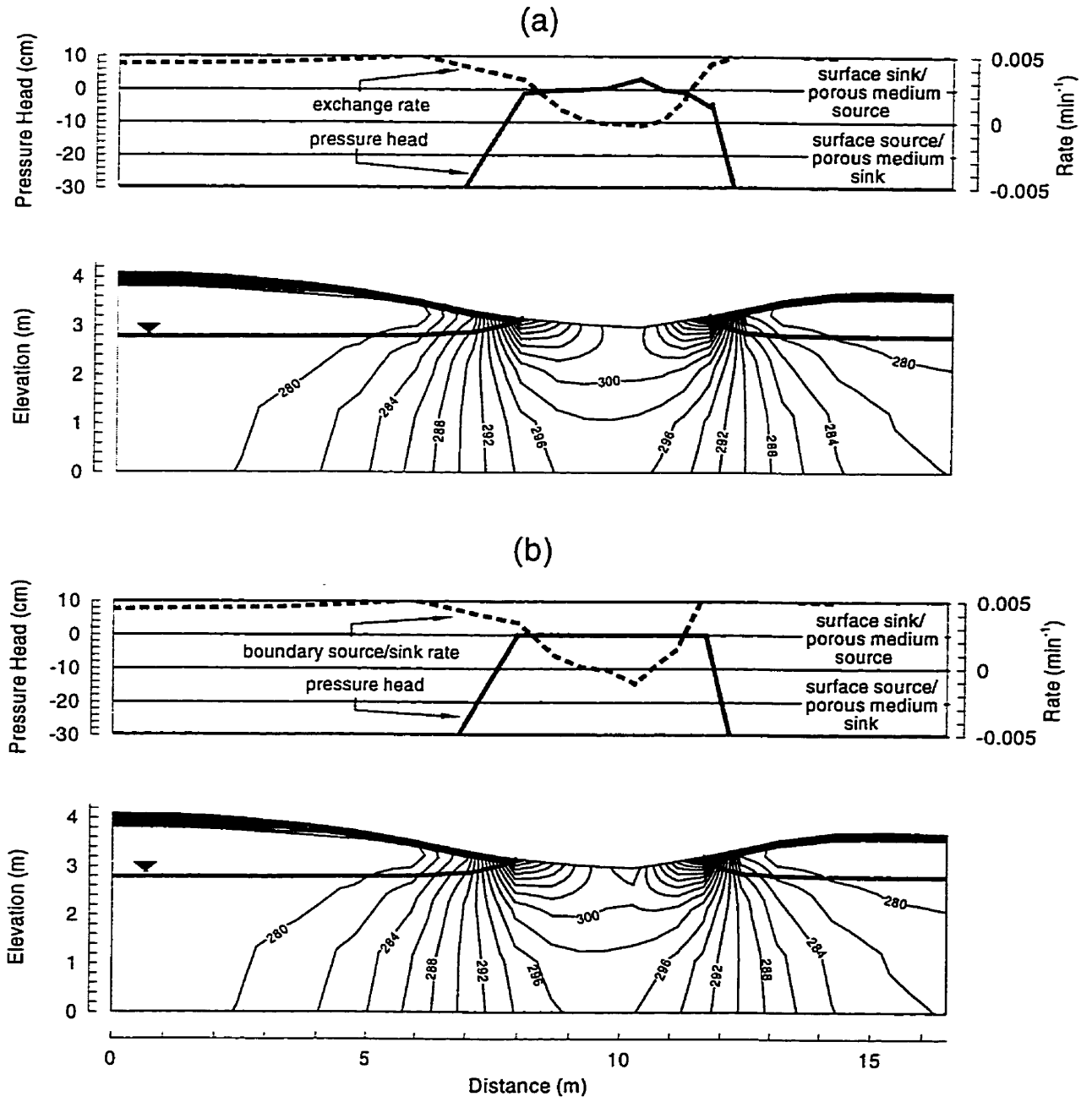

Figure 5-9. Pressure head and seepage flux at the land surface and total head (cm) distribution at 25 minutes along cross section (40 m) as predicted by (a) coupled and by (b) seepage solutions. Solution for initial hydraulic head of 278 cm and porous medium hydraulic conductivity of 1×10^{-5} m s^{-1}.

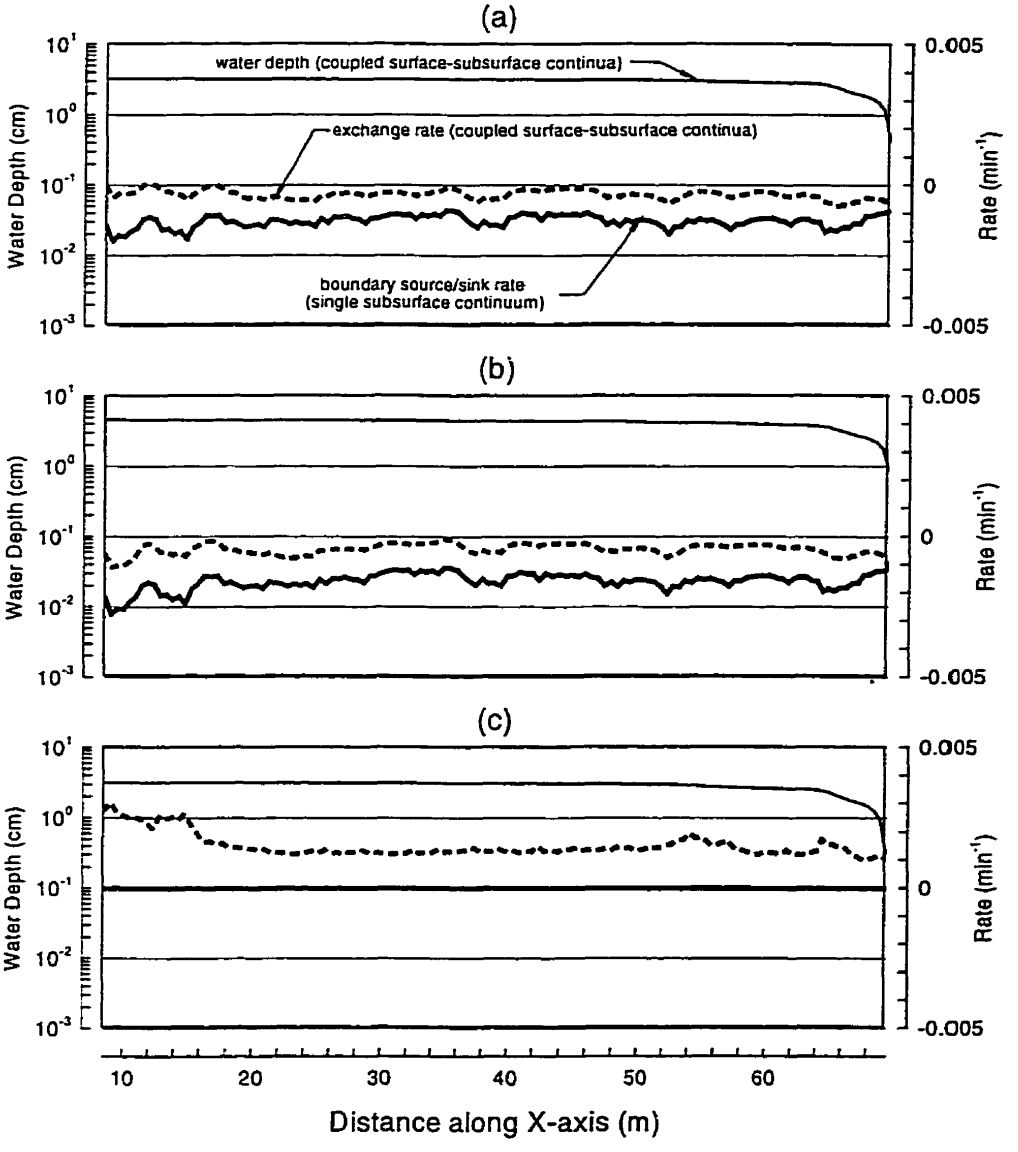

Figure 5-10. Graphs of surface water depth and rate of water exchange for first-order coupled surface-subsurface simulation and water seepage rate for single subsurface continuum with seepage faces at the land surface. Graphs correspond to a profile along the stream channel at times of (a) twenty-five minutes (b) fifty minutes, and (c) seventy-five minutes. Solution for initial hydraulic head of 278 cm and porous medium hydraulic conductivity of 1 x 10^{-5} m s^{-1}.

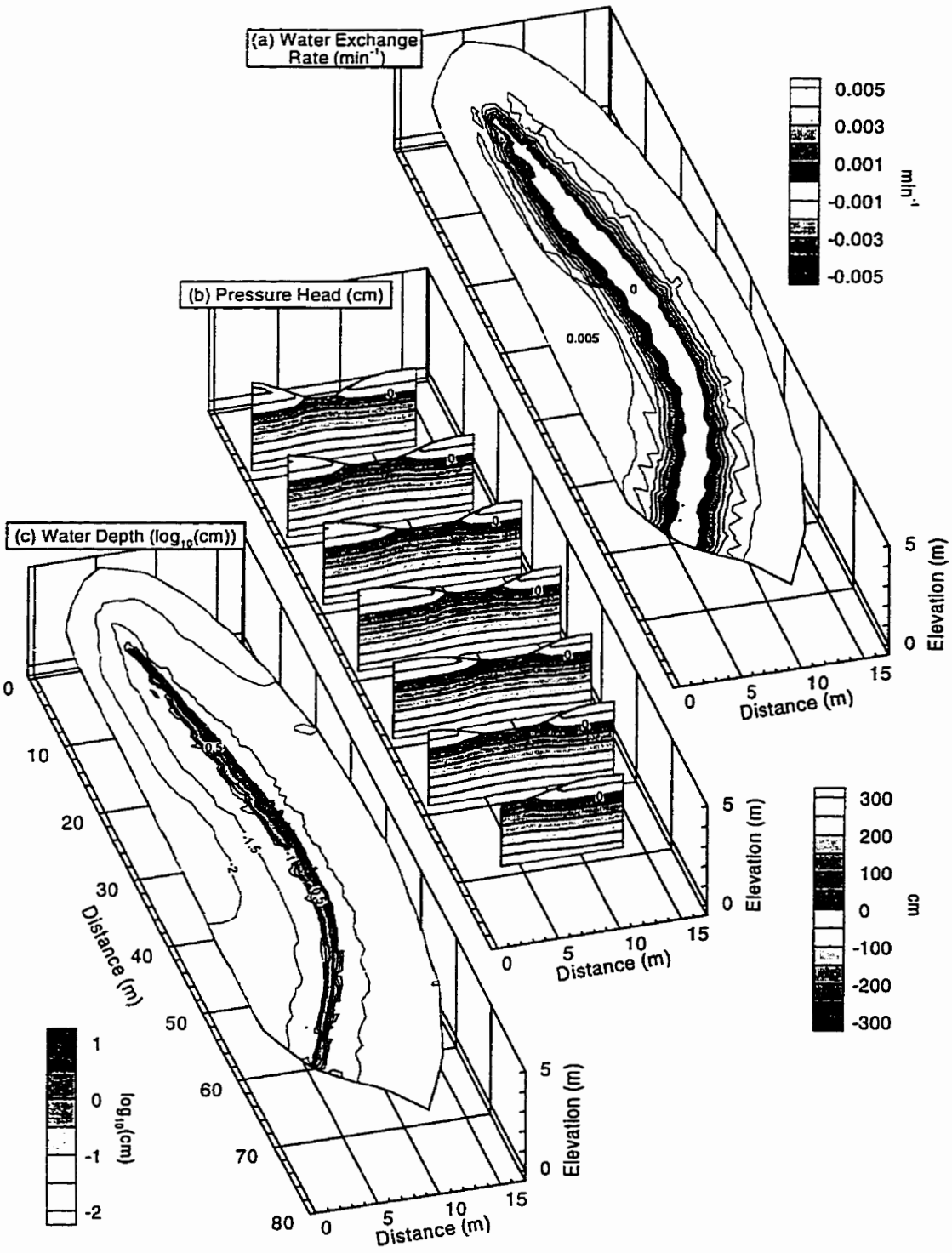

Figure 5-11. Summary of first-order-coupled flow solution at 50 minutes: (a) rate of water exchange between the porous medium and surface equations, (b) pressure head in porous medium, and (c) surface water depth. Solution for initial hydraulic head of 278 cm and porous medium hydraulic conductivity of 1 x 10^{-5} m s^{-1}.

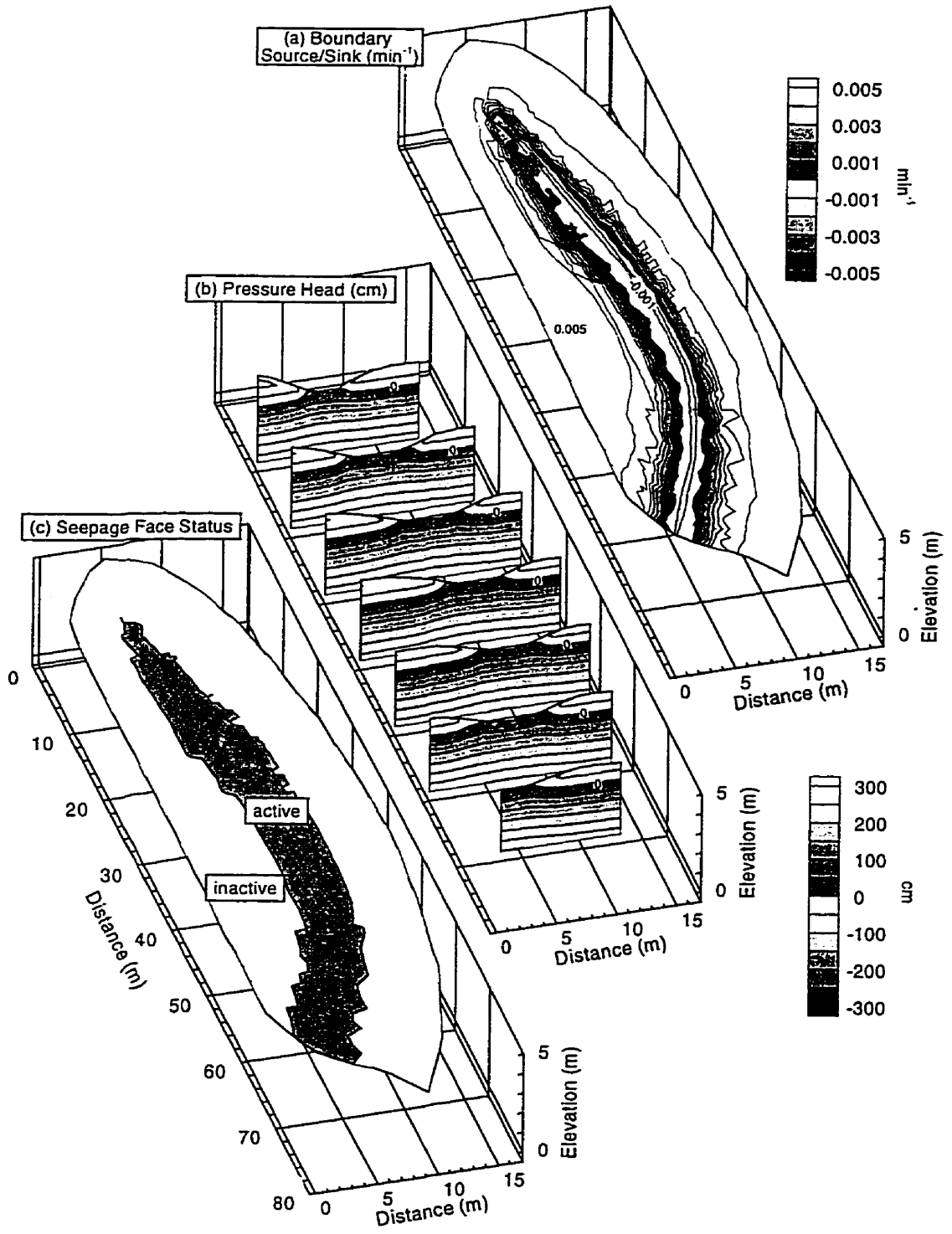

Figure 5-12. Summary of seepage-face solution at 50 minutes: (a) total boundary source/sink rate (b) pressure head in porous medium, and (c) seepage face status. Solution for initial hydraulic head of 278 cm and porous medium hydraulic conductivity of 1×10^{-5} m s^{-1}.

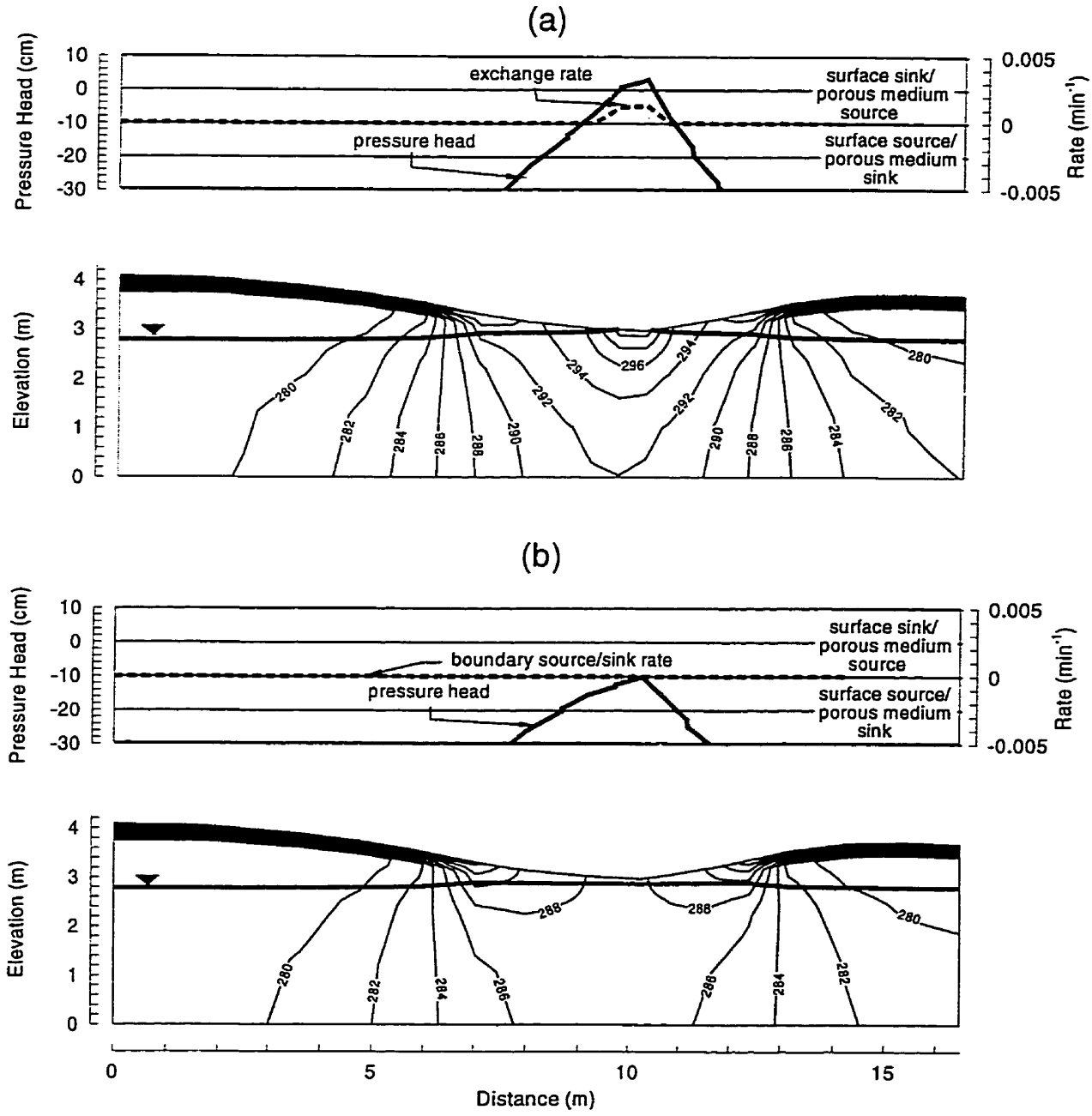

Figure 5-13. Pressure head and seepage flux at the land surface and total head distribution at 75 minutes along cross section (40 m) as predicted by (a) coupled and by (b) seepage solutions. Solution for initial hydraulic head of 278 cm and porous medium hydraulic conductivity of 1×10^{-5} m s^{-1}.

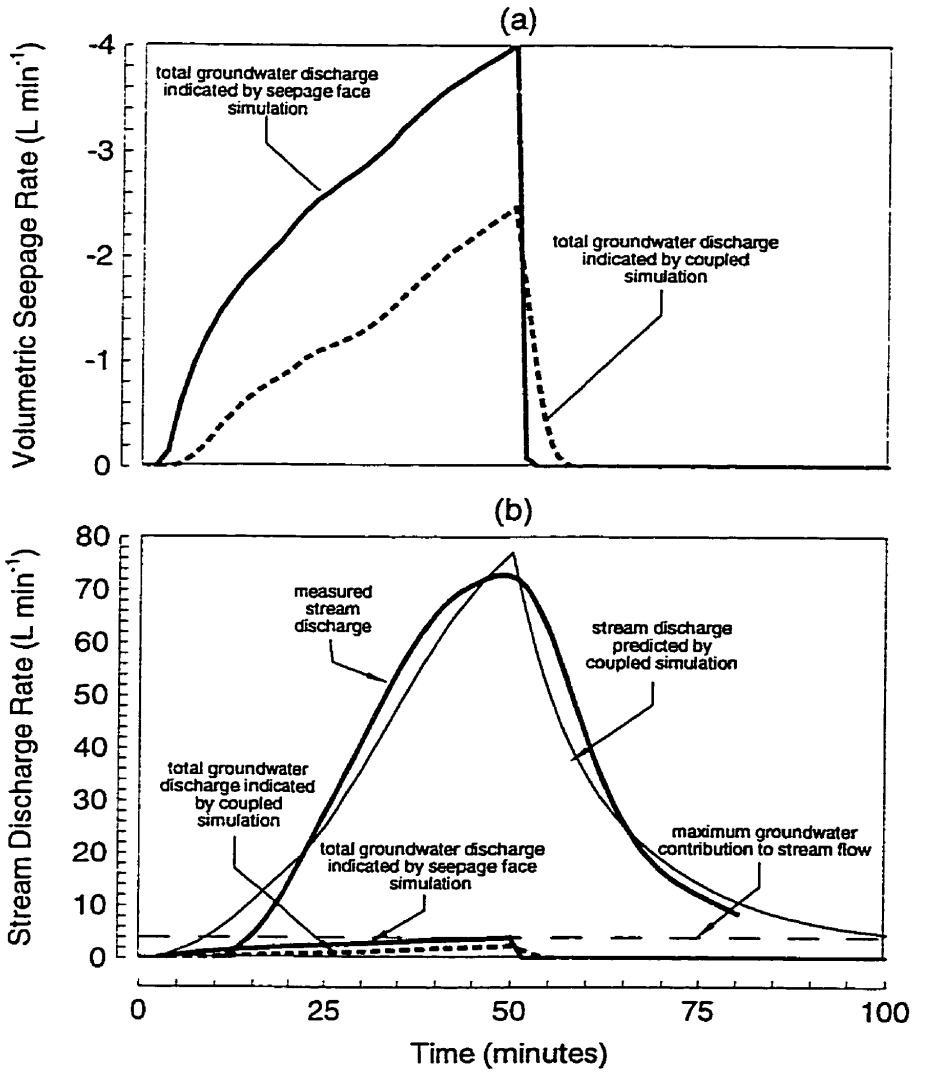

Figure 5-14. Comparison of simulated subsurface (pre-event) contributions to surface flow: (a) seepage rate for single-continuum simulation and exchange rates for coupled surface-subsurface solution with rainfall applied to surface equations; and (b) seepage and exchange rates relative to simulated surface discharge rate.

5.2.2 Tracer Transport and Hydrograph Separation

Abdul [1985] included a conservative tracer (bromide) in the artificial rainfall applied during the Borden field experiments, separating stream discharge into event (rainfall) and pre-event (groundwater) contributions based on the amount of tracer dilution. This section discusses the mechanisms by which conservative tracers originating in rainfall or below the land surface could arrive at the outflow boundary of the stream. Three tracers are utilized in the simulations, with the first (C_1) representing rainfall-derived bromide of *Abdul* [1985], and the second (C_2) and third (C_3) tracers representing water sources located above and below the initial water table (Figure 5-5).

Hydrograph separation theory indicates that the relative concentration of each individual tracer represents the fraction of discharge water originating in the corresponding source location [i.e. *Sklash and Farvolden*, 1979]. For the discrete transport equations, hydrograph separations can be written as:

$$Q_{C_1} = \sum_{i=1,nb} \frac{C_{1_i}}{C_{total_i}} Q_i \qquad Q_{C_2} = \sum_{i=1,nb} \frac{C_{2_i}}{C_{total_i}} Q_i \qquad Q_{C_3} = \sum_{i=1,nb} \frac{C_{3_i}}{C_{total_i}} Q_i \tag{5.1}$$

where nb = number of stream discharge boundary nodes, Q_i is the back-calculated stream boundary flux [$L^3\ T^{-1}$], and Q_{C_1}, Q_{C_2}, and Q_{C_3} represent the rainfall, groundwater and tension-saturated zone contributions, respectively, to total discharge. The sum of tension-saturated tracer and groundwater tracer represents the pre-event discharge component. Hydrograph separations assume that the dominant mixing and transport process is advection (i.e. plug flow or $|QC| \gg |\Lambda\xi|$).

As concentrations of the three simulated tracers were chosen to sum to unity at each point in space and time $\left(C_{total_i} = 1\right)$, the numerical values of the relative contributions are equivalent to the rate of tracer mass [$M\ T^{-1}$] exiting the system with the stream water:

$$M_{C_1} = \sum_{i=1,nb} C_{1_i} Q_i \qquad M_{C_2} = \sum_{i=1,nb} C_{2_i} Q_i \qquad M_{C_3} = \sum_{i=1,nb} C_{3_i} Q_i \tag{5.2}$$

Flux-weighted tracer concentrations [$M\ L^{-3}$] can be calculated as:

$$\overline{C_1} = \frac{M_{C_1}}{\sum_{i=1,nb} Q_i} \qquad \overline{C_2} = \frac{M_{C_2}}{\sum_{i=1,nb} Q_i} \qquad \overline{C_3} = \frac{M_{C_3}}{\sum_{i=1,nb} Q_i} \tag{5.3}$$

but are effected by discretization and numerical errors when water depths and fluxes are very small.

The laboratory-scale simulations of coupled surface-subsurface flow and transport (Section 4.7) indicate that simulated tracer concentrations in surface water are very sensitive to the selection of the discrete equations to which rainfall is applied. Application of rainfall to the porous medium equations causes mixing within the porous medium prior to discharge into the surface water, resulting in near-identical concentrations between the surface and subsurface continua. Application of rainfall to the surface equations eliminates such mixing, but required the use of an empirical coupling dispersivity to match observed concentrations during hydrograph rise and fall. Simulated concentrations are also sensitive to grid refinement adjacent to the land surface, with small vertical spacings required to resolve sharp concentration gradients and minimize the volume of porous medium with which the surface water interacts.

Figure 5-15 presents the distribution of rainfall tracer (C_1) in the surface water at fifty minutes, corresponding to both peak stream discharge and the end of the rainfall event. Tracer distributions for three rainfall boundary conditions are presented, as are tracer distributions arising from the assumption of concentration continuity between the surface water and underlying porous medium. Applying rainfall to the surface equations (Figure 5-15a) results in large concentrations of rainfall tracer along the topographic highs where water fluxes are oriented into the porous medium and water depths are negligible. Concentrations decrease along the stream axis due to discharge of water from the sand and increased diffusive exchange rates arising from larger saturations in both continua. Rainfall tracer concentrations arising from use of the dual rainfall boundary condition (Figure 5-15b), application of rainfall to the porous medium equations (Figure 5-15c), and concentration continuity assumption (Figure 5-15d) are very similar, differing noticeably only along the stream channel. In each case, however, rainfall tracer concentrations are approximately half those predicted by applying rainfall to the surface equations. Comparisons with observed patterns are

difficult, as the spatial distribution of the rainfall tracer is not available from the field experiment. *Abdul and Gillham* [1989] indicate, however, that measured concentrations of rainfall tracer in overland flow were lower adjacent to the stream. These lower concentrations were presented as evidence for the capillary fringe mechanism, with groundwater discharge acting to dilute rainfall tracer in the surface water. The coupled surface-subsurface flow simulation presented in Section 5.2.1 indicates, however, that very little discharge occurs in this region.

Figure 5-16 compares hydrograph separations based on measured stream discharge volumes and tracer concentrations (see equation (5.1)) with separations based on simulated stream discharge volumes and concentrations. Again, results for three rainfall boundary conditions and for continuity coupling are presented. Also indicated in Figure 5-16 are hydrograph separations generated by assuming negligible diffusive exchange of tracer mass between the surface and subsurface continua. Figure 5-17 presents the corresponding flux-weighted concentrations (see equation(5.3)). Separation of measured discharge using measured tracer concentrations indicates that up to 37% of stream flow is pre-event (i.e. water contained in the sand before the rainfall event). This conclusion is supported by the simulations if rainfall is applied to the surface equations and both advective and diffusive coupling are considered (Figure 5-16a). The corresponding flux-weighted concentrations (Figure 5-17a) contain considerable error at early time, however, as water depths at the outflow boundary are negligible. Neglecting diffusive coupling between continua (Figure 5-16b) predicts that stream discharge is dominated by water originating as rainfall, with rainfall tracer concentrations (Figure 5-17b) approaching unity at all times.

Application of rainfall to the discrete surface equations illustrates that interpretations of stream water origin are very sensitive to diffusive exchange of tracer mass between rapidly moving water on the land surface and slower water moving within the porous medium. The modifying effects of diffusive exchange are less evident if rainfall is applied to both the surface and porous medium equations using the dual algorithm (Figure 5-16c,d and Figure 5-17c,d) or only to the porous medium equations (Figure 5-16e,f and Figure 5-17e,f). Hydrograph separations for these simulations are not significantly different than that predicted by assuming concentration continuity

between continua (Figure 5-16g and Figure 5-17g). These hydrograph separations suggest that a large fraction of stream water is pre-event, in contradiction with the separation based on measured concentrations. While concentrations of rainfall tracer during the recession portion of the hydrograph are replicated best using the dual rainfall boundary condition (Figure 5-17c), peak concentrations are underestimated by about fifty percent, indicating that excessive mixing is being simulated.

Recall that, in the coupled flow simulation, seepage (groundwater discharge) accounted for less than five percent of stream discharge (Figure 5-14). If only advective coupling is considered (i.e. seepage or infiltration) then application of rainfall to the surface equations generates discharge with approximately the same relative contribution of event and pre-event water (i.e. about five percent). If diffusive coupling is also considered in the simulation, the simulated discharge separation corresponds well with the hydrograph separation based upon measured tracer concentrations. These simulations suggest that, while the capillary fringe is clearly responsible for the rapid hydrologic response observed by *Abdul* [1985], increased subsurface head gradients do not cause significant seepage. Rather, infiltration rates along the stream axis are reduced, with runoff formed by excess rainfall over a dynamic contributing area [e.g. *Hewlett and Hibbert*, 1967; *Dunne and Black*, 1970]. Rainfall tracer dilution occurs largely by diffusive processes as water flows over the land surface to the stream, over relatively short flow paths, and subsequently down the stream channel. The simulations indicate that tracer originating above the initial water table dominates the pre-event contribution. The following section presents an analysis of the sensitivity of hydrologic response, surface discharge volumes and hydrograph separations to hydraulic conductivity, Manning surface roughness, initial water table elevation, and surface topography.

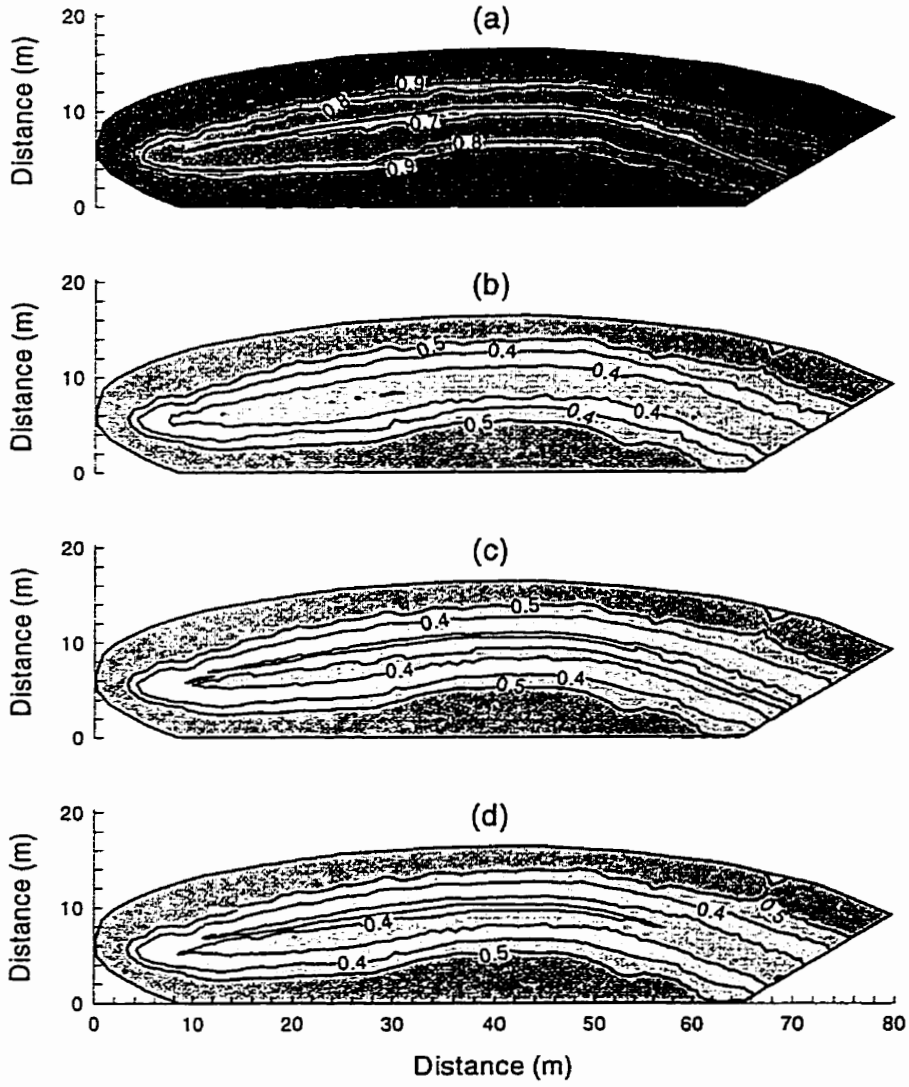

Figure 5-15. Distribution of rainfall tracer (C_1) in surface water at 50 minutes. Concentrations predicted by first-order-coupled simulations with both advective and diffusive coupling and (a) rainfall applied to surface equations, (b) rainfall applied to both the porous medium and surface equations using the dual rainfall algorithm, and (c) rainfall applied exclusively to the porous medium equations, and (d) tracer distributions resulting by assuming concentration continuity between the surface water and porous medium.

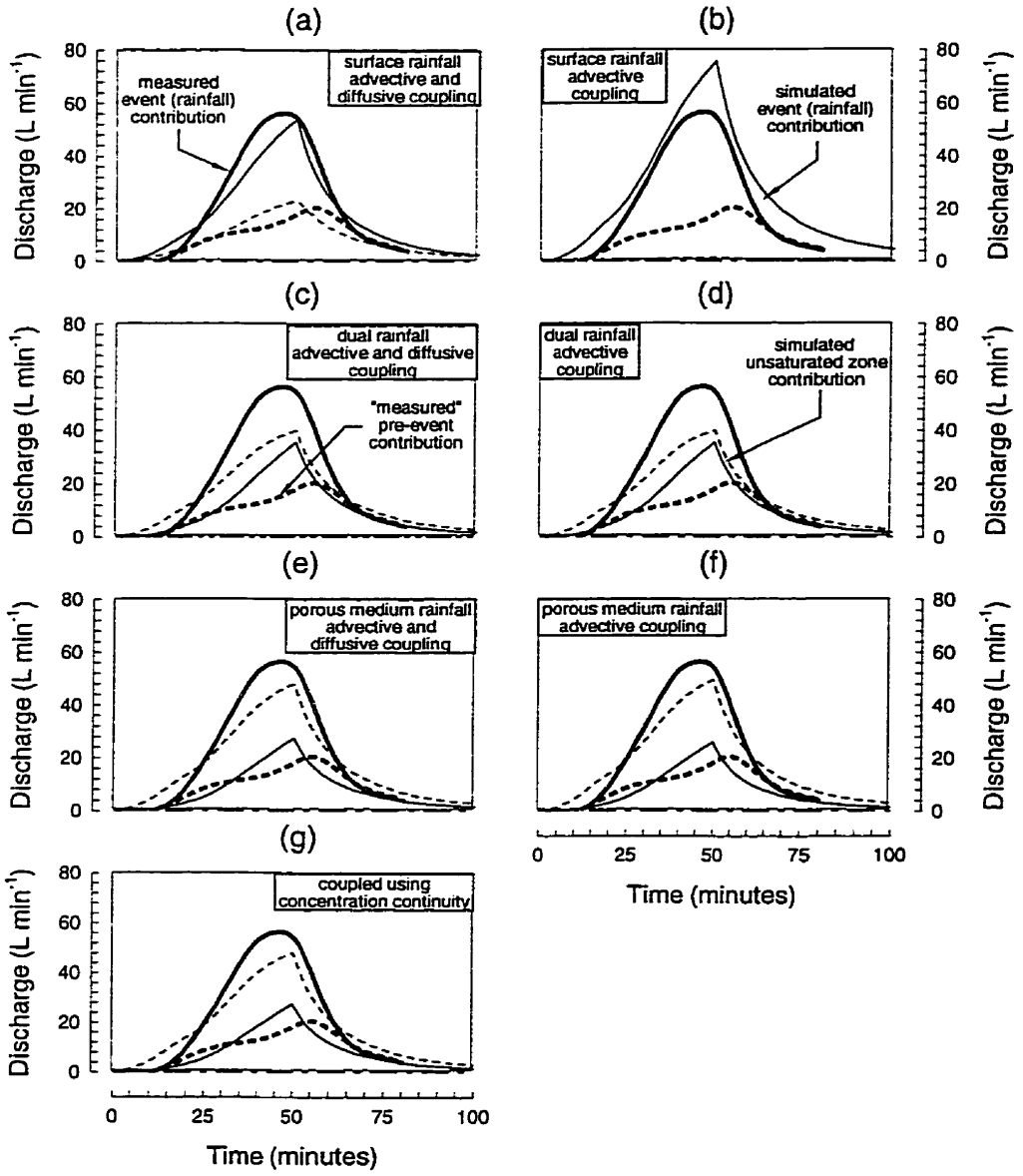

Figure 5-16. Comparison of measured and simulated hydrograph separations. Results for first-order-coupled simulations with rainfall applied to surface equations and (a) advective and diffusive coupling and (b) advective coupling only; rainfall applied to both the porous medium and surface equations using the dual rainfall algorithm with (c) advective and diffusive coupling and (d) advective coupling only; rainfall applied to porous medium equations with (e) advective and diffusive coupling and (f) advective coupling only; and (g) separation resulting from assuming concentration continuity between the surface water and porous medium.

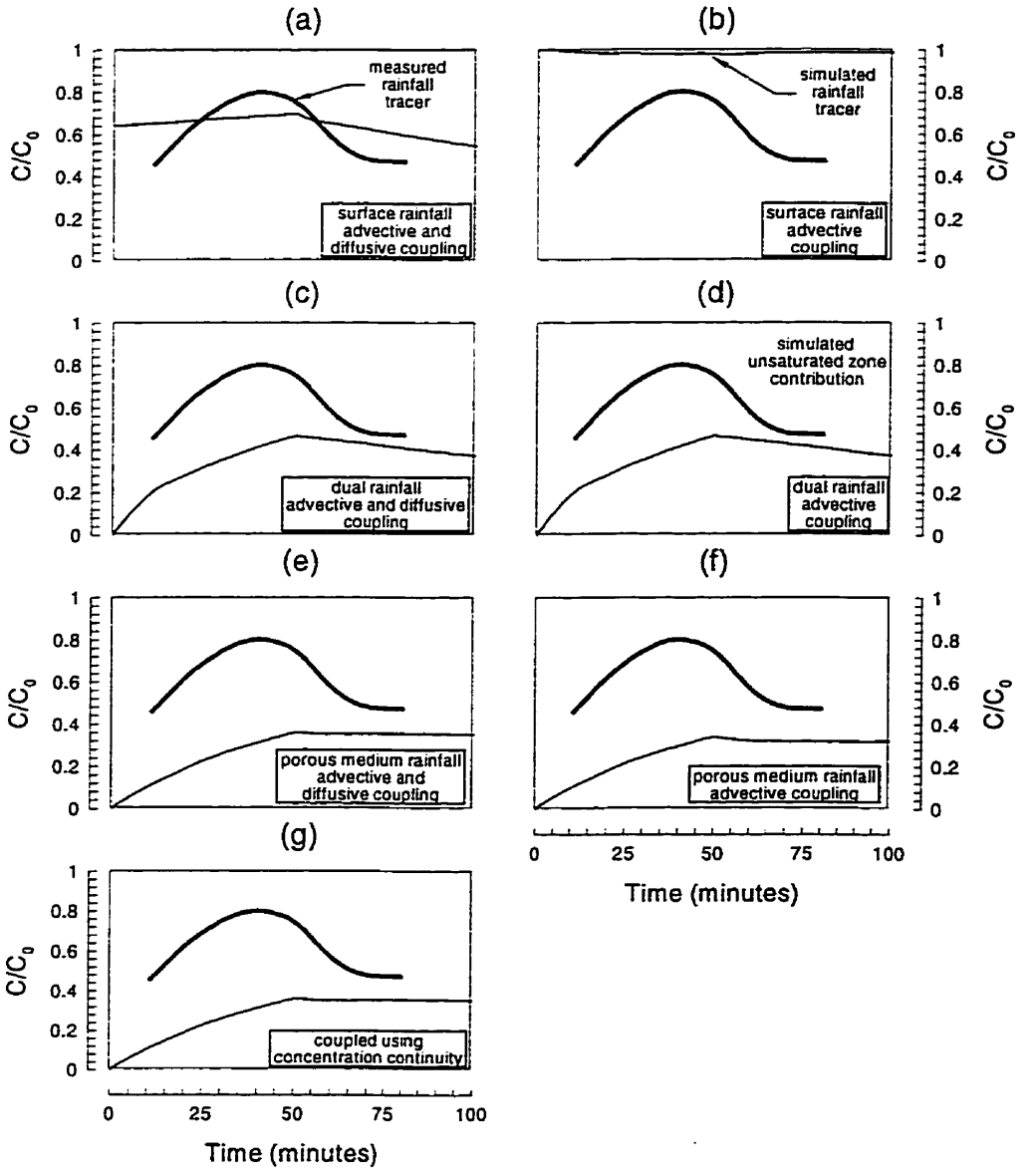

Figure 5-17. Comparison of measured and simulated rainfall tracer concentrations (C_t) in stream discharge water. Results for first-order-coupled simulations with rainfall applied to surface equations and (a) advective and diffusive coupling and (b) advective coupling only; rainfall applied to both the porous medium and surface equations using the dual rainfall algorithm with (c) advective and diffusive coupling and (d) advective coupling only; rainfall applied to porous medium equations with (e) advective and diffusive coupling and (f) advective coupling only; and (g) concentrations resulting from assuming continuity between the surface water and porous medium.

5.3 Sensitivity Analyses

Rainfall-runoff response is known from both field observations and theoretical studies [e.g. *Freeze*, 1972 a,b, 1974; *Beven*, 1977] to be a function of many interrelated parameters. The sections that follow attempt to isolate the effects on simulated hydrologic response of hydraulic conductivity, Manning roughness, initial water table elevation, and surface topography. The suite of simulations is restricted in scope to remain representative of the rainfall-runoff experiment performed by *Abdul* [1985], allowing the comparison of simulated and observed rainfall-runoff responses.

5.3.1 Hydraulic Conductivity and Manning Roughness

Although the hydraulic conductivity of the sandy aquifer is known to be spatially variable [e.g. *Sudicky*, 1986] a single lumped hydraulic conductivity value is utilized in this study. Consideration of spatial variability is beyond the scope of this work, with regard to comparison of the model results with those of the experiment, although the numerical model is fully capable of incorporating spatial variations in hydraulic conductivity. Reported values for the sandy aquifer vary from 5.0×10^{-6} m s^{-1} [*Abdul*, 1985] to 2.2×10^{-4} m s^{-1} [*Nwankwor et al.*, 1984]. The large values of *Nwankwor et al.* [1984] were determined from pump test analyses while the small values of *Abdul* [1985] were derived from flow net analyses. *MacFarlane et al.* [1983] reported hydraulic conductivity values ranging from 1×10^{-4} to 3×10^{-5} m s^{-1}. Figure 5-18 compares the measured stream hydrograph with simulated hydrographs generated with hydraulic conductivity values that span the reported range. No attempt was made to scale the relative permeability relationship as the low storage capacity of the capillary fringe dominates system response to rainfall. The thickness of the capillary fringe, therefore, is assumed constant. Topography is as indicated in Figure 5-1 and the initial water table elevation is 278 cm.

The best visual fit to the measured hydrograph (Figure 5-18a) occurs with a hydraulic conductivity of 1×10^{-5} m s^{-1}, with simulated stream discharges decreasing with increasing hydraulic conductivity. Figure 5-18b presents approximate contributing areas, calculated by dividing the ponded area of the land surface by the total surface area, and indicates that increased surface

discharge correlates with increased surface ponding and that surface ponding increases with decreasing porous medium hydraulic conductivity. Simulated groundwater discharge (seepage) rates (Figure 5-18c) are a significant fraction of surface water discharge for only the highest hydraulic conductivity values. Figure 5-19 presents hydraulic head contours and water table elevations at fifty minutes at the representative cross section for each of the hydraulic conductivities. Water table elevations coincide with the land surface along the stream axis and extend greater distances away from the stream with decreasing hydraulic conductivity. While decreasing hydraulic conductivity increases head gradients adjacent to the land surface, infiltration rates are reduced. The decreased infiltration rates promote overland flow due to rainfall excess, generating larger water depths in the stream and increasing stream discharge.

The Manning roughness coefficients utilized in the field-scale simulations are derived from literature sources [e.g. *Chow*, 1959] and calibrated values presented by *Abdul* [1985]. Two values are utilized, with roughness values typical of a sandy surface (0.03 s $m^{-1/3}$) assigned to the nodes along the stream channel and roughness values associated with short grass (0.3 s $m^{-1/3}$) assigned to nodes on the remainder of the land surface. The sensitivity of rainfall-runoff response to Manning surface roughness may be evaluated by assigning homogeneous roughness values to the entire land surface. Values utilized in the two simulations are equivalent to assuming the land surface is totally grass covered or sand covered. Porous medium hydraulic conductivity is assumed to be 1 x 10^{-5} m s^{-1} in all simulations.

Figure 5-20a compares stream discharges predicted with the two homogeneous Manning roughness values with the base case simulated discharge and with measured discharge. Stream discharge predicted using a roughness value of 0.03 s $m^{-1/3}$ is slightly greater than the base case discharge during hydrograph rise but is nearly identical during hydrograph recession. Both replicate observed stream discharges with reasonable accuracy. Assuming a roughness value of 0.3 s $m^{-1/3}$ underpredicts stream discharge until about seventy-five minutes, after which stream discharge is overpredicted. Simulated contributing areas (Figure 5-20b) for all roughness values are identical during hydrograph rise, with the larger roughness values indicating a slightly larger contributing area

during hydrograph recession. Simulated groundwater seepage (Figure 5-20c) is greatest if the land surface is assigned a homogenous roughness value of 0.3 s $m^{-1/3}$.

At a given surface water depth, velocities and water flux for the two Manning roughness values differ by an order of magnitude (see equations (2.21) and (3.6)). In the coupled rainfall-runoff simulations, therefore, water depths on the land surface are larger if Manning roughness is assumed to be 0.3 s $m^{-1/3}$. These larger water depths affect the distribution of pressure head in the porous medium at the land surface, subtly altering both the hydraulic response of the porous medium to rainfall and rate of groundwater seepage. Water depths and exchange rates at the top of the representative cross section are presented in Figure 5-21 at a time of fifty minutes for the base-case simulation and both surface roughness sensitivity analysis simulations. Also presented in Figure 5-21 are water table elevations and hydraulic head contours in the porous medium.

While water table and surface ponding locations correspond well in each case (see also the contributing area graphs in Figure 5-20b), water depths and exchange rates exhibit subtle differences. Relative to the base case (Figure 5-21a), water depths for the simulation conducted with a homogeneous roughness value of 0.03 s $m^{-1/3}$ (Figure 5-21b) are slightly smaller adjacent to the stream channel. The lower surface roughness results in increased overland flow velocities, hastening overland flow contributions to the stream channel, and increasing stream discharge during hydrograph rise. Hydrograph recessions are nearly identical, however, as surface flows are restricted to the stream channel itself after the end of the rainfall period. In contrast, assuming the entire land surface is grass-covered (Figure 5-21c) increases surface water depths both adjacent to and within the stream channel. While water depths are increased, the Manning-derived velocities are reduced, decreasing both the rate of overland flow contributions to the stream channel and discharges from the stream itself. Water depths during hydrograph recession are also larger, resulting in the slightly larger contributing area indicated in (Figure 5-20b). Further, the slight increases in overland flow depths alter subsurface gradients, increasing groundwater discharge (seepage) beside the stream channel.

This sensitivity analysis indicates that stream discharge rates and timing are intimately related to both the porous medium hydraulic conductivity and surface Manning roughness. Peak stream discharge volumes are influenced by the Manning roughness value assigned to nodes along the stream channel, with larger roughness values causing decreased peak flow rates and increased hydrograph tailing. Contributing areas are affected by small-scale topographic variations and hydraulic conductivity, which, in combination with the Manning roughness of the slopes, determine the amount of infiltration excess and the rate of overland flow contributions to the stream channel. Groundwater discharge (seepage) locations and rates are affected by both hydraulic conductivity and by the depth of surface ponding. Calibrated surface roughness and hydraulic conductivity values are likely to be related, as small-scale topographic variations are likely unknown at the field scale. The following section presents an analysis of rainfall-runoff response to the initial water table elevation and to topographic variability in and adjacent to the stream channel.

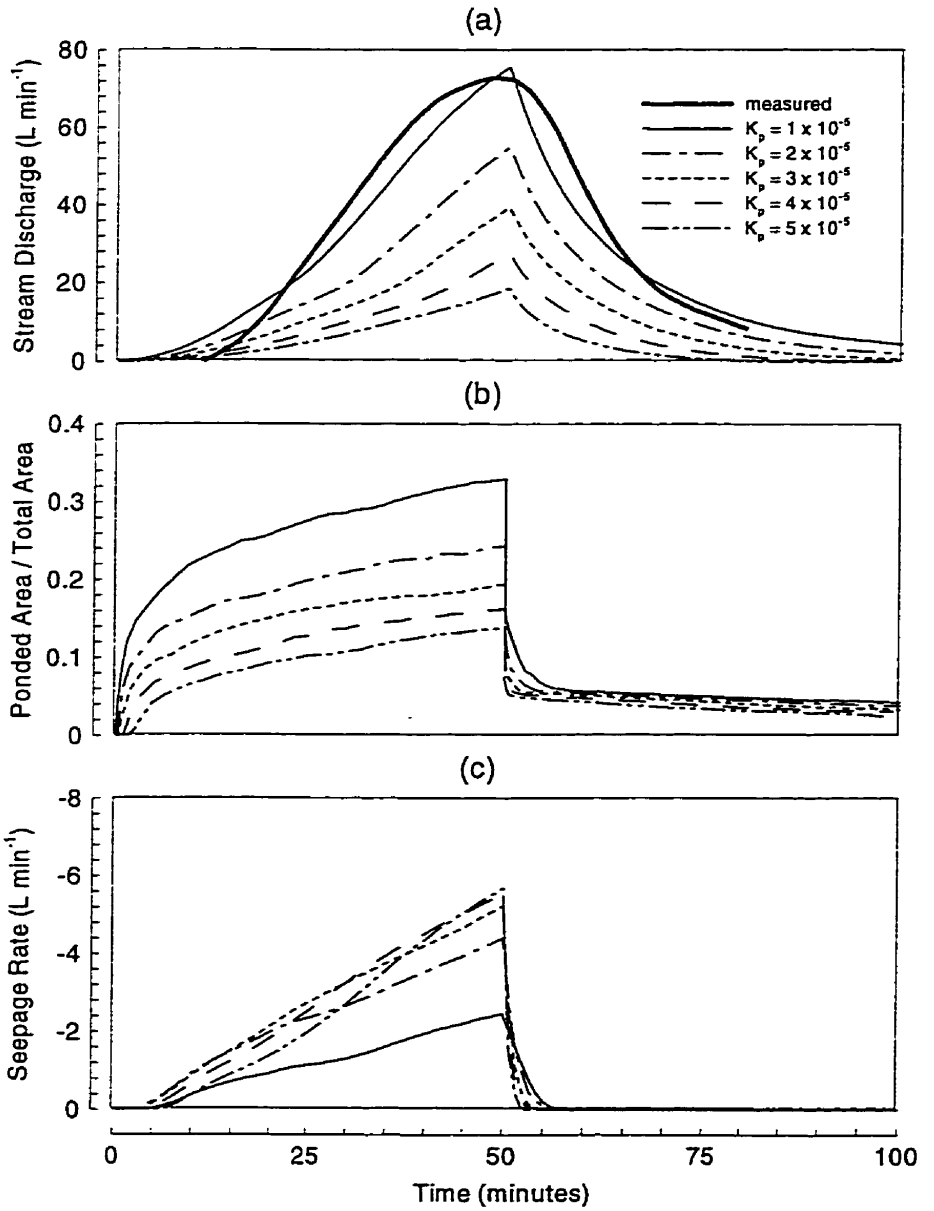

Figure 5-18. Illustration of rainfall-runoff sensitivity to porous medium hydraulic conductivity: (a) stream discharge, (b) relative contributing area, and (c) groundwater seepage. Solutions for initial hydraulic head of 278 cm and porous medium hydraulic conductivity equal to 5 x 10^{-5} m s^{-1}, 4 x 10^{-5} m s^{-1}, 3 x 10^{-5} m s^{-1}, 2 x 10^{-5} m s^{-1}, and 1 x 10^{-5} m s^{-1} (base case).

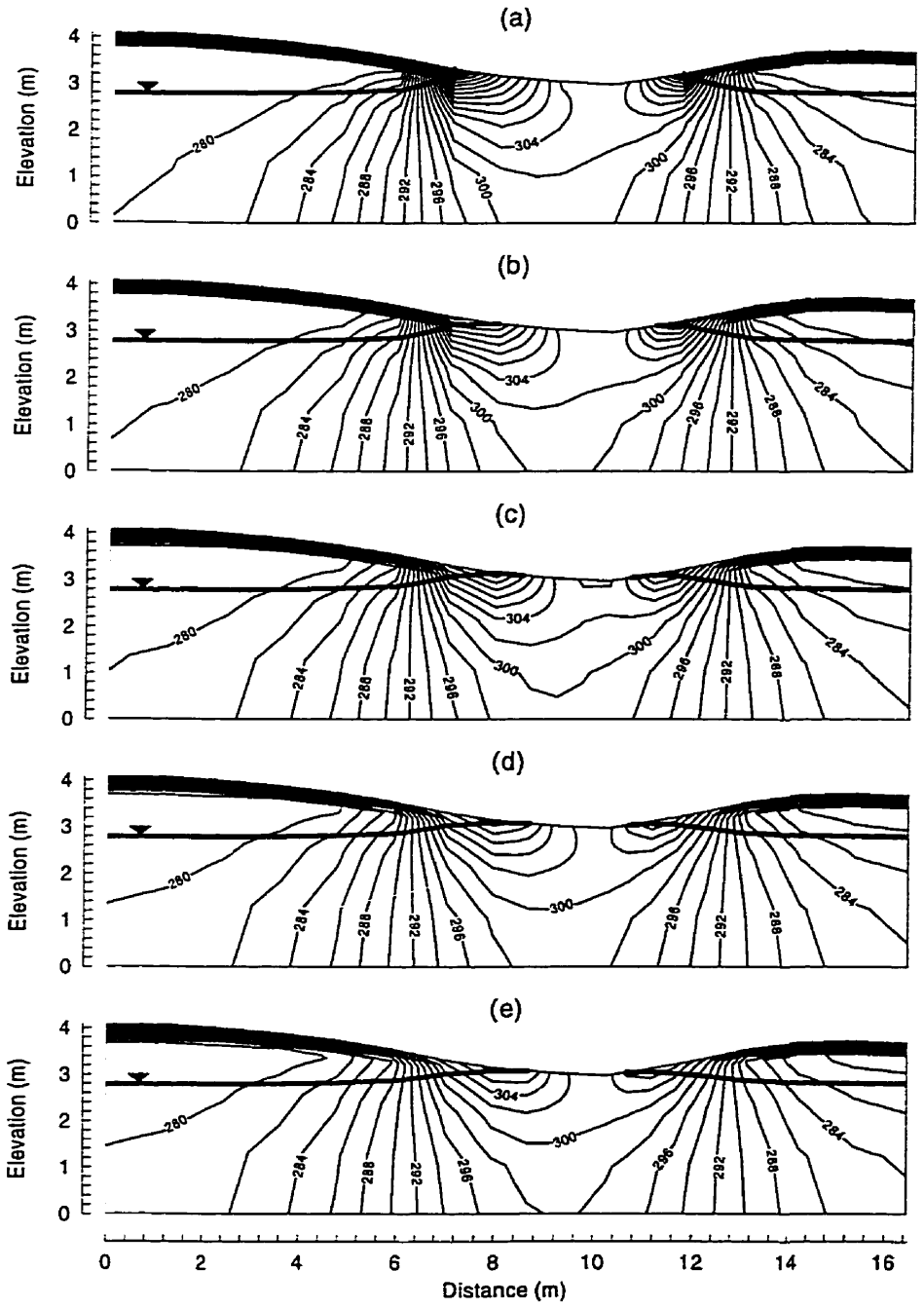

Figure 5-19. Total head and water table elevation along a representative cross section (x = 40 m) at 50 minutes for first-order-coupled simulations. Solutions for initial hydraulic head of 278 cm and porous medium hydraulic conductivity equal to (a) 1 x 10^{-5} m s^{-1} (base case), (b) 2 x 10^{-5} m s^{-1}, (c) 3 x 10^{-5} m s^{-1}, (d) 4 x 10^{-5} m s^{-1} and (e) 5 x 10^{-5} m s^{-1}.

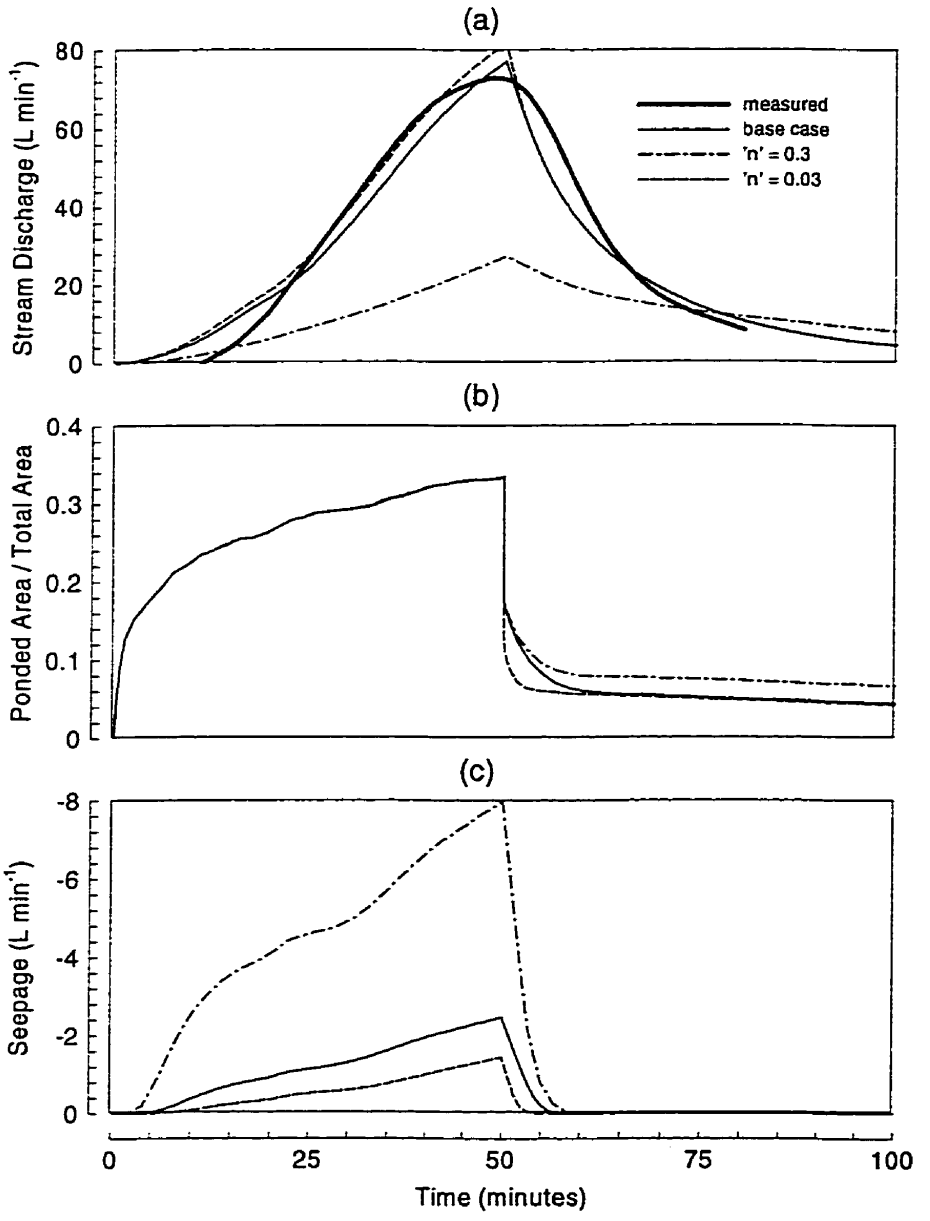

Figure 5-20. Illustration of rainfall-runoff sensitivity to Manning surface roughness: (a) stream discharge, (b) relative contributing area, and (c) groundwater seepage. Solutions for initial hydraulic head of 278 cm and porous medium hydraulic conductivity equal to 1 x 10^{-5} m/s.

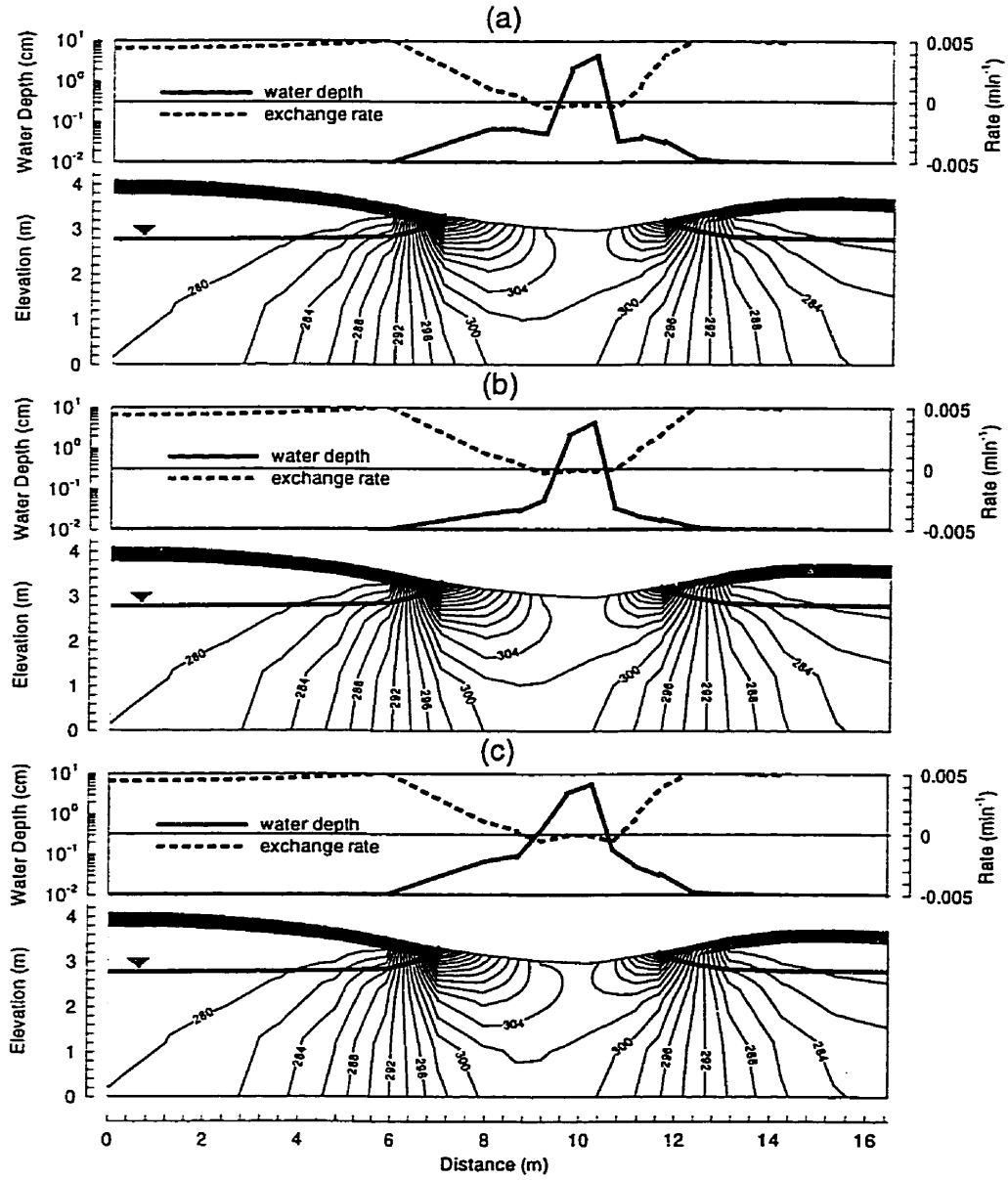

Figure 5-21. Water depths head and rates of water exchange at the land surface and total head distribution and water table elevations along a representative cross section (x = 40 m) at 50 minutes: (a) base case Manning roughness coefficients ('$n_{channel}$' = 0.03 s $m^{-1/3}$, 'n_{slopes}' = 0.3 s $m^{-1/3}$), (b) homogeneous roughness of 0.03 s $m^{-1/3}$, and (c) homogeneous roughness of 0.3 s $m^{-1/3}$. Solution for initial hydraulic head of 278 cm and porous medium hydraulic conductivity of 1 x 10^{-5} m s^{-1}.

5.3.2 Initial Water Table Elevation, Surface Topography, and Channel Incision

The topographic surface presented in Figure 5-1 was generated by digitizing and kriging elevation contours presented by *Abdul* [1985]. While an accurate survey of the field site was performed by Abdul, surveyed elevations were unavailable for use in the present study. As the contour spacing used in Abdul's figure was 0.5 meters, the discretized channel and slope configurations may not be representative of field conditions. Further, the reported stream length of 70 meters and slope of 0.17 % indicates a possible 12-centimeter range in stream bed elevation, which also may be poorly represented by the discretized topography. Finally, the initial water table is reported at a single location to lie about 22 cm below the base of the stream. Therefore, the configuration of the land surface in and adjacent to the stream and initial water table depths are both uncertain. This section presents a sensitivity analysis of rainfall-runoff response to initial water table elevations, small-scale topographic variability, and channel incision. Results for two hydraulic conductivities, 1×10^{-5} m s^{-1} and 5×10^{-5} m s^{-1}, are presented in each case. Unless explicitly stated to be different, parameters utilized in all simulations are presented in Table 5-1 and rainfall is applied to the surface equations.

The sensitivity of stream discharge to initial water table elevation is illustrated in Figure 5-22a and Figure 5-23a, for hydraulic conductivities of 1×10^{-5} m s^{-1} and 5×10^{-5} m s^{-1}, respectively. Initial water table elevations utilized are 281 cm, 284 cm and 287 cm. These elevations lie within the possible range of stream channel elevation (12 cm), and correspond to water table depths of 19 cm, 16 cm, and 13 cm below the stream channel. Simulated contributing areas and groundwater seepage rates are given in parts b and c of the respective figures. Seepage rates represent the maximum possible subsurface contributions to overland and stream flows, reflecting neither reinfiltration nor the water volume stored on the land surface.

Simulated surface discharge increases with increasing initial water table elevations. Such results are expected for both hydraulic conductivity values, as decreased storage capacity in topographic lows hastens the rapid capillary fringe water table response to rainfall, decreasing

infiltration rates and promoting the generation of overland flows due to rainfall excess. Maximum groundwater seepage contributions to the surface continuum also increase, as the rising water table raises maximum total heads at the toe of the slopes, promoting groundwater discharge at topographic lows. Higher water table elevations at the toe of the slopes also increase slightly the approximate contributing areas. Surface discharge increases much more rapidly than contributing area, however, illustrating the dynamic and intimate interaction of surface and subsurface hydrology. Contributing areas decline rapidly after rainfall ceases and approach a constant value for all initial conditions and both hydraulic conductivities. This final value, about 0.05, represents the approximate relative area of the discretized stream channel.

For the base-case topography (Figure 5-1) simulated surface water discharges provide a good visual match with measured values if the hydraulic conductivity of the porous medium is assigned a value of 1×10^{-5} m s^{-1}. This hydraulic conductivity value is on the low end of the reported range and is half an order of magnitude less than the value utilized in the simulations presented by *Abdul* [1985]. The sensitivity analysis of hydrologic response to initial conditions indicates that simulated discharges exceed measured if a hydraulic conductivity of 1×10^{-5} m s^{-1} is assumed. Conversely, if a hydraulic conductivity of 5×10^{-5} m s^{-1} is utilized, the resulting increased discharge approaches measured values, suggesting that calibrated hydraulic conductivities are intimately related to both the assumed initial conditions and discretized surface topography.

The effect of uncertainty in surface topography can be evaluated by slight modifications to the base-case finite element mesh. Four possible surface topographic variations are presented in Figure 5-26. Relative to the base case (Figure 5-1), the first two meshes, Grid 2 (Figure 5-26a) and Grid 3 (Figure 5-26b) were generated by decreasing the surface slopes adjacent to the stream. The second two meshes, Grid 4 (Figure 5-26c) and Grid 5 (Figure 5-26d) were generated by decreasing channel elevations by five and ten centimeters, respectively. Topography of the upland regions and adjacent slopes is unchanged in all meshes. Both of the incised channels, located about twelve and seventeen centimeters above the initial water table, respectively, are initially dry. Parameterization, initial conditions, and boundary conditions are identical to those utilized in Section 5.2.1. A single-

continuum seepage face simulation is also presented for Grid 5 to provide further clarification of the error introduced into the subsurface flow field and back-calculated seepage rates by neglecting ponding on the land surface.

Figure 5-27a presents hydrographs generated by simulating the Borden rainfall-runoff event using the four alternative topographic configurations and assuming a hydraulic conductivity of 1 x 10^{-5} m s^{-1}. Figure 5-27b presents approximate contributing areas, calculated by normalizing total ponded area at the end of each timestep by total area of the land surface. Figure 5-27c presents the volumetric rate of groundwater seepage (i.e. the sum of all negative water exchanges at the land surface), and total seepage rate if surface water effects on Grid 5 are neglected. Corresponding summary graphs for hydraulic conductivity of 5 x 10^{-5} m s^{-1} are presented in Figure 5-28.

For both hydraulic conductivities, simulated surface discharge increases in volume as surface elevation gradients adjacent to the stream decrease. While small increases in groundwater seepage are indicated, the relative contribution to stream discharge is small. Small seepage rates and increasing contributing areas during hydrograph rise both suggest that rainfall excess is the dominant runoff and streamflow generation mechanism. Contributing areas calculated during hydrograph recession are larger than those indicated with the base case grid, reflecting the relatively flat topography along the stream channel in grids two and three. Contributing areas decrease more rapidly for the higher hydraulic conductivity, as the infiltration of ponded surface water is more rapid. Peak discharge is overpredicted if a hydraulic conductivity value of 1 x 10^{-5} m s^{-1} is assumed, while assuming a hydraulic conductivity of 5 x 10^{-5} m s^{-1} underpredicts peak discharge.

Stream discharge decreases with increasing channel incision, with simulated discharge underpredicting observed values for both hydraulic conductivities. If a hydraulic conductivity of 1 x 10^{-5} m s^{-1} is assumed, groundwater seepage begins prior to the initiation of stream discharge and occurs at approximately twice the volumetric rate of the maximum values attained with the non-incised channels. Seepage rates decrease slightly as stream discharge is initiated, as increasing water depths within the stream channel raise the total head constraining the adjoining porous medium, decreasing both hydraulic gradients and the resulting water velocities. Decreased surface water

discharge results from greater infiltration adjacent to the stream, with rainfall entering the porous medium at the land surface and water originating in the subsurface discharging into the stream. Hydrograph recession is therefore extended, as groundwater discharge continues after the end of the rainfall event. The slow infiltration rate evident during hydrograph recession in the base case simulation (Figure 5-18) is replaced with slow drainage from the porous medium. For the more deeply incised channel (grid five), the greater influence of low subsurface water velocities is reflected in both decreased stream discharge during hydrograph rise and increased stream discharge during hydrograph recession. Little noticeable differences are evident in the graphs of contributing area, although areas are similar during hydrograph recession to previous simulations.

In contrast with simulations performed with a hydraulic conductivity of 1×10^{-5} m s^{-1}, assuming a value of 5×10^{-5} m s^{-1} in the incised-channel simulations indicates that, during hydrograph rise, discharge increases slightly with increasing channel incision (Figure 5-28a). Calculated contributing areas (Figure 5-28c) are lower for the more deeply incised channel, suggesting that subsurface flow paths are providing the additional streamflow. Contributing areas for both incised-channel simulations rapidly attain values associated with the stream channel during hydrograph rise, increasing after about fifteen minutes when the storage volume within the stream channel is filled. Contributing areas decrease rapidly after the end of the rainfall event as hydraulic heads decline and overland flow ceases adjacent to the stream. Discharge from both incised channel simulations underpredicts measured values if a hydraulic conductivity of 5×10^{-5} m s^{-1} is assumed.

Examination of the calculated seepage rates (Figure 5-28c) indicates that total seepage exceeds stream discharge if a hydraulic conductivity of 5×10^{-5} m s^{-1} is assumed. Seepage values may not be representative of potential stream flows, therefore, as they do not consider storage on the land surface or possible reinfiltration from ponded surface water sources. Of interest, however, is the back-calculated boundary flux derived by imposing seepage face conditions in the incised channel simulations. As indicated in Section 5.2.1, seepage face solutions, by neglecting the additional head constraint induced by surface ponding, will over-estimate groundwater discharge. The error is small if hydraulic conductivities of 1×10^{-5} m s^{-1} is assumed, as the coupled simulations

indicate infiltration-excess overland flow is the dominant streamflow generation mechanism. As subsurface flow paths become more dominant with increasing hydraulic conductivity, however, the effects of stream depth constraints on hydraulic head in the adjacent porous medium become more significant. Indeed, the seepage face solution prediction of groundwater discharge is nearly twice that of the coupled solution if a hydraulic conductivity of 5×10^{-5} m s^{-1} is utilized in the incised channel simulations. *Abdul's* [1985] hydrologic response simulations may be inaccurate, therefore, as he explicitly coupled such seepage to a kinematic streamflow routing model, neglecting the effect of surface ponding on pressure heads adjacent to the stream channel. Consideration of surface water ponding was also neglected in the flow net analysis presented by *Abdul* [1985] and *Abdul and Gillham* [1989] as evidence in support of enhanced groundwater discharge due to the rapid response of the capillary fringe.

Recall, however, that the spatial and temporal distribution of surface water is unknown from the field experiment, making specific comparisons difficult. The sensitivity analysis indicates that the dominance of surface or subsurface flowpaths for a single rainfall event is affected by assumed initial conditions and discretized topography, both of which are poorly defined. Total head contours and water table elevations are presented for each of the four grids at fifty minutes in Figure 5-29 and Figure 5-30 for hydraulic conductivities of 1×10^{-5} m s^{-1} and 5×10^{-5} m s^{-1}, respectively. Fifty minutes corresponds to both the end of the rainfall event and peak surface water discharge. Slight variations in topography in combination with bulk hydraulic conductivity variations of half an order of magnitude are shown to generate significantly different head distributions in the porous medium. Water table elevations and subsurface hydraulic head gradients have a large effect on flow pathways and stream discharge volumes. The following section presents and discusses hydrograph separations using concentrations of three conservative tracers in stream discharge.

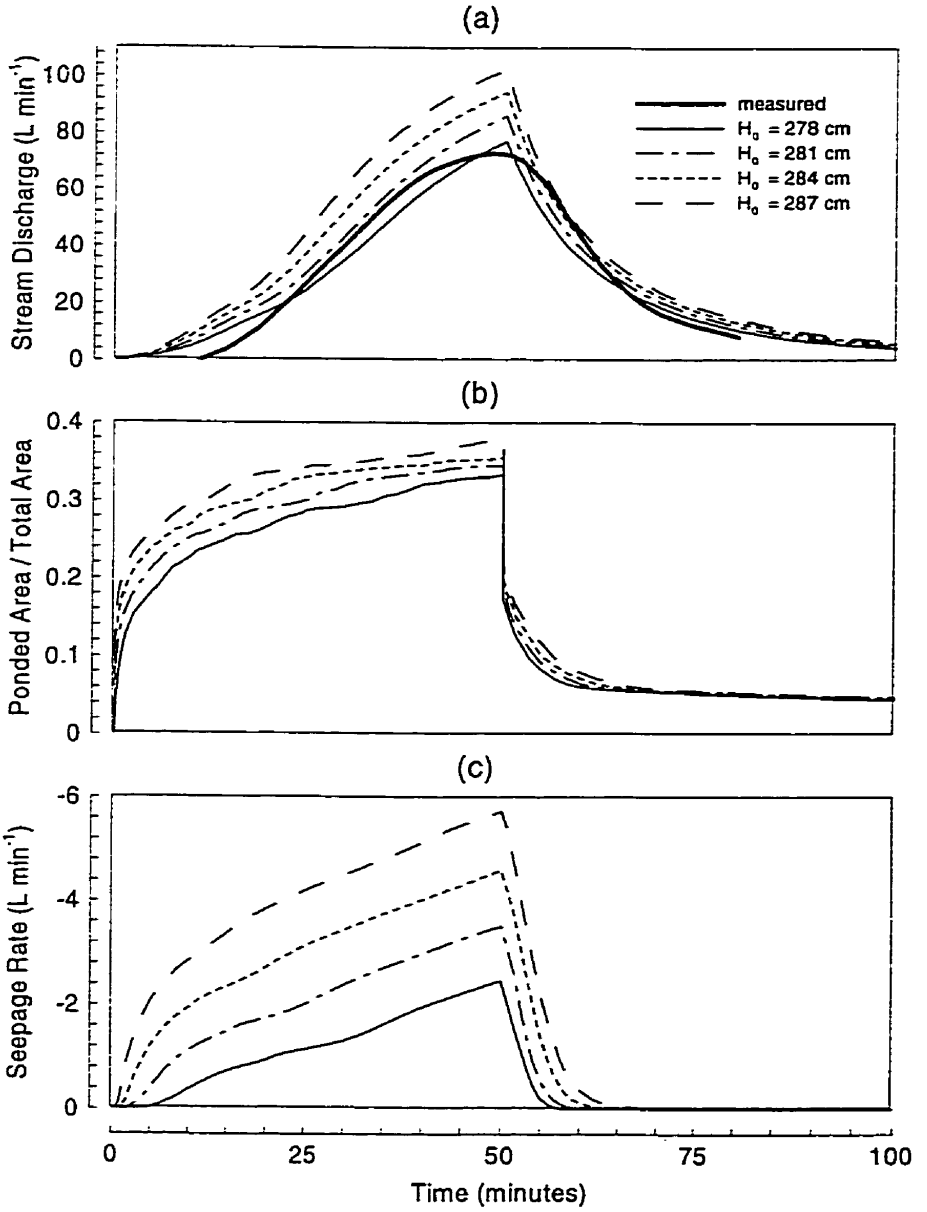

Figure 5-22. Illustration of rainfall-runoff sensitivity to initial water table elevation: (a) stream discharge, (b) relative contributing area, and (c) groundwater seepage. Solutions for porous medium hydraulic conductivity equal to 1 x 10^{-5} m/s.

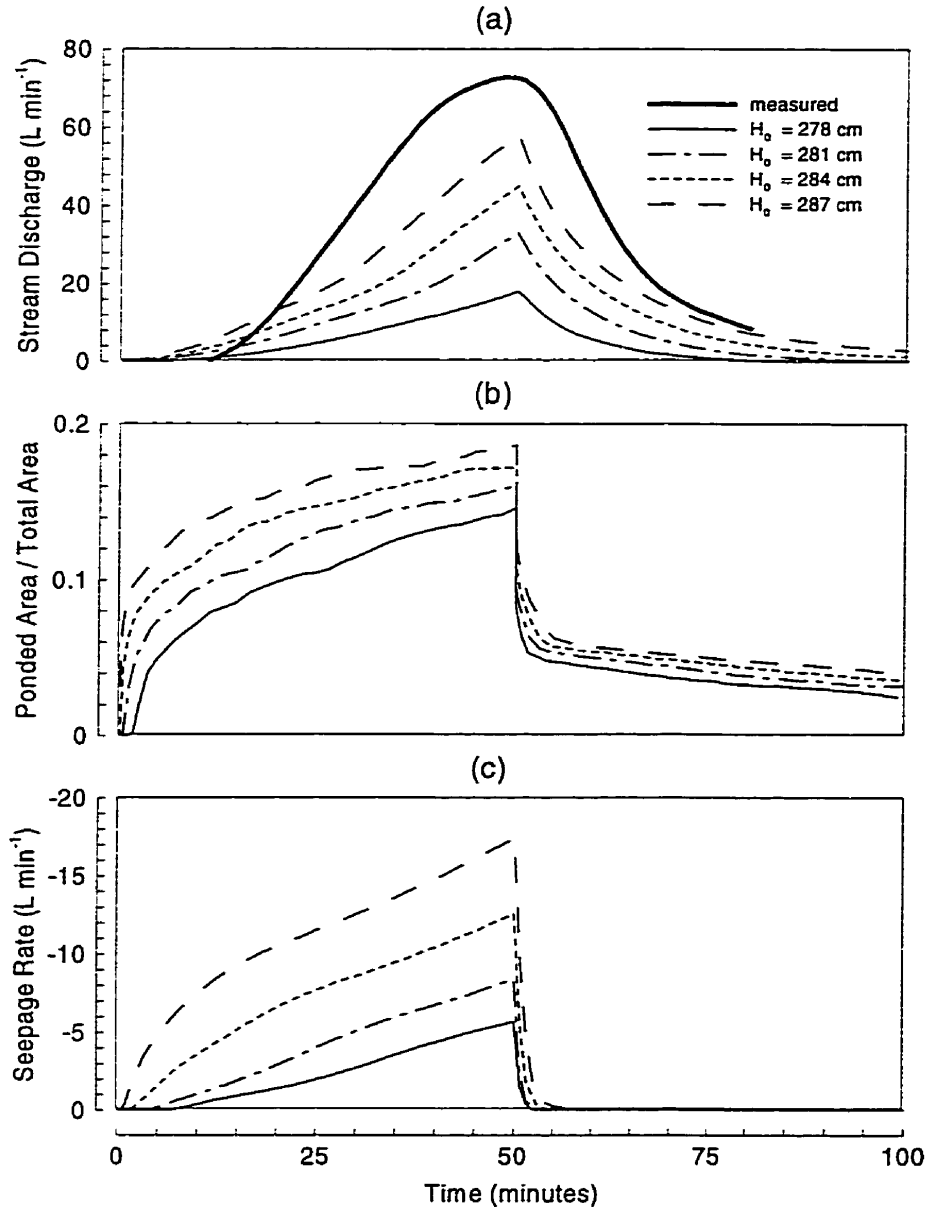

Figure 5-23. Illustration of solution sensitivity to initial water table elevation: (a) stream discharge, (b) relative contributing area, and (c) groundwater seepage. Solutions for porous medium hydraulic conductivity equal to 5 x 10^{-5} m/s.

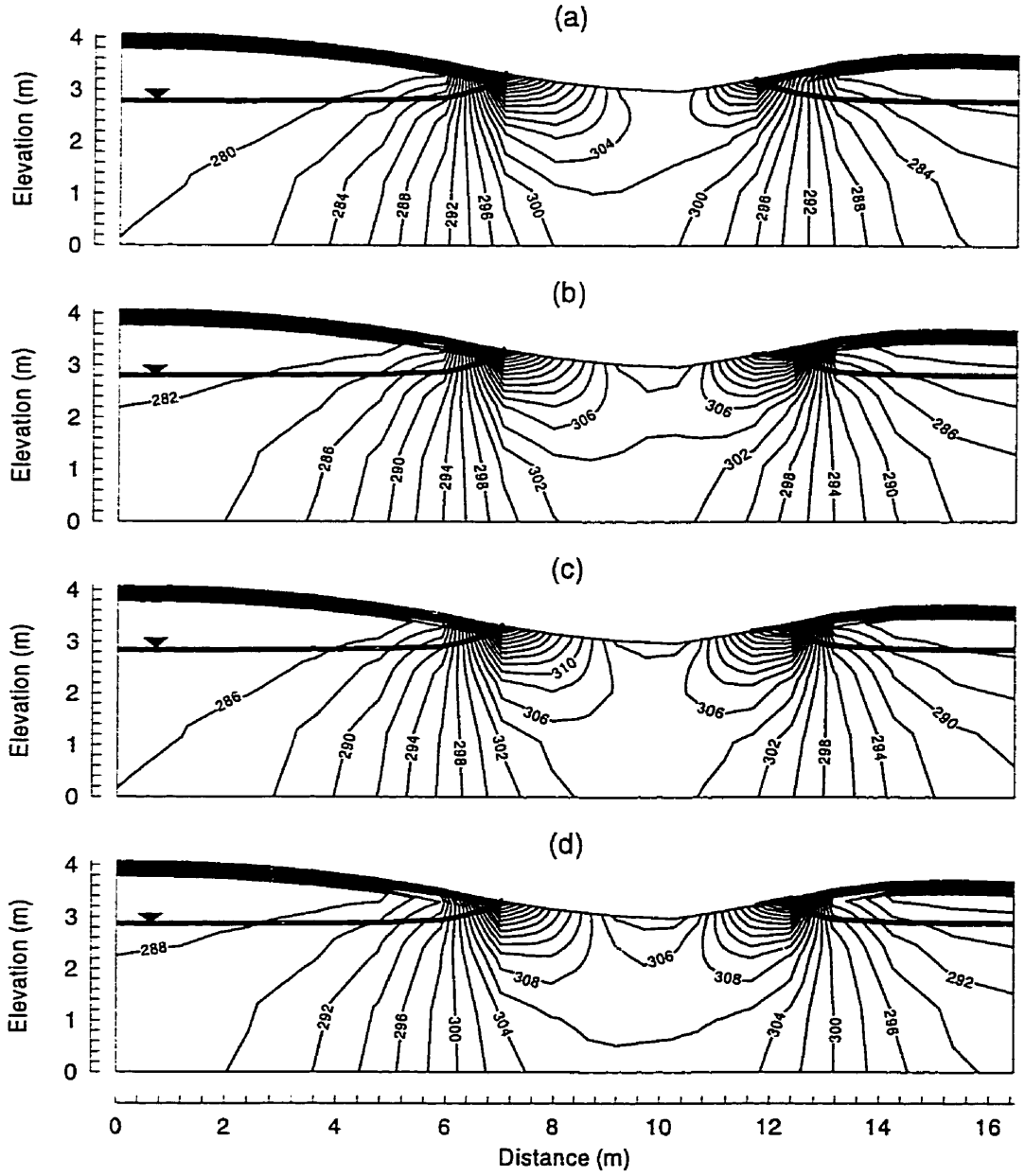

Figure 5-24. Total head distributions and water table elevations along a representative cross section (x = 40 m) at 50 minutes for initial water table elevations of (a) 278 cm (base case), (b) 281 cm, (c) 284 cm, and (d) 287 cm. Solutions for porous medium hydraulic conductivity equal to 1 x 10^{-5} m/s.

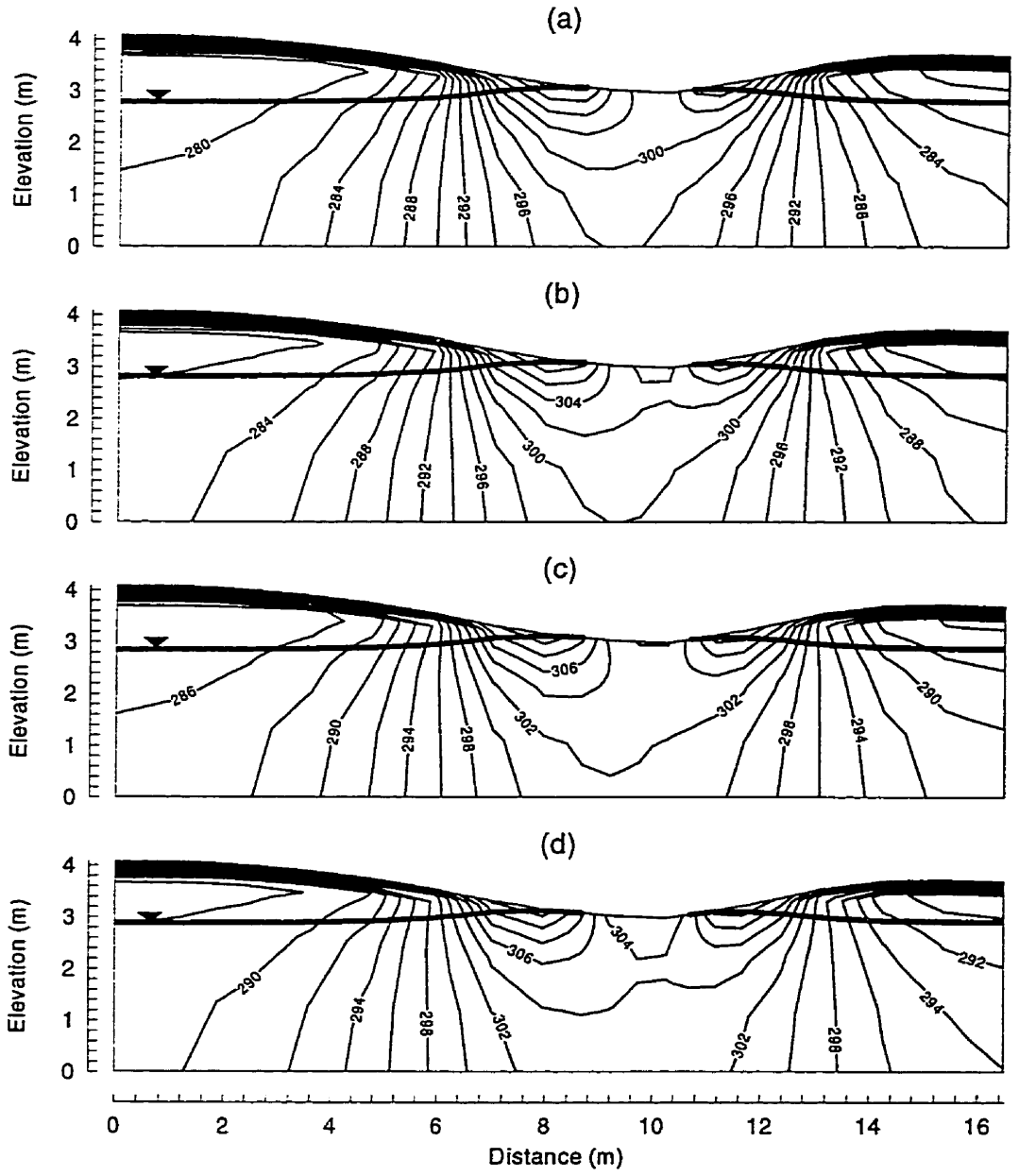

Figure 5-25. Total head distributions and water table elevations along a representative cross section (x = 40 m) at 50 minutes for initial water table elevations of (a) 278 cm (base case), (b) 281 cm, (c) 284 cm, and (d) 287 cm. Solutions for porous medium hydraulic conductivity equal to 5 x 10^{-5} m/s.

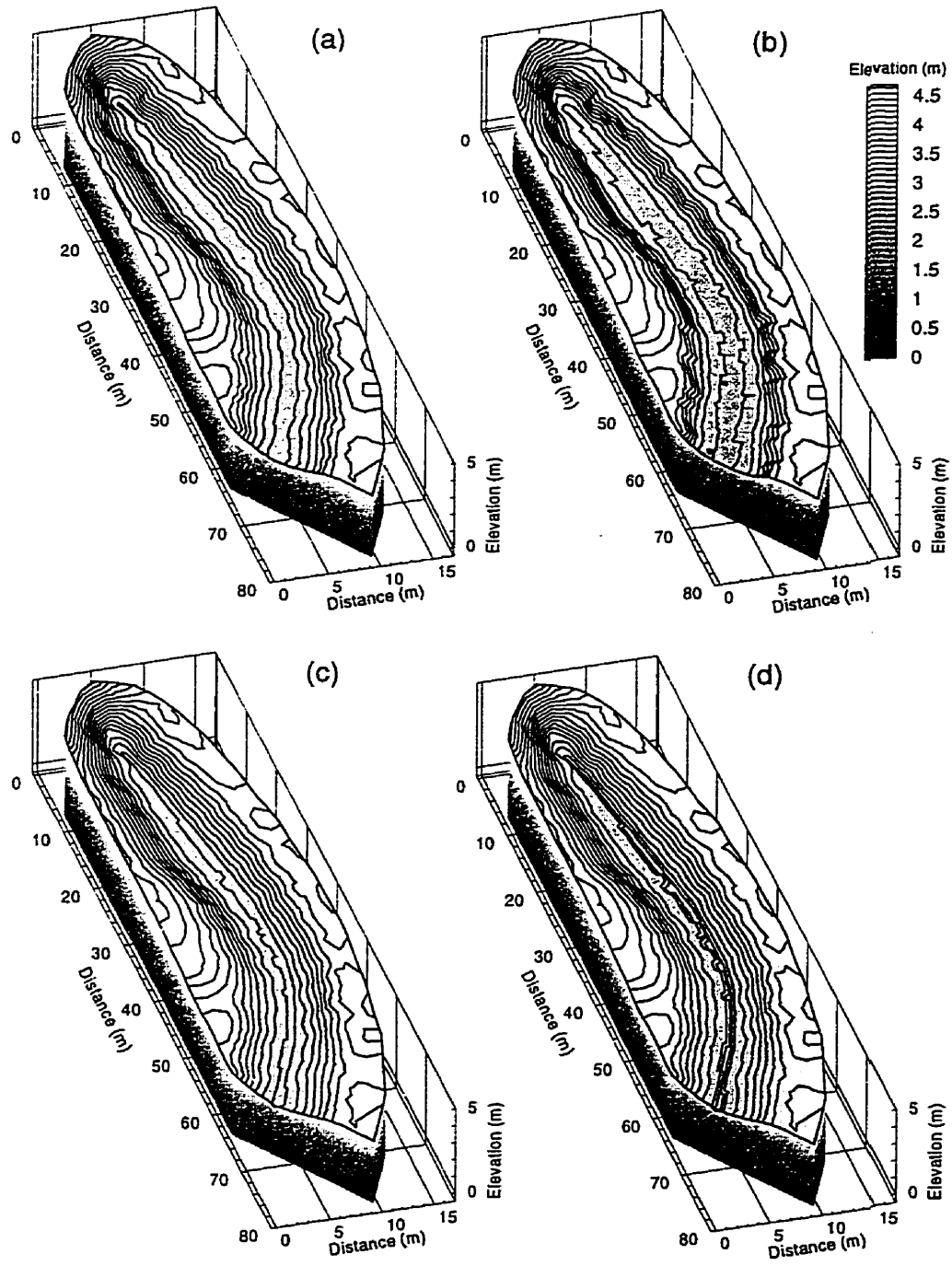

Figure 5-26. Surface elevation contours of four finite element meshes utilized to investigate the effect of topography on hydrologic response and discharge separation. Decreasing elevation gradient for (a) grid two and (b) grid three, and increasing channel incision for (c) grid four and (d) grid five.

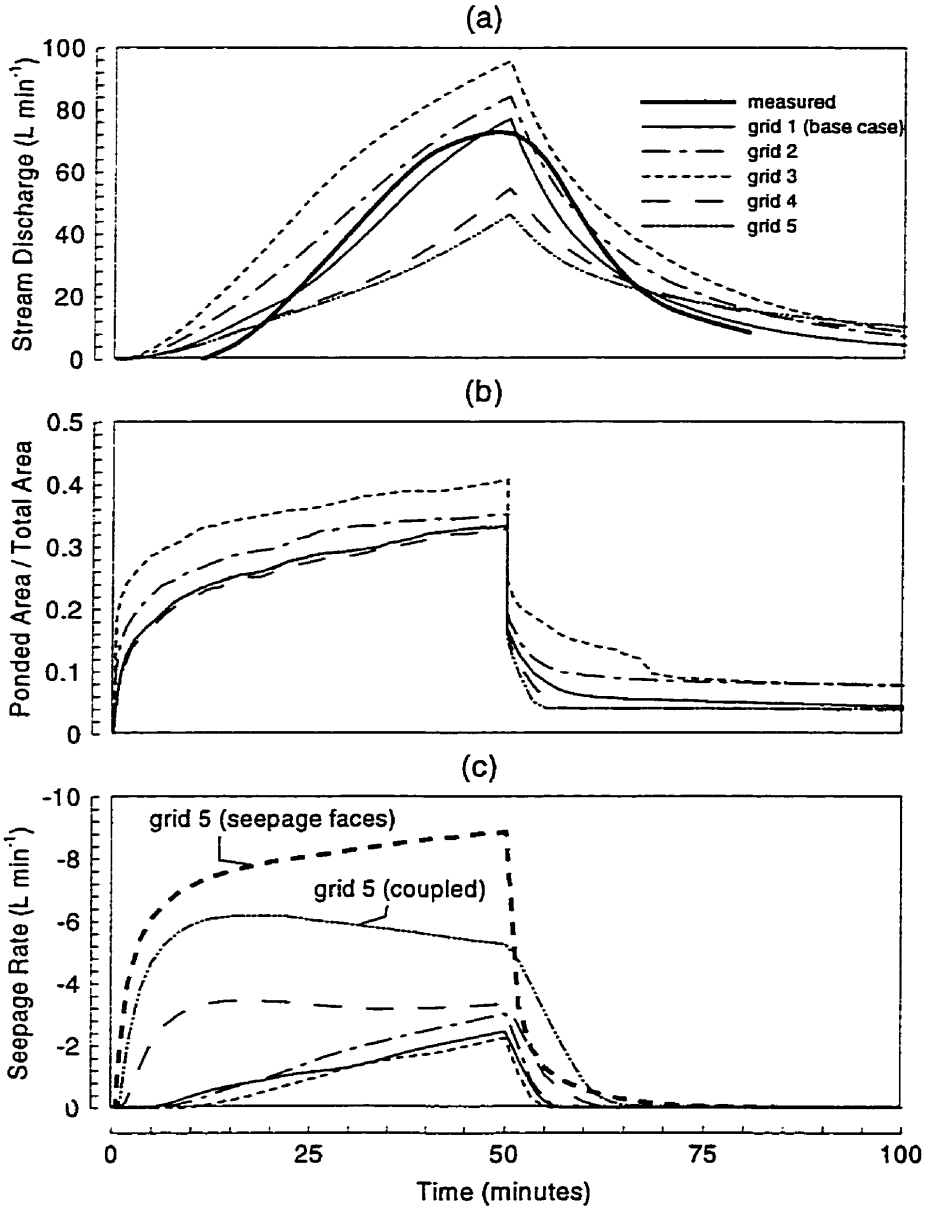

Figure 5-27. Illustration of discharge sensitivity to topography and the degree of channel incision: (a) stream discharge, (b) contributing area and (c) groundwater seepage. Solutions for initial hydraulic head of 278 cm and porous medium hydraulic conductivity equal to 1 x 10^{-5} m/s.

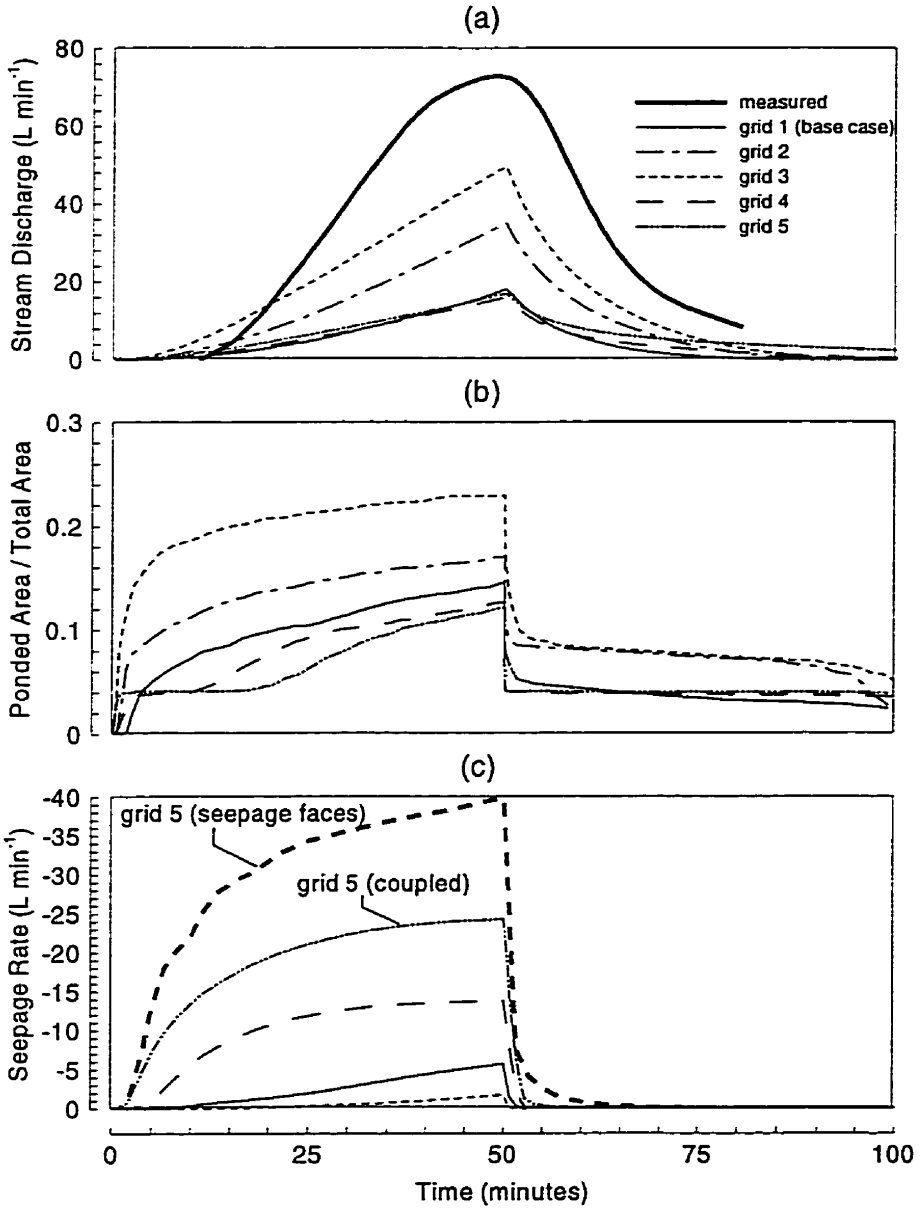

Figure 5-28. Illustration of discharge sensitivity to topography and the degree of channel incision: (a) stream discharge, (b) contributing area and (c) groundwater seepage. Solutions for initial hydraulic head of 278 cm and porous medium hydraulic conductivity equal to 5 x 10^{-5} m/s.

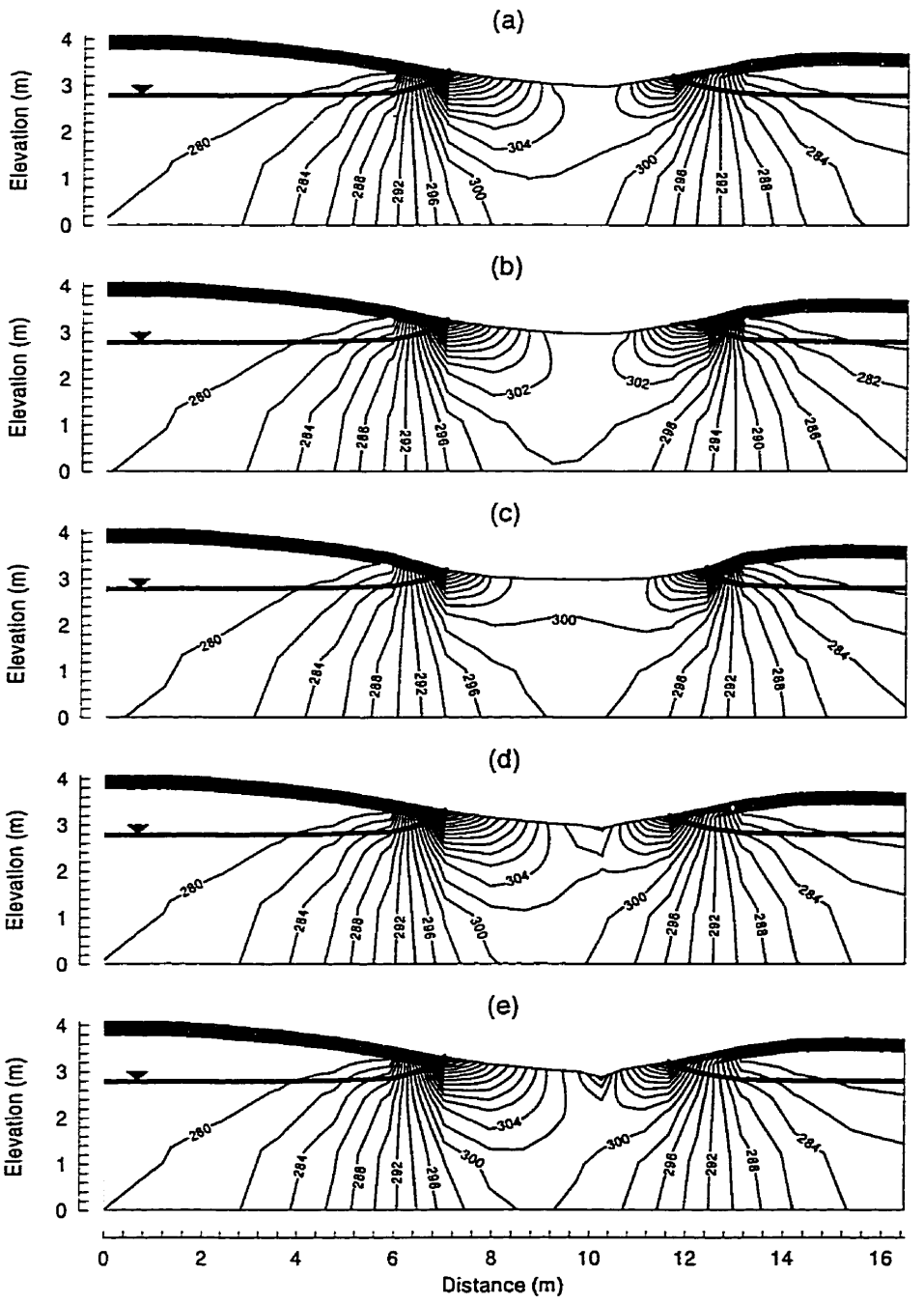

Figure 5-29. Total head distributions and water table elevations along a representative cross section (x = 40 m) at 50 minutes (a) grid one (base case), (b) grid two, (c) grid three, (d) grid four, and (e) grid five. Solutions for initial hydraulic head of 278 cm and porous medium hydraulic conductivity equal to 1 x 10^{-5} m/s.

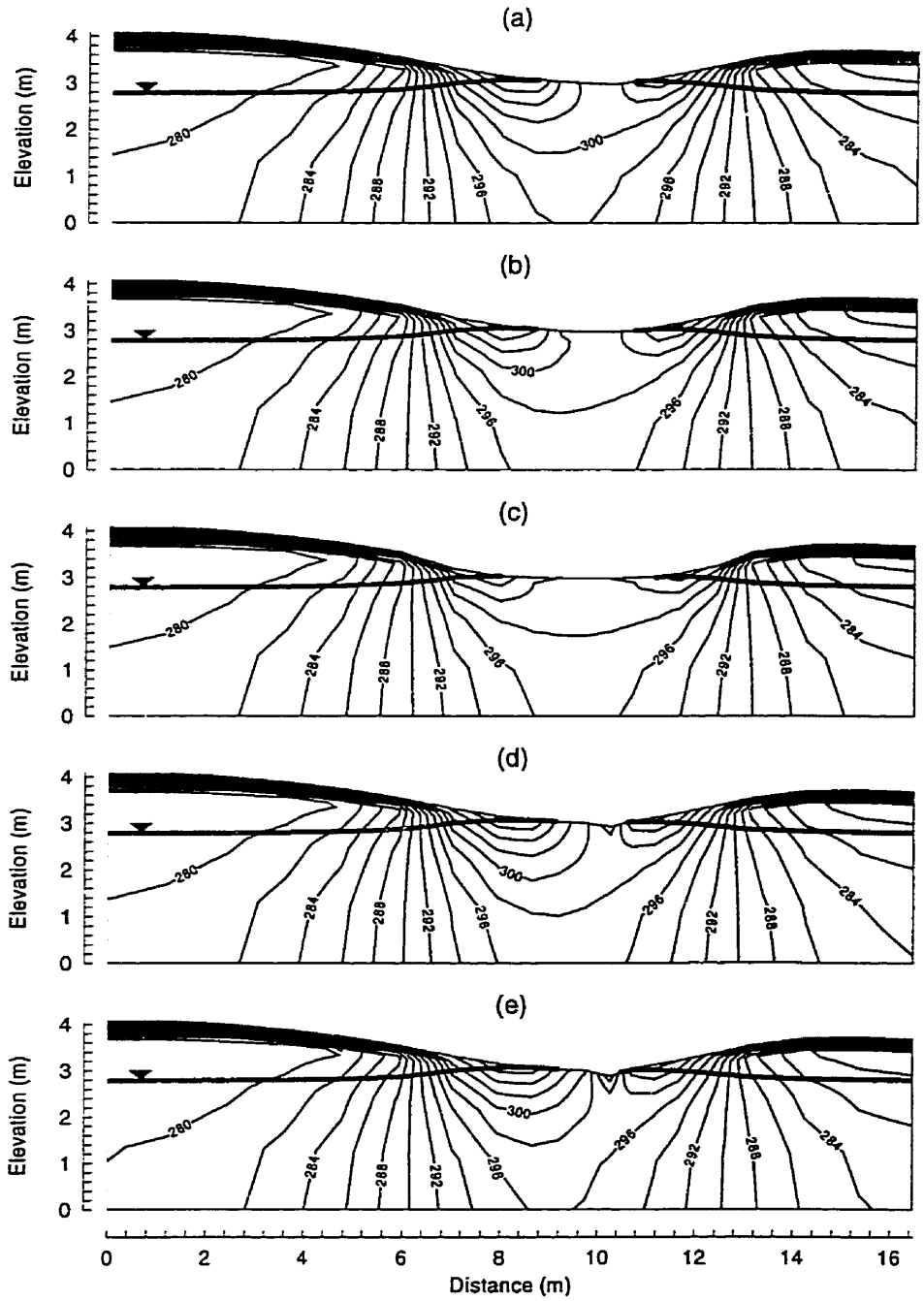

Figure 5-30. Total head distributions and water table elevations along a representative cross section (x = 40 m) at 50 minutes (a) grid one (base case), (b) grid two, (c) grid three, (d) grid four, and (e) grid five. Solutions for initial hydraulic head of 278 cm and porous medium hydraulic conductivity equal to 5×10^{-5} m/s.

5.3.3 Hydrograph Separation

The base case coupled simulation presented in Section 5.2.1 suggests that the dominant streamflow generation mechanism operating during the Borden field experiment was overland flow induced by infiltration excess over a dynamic contributing area implicitly linked to the rapid response of the capillary fringe. The corresponding analysis of tracer transport suggested that the large pre-event contributions to streamflow resulted largely from diffusive exchange (dilution) of rainfall tracer in the overland flow, with groundwater discharge (seepage or advective exchange) playing a minor role in modifying tracer concentrations in the surface water. Application of rainfall to the surface equations, in combination with both advective and diffusive coupling, was shown to reproduce both observed discharge and the observed hydrograph separation with reasonable accuracy.

This section presents and discusses separations of simulated stream discharge for the fourteen flow simulations presented in Section 5.3.1. Rainfall is applied to the surface equations and both advective and diffusive transport processes are utilized to couple the surface and subsurface continua. Figure 5-31 presents separations of stream discharge for the six simulations performed to evaluate the sensitivity of hydrologic response to initial water table elevation. Figure 5-32 presents separations of simulated stream discharge from the eight simulations performed to investigate the role of small variations in topography and channel incision on hydrologic response.

The sensitivity analysis presented in Section 5.3.1 indicates that similar flow processes are active in all simulations, with subsurface flow and groundwater discharge becoming more important with increasing channel incision and porous medium hydraulic conductivity. Simulated stream discharge volumes corresponded well with observed if the channel was not significantly incised and the porous medium hydraulic conductivity is assumed to be 1×10^{-5} m s^{-1}. Examination of hydrograph separations generated for varying initial water table elevations (Figure 5-31) indicates the relative proportion of event (rainfall) and pre-event (i.e. water initially present in the porous medium) in stream discharge remains relatively constant if hydraulic conductivity of 1×10^{-5} m s^{-1} is utilized. Increased stream discharge originates largely as infiltration excess overland flow, however, with

diffusive exchange diluting rainfall tracer in the shallow surface depths. Little stream flow originates below the initial water tables, indicating that transport and mixing processes acting at and near the land surface dominate stream water composition. Simulations performed using a hydraulic conductivity value of 5×10^{-5} m s^{-1}, while underestimating surface water discharge volumes, indicate increasing groundwater contributions to streamflow. The flow simulations indicate groundwater seepage increases with increasing water table elevation, linking the presence of groundwater tracer in streamflow with hydrologic response, and suggesting that the depths of surface-subsurface interaction increase with increasing hydraulic conductivity. Further discussion is hampered as the highest initial water table elevation also places the groundwater tracer source nine centimeters closer to the land surface.

Figure 5-32 presents simulated hydrograph separations for the four alternative topographies and the two hydraulic conductivity values. The four simulations performed with decreased surface elevation gradient (Figure 5-32a,b) result in very similar proportions of event (rainfall) and pre-event tracer (unsaturated zone) in stream discharge. Dilution of rainfall tracer occurs in the simulations largely via diffusive exchange between continua, with only small contributions resulting from direct discharge (seepage) of pre-event water from the subsurface. Surface discharges predicted by the incised-channel simulations (Figure 5-32c,d) are less than measured values for both hydraulic conductivities. The hydrologic response analysis presented in Section 5.3.1 indicates that subsurface flowpaths become more dominant as hydraulic conductivity and stream channel incision increase.

Separation of stream discharge for a hydraulic conductivity of 1×10^{-5} m s^{-1} indicates that the stream contains about equal portions of event and pre-event water. A small component of groundwater (i.e. originating below the initial water table) is evident in discharge from the more deeply incised channel. Greater groundwater contributions are expected, as the incised stream channel induces a greater vertical flow component (Figure 5-29d) and the source of the groundwater tracer lies only about ten centimeters from the bottom of the stream. Unsaturated zone tracer (i.e. originating above the initial water table) enters the stream by the same advective mechanism. The delineation of specific water sources or flow paths using hydrograph separation of stream flows is

ambiguous, as the simulations indicate that unsaturated zone tracer may also enter the stream via diffusive exchange between the porous medium and overland flow.

Assuming a hydraulic conductivity of 5×10^{-5} m s^{-1}, separation of stream discharge from the less-deeply incised channel (Figure 5-32c) indicates stream water is nearly a complete mixture of rainfall and unsaturated zone sources. In contrast, discharge from the more-deeply incised channel (Figure 5-32d) is a near-equal mixture of water from all three sources, with rainfall slightly more dominant during hydrograph rise. The hydrologic response simulations indicate that significant seepage occurs for both channel configurations, with seepage exceeding stream discharge in volume. Seepage into the channel, in combination with direct precipitation, are the dominant streamflow generation mechanisms. Vertical gradients beneath the stream are greater for the more deeply incised channel, thus providing a greater contribution of water originating below the initial water table. The separation of stream discharge using tracers therefore better reflects actual water origin, as diffusive exchange between continua is restricted in space to the stream channel itself.

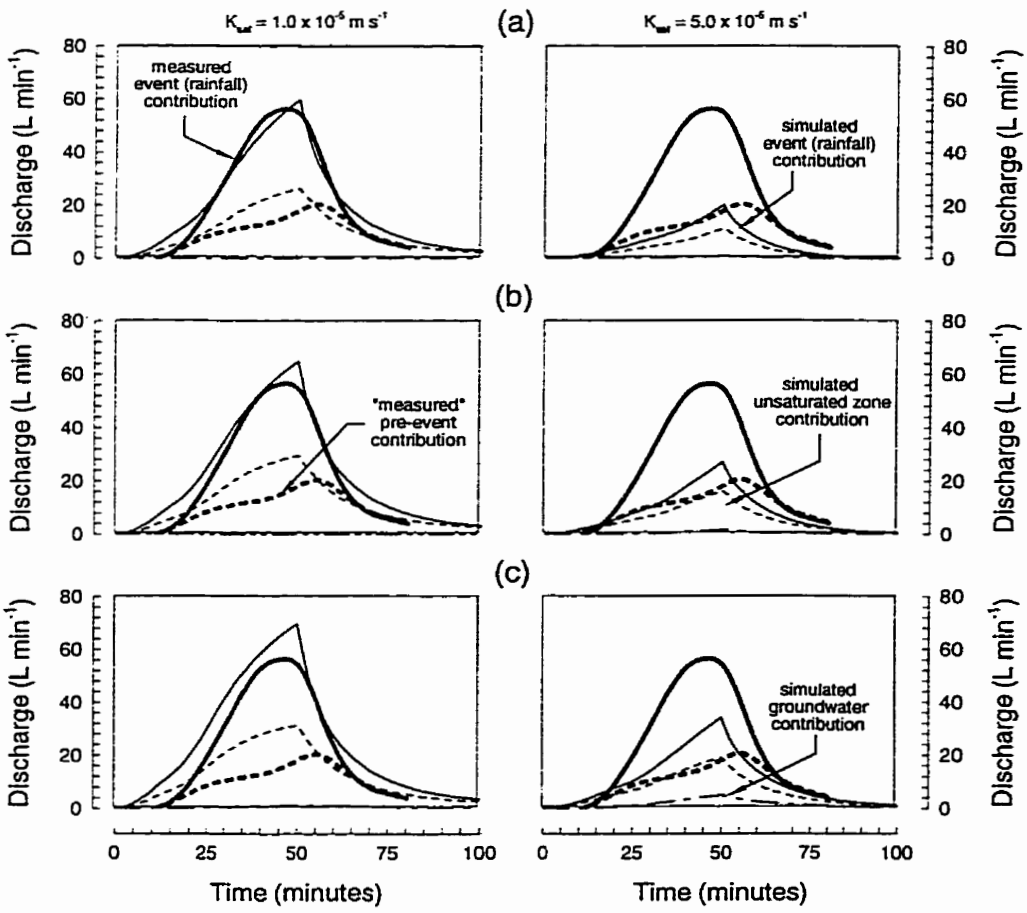

Figure 5-31. Illustration of the sensitivity of hydrograph separations to initial hydraulic head and hydraulic conductivity. Discharge for initial hydraulic head of (a) 281 cm, (b) 284 cm, and (c) 287 cm. Solutions for rainfall applied to surface equations and hydraulic conductivities of 1×10^{-5} m s^{-1} and 5×10^{-5} m s^{-1}.

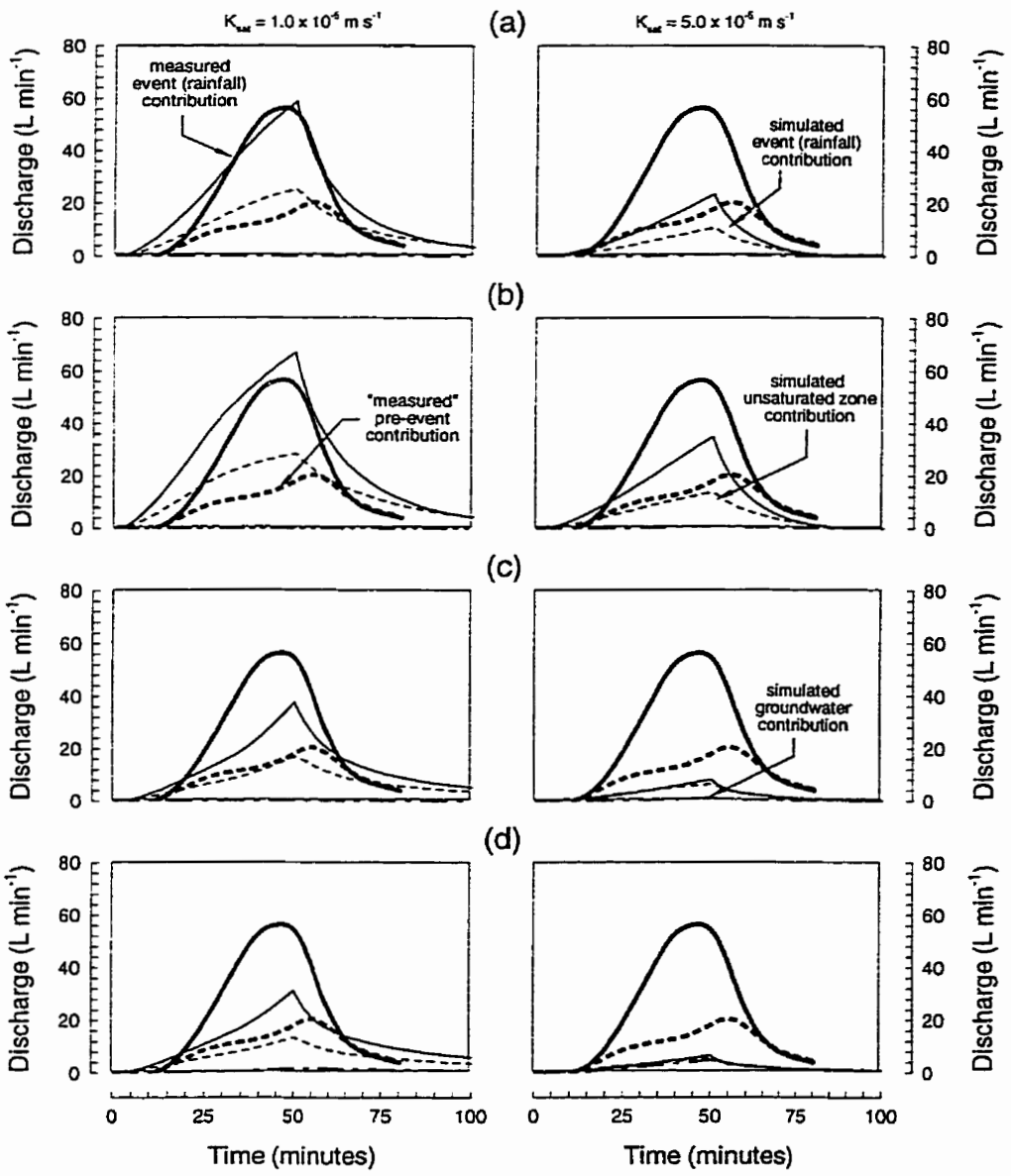

Figure 5-32. Illustration of the sensitivity of discharge tracer mass and hydrograph separations to topography, stream channel incision and hydraulic conductivity. Discharge for (a) grid two, (b) grid three, (c) grid four, and (d) grid five. Solutions for rainfall applied to surface equations, initial hydraulic head of 278 cm, and hydraulic conductivities of 1 x 10^{-5} m s^{-1} and 5 x 10^{-5} m s^{-1}.

Chapter 6 Summary and Conclusions

The numerical model developed in this work describes the flow of water and transport of solutes in three separate continua: within porous medium, fractures/macropores and on the land surface. The two-dimensional diffusion-wave equation is implemented to describe flow in shallow surface water while flow in variably-saturated porous medium and macropores was described by the three dimensional Richards' equation. Transport in both the surface and subsurface systems is described by advection-dispersion equations. Coupling of surface and subsurface flow and transport is achieved by assembling and solving one system of discrete algebraic equations so that water and solute fluxes between continua are determined as part of the solution. Linkage is through the assumption of primary variable continuity or via first-order, physically based flux relationships. Water and solute exchange between continua is assumed to be described by one-dimensional Darcy and advection-dispersion equations, respectively. Flow and transport coupling coefficients are defined as functions of characteristic length scales of interaction, fluid or solute properties, and system parameters such as saturation or permeability. Use of large exchange coefficient values promotes concentration and pressure head continuity between two interacting continua, and small values promote disequilbrium.

Specified boundary conditions can be spatially- and temporally variable, or in the case of state-dependent flux boundaries, may be specified as nonlinear functions of the local flow or transport solution. The numerical model is modular in form, is tailored towards irregular geological, surficial and areal geometries, and utilizes robust and efficient discretization and solution techniques. Surface topography and the associated effect on storage and potential gradients is imbedded in the structure of the numerical model. Development of this integrated numerical model represents the most significant contribution of this work.

The integrated numerical model differs significantly from those developed by previous workers who (1) couple surface and subsurface flow and transport models by matching boundary conditions; (2) utilize simplified time-delay routing of seepage discharge; (3) apply iterative rainfall partitioning and seepage face algorithms in groundwater flow models; (4) utilize equivalent porous medium properties to account for bypass flow; (5) invoke moving boundaries (i.e. dry/wet nodes) in surface flow models; (6) treat infiltration in surface flow models independent of water depth, subsurface porosity and permeability heterogeneity, and subsurface hydrodynamics; and (7) utilize effective lumped characteristic curves to incorporate enhanced subsurface permeability due to macropores.

6.1 Discretization and Solution Methods

The governing flow and transport equations are discretized in space using the control volume finite element (CVFE) method, allowing a consistent interpretation of flow and transport processes both within and between continua. The CVFE method combines the geometric flexibility of finite elements with the local conservation characteristics of control volumes. Simple element types are utilized to allow the efficient use of influence coefficients in the evaluation of spatial integrals. Element types can be spatially variable, a useful option in simulations combining complex geologic and topographic geometries. Each node in the finite element mesh may have multiple unknowns, with each unknown associated with different continua. A mixture of coupling schemes may be utilized, allowing different continua to be coupled via continuity assumptions or by first-order flux relationships. The spatial distribution of continua can also be variable, allowing, for example, a layer of macroporous soil adjacent to the land surface or surface processes only in topographic lows. The multiple equation and general coupling methodology can be utilized to include additional discrete features such as fractures, wells, or tile drains, or additional subdivision of the porous medium volume to allow multiple-interacting or mobile-immobile continua.

An alternative prism-based discretization is introduced and shown to be consistent with traditional two and three-dimensional finite elements, while generating significantly fewer negative

influence coefficients and utilizing less memory and computational effort. Use of these modified prisms allows placement of emphasis on designing well-structured triangular finite element meshes of the surface topography. The two-dimensional surface triangle mesh can be stacked vertically to generate three-dimensional subsurface prisms. As the vertical influences are numerically well behaved and predictable, negative influence coefficients will lie in the local x-y plane and result largely from poorly dimensioned triangles. Uncertainty associated with the spatial discretization is minimized, while lateral connectivity in the subsurface is retained to allow down-slope flow of water and solute transport. The resulting influence coefficients are similar to those generated using tetrahedra, but with a reduced nodal connectivity, lowering both storage and computational overhead. The approximation assumes that the principle components of the permeability tensor are aligned with the local coordinate axes, implying that soil layering follows topography. Further, vertical dispersive cross terms are assumed to be small. These assumptions are reasonable in this work but should be reexamined in simulations involving heterogeneous porous media or the use of large lateral dispersivities.

The system of nonlinear flow equations are solved in a fully coupled fashion so that fluid exchanges and nonlinear boundary conditions are determined as part of the iterative solution. Transport of multiple species is solved sequentially after each transient flow timestep, beginning with the first parent if chain decay is occurring. Nonlinear flux limiters are utilized in solving advective transport to minimize numerical dispersion. The discrete flow equations are linearized using Newton's method while approximate Jacobians are implemented to solve the discrete transport equations. Numerical derivatives are utilized to efficiently construct both the flow and transport Jacobians and the convergence of the flow Newton iteration loop is enhanced by primary variable switching. Adaptive time-weighting algorithms are developed and verified for both flow and transport. These algorithms partition the discrete equations into subsets corresponding to zones of active and inactive flow or transport processes. Equations at inactive nodes are solved explicitly and, as solutions are known at the new time level, can be partitioned from the flow or transport Jacobian. The remaining equations are solved fully coupled using either implicit or Crank-Nicholson time

weighting, with the solution to explicit equations appearing in the forcing vector only. Adaptive temporal weighting is shown to decrease simulation times, as assembly and solution effort is directly proportional to the size of the nonlinear system (Jacobian).

Approximate solutions to the linearized equations are generated using an iterative sparse-matrix solver employing Bi-CGSTAB or GMRES acceleration and reverse Cuthill-McKee ordering of a red-black reduced system of equations. Preconditioning is provided by incomplete lower-upper factorization (ILU) or drop-tolerance incomplete lower-upper (ILUT) factorization. ILUT factorizations are performed only on the Jacobian generated in the first flow or transport Newton iteration. Solutions to subsequent Newton iterations are preconditioned using the ILU algorithm and the data structure provided by the drop tolerance factorization. Accurate factorizations are generated, therefore, while the higher computational cost of the drop tolerance algorithm is amortized over the total number of nonlinear iterations.

6.2 Coupled Surface-Subsurface Water Flow Simulations

Detailed comparisons of coupled surface-subsurface simulations with the laboratory experiment of *Abdul* [1985] indicate that observed rainfall-runoff responses could be simulated with reasonable accuracy using measured or published parameter values. Groundwater discharge (seepage) and excess rainfall are not lost to the system in the coupled simulations, but are stored and flow on the land surface. These two-dimensional simulations also indicate that the coupled surface-subsurface approach is consistent with solutions generated using the traditional seepage face approach, as water depths on the land surface are small.

Application of the coupled numerical model to the field experiment of *Abdul* [1985] indicates that the neglect of surface water ponding in the traditional seepage face approach can produce misleading predictions of both groundwater discharge rates and locations. Surface water stored on the land surface acts as a transient, spatially-variable constraint on pressure heads in the porous medium. Simulated surface water depths in the stream, for example, rise to a depth of about five centimeters at peak stream discharge, altering subsurface head gradients and decreasing

groundwater seepage rates into the stream channel. In the coupled simulations, excess rainfall and seepage are both stored on the land surface until infiltrating or discharging to the stream. Seepage face solutions obtained after the rainfall cessation therefore differ from those indicated by the coupled model, as recharge ceases when the water table drops below the land surface. The error introduced by enforcing seepage face conditions (i.e. fixing the total head to be equivalent to the land surface elevation) increases with increasing channel incision.

The coupled simulations indicate that surface and subsurface flow processes are intimately related, as subsurface head distributions affect infiltration or seepage rates while surface water ponding depths affect head gradients adjacent to the land surface. Slight variations in topography, initial water table elevations, and bulk hydraulic conductivity can generate significantly different head distributions in the porous medium. Infiltration rates and porous medium storage capacity affect both the fraction of rainfall available for overland flow and the relative area of the land surface on which overland flow may develop. Overland flow contributing areas are also affected by small-scale topographic variations, which, in combination with the Manning roughness, determine the surface storage capacity and flow velocities. While these conclusions are not surprising, it is encouraging that stream discharge measured by *Abdul* [1985] can be simulated with reasonable accuracy using measured or literature-derived parameters and minimal calibration.

6.3 Coupled Surface-Subsurface Tracer Transport Simulations

Simulations of the transport of a conservative tracer introduced with rainfall in *Abdul's* [1985] laboratory experiment indicate that processes affecting solute concentrations in the surface water are restricted to a relatively thin region adjacent to the land surface. Concentrations in surface water are very sensitive to which equations the rainfall boundary condition (i.e. specified flux) is applied. For rainfall applied to the porous medium equations, the spatial and temporal distribution of solute exchange is affected by the movement of excess rainfall from the porous medium to the surface continuum. A dual rainfall condition, in which applied rainfall to both the porous medium and surface equation as a function of surface water depth, limits mixing due to infiltration excess.

For rainfall applied to the surface equations, mixing between the surface and subsurface continua is more heavily influenced by the magnitude of diffusive/dispersive exchange coefficient. The magnitude of advective exchange is controlled by hydrodynamics within the porous medium and not by the movement of excess rainfall from the porous medium to the surface continuum. The spatial and temporal distribution of solute exchange therefore reflects both concentration discontinuity and hydrodynamics. While having little affect on the flow solution, these subtleties in rainfall boundary condition assignment impact predictions of tracer concentrations in discharge water and, therefore, also affect interpretations of water origin.

The laboratory-scale simulations also indicate that the sensitivity of tracer concentrations in surface water to rainfall boundary condition assignment is reduced as the storage volume associated with the porous medium equations at the land surface is decreased. However, concentrations during hydrograph recession are replicated well only by assuming concentration continuity, suggesting that mixing between continua is related to more than the interaction of rainfall with the porous medium. Applying rainfall to the surface water equations results in tracer concentrations in discharge water nearly identical to those produced with the coarser discretization. Concentrations at early time and late times are over- and under-estimated, however. Inclusion of an empirical exchange dispersivity, which enhances diffusive exchange in regions where water exchange is also occurring, is shown to provide better tracer concentration predictions in discharge water. The empirical exchange dispersivity, therefore, may provide a useful calibration parameter to match simulated and observed concentrations. The value of such empirical coefficients is undoubtedly related to spatial discretization, however.

Application of the coupled surface-subsurface model to the transport of conservative tracer in the field-scale experiment of *Abdul* [1985] re-enforces the conclusion that mixing processes occurring at the land surface interface dominate tracer concentrations in stream discharge. Simulated hydrograph separations (i.e. relative concentration multiplied by stream discharge) replicate separations based on measured values with reasonable accuracy only if rainfall is applied to the surface equations and both advective (i.e. infiltration/seepage) and diffusive exchange processes are

considered. Simulated flux-weighted concentrations, however, exceed measured concentrations during hydrograph rise. Consideration of enhanced mixing using the empirical exchange dispersivity does not improve predictions. Application of rainfall exclusively to the porous medium equations or to both the surface and porous medium equations underestimates rainfall tracer concentrations at peak discharge by about fifty percent. Simulation of field-scale transport processes is considerably more complicated than at the laboratory-scale, where topography is better defined and extremely fine spatial discretization can be utilized. Successful simulation of coupled surface-subsurface transport depends on the accurate representation of the spatial and temporal variability of water exchange processes (i.e. advection) and diffusive-type processes associated with concentration differences between continua.

6.4 Streamflow Generation and the Borden Field Experiment

The set of simulations based upon the field experiment performed by *Abdul* [1985] clarifies the role of the capillary fringe on streamflow generation in the relatively homogeneous sand underlying CFB Borden. The coupled surface-subsurface flow model is able to reproduce the observed rapid water table response and resulting overland and stream flow. Observed surface discharge volumes and timing were simulated with reasonable accuracy using published or measured parameter values and minimal calibration. The simulated response of the capillary fringe to rainfall is consistent with both theory [*Gillham*, 1985] and observations [*Abdul*, 1985; *Abdul and Gillham*, 1989]. The simulations suggest that, while the low storage capacity of the capillary fringe is clearly responsible for the rapid hydrologic response observed by *Abdul* [1985], increased subsurface head gradients do not cause significant groundwater seepage. Rather, infiltration rates along the stream axis are reduced, with runoff formed largely by excess rainfall over a dynamic contributing area [e.g. *Hewlett and Hibbert*, 1967; *Dunne and Black*, 1970].

These results contradict the essential conclusion of *Abdul* [1985] and *Abdul and Gillham* [1989], who provide support for large groundwater contributions by routing seepage from two-dimensional hillslopes into a one-dimensional kinematic streamflow model. *Abdul* [1985] and *Abdul*

and Gillham [1989] provide further support for large groundwater contributions by separating stream discharge using relative concentrations of a conservative tracer (bromide) included in the artificial rainfall (i.e. hydrograph separation). The coupled surface-subsurface transport simulations performed in this work suggest that, despite the rapid, large-scale response of the capillary fringe, rainfall tracer dilution occurs largely by diffusive processes as water flows over the land surface to the stream, over relatively short flow paths, and subsequently down the stream channel. Tracer originating above the initial water table enters the surface water by similar processes, augmenting the small volumes of seepage (advective transport) caused by increased subsurface hydraulic gradients. Finally, the simulations performed in this work suggest that groundwater seepage rates are overestimated if surface water ponding in the stream channel is neglected, making conclusions based on *Abdul's* flow simulations suspect.

The sensitivity of simulated discharge tracer concentrations to diffusive exchange illustrates the ambiguity in the use of tracers to differentiate stream water origin, as tracer concentrations in the stream discharge may not reflect water sources [e.g. *Elsenbeer et al.*, 1995]. Indeed, hydrograph separation theory is fundamentally flawed if diffusive modification of tracer concentrations in surface water is prevalent in nature. Mixing at the land surface interface may provide significant fractions of pre-event tracer observed in non-incised streams [e.g. *Kennedy et al.*, 1986; *Rodhe*, 1987; *Buttle and Sami*, 1992]. Further, evaporation at the land surface may increase concentrations of dissolved species, with the isotopic signature of the remaining water becoming increasingly heavy (i.e. $^{18}O/^{16}O$ and $^{2}H/^{1}H$ increasing) [N. Kouwen, *per. comm*, 1999]. Additional field and laboratory studies, and additional simulations, are required to evaluate the generality of the previous conclusions. One can hypothesize, for example, that diffusive exchange between continua may be less important if most rainfall infiltrates, as the surface area of the stream itself is considerably smaller than the total area contributing overland flow. Diffusive exchange between surface water and the underlying porous medium would then be restricted to the stream channel itself [e.g. *Bencala*, 1983, 1984]. Advective exchange processes resulting from streambed topographic variations may then become more dominant [e.g. *Elliot and Brooks*, 1997 a,b].

6.5 Future Work

The simulations of coupled surface-subsurface flow and transport illustrate both the complexity of runoff generation mechanisms and ability of the numerical model to capture these complexities. A wide range of observed surface and subsurface hydrologic behavior can be simulated with minimal assumptions regarding the spatial and temporal variability of specific runoff or infiltration processes. Specifically, three-dimensional flow processes in the unsaturated zone are rigorously included, naturally regulating the partitioning of rainfall between the surface and subsurface systems and resolving the complex, transient flow fields resulting from infiltration into regions underlain by shallow water tables. Groundwater discharge to the land surface evolves in time and space while infiltration proceeds at the appropriate rate and location with excess water ponding or moving as overland or stream flow. Groundwater discharged to the surface and forming overland flow can re-infiltrate as conditions allow, and stream water interaction with the underlying and adjacent porous medium is dynamic and implicit. Bypass flow in macropores and the associated transport processes are intimately linked to the dynamics of the surface and porous medium continua. The interaction of surface and subsurface flow and transport processes is imbedded in the tight, implicit coupling.

The application of the integrated numerical model to real and idealized watersheds establishes a structured framework for the development and testing of hydrologic response conceptual models. The validity of assumptions utilized in less complex numerical models can be evaluated and dominant or controlling mechanisms and parameters can be identified. The intimate linkage of simulated hydrologic response and tracer transport will allow the further evaluation of hydrograph separation methodologies, particularly the relationship between rapid flow in macropores and the chemical signature of groundwater discharge. The numerical model is intended to be an integral component of and evolve with field studies of hydrologic response and solute transport in coupled surface-subsurface systems. The modular form of the numerical model allows the refinement of processes descriptions or the evaluation of alternative process conceptualizations.

Similarly, additional processes identified or hypothesized to influence hydrologic response or tracer transport can be considered.

Specific enhancements to the numerical model, and the intended objectives, include: (1) the inclusion of hysteresis in subsurface characteristic curves to evaluate hydrologic response during sequential rainfall-evaporation events; (2) the development and testing of reactive chemistry and cation exchange modules to evaluate the influence of rock-water interaction on stream water chemistry; and (3) the development and testing of sediment transport and slope stability modules to investigate the relationship between hydrology and landscape evolution. These enhancements are part of ongoing research programs at two well-documented field sites.

The first field site, R5, is a prairie rangeland catchment with shallow slopes located in Oklahoma [*USDA-ARS*, 1983; *Loague and Freeze*, 1985] while the second site, DW-1, located near Coos Bay, Oregon [*Anderson et al.*, 1997a,b; *Montgomery et al.*, 1997; *Torres et al.*, 1998], is a steep, macroporous hillslope underlain by fractured bedrock. Detailed measurements of hydrologic response to multiple rainfall events are available, as are rainfall tracer distributions, tracer and sediment concentrations in discharge water, permeability and topographic distributions, and evaporative demand. The spatial scale of these field sites is an order of magnitude larger than the Borden rainfall-runoff experiment performed by *Abdul* [1985]. Records of observed hydrologic response extend to days and months and include multiple precipitation events. Application of the numerical model to these field sites will continue the validation and verification process and provide comparisons with simpler, surface water oriented, rainfall-runoff models and analytical models of processes affecting slope stability. A general implementation of the anticipated reactive chemistry module, furthermore, will allow the investigation of nitrogen and phosphorus loadings to both groundwater and surface water.

Appendix A Spatial Discretization Issues

Negative influence coefficients can cause oscillatory behavior during the Newton iterations because discrete fluxes with incorrect orientations can be generated, leading to time step reductions and large numbers of Newton iterations to achieve convergence [*Letniowski and Forsyth*, 1991]. The simulation of dynamic coupling using large, irregular, three-dimensional grids with spatially variable properties effectively guarantees the existence of such negative terms. One possible solution is to set negative influence coefficients to zero, thus ensuring that discrete water and advective transport fluxes are oriented in the correct physical direction.

The relevance of this zeroing practice became readily apparent in a grid refinement study presented below which initiated to isolate the effects of gradient resolution on calculated infiltration and seepage rates. The permeability field was homogenous and isotropic for all simulations in this study and the grids were generated with either prisms or tetrahedra. Examination of simulation results predicted that spatially variable infiltration or seepage fluxes near the land surface did correlate with changing gradient resolution. Furthermore, solutions from grids with similar nodal spacings were considerably different.

The source of the unexpected results originates in the practice of setting negative influence coefficients to zero to ensure convergence of the Newton iteration loop. As meshes were refined, or different element types were implemented, the location and orientation of these negative terms changed. Zeroing negative influence coefficients, in effect, introduced spatial heterogeneity in the nodal connectivity, emulating spatial variation of permeability. This heterogeneity, which was difficult to detect if the percentage of zeroed-terms was small, became quite noticeable as the percentage increased. Simulations conducted without zeroing negative influence coefficients converged to nearly identical solutions as the grid was refined. Exceedingly small timesteps were

required, however, for convergence of the Newton iterations, resulting in very costly simulations. The following sections investigate the origin of negative influence coefficients arising from linear prism, isoparametric prism and tetrahedral finite elements (Figure A-1). A finite difference approximation for prism elements is then introduced and simulations based on the three-dimensional discretizations are compared.

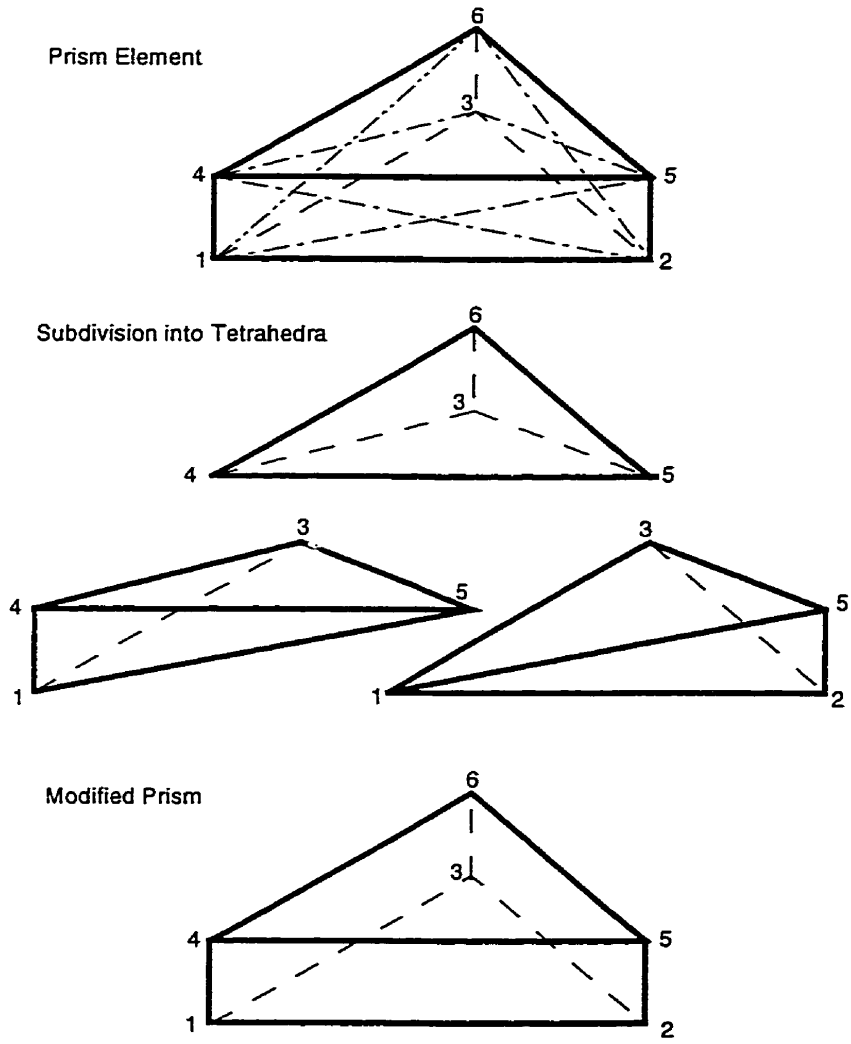

Figure A-1. Illustration of prism finite element geometry, node numbering, and nodal connectivity, along with subdivision of prism finite element into three tetrahedra, and nodal connectivity of finite difference approximation.

A.1 Prism Finite Elements

Assuming an isotropic and homogeneous permeability tensor, one can define the geometry-derived influence coefficients, $I_{i,j}^{total} = I_{i,j}^{xx} + I_{i,j}^{yy} + I_{i,j}^{zz}$, arising from a single linear triangular prism element (Figure A-1) as [*Huyakorn et al.*, 1986]:

$$I_{1,2}^{e} = \frac{dz}{3}(a_1a_2 + b_1b_2)\Delta + \frac{\Delta}{12dz} = I_{2,1}^{e} = I_{4,5}^{e} = I_{5,4}^{e}$$

$$I_{1,3}^{e} = \frac{dz}{3}(a_1a_3 + b_1b_3)\Delta + \frac{\Delta}{12dz} = I_{3,1}^{e} = I_{6,5}^{e} = I_{6,4}^{e}$$

$$I_{2,3}^{e} = \frac{dz}{3}(a_2a_3 + b_2b_3)\Delta + \frac{\Delta}{12dz} = I_{3,2}^{e} = I_{5,6}^{e} = I_{6,5}^{e}$$

$$I_{1,4}^{e} = \frac{dz}{6}(a_1a_1 + b_1b_1)\Delta + \frac{\Delta}{6dz} = I_{4,1}^{e}$$

$$I_{2,5}^{e} = \frac{dz}{6}(a_2a_2 + b_2b_2)\Delta + \frac{\Delta}{6dz} = I_{5,2}^{e}$$

$$I_{3,6}^{e} = \frac{dz}{6}(a_3a_3 + b_3b_3)\Delta + \frac{\Delta}{6dz} = I_{6,3}^{e}$$

$$I_{1,5}^{e} = \frac{dz}{6}(a_1a_2 + b_1b_2)\Delta - \frac{\Delta}{12dz} = I_{5,1}^{e} = I_{2,4}^{e} = I_{4,2}^{e}$$

$$I_{1,6}^{e} = \frac{dz}{6}(a_1a_3 + b_1b_3)\Delta - \frac{\Delta}{12dz} = I_{6,1}^{e} = I_{3,4}^{e} = I_{4,3}^{e}$$

$$I_{2,6}^{e} = \frac{dz}{6}(a_2a_3 + b_2b_3)\Delta - \frac{\Delta}{12dz} = I_{6,2}^{e} = I_{3,5}^{e} = I_{5,3}^{e}$$

where a and b are the standard linear triangular basis functions in the local x-y plane, Δ is the area of the triangular faces, dz equals the nodal separation distance in the local z dimension, and $V = dz\Delta$ is the elemental volume. Average dimensions or numerical integration is required for deformed prisms or, alternatively, the prism elements may be subdivided into tetrahedra (Figure A-1).

Calculation of the prism coefficients for the local x-y plane involves the reciprocal of the z-dimension, yielding a large positive value for elements with large aspect ratios. The following relationship must be true for influence coefficients lying in the local x-y to be non-negative:

$$k^{zz}_{ij+1/2}\frac{\Delta}{12dz} \le -\frac{dz}{3}\left(k^{xx}_{ij+1/2}a_i a_j + k^{yy}_{ij+1/2}b_i b_j\right)\Delta \text{ with } dz > 0$$

which is clearly impossible if the triangle influences are nonzero, unless the vertical permeability is zero. Setting negative influence coefficients to zero, therefore, inhibits flow in the local x-y plane for prism elements.

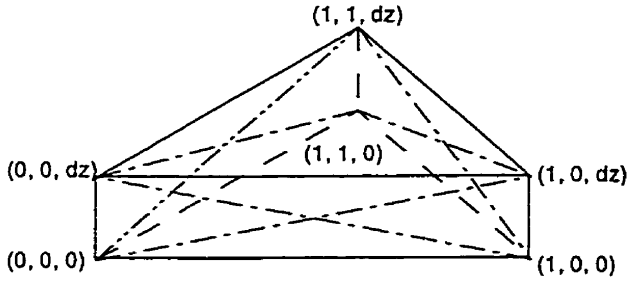

Figure A-2. Example prism finite element with large aspect ratio.

As a simple numerical example, consider a single prism formed from nodes as located in Figure A-2 where dz is the prism element thickness. Consider a vertical node spacing of one-tenth the triangle element area ($A = 0.5$) as is typical in the near-surface region of the grids utilized in this study. The influence coefficient tensor for this prism is, assuming an isotropic and homogeneous permeability field:

$$\Gamma^e = -\frac{\rho_w g k}{\mu_w}\begin{Bmatrix} & 1 & 2 & 3 & 4 & 5 & 6 \\ 1 & & 8.25\times10^{-1} & 8.33\times10^{-1} & -1.66 & -8.37\times10^{-1} & -8.33\times10^{-1} \\ 2 & & & 8.25\times10^{-1} & -8.37\times10^{-1} & -1.66 & -8.37\times10^{-1} \\ 3 & & & & -8.33\times10^{-1} & -8.37\times10^{-1} & -1.66 \\ 4 & & & & & 8.25\times10^{-1} & 8.33\times10^{-1} \\ 5 & & & & & & 8.25\times10^{-1} \\ 6 & & & & & & \end{Bmatrix}$$

One can observe that discrete fluxes calculated between nodes lying in the local x-y plane will have incorrect orientations (e.g. water will flow up-gradient), which is troublesome as the original triangles are well formed (i.e. follow the Delaunay criteria). Note that adjacent elements will also contribute to the total influence coefficient tensor for a particular node pair.

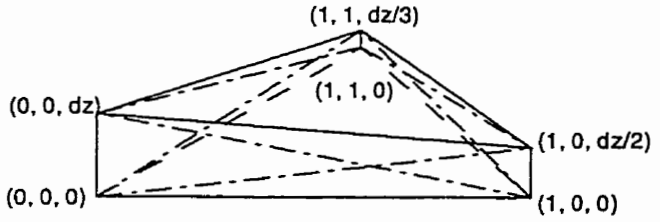

Figure A-3. Example deformed prism finite element with large aspect ratio.

For a deformed prism (Figure A-3), the influence coefficient tensor generated using an isoparametric prism element with Gauss integration [*Zienkiewicz*, 1971] is:

$$\Gamma^e = -\frac{\rho_w g k}{\mu_w}\begin{Bmatrix} & 1 & 2 & 3 & 4 & 5 & 6 \\ 1 & & 1.11 & 1.25 & -2.36 & -1.12 & -1.25 \\ 2 & & & 1.99 & -1.11 & -3.11 & -2.00 \\ 3 & & & & -1.25 & -2.00 & -3.25 \\ 4 & & & & & 1.11 & 1.25 \\ 5 & & & & & & 2.00 \\ 6 & & & & & & \end{Bmatrix}$$

which again generates negative influence coefficients in the local x-y plane.

A.2 Tetrahedral Finite Elements

Consider a single tetrahedron, T_1, formed by nodes 1, 2, 3, and 4 of the previously defined prism shown in Figure A-1. One can calculate elemental influence contributions as [*Zienkiewicz*, 1971; *Huyakorn and Pinder*, 1983]:

$$I_{1,2}^{T_1} = V^{T_1}\left[a_1 a_2 + b_1 b_2 + c_1 c_2\right]^{T_1} = I_{2,1}^{T_1} \tag{5.4}$$

$$I^{T_1}_{2,3} = V^{T_1}\left[a_2 a_3 + b_2 b_3 + c_2 c_3\right]^{T_1} = I^{T_1}_{3,2}$$

$$I^{T_1}_{3,4} = V^{T_1}\left[a_3 a_4 + b_3 b_4 + c_3 c_4\right]^{T_1} = I^{T_1}_{4,3}$$

$$I^{T_1}_{4,4} = V^{T_1}\left[a_4 a_1 + b_4 b_1 + c_4 c_1\right]^{T_1} = I^{T_1}_{1,4}$$

Two additional tetrahedra, T_2 and T_3, may be generated from the remaining elemental volume with influences determined in an identical manner. This order of subdivision is rather arbitrary, but is restricted unless nodes are added to the grid [e.g. *Letniowski and Forsyth*, 1991]. The sum of these sub-elements now determines the influences associated with the original six nodes:

$$I^{e}_{1,2} = I^{T_1}_{1,2} = I^{e}_{2,1}$$

$$I^{e}_{2,3} = I^{T_1}_{2,3} + I^{T_2}_{2,3} = I^{e}_{2,3}$$

$$I^{e}_{3,4} = I^{T_1}_{3,4} + I^{T_2}_{3,4} + I^{T_3}_{3,4} = I^{e}_{4,3}$$

$$I^{e}_{4,1} = I^{T_1}_{4,1} = I^{e}_{1,4}$$

$$I^{e}_{4,5} = I^{T_2}_{4,5} + I^{T_3}_{4,5} = I^{e}_{5,4}$$

$$I^{e}_{5,2} = I^{T_2}_{5,2} = I^{e}_{2,5}$$

$$I^{e}_{5,6} = I^{T_3}_{5,6} = I^{e}_{6,5}$$

$$I^{e}_{6,3} = I^{T_3}_{6,3} = I^{e}_{3,6}$$

Subdividing the prism into tetrahedra in this manner eliminates connections between nodes one and five, one and six, and two and six.

The influence coefficient tensor generated via subdivision of the undeformed prism element is:

$$\Gamma^e = -\frac{\rho_w g k}{\mu_w}\begin{Bmatrix} & 1 & 2 & 3 & 4 & 5 & 6 \\ 1 & & -8.33\times10^{-3} & 0.0 & -3.33 & & \\ 2 & & & -1.67\times10^{-2} & 0.0 & -3.33 & \\ 3 & & & & 0.0 & 0.0 & -3.33 \\ 4 & & & & & -1.67\times10^{-2} & 0.0 \\ 5 & & & & & & -8.33\times10^{-3} \\ 6 & & & & & & \end{Bmatrix}$$

This subdivision preserves a physical basis for flow between all nodes. Note that the vertical coefficients are numerically equivalent to $\Delta/3dz$, the equivalent of a finite difference analogue. Subdivision of the deformed prism volume into tetrahedra generates the following influence coefficient tensor:

$$\Gamma^e = -\frac{\rho_w g k}{\mu_w}\begin{Bmatrix} & 1 & 2 & 3 & 4 & 5 & 6 \\ 1 & & -8.33\times10^{-3} & 0.0 & -3.33 & & \\ 2 & & & -1.25\times10^{-2} & 4.17\times10^{-3} & -6.68 & \\ 3 & & & & 4.17\times10^{-3} & -2.77\times10^{-3} & -10.0 \\ 4 & & & & & -1.11\times10^{-2} & -4.17\times10^{-3} \\ 5 & & & & & & 0.0 \\ 6 & & & & & & \end{Bmatrix}$$

This subdivision generates negative coefficients for two connections. This simple analysis indicates that tetrahedra with large aspect ratios way also generate negative influence coefficients. Zeroing these negative terms will inhibit flow along connections corresponding to diagonal of the original prism element. A physical basis for flow in the local x-y plane is preserved, however.

A.3 Modified Prisms

Large elemental aspect ratios will frequently occur adjacent to the land surface if one is restricted to large lateral node spacings relative to those utilized vertically. Significantly, this region, lying at the interface between the subsurface and surface continua, is of most interest in this work. An alternative discretization method based on prisms is utilized in this work whereby cross-

derivative terms are lumped onto the diagonal of the elemental influence matrices, thus emulating finite-difference connections in the local z-coordinate (Figure A-4). This discretization method follows *Panday et al.* [1993] and *Therrien and Sudicky* [1996], who utilized a similar approach for block finite elements. Similarities also exist with the integrated finite difference method of *Narasimhan and Witherspoon* [1976] and *Pruess and Narasimhan* [1985]. Prism deformation is incorporated in an approximate manner by calculating separate areas and basis functions for the upper and lower triangles.

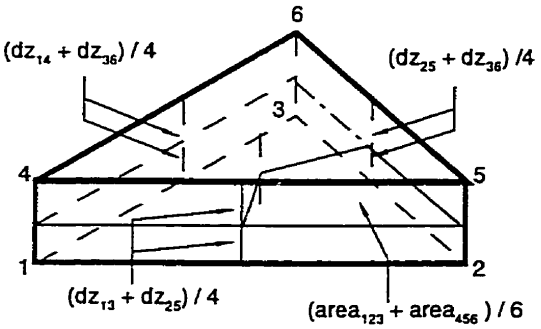

Figure A-4. Definition of variables utilized to calculate the modified prism influence coefficients.

The elemental contributions are defined for each node pair as

$$I^{xx}_{1,2} = \frac{dz_{14} + dz_{25}}{4}(a_1 a_2)\Delta_{123} = I^{xx}_{2,1} \qquad I^{yy}_{1,2} = \frac{dz_{14} + dz_{25}}{4}(b_1 b_2)\Delta_{123} = I^{yy}_{2,1}$$

$$I^{xx}_{1,3} = \frac{dz_{14} + dz_{25}}{4}(a_1 a_3)\Delta_{123} = I^{xx}_{3,1} \qquad I^{yy}_{1,3} = \frac{dz_{14} + dz_{36}}{4}(b_1 b_3)\Delta_{123} = I^{yy}_{3,1}$$

$$I^{xx}_{2,3} = \frac{dz_{25} + dz_{36}}{4}(a_2 a_3)\Delta_{123} = I^{xx}_{3,2} \qquad I^{yy}_{2,3} = \frac{dz_{25} + dz_{36}}{4}(b_2 b_3)\Delta_{123} = I^{yy}_{3,2}$$

$$I^{xx}_{4,5} = \frac{dz_{14} + dz_{25}}{4}(a_4 a_5)\Delta_{456} = I^{xx}_{5,4} \qquad I^{yy}_{4,5} = \frac{dz_{14} + dz_{25}}{4}(b_4 b_5)\Delta_{456} = I^{yy}_{5,4}$$

$$I^{xx}_{4,6} = \frac{dz_{14} + dz_{36}}{4}(a_4 a_{66})\Delta_{456} = I^{xx}_{6,4} \qquad I^{yy}_{4,6} = \frac{dz_{14} + dz_{36}}{4}(b_4 b_6)\Delta_{456} = I^{yy}_{6,4}$$

$$I^{xx}_{4,5} = \frac{dz_{25} + dz_{36}}{4}(a_4 a_5)\Delta_{456} = I^{xx}_{5,4} \qquad I^{yy}_{4,5} = \frac{dz_{25} + dz_{36}}{4}(b_4 b_5)\Delta_{456} = I^{yy}_{5,4}$$

$$I_{1,4}^{zz} = -\frac{\Delta_{123}+\Delta_{456}}{6dz_{14}} = I_{4,1}^{zz} \qquad I_{2,5}^{zz} = -\frac{\Delta_{123}+\Delta_{456}}{6dz_{25}} = I_{5,2}^{zz} \qquad I_{3,6}^{zz} = -\frac{\Delta_{123}+\Delta_{456}}{6dz_{36}} = I_{6,3}^{zz}$$

Cross derivatives are retained in the local x-y plane:

$$I_{1,2}^{xy} = \frac{dz_{14}+dz_{25}}{4}(a_1b_2+a_2b_1)\Delta_{123} = I_{2,1}^{xy}$$

$$I_{1,3}^{xy} = \frac{dz_{14}+dz_{36}}{4}(a_1b_3+a_3b_1)\Delta_{123} = I_{3,1}^{xy}$$

$$I_{2,3}^{xy} = \frac{dz_{25}+dz_{36}}{4}(a_2b_3+a_3b_2)\Delta_{123} = I_{3,2}^{xy}$$

$$I_{4,5}^{xy} = \frac{dz_{14}+dz_{25}}{4}(a_4b_5+a_5b_4)\Delta_{456} = I_{5,4}^{xy}$$

$$I_{4,6}^{xy} = \frac{dz_{14}+dz_{36}}{4}(a_4b_6+a_6b_4)\Delta_{456} = I_{6,4}^{xy}$$

$$I_{5,6}^{xy} = \frac{dz_{25}+dz_{36}}{4}(a_5b_6+a_6b_5)\Delta_{456} = I_{6,5}^{xy}$$

The influence coefficient tensor for the first example prism (Figure A-2) is:

$$\Gamma^e = -\frac{\rho_w g k}{\mu_w}\begin{Bmatrix} & 1 & 2 & 3 & 4 & 5 & 6 \\ 1 & & -1.25\times10^{-2} & 0.0 & -3.33 & & \\ 2 & & & -1.25\times10^{-2} & & -3.33 & \\ 3 & & & & & & -3.33 \\ 4 & & & & & -1.25\times10^{-2} & 0.0 \\ 5 & & & & & & -1.25\times10^{-2} \\ 6 & & & & & & \end{Bmatrix}$$

The positive numerical properties of well-formed triangular faces are retained and coefficients corresponding to vertical water flux are identical to those generated using the tetrahedral subdivision. The influence coefficient tensor for the second prism example (Figure A-3) is:

$$\Gamma^{\epsilon} = -\frac{\rho_w g k}{\mu_w}$$

	1	2	3	4	5	6
1		-9.38×10^{-3}	0.0	−3.33		
2			-5.20×10^{-3}		−6.67	
3						−10.0
4					-9.37×10^{-3}	1.95×10^{-6}
5						-5.21×10^{-3}
6						

Vertical coefficients are virtually identical to those originating in the tetrahedral subdivision and, while a single negative coefficient is generated, the numerical value is three orders of magnitude less than those generated using tetrahedra. The tetrahedra and finite difference examples are in general agreement, allowing flow both vertically and in the local x-y plane.

An example of the type presented above for flow is unsatisfactory for dispersive transport, as the mechanical dispersion tensor will vary in magnitude and orientation as the flow field evolves. Discrete diffusive solute fluxes, however, are governed by the geometric coefficients introduced above for flow. For simplicity, consider a constant dispersion coefficient, D, in a saturated medium of constant porosity. For a non-deformed prism element, the dispersive transport tensor is:

$$\Lambda^{\epsilon} = -D$$

	1	2	3	4	5	6
1		8.71×10^{-1}	8.30×10^{-1}	−1.66	-7.93×10^{-1}	-7.52×10^{-1}
2			7.88×10^{-1}	-8.77×10^{-1}	−1.66	-7.94×10^{-1}
3				-9.18×10^{-1}	-8.77×10^{-1}	−1.66
4					7.88×10^{-1}	8.29×10^{-1}
5						8.71×10^{-1}
6						

for the tetrahedral subdivision it is:

$$\Lambda^e = -D\begin{Bmatrix} & 1 & 2 & 3 & 4 & 5 & 6 \\ 1 & & 0.0 & -1.75\times10^{-1} & -3.50 & & \\ 2 & & & -1.75\times10^{-1} & 1.75\times10^{-1} & -3.68 & \\ 3 & & & & 3.25\times10^{-1} & 1.75\times10^{-1} & -3.50 \\ 4 & & & & & -1.75\times10^{-1} & -1.75\times10^{-1} \\ 5 & & & & & & 0.0 \\ 6 & & & & & & \end{Bmatrix}$$

and for the finite-difference approximation it is:

$$\Lambda^e = -D\begin{Bmatrix} & 1 & 2 & 3 & 4 & 5 & 6 \\ 1 & & 0.0 & -1.25\times10^{-2} & -3.33 & & \\ 2 & & & 0.0 & & -3.33 & \\ 3 & & & & & & -3.33 \\ 4 & & & & & 0.0 & -1.25\times10^{-2} \\ 5 & & & & & & 0.0 \\ 6 & & & & & & \end{Bmatrix}$$

Both the prism and tetrahedral discretizations generate negative dispersive transport coefficients, indicating that solute mass will be transported against the concentration gradient. Similar coefficients are generated with the deformed prisms.

A.4 Comparison of Solutions with Alternative Discretizations

A series of simulations was performed to evaluate the sensitivity of discharge volume and tracer concentrations to spatial discretization, because the fine nodal spacing utilized in the laboratory-scale simulations (see Section 4.7) is impractical at the field scale (see Chapter 5). The geometry utilized in the discretization sensitivity analysis (Figure A-5) represents a generic cross section extracted from *Abdul's* [1985] field experiment. Flow and transport parameters and initial conditions are identical to those utilized in the field-scale simulations. While rainfall rates and durations are also identical, the stream is replaced with a critical depth boundary condition. These two dimensional simulations, summarized in Figure A-6, indicate that discharge predictions are sensitive to hydraulic gradient resolution adjacent to the land surface. Predictions are less sensitive to

horizontal spacing for the relatively shallow slopes considered. Coarse discretization at depth, in combination with fine spacing at the land surface, maintains reasonable accuracy while minimizing computational effort.

The problem was made quasi-three dimensional by connecting two identical cross sections, spaced by one meter, to compare solutions based upon three-dimensional elements. Three element types are compared: tetrahedra, isoparametric prisms, and modified prisms. Element thicknesses vary along the x-axis, allowing a comparison of influence coefficients generated with deformed elements. Tetrahedra are generated by subdividing the prisms [e.g. *Letniowski and Forsyth*, 1991] while the modified prisms emulate finite differences along the vertical axis [e.g. *Panday et al.*, 1993]. Table A-2 presents a summary of influence coefficient and solution statistics for the three-dimensional elements. The modified prisms generate the least number of negative influence coefficients, the magnitude of which approach roundoff error. Tetrahedra and isoparametric prisms generated about the same number of negative influence coefficients, but the magnitude of the tetrahedra-derived values is about an order of magnitude less than the isoparametric-prism derived values. The modified prisms required approximately 72 % and 60% of the memory and computation time of tetrahedra, respectively. Retaining negative coefficients in the isoparametric prisms caused considerable convergence difficulties. Setting the coefficients to zero allowed convergence, but the solution was inconsistent with results obtained with other discretizations.

A comparison of discharge versus time and hydraulic head at 50 minutes is presented in Figure A-6 for the two-dimensional elements. Figure A-7 presents the corresponding results for simulations conducted using tetrahedra and isoparametric prisms, performed with and without retaining negative influence coefficients, and with modified prisms. The modified prisms are shown to generate flow solutions nearly identical to the corresponding two-dimensional results, although recharge tracer concentrations are slightly under-predicted at peak discharge, and slightly over-predicted during hydrograph recession. Both tetrahedra-based solutions agree well with the two-dimensional results, as negative influence coefficients arising from tetrahedra tend to correspond to edges interior to the original prisms (see Section A.2): the two-dimensional flow field in this

example reduces the effect of these terms. The two solutions based upon isoparametric prisms differ significantly, as negative influence coefficients correspond to the main prism edges (see Section A.1).

A subset of the field-scale simulations (Chapter 5) were repeated using tetrahedra and isoparametric prisms to evaluate the error introduced by the modified prisms. Fully implicit time weighting is utilized for flow and adaptive implicit-explicit time weighting is utilized for transport. A summary of the flow influence coefficient and of the solution statistics is presented in Table A-3. As indicated by the cross section example, both tetrahedra and isoparametric prisms generate large numbers of negative influence coefficients while the modified prisms generate significantly less. The simulation conducted with the modified prisms, furthermore, required considerably less computational effort than utilizing tetrahedra or isoparametric prisms, largely due to the reduced effort required to assemble and solve the flow and transport Jacobians.

The flow solutions generated by tetrahedra and isoparametric prisms are summarized in Figure A-8, which presents water table locations and total head contours at fifty minutes. Removing negative influence coefficients (i.e. setting them to zero) affects both solutions in and adjacent to the stream, although the effect is much more noticeable with the isoparametric prisms. Retaining the negative terms generates total head contours very similar to the modified prisms, but at considerably greater computational effort.

Figure A-9 presents the corresponding surface water discharge volumes and tracer concentrations versus time for rainfall applied using the dual algorithm and for rainfall applied exclusively to the surface equations. Removing negative influence coefficients is shown to cause decreased surface water discharge: this reduction is most significant for the isoparametric prisms. Retaining negative influence coefficients, however, results in discharges that agree well with the modified prism solution. Hydrograph separations are relatively unaffected by the choice of spatial discretization as interactions at the land surface dominate tracer concentrations in surface water.

Discretization	Grid Statistics		Solution Statistics			
	Equations[1]	Elements[1]	Time Steps[2]	Solution Time[3]	Newton Iterations	
					Flow	Transport
Fine	3131 / 101	6000 / 100	3 / 67	2.8	255	414
Coarse Horizontal	651 / 21	1200 / 20	0 /63	0.34	209	390
Coarse Horizontal and Vertical	147 / 21	240 / 20	2 / 65	0.08	222	388
Refined at Land Surface	294 / 21	520 / 20	0 / 63	0.14	210	394

[1] porous medium / surface; [2] failed / total; [3] minutes (300 MHz Pentium II), flow and transport of three solutes

Table A-1. Summary of grid and solution statistics for sensitivity analysis of two-dimensional spatial discretization. Fully implicit time weighting is utilized for both flow and transport.

Discretization	Flow Influence Coefficients		Solution Statistics			
	Negative / Total	Minimum	Time Steps[1]	Solution Time[2]	Newton Iterations	
					Flow	Transport
Isoparametric Prisms	1056 / 3933	-4.6×10^{-5}				
retained			1 / 65	0.78	227	486
removed			2 / 65	0.66	217	427
Tetrahedra	833 / 2874	-3.3×10^{-6}				
retained			0 / 63	0.53	217	400
removed			2 / 65	0.52	227	406
Modified Prisms	186 / 1827	-2.8×10^{-21}	0 / 63	0.32	209	394

[1] failed / total; [2] minutes (300 MHz Pentium II), flow and transport of three solutes

Table A-2. Summary of flow influence coefficient and solution statistics for sensitivity analysis of three-dimensional spatial discretization of the example cross section. Fully implicit time weighting is utilized for both flow and transport.

Discretization	Flow Influence Coefficients	Solution Statistics			
	Negative / Non-Zero	Time Steps[1]	Solution Time[2]	Newton Iterations	
				Flow	Transport
Isoparametric Prisms	42,335/ 157,234				
retained		4 / 67	60.0	422	758
removed		7 / 77	53.8	464	670
Tetrahedra	43,000 / 134,838				
retained		4 / 71	50.3	445	790
removed		3 / 69	42.2	394	700
Modified Prisms	160 / 68,750	3 / 69	25.8	420	699

[1] failed / total; [2] minutes (300 MHz Pentium II), flow and transport of three solutes

Table A-3. Summary of flow influence coefficient and solution statistics for field-scale three-dimensional spatial discretizations based upon isoparametric prism, tetrahedra, and modified prism influence coefficients. Solutions for porous medium hydraulic conductivity equal to 1×10^{-5} m s^{-1}, initial hydraulic head of 278 cm, and adaptive transport time weighting.

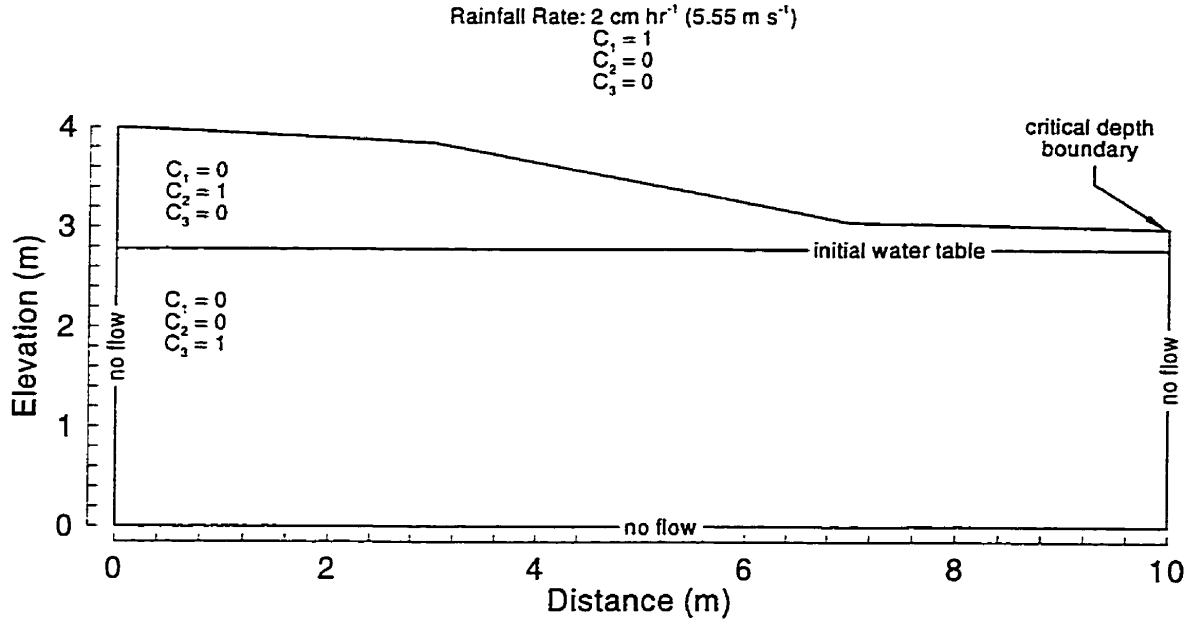

Figure A-5. Geometry, initial and boundary conditions for example cross section.

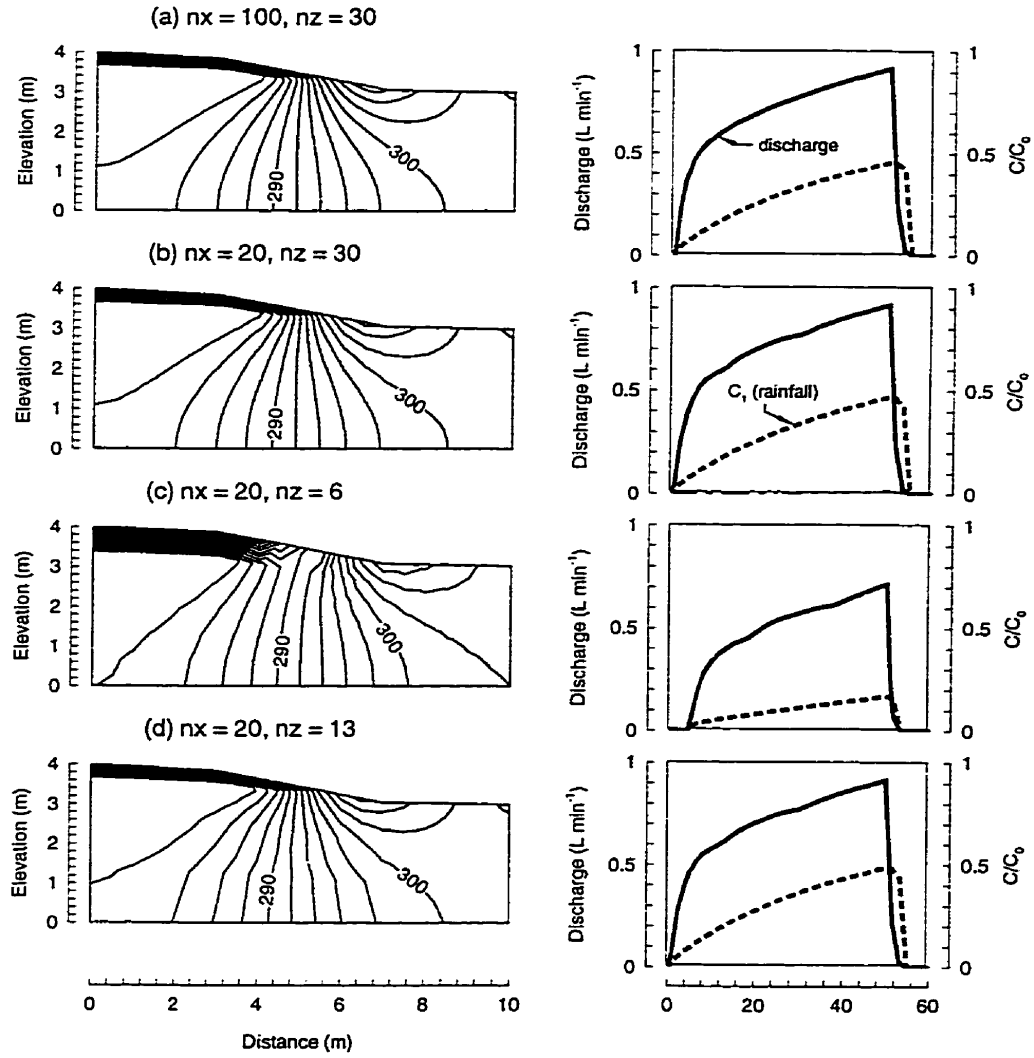

Figure A-6. Total head (cm) at 50 minutes and discharge volume and rainfall tracer concentrations versus time for coupled surface-subsurface flow and transport on a cross section. Comparison of solutions given by: (a) fine spatial discretization, (b) coarse vertical and fine horizontal spacing, (c) coarse horizontal and vertical spacing, and (d) coarse horizontal and vertical spacing refined adjacent to the land surface. Solution for dual rainfall boundary condition and porous medium hydraulic conductivity equal to 5×10^{-5} m s^{-1}.

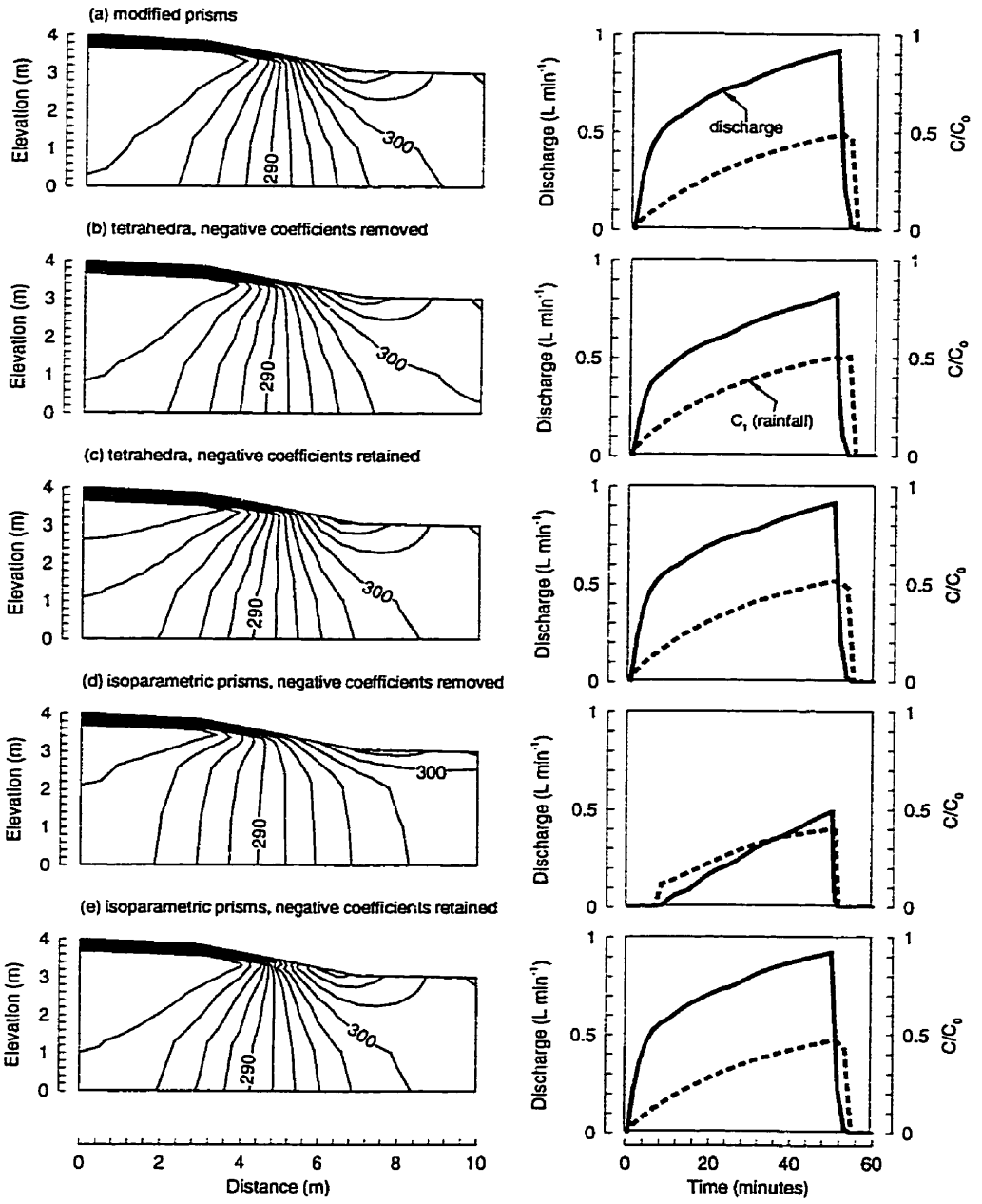

Figure A-7. Total head (cm) at 50 minutes and discharge volume and rainfall tracer concentrations versus time for coupled surface-subsurface flow and transport on a quasi-three dimensional cross section. Comparison of solutions given by: (a) modified prisms, (b) tetrahedra with negative coefficients removed, (c) tetrahedra with negative coefficients retained, (d) isoparametric prisms with negative coefficients removed, and (e) isoparametric prisms with negative coefficients retained. Solution for dual rainfall boundary condition and porous medium hydraulic conductivity equal to 5×10^{-5} m s^{-1}.

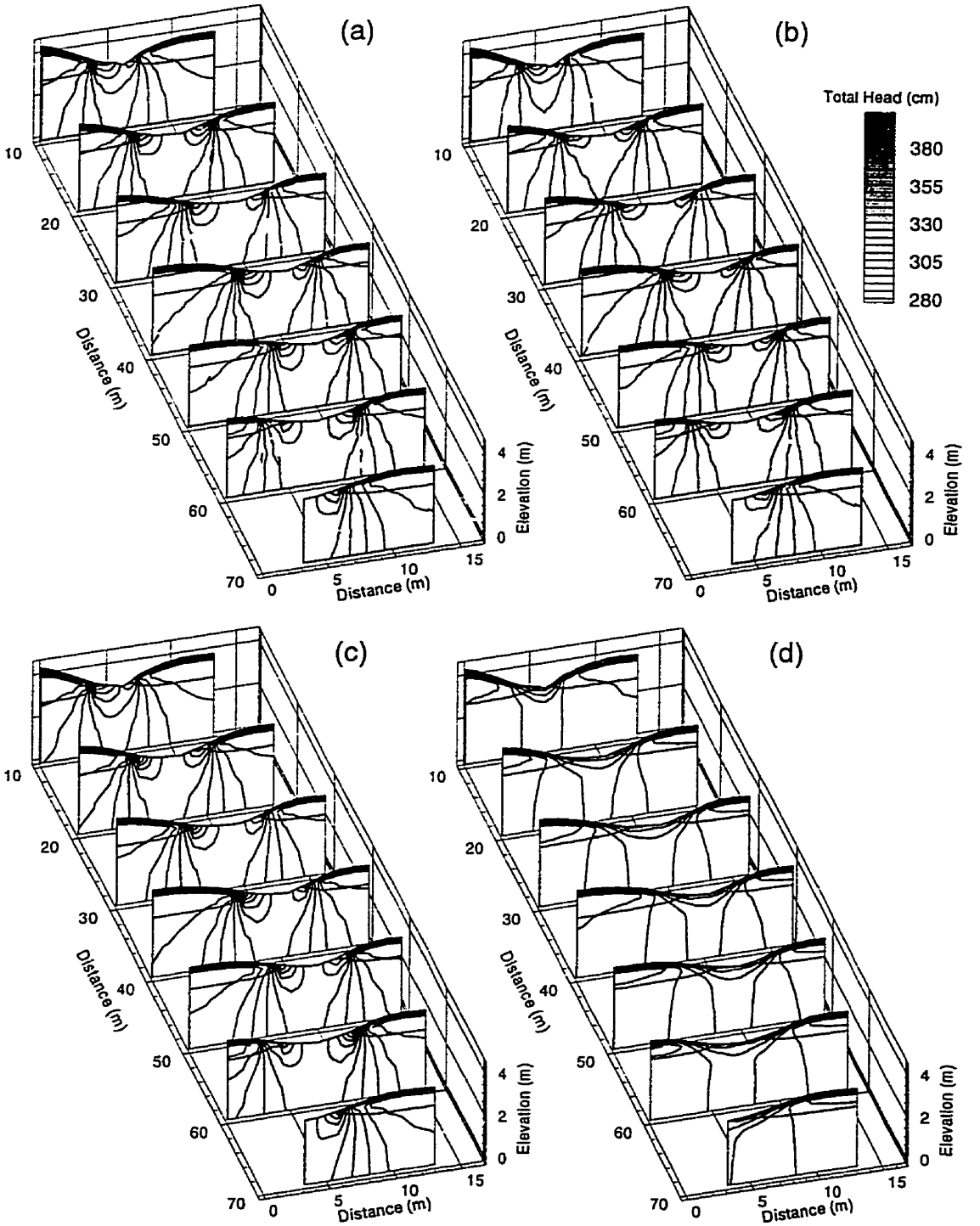

Figure A-8. Water table location and contours of total head in porous medium at 50 minutes for: (a) tetrahedra, negative coefficients removed (b) tetrahedra, negative coefficients retained (c) isoparametric prisms, negative coefficients retained, and (d) isoparametric prisms, negative coefficients removed. Solution for initial hydraulic head of 278 cm, dual rainfall boundary condition, and porous medium hydraulic conductivity equal to 1×10^{-5} m s^{-1}.

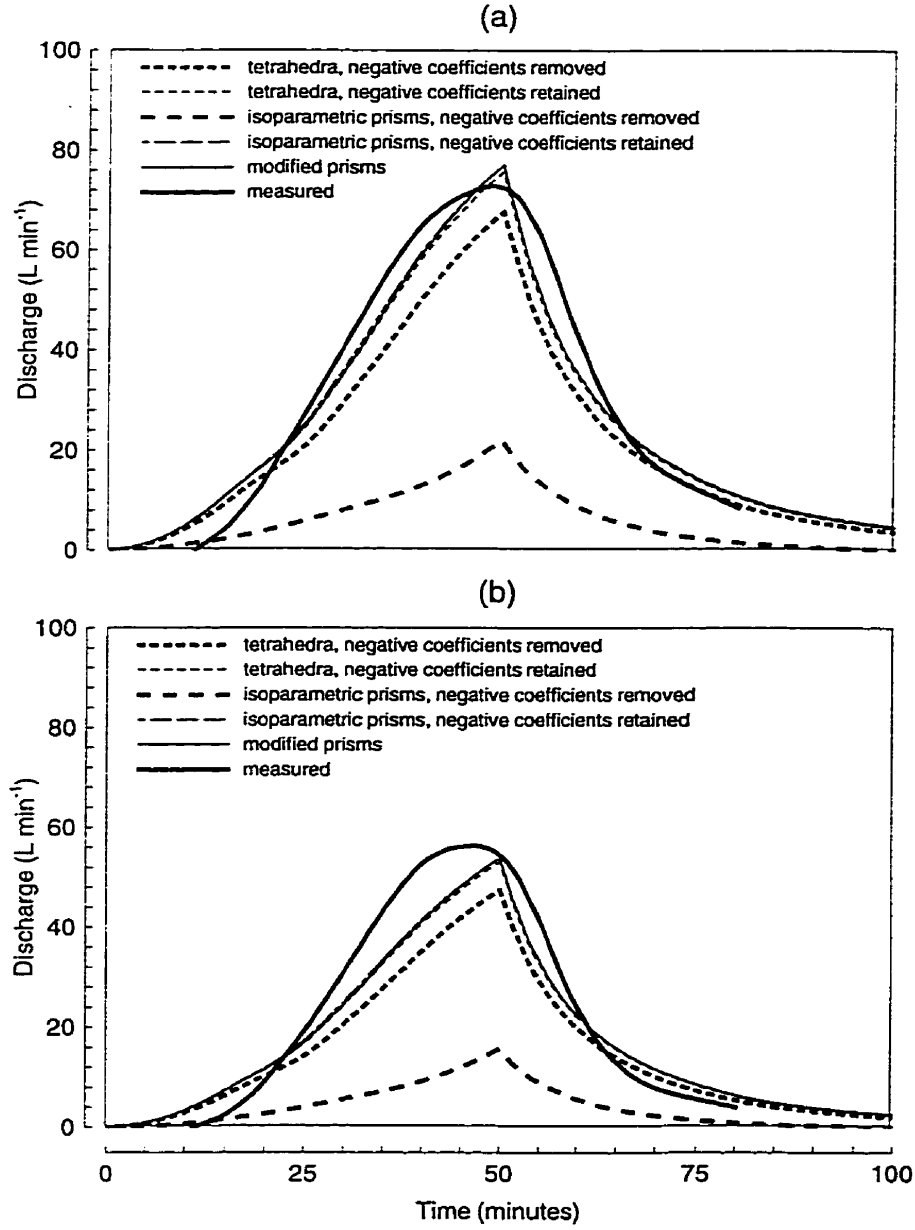

Figure A-9. Illustration of the sensitive of field-scale coupled surface-subsurface flow and transport solutions to subsurface discretization. Comparison of (a) measured and simulated stream discharges and (b) comparison of measured and simulated hydrograph separations. Solutions for initial hydraulic head of 278 cm and porous medium hydraulic conductivity equal to 1×10^{-5} m s^{-1}.

References

Abbott, M.B., J.C. Bathurst, J.A. Cunge, P.E. O'Connell, and J. Rasmussen, An introduction to the European Hydrological System – Système Hydrologique Européen, "SHE", 1: History and philosophy of a physically-based, distributed modelling system, *J. Hydrol.*, 87, 45-59, 1986a.

Abbott, M.B., J.C. Bathurst, J.A. Cunge, P.E. O'Connell, and J. Rasmussen, An introduction to the European Hydrological System – Système Hydrologique Européen, "SHE", 2: Structure of a physically-based, distributed modeling system, *J. Hydrol.*, 87, 61-77, 1986b.

Abdul, A.S., *Experimental and Numerical Studies of the Effect of the Capillary Fringe on Streamflow Generation*, Ph.D. Thesis, University of Waterloo, Waterloo, Ontario, 210 pp., 1985.

Abdul, A.S. and R.W. Gillham, Field studies of the effects of the capillary fringe on streamflow generation, *J. Hydrol.*, 112, 1-18, 1989.

Ahuja, L.R., Characterization and modeling of chemical transfer to runoff, *Adv. Soil Sci.*, 4, 149-188, 1986.

Akan, A.O. and B.C. Yen, Mathematical model of shallow water flow over porous media, *J. Hyd. Div., ASCE*, H14, 479-494, 1981.

Akanbi, A.A. and N.D. Katapodes, Model for flood propogation on initially dry land, *J. Hydr. Eng., ASCE*, 114(7), 689-706, 1988.

Akindunni, F.F. and R.W. Gillham, Unsaturated and saturated flow in response to pumping of an unconfined aquifer: numerical investigation of delayed drainage, *Ground Water*, 30(6), 873-884, 1992.

Al, T.A. and D.W. Blowes, Storm-water hydrograph separation of runoff from a mine-tailings impoundment formed by thickened tailings discharge at Kidd Creek, Timmins, Ontario, *J. Hydrol.*, 180, 55-78, 1996.

Anderson, M.G. and T.P. Burt (editors), *Hydrological Forecasting*, Wiley, New York, 604 pp., 1985.

Anderson, M.G. and T.P. Burt (editors), *Process Studies in Hillslope Hydrology*, Wiley, New York, pp 539, 1990.

Anderson, S.P., W.E. Dietrich, D.R. Montgomery, R. Torres, and K. Loague. Concentration-discharge relationships in runoff from a steep unchanneled catchment. *Water Resour. Res.*, 33, 211-225, 1997a.

Anderson, S.P., W.E. Dietrich, D.R. Montgomery, R. Torres, M.E. Conrad, and K. Loague. Subsurface flowpaths in a steep, unchanneled catchment. *Water Resour. Res.*, 33, 2637-2653, 1997b.

Aqua Terre Consultants, *Review and Evaluation of Approaches to Simulate Flow and Solute Transport through Macroporous Media*, Prepared for U.S. EPA, Athens, GA, 1991.

Bailey, G.W., R.R. Swank, and H.P. Nicholson, Predicting pesticide runoff from agricultural land: a conceptual model, *J. Environ. Qual.*, 3(2), 95-102, 1974.

Barenblatt, G.I, I.P. Zheltov, and I.H. Kochina, Basic concepts in the theory of seepage of homogeneous fluids in fissured rocks, *J. Appl. Math. Mech.*, Engl. Transl., 24(5), 1286-1303, 1960.

Barker, J.A., Block-geometry functions characterizing transport in densely fissured media, *J. Hydrol.*, 77, 263-279, 1985.

Bathurst, J.C., Physically-based distributed modelling of an upland catchment using the Systèm Hydrologique Européen, *J. Hydrol.*, 87, 79-102, 1986a.

Bathurst, J.C., Sensitivity analysis of the Systèm Hydrologique Européen for an upland catchment, *J. Hydrol.*, 87: 103-124, 1986b.

Bathurst, J.C., J.M. Wicks, and P.E. O'Connell, The SHE/SHESED Basin Scale Water Flow and Sediment Transport Modelling System, pp 563-594 in *Computer Models of Watershed Hydrology*, Water Resour. Publ., Fort Collins, Colorado, 1996.

Bear, J., *Dynamics of Fluids in Porous Media.*, American Elsevier, New York, NY, 764 pp., 1972.

Bear, J., C. Braester, and P. Menier, Effective and relative permeabilities of anisostropic porous media, *Transp. Porous Media*, 2, 301-316, 1987.

Beck, M.B., F.M. Kleissen, and H.S. Wheater, Identifying flow paths in models of surface water acidification, *Rev. Geophys.*, 28(2): 207-230, 1990.

Behie, G.A. and P.A. Forsyth, Incomplete factorization methods for fully-implicit simulation of enhanced oil recovery, *SIAM J. Sci. Stat. Comput.*, 5(3), 543-561, 1984.

Bencala, K.E., Simulation of solute transport in a mountain pool-and-riffle stream with a kinetic mass transfer model, *Water Resour. Res.*, 19(3), 732-738, 1983.

Bencala, K.E., Interactions of solutes and streambed sediment 2. A dynamic analysis of coupled hydrologic and chemical processes that determine solute transport, *Water Resour. Res.*, 20(12), 1804-1814, 1984.

Bencala, K.E., V.C. Kennedy, G.W. Zellweger, A.P. Jackman, R.J. Avanzino, Interactions of solutes and streambed sediment 1. An experimental analysis of cation and anion transport in a mountain stream, *Water Resour. Res.*, 20(12), 179-1803, 1984.

Betson, R.P. and J.P. Marius, Source areas of storm runoff, *Water Resour. Res.*, 5, 574-582, 1969.

Beven, K.J., Hillslope hydrographs by the finite element method, *Earth Surf. Processes*, 2, 13-28, 1977.

Beven, K.J., The hydrological response of headwater and sidelope areas, *Hydrol. Sci. Bull*, 23, 419-437, 1978.

Beven, K.J., Distributed Models, pp 405-435 in *Hydrologic Forecasting*, M.G. Anderson and T.P. Burt (ed), Wiley, 1985.

Beven, K.J., Changing ideas in hydrology – the case of physically based models, *J. Hydrol.*, 105, 157-172, 1989.

Beven, K.J. and R.T. Clarke, On the variation of infiltration into a homogeneous soil matrix containing a population of macropores, *Water Resour. Res.*, 22(3), 383-388, 1986.

Beven, K.J. and P. Germann, Macropores and water flow in soils, *Water Resour. Res.*, 18(5), 1311-1325, 1982.

Beven, K.J. and M.J. Kirkby, A physically based variable contributing area model of basin hydrology, *Hydrol. Sci. Bull.*, 24(1), 43-69, 1979.

Bicknell, B.R., J.C. Imhoff, J.L. Kittle Jr., A.S. Donigian Jr., and R.C. Johanson, *Hydrological Simulation Program – FORTRAN, User's Manual for Release 10*, U.S. EPA Environmental Research Laboratory, Athens, GA, 1993.

Binley, A.M., A. Calver, and E.M. Morris, *The Institute of Hydrology Distributed Model,* Institute of Hydrology Rept. 98, Institute of Hydrology, Oxon, U.K, 1987.

Binley, A.M., J. Elgy, and K.J. Beven, A physically based model of heterogeneous hillslopes, 1, Runoff production, *Water Resour. Res.*, 25(6), 1219-1226, 1989a.

Binley, A.M., K.J. Beven, and J. Elgy, A physically based model of heterogeneous hillslopes, 2, Effective hydraulic conductivities, *Water Resour. Res.*, 25(6), 1227-1234, 1989b.

Bishop, K.H, H.Grip, and A. O'Neill, The origins of acid runoff in a hillslope during storm events, *J. Hydrol.*, 116,35-61, 1990.

Blowes, D.W. and R.W. Gillham, The generation and quality of streamflow on inactive uranium tailings near Elliot Lake, Ontario, *J. Hydrol.*, 97, 1-22, 1988.

Bodvarrson, G.S. and T.M Bandurraga, *Development and Calibration of the Three-Dimensional Site-Scale Unsaturated Zone Model of Yucca Mountain, Nevada*, Lawrence Berkeley National Laboratory, LBNL-39315, 563 pp., 1996.

Bonell. M., Progress in the understanding of runoff generation dynamics in forests, *J. Hydrol.*, 150, 217-275, 1993.

Braden, J.B. and D.L. Uchtman, Agricultural nonpoint pollution control: An assessment, *J. Soil Water Conserv.*, 40, 23-46, 1985.

Bren, L.J., Riparian zone, stream, and floodplain issues: A review, *J. Hydrol.*, 150, 277-299, 1993.

Bronstert, A. and E.J. Plate, Modelling of runoff generation and soil dynamics for hillslopes and microcatchments, *J. Hydrol.*, 189, 177-195, 1997.

Brooks, R.H. and A.T. Corey, *Hydraulic Properties of Porous Media*, Hydrology Paper No. 3, Colorado State Univ., Fort Collins, Colorado, 1964.

Brown, D.L., *An Analysis of Transient Flow in Upland Watersheds: Interactions between Structure and Process*, Ph.D. Dissertation, Dept. of Soil Science, Univ. of California, Berkeley, California, 225 pp., 1995.

Brusseau, M.L. and P.S.C. Rao, Modeling solute transport in structured soils: a review, *Geoderma*, 46, 169-192, 1990.

Burnett, R.D. and E.O. Frind, Simulation of contaminant transport in three dimensions. 2. Dimensionality effects, *Water Resour. Res.*, 23, 695-705, 1987.

Burns, D.A. Speciation and equilibrium relations of soluble aluminum in a headwater stream at base flow and during rainfall events, *Water Resour. Res.*, 25(7), 1653-1665, 1989.

Buttle, J.M, Isotope hydrograph separations and rapid delivery of pre-event water from drainage basins, *Progress in Physical Geography*, 18, 16-41, 1994.

Buttle, J.M. and K. Sami, Testing the groundwater ridging hypothesis of streamflow generation during snowmelt in a forested catchment, *J. Hydrol.*,135, 53-72, 1992.

Calver, A. and W.L. Wood, The Institute of Hydrology Distributed Model, pp 595-626 in *Computer Models of Watershed Hydrology*, V.P. Singh (ed), Water Resour. Publ., Fort Collins, Colorado, 1996.

Castro, N. M and G.M. Hornberger, Surface-subsurface water interactions in an alluviated mountain steam channel, *Water Resour. Res.*, 27(7), 1613-1621, 1991.

Chorley, R.J. The hillslope hydrological cycle, in M.J. Kirkby (ed), *Hillslope Hydrology*, Wiley, New York, pp. 1 - 42, 1978.

Chow, V.T., *Open-channel hydraulics*. McGraw-Hill Book Co., New York, N.Y, 1959.

Chow, V.T. and A. Ben-Zvi, Hydrodynamic modeling of two-dimensional watershed flow, *J. Hyd. Div., ASCE*, 99(HY11), 2023-2040, 1972.

Christophersen, N. and C. Neal, Linking hydrological, geochemical, and soil chemical processes on the catchment scale: an interplay between modeling and field work, *Water Resour. Res.*, 26(12), 3077-3086, 1990.

Cirmo, C.P. and J.J. McDonnell, Linking the hydrologic and biogeochemical controls of nitrogen transport in near-stream zones of temperate-forested catchments: a review, *J.Hydrol.*, 199, 88-120, 1997.

Clement, T.P., W.R. Wise, and F.J. Moltz, A physically based, two-dimensional, finite-difference algorithm for modeling variably-saturated flow, *J. Hydrol.*, 161, 71-90, 1994.

Cooley, R.L., Some new procedures for numerical simulation of variably-saturated flow problems, *Water Resour. Res.*, 19(5), 1271-1285, 1983.

Cooper, H.H. and M.I. Rorabaugh, Groundwater movements and bank storage due to flood stages in surface streams, *U.S. Geol. Surv. Water Supply Pap.*, 1536-J, 343-363, 1963.

Costa, V.A.F., L.A. Oliveira, and A.R. Figueiredo, A control-volume based finite element method for three-dimensional incompressible turbulent fluid flow, heat transfer, and related phenomena, *Int. J. Num. Meth. Fluids*, 21, 591-613, 1995.

Crawford, N.H. and R.K. Linsley, *Digital Simulation of Hydrology, Stanford Watershed Model IV*, Stanford University Technical Report No. 39, Stanford University, Palo Alto, CA, 1966.

Cunningham, A.B. and P.J. Sinclair, Application and analysis of a coupled surface and groundwater model, *J. Hydrol.*, 43, 129-148, 1979.

Cuthill, E. and J. McKee *Reducing the bandwidth of sparse symmetric matrices*, in Proceedings, 24th National Conference of the Association for Computing Machinery, pp. 157-172, Brandon, New York, 1969.

Davidson, M.R., Numerical calculation of saturated-unsaturated infiltration in a cracked soil, *Water Resour. Res.*, 21, 709-714, 1985a.

Davidson, M.R., Asymptotic behavior of infiltration in soils containing cracks or holes, *Water Resour. Res.*, 21(9), 1345-1354, 1985b.

Dawdy, D.R. and J.M Berman, Effect of rainfall variability on streamflow simulation, *Water Resour. Res.*, 5, 56-91, 1969.

di Giammarco, P., E. Todini, and P. Lamberti, A conservative finite elements approach to overland flow: the control volume finite element formulation, *J. Hydrol.*, 175, 267-291, 1996.

Donigian, A.S., D.C. Beyerlein, H.H. Davis, and N.H. Crawford, *Agricultural Runoff Management (ARM) Model Version II: Refinement and Testing,* USEPA Rep. 600/3-77-098. U.S.EPA Environ. Res. Lab., Athens, GA., 1977.

Donigian, A.S. Jr, B.R. Bicknell, and J.C. Imhoff, Hydrological Simulation Program - FORTRAN (HSPF), pp 395-442 in *Computer Models of Watershed Hydrology*, V.P. Singh (ed), Water Resour. Publ., Fort Collins, Colorado, 1996.

Dunne, G.H. and R.E. Phillips, Equivalent diameter of simulated macropore systems during saturated flow, *Soil Sci. Soc. Am. J.*, 55, 1244-1248, 1991.

Dunne, T., Field studies of hillslope flow processes, in M.J. Kirkby (ed), *Hillslope Hydrology*, Wiley, New York, pp. 227 - 293, 1978.

Dunne, T., Relation of field studies and modeling in the prediction of storm runoff, *J. Hydrol.*, 65, 25-48, 1983.

Dunne, T. and R.D. Black, An experimental investigation of runoff prediction in permeable soils, *Water Resour. Res.*, 6, 478-490, 1970.

Dunne, T., W. Zhang, and B.F. Aubry, Effects of rainfall, vegetation, and microtopography on infiltration and runoff, *Water Resour. Res.*, 27(9), 2271-2285, 1991.

Edwards, W.M., R.R. van der Ploeg, and W. Ehlers, A numerical study of the effects of noncapillary-sized pores upon infiltration, *Soil Sci. Soc. Am. J.*, 43, 851-856, 1979.

Elliott, A.H. and N.H. Brooks, Transfer of nonsorbing solutes to a streambed with bed forms: Theory, *Water Resour. Res.*, 33(1), 123-136, 1997a.

Elliott, A.H. and N.H. Brooks, Transfer of nonsorbing solutes to a streambed with bed forms: Laboratory Experiments, *Water Resour. Res.*, 33(1), 137-151, 1997b.

Elsenbeer, H., D. Lorieri, and M. Bonell, Mixing model approaches to estimate storm flow sources in an overland flow-dominated tropical rain forest catchment, *Water Resour. Res.*, 31(9): 2267-2278, 1995.

Eshleman, K.N., J.S. Pollard, and A.K. O'Brien, Determination of contributing areas for saturation overland flow from chemical hydrograph separations, *Water Resour. Res.*, 29(10): 3577-3587, 1993.

Feddes, R.A, P.J. Kowalik, and H. Zaradny, *Simulation of Field Water Use and Crop Yield, Simulation Monographs*, 188 pp., Pudoc, Wageningen, The Netherlands, 1978.

Feddes, R.A., P. Kabat, P.J.T. van Bakel, J.J.B Bronswijk, and J. Halbertsma, Modelling soil water dynamics in the unsaturated zone – state of the art, *J. Hydrol.*, 100, 69-111, 1988.

Feng, K. and F.J. Molz, A 2-D, diffusion-based, wetland flow model, *J. Hydrol.*, 196: 230-250, 1997.

Forster, C. and L. Smith, Groundwater flow systems in mountainous terrain, 1. Numerical modelling technique, *Water Resour. Res.*, 24(7), 999-1010, 1988.

Forsyth, P.A., Comparison of the single-phase and two-phase numerical formulation for saturated-unsaturated groundwater flow, *Comput. Methods Appl. Mech. Engr.*, 69, 243-259, 1988.

Forsyth, P.A. and R.B. Simpson, A two-phase, two component model for natural convection in a porous medium, *Int. J. Num. Meth. Fluids*, 12, 655-682, 1991.

Forsyth, P.A., Three dimensional modelling of steam flush for DNAPL site remediation, *Int. J. Num. Meth. Fluids*, 19, 1055-1081, 1994.

Forsyth, P.A., Y.S. Wu, and K. Pruess, Robust numerical methods for saturated-unsaturated flow with dry initial conditions in heterogeneous media, *Adv. Water Resour.*, 18, 25-38, 1995.

Forsyth, P.A., A.J.A. Unger, and E.A. Sudicky, Nonlinear iteration methods for nonequilibrium multiphase subsurface flow, *Adv. Water Res*, 21, 433-449, 1998.

Freeze, R.A., Three-dimensional transient saturated-unsaturated flow in a groundwater basin, *Water Resour. Res.*, 7(2), 347-366, 1971.

Freeze, R.A., Role of subsurface flow in generating surface runoff 1. Base flow contributions to channel flow, *Water Resour. Res.*, 8(3), 609-624, 1972a.

Freeze, R.A., Role of subsurface flow in generating surface runoff 2. Upstream source areas, *Water Resour. Res.*, 8(5), 1272-1283, 1972b.

Freeze, R.A., Streamflow generation, *Rev. Geophys. and Space Phys.*, 12(4), 627-647, 1974.

Freeze, R.A., Mathematical models of hillslope hydrology, in M.J. Kirkby (ed), *Hillslope Hydrology*, Wiley, New York, pp. 177 - 225, 1978.

Freeze, R.A., A stochastic-conceptual analysis of rainfall-runoff processes on a hillslope, *Water Resour. Res.*, 16(2), 391-408, 1980.

Freeze, R.A. and R.L. Harlon, Blueprint for a physically-based, digitally-simulated hydrologic response model, *J. Hydrol.*, 9, 237-258, 1969.

Freeze, R.A. and P.A Witherspoon, Theoretical analysis of regional groundwater flow, 3, Quantitative interpretations, *Water Resour. Res.*, 4, 581-590, 1968.

Frind, E.O., Simulation of long-term transient density-dependent transport in groundwater contamination problems, *Adv. Water Resour.*, 5(2), 73-88, 1982.

Gee, G.W., C.T. Kincaid, R.J. Lenhard, and C.S. Simmons, Recent studies of flow and transport in the vadose zone, *Rev. Geophys. Suppl.*, 227-238, 1991.

Genereux, D.P., H.F. Hemond, and P.J. Mulholland, Spatial and temporal variability in streamflow generation on the West Fork of Walker Branch Watershed, *J. Hydrol.*, 142, 137-166, 1993.

Germann, P.F., Kinematic wave approach to infiltration and drainage into and from soil macropores, *Trans. Am. Soc. Agric. Eng.*, 28(3), 990-996, 1985.

Germann, P.F., Approaches to rapid and far-reaching hydrologic process in the vadose zone, *J. Contam. Hydrol.*, 3, 115-127, 1988.

Gerke, H.H. and M.T. van Genuchten, A dual-porosity model for simulating the preferential movement of water and solutes in structured porous media, *Water Resour. Res.*, 29(2), 305-319, 1993a.

Gerke, H.H. and M.T. van Genuchten, Evaluation of a first-order water transfer term for variably-saturated dual-porosity flow models, *Water Resour. Res.*, 29(4), 1225-1238, 1993b.

Gerke, H.H. and M.T. van Genuchten, Macroscopic representation of structural geometry for simulating water and solute movement in dual-porosity media, *Adv. Water Resour.*, 19(6), 343-357, 1996.

Germann, P.F. Macropores and hydrologic hillslope processes, pp 327-363 in *Process Studies of Hilllslope Hydrology*, M.G. Anderson and T.P. Burt (ed), Wiley, 1990.

Germann, P.F. and K. Beven, Kinematic wave approximation to infiltration into soils containing sorbing macropores, *Water Resour. Res.*, 21(7), 990-996, 1985.

Giambelluca, T.W. and K. Loague, Evaporation from an experimental catchment near Coos Bay, Oregon. *J. Hydrol.* (in preparation), 1998.

Gillham, R.W., The capillary fringe and its effect on water-table response, *J. Hydrol.*, 67(4), 307-324, 1985.

Gillham, R.W., A. Klute, and D.F. Heerman, Hydraulic properties of a porous medium; measurement and emperical representation, *Soil Sci. Soc. Amer. Proc.*, 40, 203-207.

Gillham, R.W., E.A. Sudicky, J.A. Cherry, and E.O Frind. An advection-diffusion concept for solute transport in heterogeneous unconconsolidated geologic deposits, *Water Resour. Res.*, 20:369.

Gottardi, G. and M. Venutelli, A control-volume finite-element model for two-dimensional overland flow, *Adv. Water Resour.*, 16, 277-284, 1993.

Govindaraju, R.S. and M.L. Kavvas, Dynamics of moving overland flows over infiltrating surfaces at hillslopes, *Water Resour. Res.*, 27(8), 1885-1898, 1991.

Govindaraju, R.S., Modeling overland flow contamination by chemicals mixed in shallow soil horizons under variable source area hydrology, *Water Resour. Res.*, 32(3), 753-758, 1996.

Grayson, R.B., I.D. Moore, and T.A. McMahon, Physically based hydrologic modeling, 1. A terrain-based model for investigative purposes, *Water Resour Res.*, 28(10), 2639-2658, 1992.

Green, N.H. and C.A. Ampt, Flow of air and water through soils, *J. Agric. Sci.*, 4, 1-24, 1911.

Gwo, J.P., P.M. Jardin, G.T. Yeh, and G.V. Wilson, *MURF user's guide: A finite-element model of multiple-pore-region flow through variably-saturated subsurface media* (Report ORNL-GWPO-011), Oak Ridge National Laboratory, Oak Ridge, TN, 1994.

Harvey, J.W. and K.E. Bencala, The effect of streambed topography on surface-subsurface water exchange in mountain catchments, *Water Resour. Res.*, 29(1), 89-98, 1993.

Havis, R.N., R.E. Smith, D.D. Adrian, Partitioning solute transport between infiltration and overland flow under rainfall, *Water Resour. Res.*, 28(10), 2569-2580, 1992.

Hewlett, J.D. and R. Hibbert, Factors affecting the response of small watersheds to precipitation in humid areas, in *International Symposium of Forest Hydrology*, edited by W.E. Sopper and H.W. Lull, pp. 275-290, Pergamon, New York, 1967.

Hoogmoed, W.B. and J. Bouma, A simulation model for predicting infiltration into cracked clay soil, *Soil Sci. Soc. Am. J.*, 44, 458-461, 1980.

Horton, R.E., The role of infiltration in the hydrological cycle, *Eos Trans. AGU*, 14, 446-460, 1933.

Hromadka, T.V., C.E. Berenbrock, J.R. Freckleton, and G.L. Guyman, A two-dimensional dam-break flood plain model, *Adv. Water Resour.*, 8, 7-14, 1985.

Hromadka, T.V., R.H. McCuen, and C.C. Yen, Comparison of overland flood hydrograph models, *J. Hydr. Eng., ASCE*, 13(11), 1422-1440, 1987.

Huber, W.C., EPA Storm Water Management Model – SWMM, pp 783-808 in *Computer Models of Watershed Hydrology*, Water Resour. Publ., Fort Collins, Colorado, 1996.

Huber, W.C. and R.E. Dickenson, *Storm Water Management Model User's Manual, Version 4*, EPA/600/3-88/001a, U.S. EPA, Athens, GA, 1988.

Huyakorn, P.S. and G.F. Pinder, *Computational Methods in Subsurface Flow*, Academic Press, New York, 1983.

Huyakorn, P.S., B.G. Jones, and P.F. Anderson, Finite element algorithms for simulating three-dimensional groundwater flow and solute transport in multilayer systems, *Water Resour. Res.*, 22(3), 361-374, 1986a.

Huyakorn, P.S., E.P. Springer, V. Guvanasen, and T.D. Wadsworth, A three-dimensional finite-element model for simulating water flow in variably-saturated porous media, *Water Resour. Res.*, 22(13), 1790-1808, 1986b.

Huyakorn, P.S., S.D. Thomas, and B.M. Thompson, Techniques for making finite elements competitive in modeling flow in variably-saturated porous media, *Water Resour. Res.*, 20(8), 1790-1808, 1984.

HydroGeoLogic, Inc., *CMM - A semi-analytical computer model for simulating ground water fate and transport of contaminants subject to chained-decay reactions,* Prepared for USEPA Office of Solid Waste, Contract No. 68-WO-0029, 1991.

Izzard, C.F., Hydraulics of runoff from developed surfaces, *Proceedings, Highway Research Board*, 26, 129-146, 1946.

Jackman, A.P., R.A. Walters, and V.C. Kennedy, Transport and concentration controls for chloride, strontium, potassium and lead in Uvas Creek, a small cobble-bed stream in Santa Clara County, California, U.S.A., 2, Mathematical Modelling, *J. Hydrol.*, 75, 111-141, 1984.

Jackson, C.R., Hillslope infiltration and lateral downslope unsaturated flow, *Water Resour. Res.*, 28(9), 2533-2539, 1992.

Jarvis, N.J., P.E. Jansson, P.E. Dik, and I. Messing, Modelling water and solute transport in macoporous soil: 1. Model description and sensitivity analysis, *J. Soil Sci.*, 42, 59-70, 1991.

Kennedy, V.C., C. Kendall, G.W. Zellweger, T.A. Wyerman, and R.J. Avanzino, Determination of the components of stormflow using water chemistry and environmental isotopes, Mattole River Basin, California, *J. Hydrol.*, 84, 107-140, 1986.

Kirkby, M.J. (editor), *Hillslope Hydrology,* Wiley, New York, pp. 389, 1978.

Kirkby, M.J., Hillslope runoff processes and models, *J. Hydrol.*, 100, 315-339, 1988.

Kirkby, M.J. and R.J. Chorley, Throughflow, overland flow, and erosion, *Int. Assoc. Sci. Hydrol. Bull*, 12, 5021, 1967,

Kouwen, N., Modern approaches to design of grassed channels, *J. Irrig. Drain. Eng.*, 118(5), 733-743, 1992.

Kropinski, M.C.A., Numerical techniques for saturated-unsaturated flow. M.Sc. thesis, University of Waterloo, Dept. of Applied Mathematics, Waterloo, Ontario, 1990.

Leonard, R.A., Movement of pesticides into surface waters, pp. 303-349 in *Pesticides in the Soil Environment*, SSSA Book Ser., Vol. 2, H.H. Cheng (ed), Soil Science Society of America, Madison, WI, 1990.

Letniowski, F.W. and P.A. Forsyth, A control volume finite element method for three-dimensional NAPL groundwater contamination, *Int. J. Num. Meth. Fluids*, 13, 955-970, 1991.

Loague, K.M. and R.A. Freeze, A comparison of rainfall-runoff modeling techniques on small upland catchments, *Water Resour. Res.*, 21: 229-248, 1985.

Lundin, L., Soil water chemistry dependence on water pathways and turnover, *Water, Air, and Soil Poll.*, 85: 1695-1700, 1995.

Luxmoore, R.J., P.M Jardine, G.V. Wilson, J.R. Jones, and L.W. Zelazny, Physical and chemical controls of preferred path flow through a forested hillslope, *Geoderma*, 46, 139-154, 1990.

MacFarlane, D.S., J.A. Cherry, R.W. Gillham, and E.A. Sudicky, Migration of contaminants in groundwater at a landfill: A case study 1. Groundwater flow and plume delineation. In: J.A. Cherry (Guest Editor), Migration of Contaminants in Groundwater at a Landfill: A Case Study, *J. Hydrol.*, 63, 1-29, 1983.

MacQuarrie, K.T.M. and E.A. Sudicky, On the incorporation of drains into three-dimensional variably saturated groundwater flow models, *Water Resour. Res.*, 32(2), 477-482, 1996.

Manning, R., On the flow of water in open channels and pipes, *Trans. Inst. Civ. Eng. Ireland*, 20, 161-207, 1891.

Maulem, Y., A new model for predicting the hydraulic conductivity of unsaturated porous media, *Water Resour. Res.*, 12(3), 513-522, 1976.

McCord, J.T., D.B. Stephens, and J.L. Wilson, Hysteresis and state-dependent anisotropy in modeling unsaturated hillslope hydrologic processes, *Water Resour. Res.*, 27, 1501-1518, 1991.

McDonnell, J.J., A rationale for old water discharge through macropores in a steep, humid catchment. *Water Resour. Res.*, 26(11), 2821-2832, 1990.

McDonnell, J.J. and J.M. Buttle, Comment on Jayatilaka, C.J. and R.W. Gillham "A deterministic-empirical model of the effect of the capillary fringe on near-stream area runoff 1. Description of the model. *J. Hydrol.*, 184: 299-315", Submitted to *J. Hydrol.*, 1997.

McKnight, D.M. and K.E. Bencala, The chemistry of iron, aluminum, and dissolved organic material in three acidic, metal-enriched, mountain streams, as controlled by watershed and in-stream processes, *Water Resour. Res.*, 26(12): 3087-3100, 1990.

McMahon, P.B and J.K. Bohlke, Denitrification and mixing in a stream-aquifer system: effects on nitrate loading to surface water, *J. Hydrol.*, 186, 105-128, 1996.

Meselhe, E.A. and F.M Holly, Simulation of unsteady flow in irrigation canals with dry bed, *J. Hydraul. Eng.*, 119(9), 1021-1039, 1993.

Metcalf and Eddy, Inc., Univerisity of Florida, and Water Resource Engineers, Inc., *Storm Water Management Model, Volume I – Final Report,* EPA Report 11024DOC07/71, U.S. EPA, Washington, DC, 1971.

Millington, R.J., Gas diffusion in porous media, *Science*, 130: 100-102, 1959.

Millington, R.J. and J.M. Quirk, Permeability of porous solids, *Trans. Faraday Soc.*, 57: 1200-1207, 1961.

Molz, F.J., Models of water transport in the soil-plant system: a review, *Water Resour. Res.*, 1981.

Montgomery, D.R., W.E. Dietrich, R. Torres, S.P. Anderson, J.T. Heffner, and K. Loague. Hydrologic response of a steep, unchanneled valley to natural and applied rainfall. *Water Resour. Res.*, 33, 91-109, 1997.

Moore, I.D. and G.F. Foster, Hydraulics and overland flow, in *Process Studies in Hillslope Hydrology*, edited by M.G. Anderson and T.P. Burt, pp 215-254, Wiley, New York, 1990.

Mosley, M.P., Streamflow generation in a forested watershed, New Zealand, *Water Resour. Res.*, 15(4): 795-806, 1979.

Mosley, M.P., Subsurface flow velocities through selected forest soils, South Island, New Zealand, *J. Hydrol.*, 55, 65-92, 1982.

Mulder, J., N. Christophersen, K. Kopperud, and P.H. Fjeldal, Water flow paths and the spatial distribution of soils as a key to understanding differences in streamwater chemistry between three catchments (Norway), *Water, Air, and Soil Poll.*, 81: 67-91, 1995.

Mulholland, P.J., G.V. Wilson, and P.M. Jardine, Hydrogeochemical response of a forested watershed to storms: Effects of preferential flow along shallow and deep pathways, *Water Resour. Res.*, 26(12): 3021-3036, 1990.

Narasimhan, T.N. and P.A. Witherspoon, An integrated finite difference method for analyzing fluid flow in porous media, *Water Resour. Res.*, 12(1), 57-64, 1976.

Narasimhan, T.N., P.A. Witherspoon, and A.L. Edwards, Numerical model for saturated-unsaturated flow in deformable porous media: 1. The algorithm, *Water Resour. Res.*, 14(2), 255-261, 1978.

Neretnieks, I. and A. Rasmuson, An approach to modelling radionuclide migration in a medium with strongly varying velocity and block sizes along the flow path, *Water Resour. Res.*, 20(12), 1823-1836, 1984.

Neumann, S.P., Saturated-unsaturated seepage by finite elements, *J. Hyd. Div., ASCE,* HY12, 2233-2250, 1973.

Nielsen, D.R., M. Th. van Genuchten, and J.W. Biggar, Water flow and solute transport processes in the unsaturated zone, *Water Resour. Res.*, 22(9), 895-1088, 1986.

Nolan, K.M. and B.R. Hill, Storm-runoff generation in the Permanente Creek drainage basin, west central California - an example of flood-wave effects on runoff compositions, *J. Hydrol.*, 113, 343-367, 1990.

Nwankwor, G.I., J.A. Cherry, and R.W. Gillham, A comparative study of specific yield determinations for a shallow sand aquifer, *Ground Water*, 22(6), 764-772, 1984.

O'Connell, P.E. and E. Todini, Modelling of rainfall, flow and mass transport in hydrologic systems: an overview, *J. Hydrol.*, 175, 3-16, 1996.

O'Loughlin, E.M., Saturated regions in catchments and their relations to soil and topographic properties, *J. Hydrol.*, 53, 229-246, 1981.

Ogden, F.L and P.Y. Julien, Runoff sensitivity to temporal and spatial rainfall variability at runoff plane and small basin scales, *Water Resour. Res.*, 29(8), 2589-2597, 1993.

Panday, S., P.S. Huyakorn, R. Therrien, and R.L. Nichols, Improved three-dimensional finite element techniques for field simulation of variably-saturated flow and transport, *J. Contam. Hyd.*, 12, 3-33, 1993.

Paniconia, C. and E.F. Wood, A detailed model for simulation of catchment scale subsurface flow processes, *Water Resour. Res.*, 29(6), 1601-1620, 1993.

Patankar, S.V., *Numerical Heat Transfer and Fluid Flow*, Hemisphere Publishing Corp., New York, 197 pp., 1980.

Pearce, A.J., Streamflow generation processes: and Austral view, *Water Resour. Res.*, 26(12), 3037-3047, 1990.

Perkins, S.P. and A.D. Koussis, Stream-aquifer interaction model with diffusive wave routing, *J. Hydraul. Eng.*, 122, 4, 1996.

Peyton, R.L. and G. Sanders, Mixing in overland flow during rainfall, *J. Enivron. Eng. Div. ASCE*, 116(4), 764-784, 1990.

Pilgrim, D.H., D.D. Huff, and T.D. Steele, A field evaluation of subsurface and surface runoff, II, Runoff proceses, *J. Hydrol.*, 38, 319-341, 1978.

Pinder, G.F. and S.P. Sauer, Numerical simulation of flood wave modification due to bank storage effects, *Water Resour. Res.*, 7(1), 111-121, 1971.

Playán, E., W.R. Walker, and G.P. Merkley, Two-dimensional simulation of basin irrigation. 1: Theory, *J. Irrig. Drainage Eng.*, 120(5), 837-856, 1994.

Pohll, G.M, J.J. Warwick, and S.W. Tyler, Coupled surface-subsurface hydrologic model of a nuclear subsidence crater at the Nevada test site, *J. Hydrol.*, 186, 43-62, 1996.

Ponce, V.M., R.M. Li, and D.B. Simons, Applicability of kinematic and diffusion models, *J. Hyd. Div. ASCE*, 104, 353-360, 1978.

Pruess, K., *TOUGH2 - A general purpose numerical simulator for multiphase fluid and heat flow*, Lawrence Berkeley Laboratory Report LBL-29400, Lawrence Berkeley National Laboratory, Berkeley, CA, 1991.

Preuss, K. and T.N. Narashimhan, A practical method for modelling fluid and heat flow in fractured porous media, *Soc. Petrol. Eng. J.*, 25, 14-26, 1985.

Preuss, K. and J.S.Y. Wang, Numerical modeling of isothermal and nonisothermal flow in unsaturated-saturated fractured rock- A review, in: D.D. Evans and T.J. Nicholson (eds.), *Flow and Transport Through Unsaturated Fractured Rock*, pp. 11-22, Am. Geophys. Union, Washington, DC, 1987.

Quemer, E.P., Description and application of the combined surface and groundwater flow model MOGROW, *J. Hydrol.*, 192, 158-188, 1997.

Ragan, R.M *An experimental investigation of partial area contribution*, Publ. 76, Int. Ass. Sci. Hydrol., Berne, pp 241-249, 1968.

Rasmuson, A., T. Gimmi, and H. Fluhler, Modeling reactive gas uptake, transport, and transformation in aggregated soils, *Soil Sci. Am. J.*, 54, 1206-1213, 1990.

Ray, C., T.R. Ellsworth, A.J. Valoochi, and C.W. Best, An improved dual porosity model for chemical transport in macroporous soils, *J. Hydrol.*, 19,: 270-292, 1997.

Refsgaard, J. and B. Storm, MIKE SHE, pp 809-846 in *Computer Models of Watershed Hydrology*, Water Resour. Publ., Fort Collins, Colorado, 1996.

Richards, L.A., Capillary conduction of liquids in porous mediums, *Physics*, 1, 318-333, 1931.

Richardson, C.P and A.D. Parr, Modified Fickian model for solute uptake by runoff, *J. Env. Eng.*, 114(4), 792-809, 1988.

Richardson, C.P and A.D. Parr, Friction and free-surface flow over porous media, *J. Hydr. Eng.*, 117(11), 1496-1512, 1991.

Rivlin, J. and R. Wallach, An analytical solution for the lateral transport of dissolved chemicals in overland flow, *Water Resour. Res.*, 31(4), 1031-1040, 1995.

Rodhe, A., On the generation of stream runoff in till soils, *Nordic Hydrol.*, 20, 1-8, 1989.

Saad, Y., *Iterative Methods for Sparse Linear Systems,* PWS Publishing Company, Boston, 447 pp., 1996.

Saad, Y. and M.H. Schultz, GMRES: A generalized minimal residual algorithm for solving nonsymmetric linear systems, *SIAM J. Sci. Stat. Comp.*, 7, 856-869, 1986.

Savant, S.A., D.D. Reible, and L.J. Thibodeaux, Convective transport within stable river sediments, *Water Resour. Res.*, 23, 1763-1768, 1987.

Schuurmans, W., *A model to study the hydraulic performance of controlled irrigation canals*, MSc thesis, Delft University of Technology, Delft, The Netherlands.

Sharma, M.L., R.J. Luxmoore, R. DeAngelis, R.C. Ward, and G.T. Yeh, Subsurface water flow simulated for hillslopes with spatially dependent soil hydraulic characteristics, *Water Resour. Res.*, 23(8), 1523-1530, 1987.

Simunek, J., K. Huang, and M.Th. van Genuchten, *The SWMS_3D Code for Simulating Water Flow and Solute Transport in Three-Dimensional Variably-Saturated Media, Version 1.0,* Research Report No. 139, U.S. Salinity Laboratory, USDA, ARS, Riverside, California, 1985.

Singh, V.P., *Kinematic Wave Modeling in Water Resources: Surface Water Hydrology*, John Wiley & Sons, Inc., New York, 1399 pp., 1996a

Singh, V.P., *Computer Models of Watershed Hydrology*, Water Resour. Publ., Fort Collins, Colorado, 1996b.

Sklash, M.G. Environmental isotope studies of storm and snowmelt runoff generation, Ch. 12 in *Process Studies of Hillslope Hydrology*, M.G. Anderson and T.P. Burt, editors, pp. 401-435, 1990.

Sklash, M.G. and R.N. Farvolden, The role of groundwater in storm runoff, *J. Hydrol.*, 43, 45-65, 1979.

Smettem, K.R.J., D.J. Chittleborough, B.G. Richargds, and F.W. Leaney, The influence of macropores on runoff generation from a hillslope soil with a contrasting textural class, *J. Hydrol.*, 122, 235-252, 1991.

Smith, R.E and D.A. Woolhiser, Overland flow on an infiltrating surface, *Water Resour. Res.*, 7(4), 899-913, 1971.

Smith, R.E. and R.H.B. Hebbert, Mathematical simulation of interdependent surface and subsurface hydrologic processes, *Water Resour. Res.*, 19(4), 987-1001, 1983.

Snow, D.T., Anisotropic permeability of fractured media, *Water Resour. Res.*, 5(6), 1273-1289, 1969.

Snyder, J.K. and D.A. Woolhiser, Effects of infiltration on chemical transport into overland flow, *Trans. ASCE*, 1450-1457, 1985.

Stephenson, D. and M.E. Meadows, *Kinematic Hydrology and Modelling*, Elsevier, New York, 250 pp., 1986.

Steenhuis, T.S. and M.F. Walter, Closed form solutions for pesticide loss in runoff water, *Trans. ASCE* 23: 615-620, 1980.

Stauffer, F. and T. Dracos, Experimental and numerical study of water and solute infiltration in layered porous meda, *J. Hydrol.*, 84, 9-34, 1986.

Sudicky, E.A., A natural gradient experiment on solute transport in a sand aquifer; spatial variability of hydraulic conductivity and its role in the dispersion process, *Water Resour. Res.*, 22(13), 2069-2082, 1986.

Sudicky, E.A., The Laplace transform Galerkin technique for efficient time-continuous solution of solute transport in double-porosity media, *Geoderma*, 46: 209-232, 1990.

Sudicky, E.A. and E.O. Frind, Contaminant transport in fractured porous media: Analytical solutions for a system of parallel fractures, *Water Resour. Res.*, 18(3), 1634-1642,1982.

Sudicky, E.A., A.J.A. Unger, and S. Lacombe, A noniterative technique for the direct implementation of well-bore boundary conditions in three-dimensional heterogeneous formations, *Water Resour. Res.*, 32(2), 411-415, 1995.

Therrien, R., E.A. Sudicky, and R.G. McLaren, *User's Guide for NP 3.1, A preprocessor for FRAC3DVS 3.1: An Efficient Simulator for Three-Dimensional, Saturated-Unsaturated Groundwater Flow and Chain Decay Transport in Porous or Discretely-Fractured Porous Formations*, Dept. of Earth Sciences, University of Waterloo, Canada, 77 pp, 1995.

Therrien, R. and E.A. Sudicky, Three-dimensional analysis of variably-saturated flow and transport in discretely fractured porous media, *J. Contam. Hydrol.*, 23,1-44, 1996.

Thibodeaux, L.J. and J.D. Boyle, Bedform-generated convective transport in bottom sediments, *Nature*, 325, 341-343, 1987.

Toth, J., A theoretical analysis of groundwater flow in small drainage basins, *J. Geophys. Res.*, 68, 4795-4812, 1963.

Torres, R., W.E. Dietrich, D.R. Montgomery, S.P. Anderson, and K. Loague. Unsaturated zone processes and the hydrologic response of a steep, unchanneled catchment. *Water Resources Research* (in press), 1998.

Updegraff, C.D, C.E. Lee, and D.P. Gallegos, DCM3D, a dual-continuum, three-dimensional ground-water flow code for saturated, fractured, porous media (Report SAND90-7015), Sandia National Laboratories, Albequerque, NM, 1991.

Unger, A.J.A., P.A. Forsyth, and E.A. Sudicky, Variable spatial and temporal weighting schemes for use in multi-phase compositional problems, *Adv. Water Resour.*, 19(1), 1-27, 1996.

U.S. Department of Agriculture, Agricultural Research Services (USDA-ARS). Hydrology, Erosion and Water Quality Studies in the Southern Great Planes Research Watershed, Southwestern Oklahoma, 1961-1078. Agricultural Reviews and Manuals, ARM-S-29, 1983.

U.S. Environmental Protection Agency (USEPA), Clean Water Action Plan: Restoring America's Waters, EPA-840-R-98-001, available at http://www.epa.gov/cleanwater, 1998.

VanderKwaak, J.E. and E.A. Sudicky, Natural coupling of surface and groundwater flow in numerical models, *EOS Trans. AGU*, 77(45), F219, 1995.

VanderKwaak, J.E. and E.A. Sudicky, Simulating flow and transport in coupled surface-subsurface hydrologic systems, *EOS Trans. AGU*, 77(46), F264, 1996.

VanderKwaak, J.E., P.A. Forsyth, K.T.B. MacQuarrie, and E.A. Sudicky, *User's Guide, WatSolv Sparse Matrix Iterative Solver Package, Version 2.16,* Waterloo Centre for Groundwater Research, Univ. of Waterloo, Waterloo, Ontario. 23 pp, 1997.

Vaux, W.G., Intragravel flow and interchange of water in a streambed, *Fish. Bull.,* 66, 479-489, 1968.

van der Vorst, H, Bi-CGSTAB: A fast and smoothly converging variant of Bi-CG for the solution of nonsymmetric linear systems, *SIAM J. Sci. Stat. Comput.,* 13, 631-664, 1992.

van Genuchten, M. Th., A closed-form equation for predicting the hydraulic conductivity of unsaturated soils, *Soil Sci. Soc. Am.,* 44, 892-898, 1980.

van Genuchten, M. Th. and F.N. Dalton, Models for simulating salt movement in aggregated field soils, *Geoderma,* 38, 165-183, 1986.

van Genuchten, M. Th. and W.A. Jury, Progress in unsaturated flow and transport modeling, *Reviews of Geophysics,* 25(2), 135-140, 1987.

van Genuchten. M. Th. and P.J. Wierenga, Mass transfer studies in sorbing porous media: analytical solution, *Soil Sci. Soc. Am. J.,* 40, 473-480, 1976.

van Leer, B., Towards the ultimate conservative difference scheme II Monotonicitiy and conservation combined in a second order scheme, *J. Comp. Phys.,* 14, 361-370, 1974.

Vauclin, M., D. Khanji, and G. Vachaud, Experimental and Numerical Study of a Transient, Two-Dimensional Unsaturated-Saturated Water Table Recharge Problem, *Water Res. Res.,* 15(5), 1089-1101, 1979.

Vieira, J.H.D., Conditions governing the use of approximations for the Saint-Venant equations for shallow surface water flow, *J. Hydrol.,* 60, 43-58, 1983.

Waddington, J.M., N.T. Roulett, and A.R. Hill. Runoff mechanisms in a forested groundwater discharge wetland, *J. Hydrol.,* 147, 37-60, 1993.

Wallach, R., W.A. Jury, W.F. Spencer, Transfer of chemicals from soil solution to surface runoff: a diffusion-based soil model, *Soil Sci. Soc. Am. J.,* 52(3), 612-618, 1988.

Wallach. R., W.A. Jury, and W.F. Spencer, The concept of convective mass transfer for prediction of surface-runoff pollution by soil surface applied chemicals, *Trans. ASAE*, 32(3), 906-912, 1989.

Wallach, R.T, M.T. van Genuchten, and W. F. Spencer, Modeling solute transfer from soil to surface runoff: the concept of effective depth of transfer, *J. Hydrol.*, 109, 307-317, 1989.

Wallach, R. and M.T. van Genuchten, A physically based model for predicting solute transfer from soil solution to rainfall-induced runoff water, *Water Resour. Res.*, 26(9), 2119-2126, 1990.

Wang, J.S.Y and T.N. Narasimhan, Hydrologic mechanisms governing fluid flow in partially saturated, fractured, porous medium, *Water Resour. Res.*, 21(12): 1861-1874, 1985.

Warren, J.E. and P.J. Root, The behavior of naturally fractured reservoirs, *Soc. Petrol. Eng. J., AIME*, 228, 3(3), 245-255, 1963.

Wheater, H.S., K.H. Bishop, and M.B., The identification of conceptual hydrological models for surface water acidification, *Hydrol. Proc.*, 1: 89-109, 1986.

White, R.E., The influence of macropores on the transport of dissolved and suspended matter throuth soil, *Adv. in Soil Sci.*, 3, Springer-Verlag, New York, pp 95-120, 1985.

Whipkey, R.Z., Subsurface stormflow from forested slopes, *Bull. Int. Assoc. Sci. Hydrol.*, 10, 74-85, 1965.

Whipkey, R.Z. and M.J. Kirkby, Flow within the soil, pp 121-144 in *Hillslope Hydrology*, M.J. Kirby (ed), Wiley, New York, 1978.

Wilson, G.V, P.M. Jardine, R.J. Luxmoore, L.W. Zelazny, D.E. Todd, and D.A. Lietzke, Hydrogeochemical processes controlling subsurface transport from an upper subcatchment of Walker Branch Watershed during storm events, 2, Solute transport processes, *J. Hydrol.*, 1990.

Winter, T.C., The interaction of lakes with variably-saturated porous media, *Water Resour. Res.*, 19: 1203-1218, 1983.

Wooding, R.A., A hydraulic model for the catchment-stream problem. 1. Kinematic wave theory, *J. Hydrol.*, 3, 254-267, 1966a.

Wooding, R.A., A hydraulic model for the catchment-stream problem. 2. Numerical solution, *J. Hydrol.*, 3, 268-282, 1966b.

Woolhiser, D.A., R.E. Smith, and D.C. Goodrich, *KINEROS, A Kinematic Runoff and Erosion Model: Documentation and User Manual.* U.S. Department of Agriculture, Agricultural Research Service, ARS-77, 130 pp., 1990.

Woolhiser, D.A., R.E. Smith, and J.-V. Giraldez, Effects of spatial variability of saturated hydraulic conductivity on Hortonian overland flow, *Water Resour. Res.*, 32(3), 671-678, 1996.

Wu, Y.S., P.A. Forsyth, and H. Jiang, A consistent approach for applying numerical boundary conditions for multiphase subsurface flow, *J. Contam . Hyd.*, 23, 157-184, 1996.

Xanthopoulos, Th. and Ch. Koutitas, Numerical simulation of a two-dimensional flood wave propagation due to dam failure, *J. Hyd. Res.*, 14(4), 321-331, 1976.

Zaslevsky, D. and G. Sinai, Surface hydrology, 1, In surface transient flow, *J. Hydraul. Div. ASCE*, 107, 65-93, 1981.

Zhang, W. and T.W. Cundy, Modeling of two-dimensional overland flow, *Water Resour. Res.*, 25(9), 2019-2035, 1989.

Zienkiewicz, O.C., *The Finite Element Method in Engineering Science*, McGraw-Hill, London, 1971.

Zimmerman, R.W., T. Hadgu, and G.S. Bodvarsson, A new lumped-parameter model for flow in unsaturated dual-porosity media, *Adv. Water Resour.*, 19(5), 317-327, 1996.